DISSERTATION
submitted to the
Combined Faculties of the Natural Sciences and Mathematics
of the Ruperto-Carola-University of Heidelberg, Germany
for the degree of
Doctor of Natural Sciences

Put forward by
M.Sc. David Gerbert
Born in Heidelberg

Oral Examination: 20.4.2017

Charge Transfer and Band Formation at Metal/Organic Interfaces

Referees: Prof. Dr. Annemarie Pucci
Prof. Dr. Wolfgang Kowalsky

Charge Transfer and Band Formation at Metal/Organic Interfaces – Both, well-defined molecular ordering and the electronic structure at metal/organic interfaces and within thin molecular films are fundamental for charge carrier injection and charge transport in organic electronic devices. This thesis presents a combined study of temperature-programmed desorption, ultraviolet and two-photon photoemission spectroscopy targeting the underlying correlation between charge transfer, hybridization and band formation. Angle-resolved photoemission measurements expose that hybridization at metal/organic interfaces implies a charge carrier density redistribution which in combination with band formation presumably enables improved charge injection. As hybrid bands crossing the Fermi energy additionally determine the transferred amount of charge, charge transfer may serve as sufficient prerequisite for underlying hybridization or band formation at metal/organic interfaces. The observation of an extended space charge region and unoccupied intermolecular hybridization in epitaxial films additionally proves increased charge carrier injection properties in thin molecular films with well-defined molecular ordering and electronic structure.

Ladungstransfer und Bandausbildung an Metall/Organik-Grenzflächen – Sowohl die Anordnung der Moleküle, als auch die elektronische Struktur an Metall/Organik-Grenzflächen oder in dünnen Molekülfilmen beeinflussen grundlegend die Ladungsinjektion und den Ladungstransport in optoelektronischen Bauelementen. Im Rahmen dieser Arbeit wird mittels Temperatur-programmierter Desorptionsspektroskopie, UV-Photoelektronenspektroskopie und Zwei-Photonen-Photoelektronenspektroskopie der zugrunde liegende Zusammenhang zwischen Ladungstransfer, Hybridisierung und Bandausbildung untersucht. Winkelaufgelöste Photoemissions-Messungen zeigen, dass Hybridisierung eine Ladungsdichte-Umverteilung an Metall/Organik-Grenzflächen bewirkt, die in Kombination mit Bandausbildung eine verbesserte Ladungsinjektion ermöglicht. Da zusätzlich auch Hybridbänder nahe der Fermi-Energie den vorherrschenden Ladungstransfer bestimmen, kann dieser als hinreichender Hinweis auf eine Hybridisierung oder gar Bandausbildung an Metall/Organik Grenzflächen angesehen werden. Das Ausbilden einer ausgedehnten Raumladungszone und unbesetzter, intermolekularer Hybridbänder in epitaktischen Filmen unterstreicht außerdem die dadurch erhöhte Ladungsinjektion in dünnen Molekülfilmen mit wohldefinierter Molekülordnung und elektronischer Struktur.

Contents

List of Figures

List of Tables

1. Introduction

In the last decade, organic (opto)electronic devices became more popular and frequently used. Especially state of the art smart phone displays or TV screens apply organic light emitting diodes (OLEDs) due to their high energy efficiency, low-weight and low-cost character [1–4]. The great possibility to manufacture organic materials by evaporation or printing processes enables their application on flexible or transparent substrates which opens new fields of applications of organic electronic devices in lighting and display technology [1–12], photovoltaics [13–22], sensor technology [23–28] and data storaging [29–33]. Therefore the invention and development of organic electronic devices is accompanied by huge efforts in academical research to gain fundamental comprehension of their functionality and performance-determining characteristics. From a chemical point of view the design of new promising molecules and the tuning of employed molecules' properties represents the main objective to gain good air stability, processability, as well as high inter- and intramolecular charge carrier mobilities [34–38]. For physics the improvement of efficiency and performance due to an enhanced charge carrier injection, charge carrier transport and light emission or absorption is subject of countless studies [39–43]. In this context, charge carrier injection was often found to dominantly determine the performance of organic (opto)electronic devices. Many experimental and theoretical studies targeted charge carrier injection improvement in the last decade, however, up to today, a comprehensive understanding of possibly participating mechanisms is missing [44–51]. It is reliable, that the structural arrangement of molecules in thin films and at metal/organic interfaces plays a crucial role in charge transport and charge injection characteristics [52–55]. But little is known about the underlying mechanism: How do charge carriers get from an electrode into an adsorbed organic semiconductor? From an electronic point of view the charge carriers have to overcome an injection barrier which determined by the difference in binding energy before and after the transfer [46, 51, 56, 57]. But it is difficult to connect this energetic barrier to molecular ordering at metal/organic interface.

One possibility to explain a connection between molecular ordering and charge carrier injection might be hybrid band formation between metal bands and molecular electronic states directly at the interface. In doing so a well-ordered adsorbate layer is the fundamental prerequisite to achieve a well-defined interfacial electronic structure with possible hybrid band formation as also known from particular molecular crystals [58–65]. Indeed, a few of experimental studies substantiate band formation at metal/organic interfaces [66–71].

Another essential prerequisite for hybridization at metal/organic interfaces should be a certain electronic interaction between metal and adsorbate as for instance a charge transfer type interaction. In general charge transfer describes the reorganization of charge density caused by the interaction between two different molecules or an inorganic (metallic) surface and a molecule. This process gains its importance for organic electronic devices from the fact that metal/organic interfaces or doped molecular thin films are present in all different forms of these components. It is known since the 1960s (and was honored with the Nobel prize in chemistry in 2000 for A. J. Heeger, A. G. MacDiarmid and H. Shirakawa) that doping can enormously increase the conductivity of organic thin films [34, 41, 72–83]. Even charge injection per se can benefit from a charge transfer type interaction [44, 45, 47, 50, 56, 84–90].

Briefly, well-defined metal/organic interfaces which are characterized by a well-defined geometric structure as well as a charge transfer type interaction should be predestined for the study of hybridization and band formation. The main purpose of this thesis is the investigation of the electronic structure of metal/organic interfaces which feature a charge transfer type interaction in order to study a possible connection between charge transfer, hybridization and band formation. Separately, charge transfer, hybridization and band formation at metal/organic interfaces have been intensively investigated in the last decades using a wide range of different spectroscopic methods such as Raman spectroscopy [91], high-resolution electron energy loss spectroscopy (HREELS) [92, 93], scanning tunneling microscopy and spectroscopy (STM & STS) [66, 68, 71, 94–98], ultraviolet and X-ray photoemission spectroscopy (UPS & XPS) [47, 48, 99–103], angle-resolved photoemission (ARPES) [67, 69, 71, 104] or time- and angle-resolved two-photon photoemission spectroscopy (TR2PPE & AR2PPE) [105–108]. Conventional ARPES is a popular experimental tool to analyze the occupied band structure of metals or inorganic semiconductor surfaces and their interfaces with thin organic films [109–112]. It permits direct access to band dispersion in the reciprocal lattice space and enables the possibility to investigate occupied band formation at metal/organic interfaces. Two-photon photoemission spectroscopy (2PPE) in addition allows the investigation of band formation via the dispersion of unoccupied electronic states as also known for

STS [66, 68, 71, 95, 108, 113, 114]. Moreover, 2PPE can be performed in a time-resolved manner which facilitates the characterization of excited electronic states [115–124]. This combination of powerful possibilities constitutes 2PPE as unique experimental tool to investigate the electronic structure of metal/organic interfaces and thin adsorbate layers.

The present thesis exposes a connection between band formation and charge transfer at metal/organic interfaces by means of UPS and 2PPE. For this purpose the electronic structure of three different organic semiconductor adsorbates is determined on the Au(111) surface. Furthermore, temperature-programmed desorption (TPD) is used to study possible intermolecular interactions of adsorbates especially in the submonolayer regime. More precisely, this thesis addresses the electronic structure of two famous organic acceptor molecules, namely tetracyanoquinodimethane (TCNQ) and its fluorinated derivative tetrafluoro-tetracyanoquinodimethane (F_4TCNQ), adsorbed on Au(111). The electronic structure of these interfaces are compared with the electronic structure of tetrathiafulvalene (TTF), a donor molecule, adsorbed on the same metal surface. It turns out that these three metal/organic interfaces cover three possible charge states of the adsorbed molecules on a Au(111) surface: neutral (TCNQ), negatively charged (F_4TCNQ) and positively charged (TTF). The electronic structure of both, the F_4TCNQ/Au(111) interface as well as the TTF/Au(111) interface, give evidence for an interfacial hybridization of metal bands and adsorbate-induced electronic states, whereas in first instance the TCNQ/Au(111) interface displays no indications for a charge transfer type interaction. Nonetheless, a photo-induced charge transfer can be also observed at the TCNQ/Au(111) interface. Subsequently performed ARPES and AR2PPE studies expose hybridization and band formation at the F_4TCNQ/Au(111) as well as the TTF/Au(111) interface. Whereas the latter is characterized by delocalized interfacial hybrid bands, the F_4TCNQ/Au(111) interface constitutes the first metal/organic hybrid interface at which both, interfacial hybrid bands and intermolecular hybrid bands, can be simultaneously observed. This fact is verified by coverage-dependent measurements which expose intermolecular hybrid band formation and the formation of an extended space charge region in epitaxial F_4TCNQ films. Moreover, a TR2PPE study reveals that the well-defined electronic structure strongly impacts hot electron dynamics at the TTF/Au(111) interface.

Conclusively, the results of this thesis suggest a correlation between hybridization, charge transfer and band formation at metal/organic interfaces. Generally hybridization at metal/organic interfaces implies a redistribution of the interfacial charge carrier density. In case of band formation, these charge carriers are delocalized parallel to the surface which presumably enables improved charge injection across the interface. Additionally, the hybridization induced charge redistribution in combination with hybrid bands crossing the Fermi energy determines the transferred amount of charge at a metal/organic interface. That is why the observation of charge transfer may prospectively serve as sufficient prerequisite for underlying hybridization and/or band formation at well-ordered metal/organic interfaces.

Outline

The presented thesis is structured as follows: First, chapter 2 introduces basic theoretical concepts to describe the electronic properties of metal/organic interfaces. Therefore a basic overview about the electronic structure of condensed matter and electronic states at metal surfaces is followed by the description of theoretical models which are commonly applied to explain charge transfer mechanisms and energy level alignment at metal/organic interfaces. Furthermore, chapter 3 covers physical principles of UPS and 2PPE and briefly illustrates the experimental setup, measurement procedures and recent research on metal/organic interfaces by means of 2PPE. These contents are followed by preparatory discussions of the Au(111) surface's electronic structure in chapter 4 and temperature-programmed desorption studies which support an introduction of the investigated metal/organic interfaces in chapter 5. Chapter 6 contains first UPS and 2PPE results in order to determine the electronic structure of the TCNQ/Au(111), the F_4TCNQ/Au(111) and the TTF/Au(111) interface. It represents the basis for subsequent chapters which cover a characterization of a photo-induced charge transfer at the TCNQ/Au(111) interface (chapter 7) and the demonstration of an extended space charge region in combination with unoccupied band formation in epitaxial F_4TCNQ films (chapter 8). In chapter 9 band formation at the F_4TCNQ/Au(111) as well as the TTF/Au(111) interface is discussed with regard to a possible general correlation between hybridization, band formation and charge transfer at metal/organic interfaces. Time-resolved 2PPE investigations targeting hot electron dynamics at metal/organic interfaces complete the results of this thesis in chapter 10.

2. Theoretical Fundamentals

The following chapter contains basic theoretical concepts which are needed to discuss the electronic structure of metal/organic interfaces. For this purpose the electronic structure of metal surfaces provides an ideal starting point which is followed by organic semiconductor fundamentals and the most common charge transfer models. The last section explicitly deals with the electronic structure at metal/organic interfaces, the impact of charge transfer and a possible classification of these interfaces.

2.1. Electronic Structure of Condensed Matter - an Overview

In a first easy descriptive approach conduction electrons of a perfect solid can be regarded as free. Explicitly this implies two simplifying assumptions:

- The motions of atomic nuclei and electrons can be separated due to their different speed ranges (adiabatic approximation or Born-Oppenheimer approximation).
- There is no interaction between electrons. Thus, the consideration can be confined on one single electron.

With these assumptions an electron in a solid can be described by a box-shaped potential in which the electron has only kinetic energy. As a result, the steady state Schrödinger equation can be formulated as:

$$-\frac{\hbar^2}{2m}\Delta\psi(\vec{r}) = E\psi(\vec{r}), \tag{2.1}$$

in which $\hbar$ represents the *Planck constant* divided by 2π, m the electron's mass, Δ the *Laplace operator*, $\psi(\vec{r})$ the position-dependent wave function and E the energy eigenstates. The simplest solution of this equation is a plane wave:

$$\psi_k(\vec{r}) = \frac{1}{\sqrt{V}} \mathrm{e}^{\mathrm{i}\vec{k}\cdot\vec{r}}, \tag{2.2}$$

with wave vector $\vec{k}$ and normalization factor:

$$\int\limits_V \mathrm{d}^3 r \, |\psi_k(\vec{r})|^2 = 1. \tag{2.3}$$

Applying this plane wave function to the Schrödinger equation the eigenvalues E of free electrons are:

$$E(\vec{k}) = \frac{\hbar^2 k^2}{2m}. \tag{2.4}$$

This equation represents the dispersion relation for free electrons in a solid. In consideration of the crystal's periodicity (appropriate boundary conditions) only some certain wave vectors are allowed which results in a density of states (DOS) also in the energy range. For both spin possibilities the three-dimensional DOS $D(E)$ can be calculated to be:

$$D(E) = \frac{V}{2\pi^2} \left(\frac{2m}{\hbar^2}\right)^{3/2} E^{1/2}. \tag{2.5}$$

In thermal equilibrium these states are occupied with Fermions following the Fermi-Dirac distribution:

$$f(E) = \frac{1}{\mathrm{e}^{(E-\mu)/\mathrm{k_B} T} + 1}, \tag{2.6}$$

in which μ constitutes the chemical potential, T the temperature and $\mathrm{k_B}$ the Boltzmann constant. The energy to which all states are occupied is called Fermi energy (E_F). It is well-defined by the electron density $n = N/V$ which can be derived by an integration about all occupied states:

$$n = \frac{N}{V} = \int\limits_0^\infty D(E) f(E,T=0) \mathrm{d}E = \int\limits_0^{E_\mathrm{F}} D(E) \mathrm{d}E. \tag{2.7}$$

Finally, E_{F} is determined by the mass m and concentration n of electrons:

$$E_{\mathrm{F}} = \frac{\hbar^2}{2m}(3\pi^2 n)^{2/3}. \tag{2.8}$$

As a résumé of these equations, figure 2.1 illustrates the dispersion relation and the DOS of a free three-dimensional electron gas. For $T = 0$ all states below E_{F} are occupied, above E_{F} they are empty.

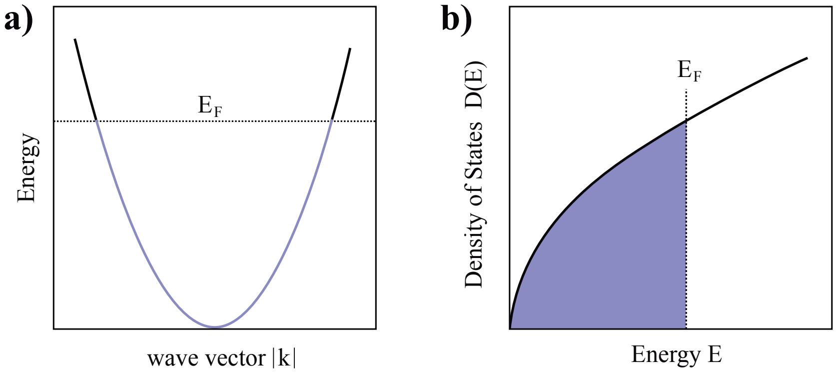

Figure 2.1.: a) Dispersion relation and b) density of states (DOS) of a free three-dimensional electron gas. For $T = 0$ all electronic states below the Fermi energy (E_{F}) are occupied and empty above E_{F}.

This easy approach of free electrons in a perfect solid is capable of describing some physical properties of metals, however, there are some obvious limits (e.g. diamond is an insulator but has a periodic lattice). For a more profound understanding it has to be considered that electrons move in a periodic potential. According to this, the eigenvalues E of the Schrödinger equation repeat periodically in the reciprocal lattice space:

$$E(\vec{k}) = \frac{\hbar^2 k^2}{2m} = E(\vec{k} + \vec{G}) = \frac{\hbar^2}{2m}|\vec{k} + \vec{G}|^2. \tag{2.9}$$

This solution can be illustrated as an infinite number of free electron parabola shifted against each other with the reciprocal lattice vector $\vec{G}$. But in this sense a non-zero amplitude of the periodic potential results in an energetic splitting at the Brillouin zone edge as is shown in figure 2.2. The higher this potential difference to the free electron case, the larger these energetic regions in which the DOS is zero. In the following, regions with non-zero DOS are called *bands* and regions of (almost) zero DOS *band gap*.

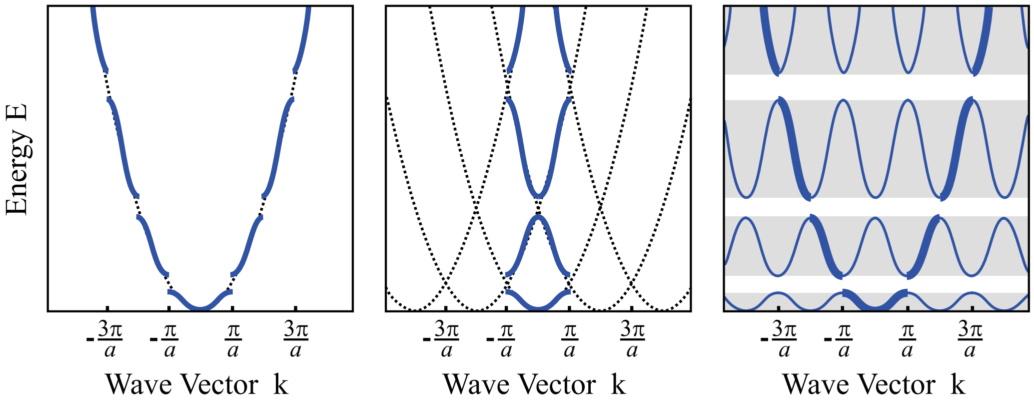

Figure 2.2.: Dispersion relation of a free electron gas in a one-dimensional periodic lattice in the *extended*, *reduced* and *periodic* zone scheme (from left to right). Dotted lines illustrate the free electron-like behavior, whereas blue lines indicate the dispersion relation of electrons in a periodic potential with non-zero amplitude which results in a splitting at the Brillouin-zone edge. The resulting regions with non-zero DOS are marked gray in the *periodic* zone scheme.

This simplified band model provides an adequate definition of metals, semiconductors and insulators. If a band crosses E_F it contains occupied as well as unoccupied electronic states at the same energy which enables conducting electrons to travel through the solid without losing energy. Such a material is usually called *metal*, whereas in semiconductors and insulators E_F is located in a band gap between the valence band and the conduction band. The gap size distinguishes semiconductors from insulators. If thermal energy or doping impurity atoms enables the population of the conduction band or the depopulation of the valence band, a material is called semiconductor. A more detailed and comprehensive study of the electronic structure of condensed matter can be found in various solid state physics textbooks [63, 125–128].

This band model and its resulting electronic band structure of solids can be especially applied to metals, such as gold, which is used as a single-crystal metal substrate in the present thesis. Though the electronic structure of metal surfaces looks significantly different in comparison to the electronic structure of the bulk, as the break of symmetry at surfaces and interfaces leads to the existence of so-called surface states.

2.2. Electronic States at Metal Surfaces

The breakdown of crystal lattice periodicity at surfaces induces a box-like potential which is bordered on one side by the potential barrier due to the work function (Φ, usually defined as the energetic difference of vacuum energy (E_{vac}) and Fermi energy (E_F) [63, 125, 126]) and on the other side bordered by the energy gap around the Fermi energy [129–131]. Figure 2.3 illustrates these boundary conditions at the metal/vacuum interface with both possible solutions for the real part $Re(\Psi)$ of the Schrödinger equation: a bulk-type and a surface-type solution. Conclusively, this potential well gives rise to new electronic states which exist only at the surface but which are delocalized in the direction parallel to the surface. First theoretical descriptions and interpretations of these electronic surface states date back to initial works by Tamm and Shockley. In particular Shockley surface states (SSs) are found to sufficiently describe first experimental observations of electronic metal surface states [132–135]. They are energetically located in the band gap and are characterized by a free electron-like dispersion in the direction parallel to the surface.

Due to their strong localization in normal direction to the surface, SSs are very sensitive to modifications of the surface. For example adsorption of atoms or molecules and possible accompanying charge transfer mechanisms on the metal surface can lead to a shift in energetic position, intensity reduction or complete quenching of SSs [108, 136–143]. These processes have recently been investigated especially for the adsorption of Perylenetetracarboxylic dianhydride (PTCDA) on different metal surfaces and led to a fundamental discussion about the electronic structure of metal/organic interfaces [66, 70, 104, 106, 141, 144–148].

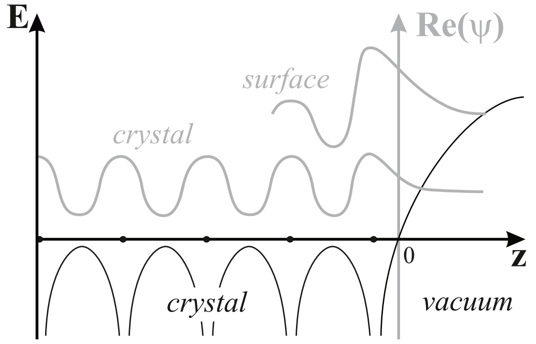

Figure 2.3: One-dimensional model of a periodic crystal potential with simplified boundary conditions at the surface. There are two possible solutions for the real part $Re(\Psi)$ of the Schrödinger equation: one bulk-type and one surface-type solution. The latter decays into both, the bulk crystal and the vacuum and therefore exists only at the surface but is delocalized parallel to the surface due to transverse symmetry. This solution gives rise to the existence of so-called Shockley Surface States (SSs).

Another type of electronic states which can appear at metal surfaces are a Rydberg-like series of so-called image potential states (IPSs) [130, 149–155]. Their origin can be motivated from the interaction between an electron located in front of a polarizable surface and its own positive image charge, which gets induced by charge displacement. Therefore a charge located in front of a metal in distance z feels an attractive Coulomb-like potential $V(z)$ from the interaction with its own image charge:

$$V(z) = -\frac{e^2}{16\pi\varepsilon z}, \tag{2.10}$$

in which e represents the elementary charge and ε is the dielectric background. Consequently, IPSs can be described with an one-dimensional hydrogen-model and due to transverse symmetry electrons in these electronic states are delocalized parallel to the metal surface. Thus, IPSs feature a dispersion with an effective mass close to one electron mass m_e [131, 151]. Conclusively, there exists an additional Rydberg-like series of electronic bands at metal surfaces whose energetic eigenvalues can be calculated to be pinned to E_Vac:

$$E_\mathrm{n} = E_\mathrm{vac} - \frac{0.85\,\mathrm{eV}}{(\mathrm{n}+a)^2}, \quad \mathrm{n} = 1, 2, 3 \ldots. \tag{2.11}$$

Herein n is the quantum number and a represents the quantum defect which increases for a decreasing potential barrier [153, 156]. Figure 2.4 illustrates the energetic position and probability density function of image potential states perpendicular to a metal surface. It is accompanied by a sketch of the image charge model which shows the confinement of IPSs at the metal surface as well as the large energetic gap to occupied electronic states below $\mathrm{E_F}$. According to this energetic gap and the coupling to bulk states, elastic and inelastic electron-electron scattering rates are increased for IPSs which leads to a decay on femtosecond timescale [157, 158]. Additionally, the probability density shifts away from the surface with increasing quantum number n, involving a reduced electronic coupling and a resulting increased lifetime [130, 156, 158–160]. In the past decades various studies have been performed to investigate the influence of adsorbed molecules on the energetic position and lifetime of IPSs [113, 154, 161–166]. The main reason for their impact is the fact, that the work function of a metal substrate usually gets changed due to adsorbate-induced charge rearrangement and Pauli-repulsion (Push-back effect) (for details see section 2.5.1). As IPSs are pinned to the vacuum level they usually experience an adsorbate-induced energetic shift relative to E_F.

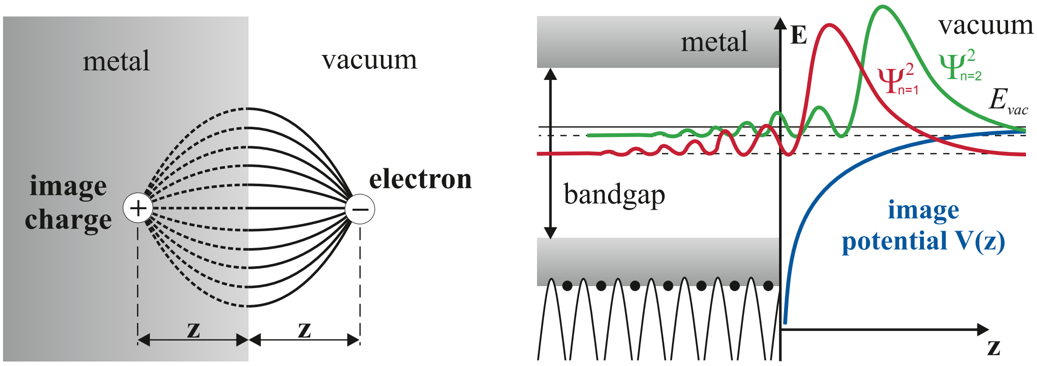

Figure 2.4.: Image charge model (left) and confinement of IPSs at a metal surface (right). The blue line represents the image potential $V(z)$, whereas the red and green line figures the probability density function of the first and second IPS.

2.3. Electronic Structure of Organic Semiconductors

In some strongly restricted cases even the electronic structure of organic molecules can be discussed in a band-like fashion, as it is an accepted standard for metals and inorganic semiconductors [40, 167]. Unfortunately, the requirements for band-like charge transport, like high crystallinity and high intermolecular charge density overlap, are challenging for organic thin films. Nevertheless, there are few organic materials in which band-like charge carrier transport has been observed [58–69, 71, 125]. It is the purpose of this section to sketch the underlying concept from atomic energy levels to molecular orbitals. Generally, organic semiconductors are hydrocarbon-based molecular structures which are often combined with sulfur or halogen atoms (for an overview of famous and often used organic semiconductors, see [36–38, 42, 168]). First investigations in the early 20th century dealt with the photo-induced conductivity of anthracene, however, first metal-like conductivities were observed in the 1970s in polyacetylene, honored with the Nobel prize for A. J. Heeger, A. G. MacDiarmid and H. Shirakawa in 2000 [72, 73, 78, 81, 169–171]. In such organic compounds conductivity and semiconducting properties can be explained by the formation of atomic hybrid orbitals and the resulting interatomic covalent carbon double bonds. In total, one single carbon atom has six electrons: two in the 1s and the 2s orbital each and one electron in two of three 2p orbitals. This configuration is sketched in figure 2.5a. An intermolecular bonding of a carbon atom with another atom can lead to a linear combination of involved atomic orbitals resulting in so-called hybrid orbitals.

For the conductivity and semiconducting properties of organic compounds the sp^2-hybridization of carbon plays a key role. In this hybridization wave functions of the 2s and two 2p atomic orbitals are combined to three trigonal planar $2sp^2$ hybrid orbitals. The third 2p orbital (from now on $2p_z$) remains unchanged and stands perpendicular to the $2sp^2$-plane. All $2sp^2$ hybrid orbitals and the remaining 2p orbital are singly occupied with one electron and can form covalent bonds with neighboring atoms. Figure 2.5b and c exemplarily illustrate the bonding between two sp^2-hybridized carbon atoms. The spatial proximity of both sp^2-hybridized carbon atoms induces a spatial orbital overlap of two sp^2 orbitals and two $2p_z$ orbitals each. This results in the formation of a rather localized, stronger σ-bond (splitted into bonding σ- and antibonding σ^*-orbital) and a more delocalized but weaker π-bond (splitted into bonding π- and antibonding π^*-orbital).
Organic molecules which consist of a carbon backbone with alternating single- and double bonds therefore feature a so-called conjugated system of double bonds. This conjugated system implies that electrons of π-bonds are approximately delocalized over the entire molecule as it is shown for benzene in figure 2.5d. In a molecule's ground state, the electron-occupied π orbital with the highest energy (highest occupied molecular orbital, HOMO) and the unoccupied π^* orbital with the lowest energy (lowest unoccupied molecular orbital, LUMO) are of special importance for the semiconducting properties of these organic compounds. Usually the energetic difference between HOMO and LUMO, called band gap, is found within the range of 1.5 and 4.0 eV which enables the optical excitation of charge carriers. Intramolecular charge carrier transport proceeds along these delocalized π-electron-systems. It is known since the 1960s that doping organic materials can enormously increase the conductivity of organic thin films [34, 41, 72–83]. This applies not only for small molecules, like benzene and anthracene, but also for for polymers like polyacetylene. Therefore intermolecular charge transfer plays an important role in almost every organic (opto)electronic device.

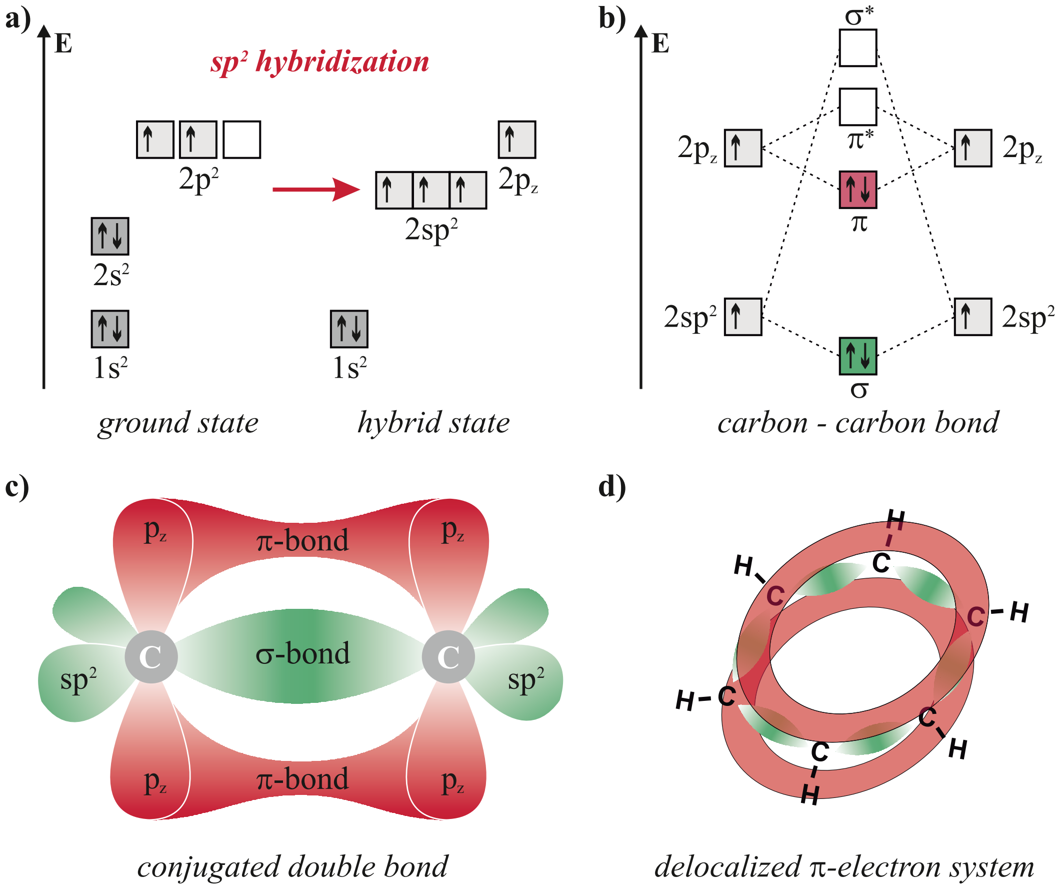

Figure 2.5.: Scheme of the formation of a delocalized π-electron system. Involved carbon atoms experience energetically favorable sp^2-hybridization a) which leads to the formation of rather localized σ-bonds and more delocalized π-bonds b). The electron density of these bonds is located as sketched in c) and is therefore responsible for the formation of conjugated chains or delocalized π-electron systems in carbon-based molecular structures such as for example in benzene d).

2.4. Charge Transfer Mechanisms

It is a common technology to introduce impurity atoms with the aim of increasing the number of free charge carriers in inorganic semiconductors. In doing so typical dopant concentrations are in the range of 10^{-7} to $10^{-3}\,\%$ [126]. While n-doping describes the introduction of impurity atoms holding one electron more than the lattice atoms which shall be replaced, p-doping describes the introduction of impurity atoms with one electron less that the lattice atoms which leads to an increased density of holes. At room temperature these added charge carriers are weakly bound to the impurity atom and therefore can participate at charge carrier transport mechanisms.

Doping organic semiconductors is comparable to doping inorganic semiconductors since in both cases additional charge carriers are created by introducing other materials. In doped organic semiconductors, however, introduced charge carriers are stronger bound by Coulomb interactions than in their inorganic analogs which is one of the reasons for the much higher doping concentrations usually used in organic semiconductors (up to several percent). There is a huge variety of dopants for organic semiconductors ranging from small atoms and metal oxides to different organic semiconductors which enables myriads of possible dopant-matrix combinations [41, 82, 172]. In all these cases dopant-matrix combinations can be treated as so-called *charge transfer complexes* (CTC), in which the introduced dopant share their (additional) charge with usually one neighboring matrix molecule. For an adequate description of CTCs there are two often consulted models: the most common *integer charge transfer* model (ICT) and the *hybrid charge transfer* model (HCT). Nonetheless, they are not equivalent. So one has to find the convenient charge transfer model for each material class combination in CTCs. This is why this section will shortly introduce the herein mentioned charge transfer models.

It has to be pointed out that, to some extent, these charge transfer models are not only suitable for describing CTCs in amorphous organic semiconductor matrices but also for the description of fundamental processes at metal/organic, inorganic/organic and organic/organic interfaces and heterojunctions [46, 173–177]. Even emitter-matrix combinations in OLEDs can be treated as CTCs [41, 178, 179]. In OPVs so-called *charge transfer excitons* are important quasiparticles (electron-hole pairs bound by Coulombic interaction) to describe the first steps from a photo-induced charge injection at donor-acceptor interfaces and heterojunctions, or even in homomolecular films, to the formation of free charge carriers [13, 180–184].

2.4.1. The Integer Charge Transfer Model

The ICT model explains charge transfer by the transfer of an electron from a donor to an acceptor molecule. From a chemical point of view the ICT model can be expressed in a reaction equation, exemplarily shown below for p-type doping, in which M constitutes a random matrix molecule and $\tilde{\mathrm{M}}$ the neighboring matrix molecule of the acceptor molecule A [172]:

$$\mathrm{M} + \tilde{\mathrm{M}}\mathrm{A} \rightleftharpoons \mathrm{M} + [\tilde{\mathrm{M}}^{+}\mathrm{A}^{-}] \rightleftharpoons \mathrm{M}^{+} + \tilde{\mathrm{M}}\mathrm{A}^{-}. \tag{2.12}$$

In the intermediate CTC ($\tilde{\mathrm{M}}^{+}\mathrm{A}^{-}$) one electron was completely transferred from the donor to the acceptor molecule. The second step, the so-called dissociation or charge separation step, is usually not energetically favorable due to the Coulomb interaction between electron and hole, which in sum with polarization effects, is also called binding energy of the charge transfer exciton. For molecule-molecule CTCs an efficient charge transfer is generally possible if the LUMO of the acceptor molecule energetically lies in the same region as the HOMO of the donor molecule. Of course, the above mentioned restrictions such as high molecular orbital overlap still have to be taken into account. As the introduced ICT model enables a simple form of understanding adsorbate-induced work function changes at metal/organic interfaces, which is one of the topics of the present thesis, its applicability is briefly introduced in this section. In doing so, this requires an introduction to interfacial energetics which will be discussed later in section 2.5. Nevertheless, terms like *vacuum level alignment*, *Fermi level alignment* and *Schottky-Mott limit* are already used in this section. For a clear definition of this terminology please read section 2.5.

Adsorbate-induced work function changes at metal/organic interfaces can be simply categorized in three cases as illustrated in figure 2.6. In case a) the substrate's work function gets reduced and in case b) raised due to adsorption of organic molecules while in case c) the work function remains unchanged [48, 89, 101, 185–188]. Regarding the energetics of a metal substrate, this can be characterized in a simplified manner using only one parameter: the work function Φ. An adsorbate layer consisting of organic semiconductor molecules can be described using two electronic parameters: ionization potential (IP, energetic difference between vacuum energy and HOMO) and electron affinity (EA, energetic difference between vacuum energy and LUMO). In addition to these material parameters, the ICT model incorporates Coulomb energies $\mathrm{B}^{-/+}$ associated with the energies of a molecule owning an additional charge $\mathrm{e}^{-}/\mathrm{h}^{+}$ and estimates lower and upper pinning levels $\mathrm{W}^{-/+}$ (also labeled $\mathrm{E}_{\mathrm{ICT}-/+}$

in literature) [186, 188]:

$$\mathrm{W}^- = \mathrm{EA} + \mathrm{B}^-, \qquad \mathrm{W}^+ = \mathrm{IE} + \mathrm{B}^+. \tag{2.13}$$

Contacting metal substrate and organic semiconductor energetics the three above mentioned cases can be redefined:

- **a)** $\underline{\Phi_{\mathrm{Sub}} > \mathrm{W}^+}$: In this case the HOMO is located above the $\mathrm{E_F}$ of the substrate which causes n-type doping of the molecule by Fermi level alignment between HOMO and $\mathrm{E_F}$. This implicates a work function change $\Delta\Phi < 0$.
- **b)** $\underline{\Phi_{\mathrm{Sub}} < \mathrm{W}^-}$: In this case the LUMO is located below the $\mathrm{E_F}$ of the substrate which causes p-type doping of the molecule by Fermi level alignment between LUMO and $\mathrm{E_F}$. This implicates a work function change $\Delta\Phi > 0$.
- **c)** $\underline{\mathrm{W}^- < \Phi_{\mathrm{Sub}} < \mathrm{W}^+}$: This regime is characterized by a missing charge transfer type interaction which leads to vacuum level alignment ($\Delta\Phi = 0$).

These three cases give rise to an equally tripartite work function dependence of $\Phi_{\mathrm{Org+Sub}}$ as sketched in figure 2.6d. For case c) there is a linear relationship between $\Phi_{\mathrm{Org+Sub}}$ and Φ_{Sub} which matches the Schottky-Mott limit due to the missing ICT type interfacial interaction. In Φ_{Sub} ranges with occurring ICT type interaction (case a) and b)) $\Phi_{\mathrm{Org+Sub}}$ stays constant due to its equivalency with the lower and upper pinning levels $\mathrm{W}^{-/+}$.

The simplicity of this ICT model makes it subject to obvious restrictions. Neither fundamental interfacial effects like Pauli-repulsion (or Push-back effect; electron wave function spill-out gets reduced by adsorption) nor possible structural or electronic rearrangements at the interface are taken into account. Main critical issue of the ICT model is the fact that integer charges are transferred, whereas partial charge transfer can not be explained. Nonetheless, there are metal/organic interfaces which can be qualitatively described by this ICT model [48, 101, 185, 189–191]. Results from Crispin *et al.*[89] and Lange *et al.*[187] demonstrating the entire tripartite work function dependence of $\Phi_{\mathrm{Org+Sub}}$ for one individual metal/organic interface should be highlighted here.

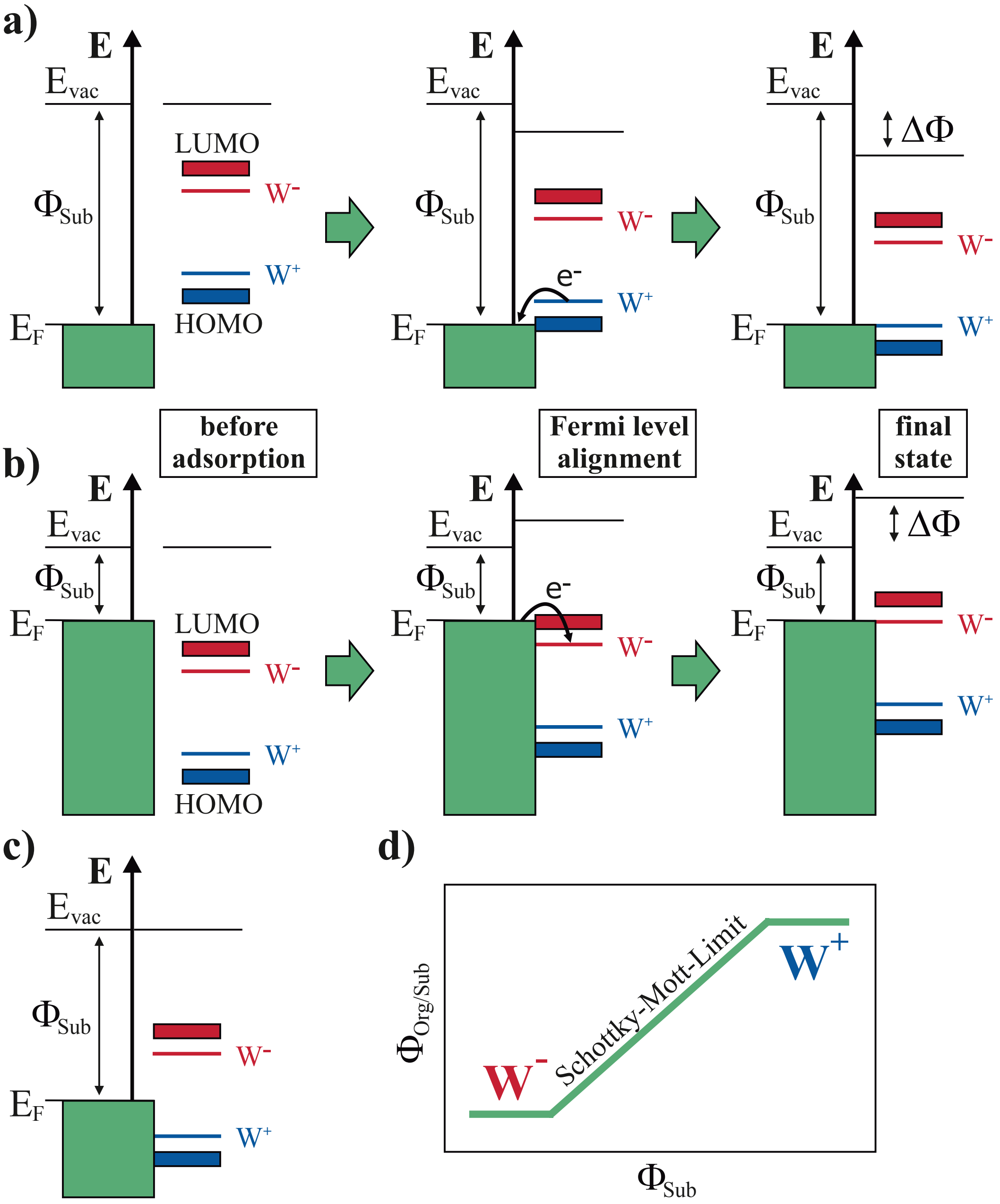

Figure 2.6.: Visualization of the integer charge transfer model describing adsorbate-induced work function modifications at metal/organic interfaces. a) n-type doping or b) p-type doping leads to an electron/hole transferred from a molecule to the metal substrate implying Fermi level alignment and interface dipole formation. c) Covers the Schottky-Mott limit resulting in vacuum level alignment without a charge transfer type interaction and d) sketches the tripartite work function dependence of $\Phi_{Org+Sub}$.

2.4.2. The Hybrid Charge Transfer Model

In order to overcome the restrictions of the ICT model, the HCT model has proven to be quite applicable [83, 192–197]. It enables an explanation for partial charge transfer and the formation of new electronic states in organic/organic CTCs, as well as at metal/organic, inorganic/organic and organic/organic interfaces. In sum, the HCT model describes charge transfer as a result of the hybridization of electronic states of two different molecules or at an interface. Consequently, the impact of geometrical ordering on the orbital overlap and the impact of the participating electronic states' positions on the energetic rearrangement gets qualitatively understandable.

In the simplest case of hybridization of one molecule's HOMO with a different molecule's LUMO induces the formation of a bonding and antibonding hybrid state (see figure 2.7b). Accordingly, the new hybrid states are not located on one original single molecule but shared by both molecules of the CTC. As electrons from one original occupied HOMO are shared with a different molecule in a CTC via electronic hybridization, this also implies a rearrangement and extension of the electron's probability of presence. Due to this extended, rearranged electron's probability in a CTC, a specific amount of negative charge (ρ^-) is transferred to the acceptor molecule. For this reason the amount of transferred charge depends on the electronic hybridization-induced charge rearrangement and thus is usually partial (in the range between 0 and 2). HCT is often used to explain CTCs and charge transfer at metal/organic, inorganic/organic and organic/organic interfaces which feature new arising electronic states, sometimes called *interface states* [90, 192, 193, 195, 197–199].

For the sake of completeness, the existence of another charge transfer model, called *induced density of interfacial states* model, has to be mentioned here which is applicable for weakly-interacting organic semiconductor containing interfaces [200–202]. Using this model partial (fractional) charge transfer without a molecular electronic rearrangement and the formation of CTCs is possible due to the introduction of a Fermi level equivalent *charge neutrality level* (CNL) for organic semiconductors. Comparably to Fermi level alignment CNL-E_F alignment can be applied to explain adsorbate-induced work function changes at weakly-interacting metal/organic interfaces.

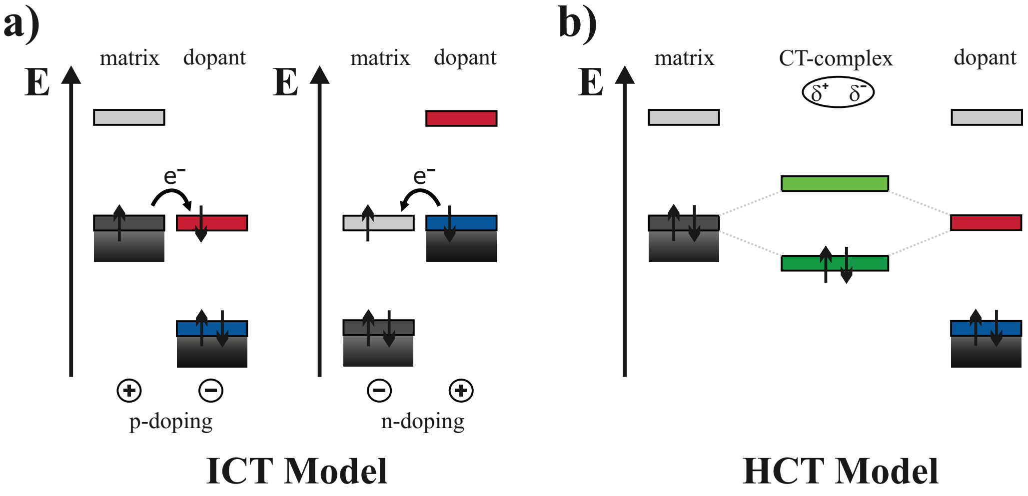

Figure 2.7.: Comparison of the ICT model a) and the HCT model b). In the ICT model an integer charge is transferred from donor to acceptor molecule. Depending on which of them is the dopant, it is termed p-doping or n-doping. The HCT model explains partial charge transfer by hybrid state formation in a CTC (here green).

2.5. Electronic Structure of Metal/Organic Interfaces

It was shortly introduced in section 2.4.1 that ICT may have strong impact on the work function of a metal/organic interface. But a huge diversity of effects have to be taken into account to describe energy level alignment and work function shifts at inorganic/organic and organic/organic interfaces. Since this thesis deals basically with metal/organic interfaces, the focus of the following section is on the description of fundamental processes regarding energy level alignment (ELA) and work function changes especially at metal/organic interfaces.

2.5.1. Energy Level Alignment

Generally there are two different model-like regimes of ELA at metal/organic interfaces: vacuum level alignment (VLA, also called Schottky-Mott limit) and Fermi level alignment (FLA) [51, 54, 56, 57, 86, 203–205]. In case of VLA the work function Φ remains constant during adsorption of molecules on a metal substrate, indicating different electron Δ_e and hole injection barriers Δ_h for different metal substrates according to the different substrates' work functions (as is illustrated in figure 2.8). VLA is only possible if the metal substrate's E_F is located in between the EA and IP of a single unaffected (free) molecule [206]. Thus, assuming VLA electron Δ_e and hole injection barriers Δ_h can be calculated as:

$$\Delta_\mathrm{e} = \Phi - \mathrm{EA}, \qquad \Delta_\mathrm{h} = \mathrm{IP} - \Phi. \tag{2.14}$$

In contrast, in FLA regime, the metal substrate's E_F gets pinned either to the energetic position of the IP or to the EA of the adsorbate molecule (enabling ICT). Accordingly, the work function varies for different substrates while the injection barriers can equal zero or E_G which is the energetic IP-EA difference. Figure 2.8 illustrates a comparison of VLA and FLA with special regard to the work function and electron/hole barriers. For FLA the adsorbate-induced work function difference $\Delta\Phi$ can be regarded as an interplay between an interfacial charge transfer induced dipole μ_CT, the molecule's dipole moment perpendicular to the surface normal $\mu_{\mathrm{mol},\perp}$ and the adsorbate-induced back-shift of electrons spilling out the metal surface according to *Smoluchowski* effect $\Delta\Phi_\mathrm{PB}$ (usually called *Push-back* effect or *Pauli Repulsion* or *Cushion* effect) [54, 207–213]:

$$\Delta\Phi = \Delta\Phi_{\mathrm{PB}} + \mu_{\mathrm{CT}} + \mu_{\mathrm{mol},\perp}. \tag{2.15}$$

The influence of all these effects depends on the geometric structure of the adsorbate and the metal-molecule interaction directly at the interface [90, 214]. In addition, thicker adsorbate layers can influence the substrate's work function due to so-called *band bending* (BB) and the formation of a space charge region as will be discussed in the following [55, 57, 215–218]. Moreover, it is worth mentioning that work function changes of several ten electron volt have been demonstrated in ordered films of dipolar molecules (so-called *giant surface potential*) [219–222].

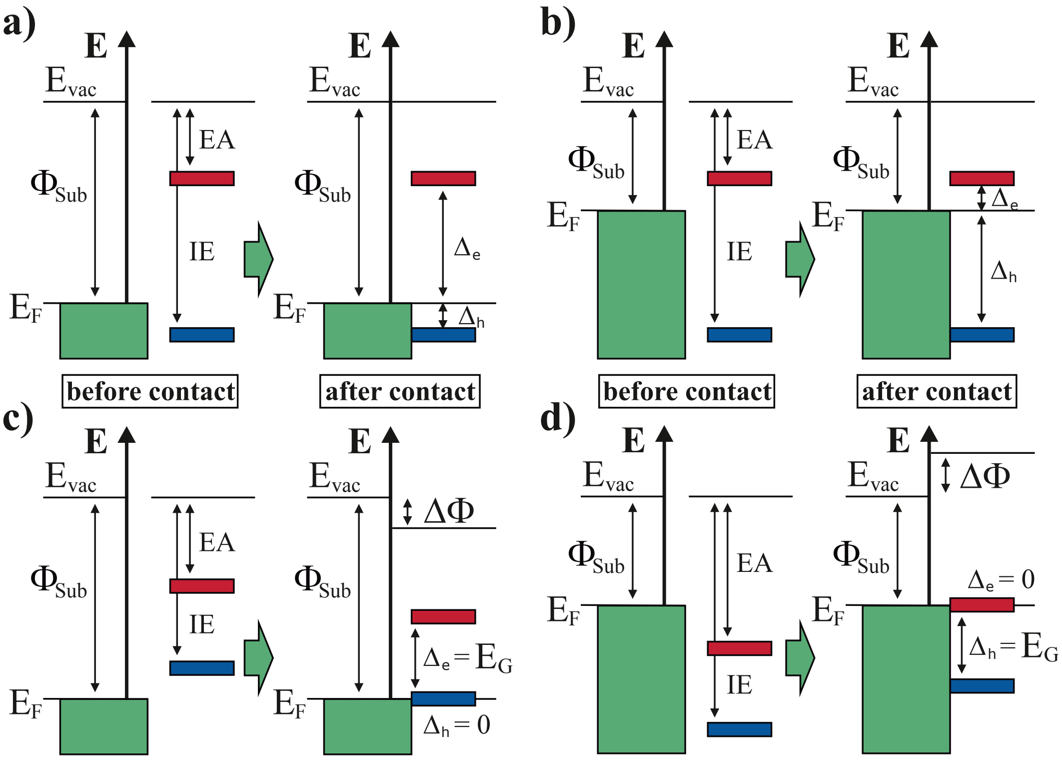

Figure 2.8.: Energy level alignment (ELA) at metal/organic interfaces. a) And b) illustrate vacuum level alignment (VLA) without adsorbate-induced work function change for high and low substrate work function. In contrast, Fermi level alignment (FLA) describes the alignment of the adsorbate's IP or EA to the metal surface's Fermi energy. It usually implies an adsorbate-induced work function change for high c) and low d) substrate work functions according to the ICT model.

2.5.2. Band Bending and Space Charge Region Formation

The introduced ELA models describe the energetic alignment of organic semiconductor energy levels (HOMO, LUMO) and adsorbate-induced work function shifts on metal surfaces. This implies a misalignment of organic semiconductor energetics at a metal/organic interface compared with thicker adsorbate films or in the bulk. Surface band bending, developed by Schottky and Mott for the adjustment of semiconductor bands in contact with metal surfaces, can also be applied to metal/organic interfaces in order to model this transition from interfacial to semiconductor bulk energetics [216, 223–226]. For this purpose the Fermi level equivalent for organic semiconductors CNL has to be used.
At metal/organic interfaces an ELA-induced difference between E_F and CNL induces a local imbalance in charge neutrality which generates an electric field at the interface (additional to any charge transfer impacts). In consequence of standard low free charge carrier density in organic materials this imbalance can not be screened in an organic semiconductor film which leads to an electric field and to an interfacial variation of the charge carrier density. For an n-type semiconductor the interfacial charge carrier density gets reduced. This leads to the formation of a so-called *depletion layer* in which the organic semiconductor energetics bend downwards. Whereas for p-type semiconductors, the interfacial charge carrier density increases which leads to the formation of a so-called *accumulation layer* resulting in an upward band bending. Figure 2.9 illustrates both cases for FLA at metal/organic interfaces.

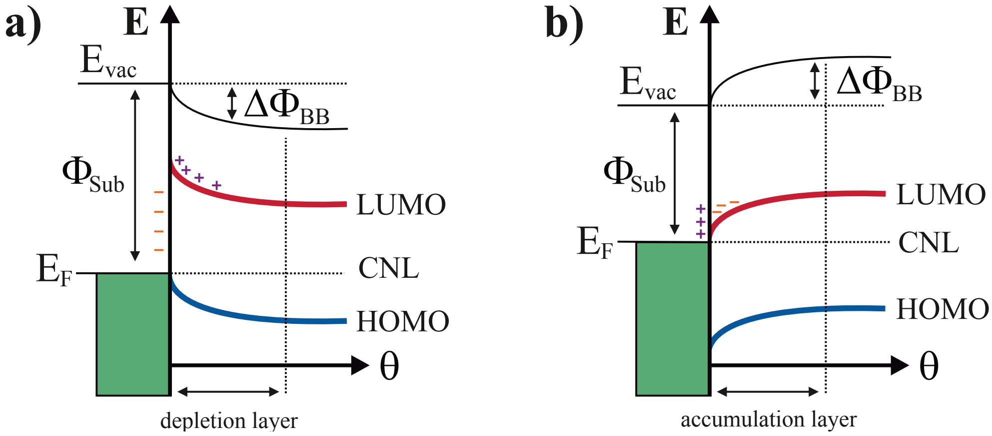

Figure 2.9.: Band bending at metal/organic interfaces. a) Illustrates downward and b) upward band bending for interfaces in Fermi level alignment (FLA) regime which induces a work function change $\Delta\Phi_{\mathrm{BB}}$ for increasing adsorbate film thickness (θ).

It indicates that the work function evolution in a space charge region does only equalize the band bending induced energetic shift of the bands themselves if there is also VLA directly at the metal/organic interface. In case of FLA (for HOMO or LUMO) additional work function shifts just at the interface usually reduce the work function change in higher adsorbate layers [51, 227]. The degree and expansion of band bending, i.e. depletion and accumulation layers, depends on the metal/organic interfacial interaction, on the geometrical disorder in the organic semiconductor film, on the charge carrier density and on the difference between E_F and CNL. For thick adsorbate layers the CNL equals the E_F which gives rise to an additional thickness-dependent band-bending-induced work function shift $\Delta\Phi_{\mathrm{BB}}(d)$. The adsorbate thickness range, in which the work function varies (for instance due to band bending), is also called *space charge region*. Yet, the impact of a band bending induced work functions shift can be also observed directly at the metal/organic interface which leads to a modification of equation 2.15 into:

$$\Delta\Phi = \Delta\Phi_{\mathrm{PB}} + \mu_{\mathrm{CT}} + \mu_{\mathrm{mol},\perp} + \Delta\Phi_{\mathrm{BB}}(d). \tag{2.16}$$

Unfortunately, the most basic model to describe space charge regions, the Schottky model, often does not sufficiently fit to experimental work function evolution data of metal/organic interfaces [187, 218, 228, 229]. It describes the DOS of charged molecules in the film as delta function-like which further on leads to a constant carrier density for increasing thickness. In contrast, a simplified distributed density of states model introduced by Mankel *et al.* [218] assumes a constant DOS (in energy) which results in a decreasing charged molecule concentration for increasing film thickness. This model provides an equation for the work function shift as a function of the film thickness d, the maximum work function shift $\Delta\Phi_{max}$ and the density of states (DOS):

$$\Delta\Phi_{\mathrm{BB}}(d) = \Delta\Phi_{max}\left[1 - \frac{1}{\cosh(kd)}\right] \qquad \text{with} \qquad k = e\sqrt{\frac{\mathrm{DOS}}{\varepsilon\varepsilon_0}}. \tag{2.17}$$

Recently, this model has been applied to adequately reconstruct work function evolution data and to derive a constant DOS value at inorganic/organic interfaces [218, 230]. Nonetheless, it is not restricted to the interpretation of space charge regions predominantly induced by band bending as will be shown in chapter 8. The importance of band bending at metal/organic interfaces arises from the critical impact of the energetic position of electronic states or bands in organic semiconductor thin films relative to the metal's E_{F} for the operation of organic electronic devices. Usually, organic electronic devices in minimum contain one metal/organic interface which implicates possible consequences of interfacial charge transfer type interactions and band bending on the electronic device properties and performances. After this introductory part about theoretical principles the following chapter contains experimental fundamentals and a description of the experimental setup.

3. Two-Photon Photoemission Spectroscopy at Metal/Organic Interfaces

Since its first observation by Hertz and Hallwachs in 1887 and its quantum-mechanical formulation by Einstein in 1905, the photoelectric effect was applied to investigate the electronic structure and properties of atoms, molecules, solids, surfaces and interfaces [231–233]. Now photoemission (or photoelectron) spectroscopy (PES) is well established and most frequently applied as the basic experimental tool to investigate any kind of conducting or semiconducting materials or surfaces [234]. Using photons with a photon energy $E = \mathrm{h}\nu$ higher than the material's work function Φ leads to the emission of electrons with a certain kinetic energy E_{kin} which depends on the electron's initial binding energy E_{Bind} relative to E_{F}:

$$E_{\mathrm{kin}} = \mathrm{h}\nu - \Phi + E_{\mathrm{Bind}}. \tag{3.1}$$

Herein h represents *Planck's constant* and ν the frequency of light. Even though, according to Lambert-Beer's law, the penetration depth of light in matter is in the order of wavelengths, PES is a surface sensitive technique. This is because the inelastic mean free path λ_{MFP} of photo-excited electrons depends on the initial photon energy and lies in the nanometer regime due to various electron scattering mechanisms [235–237]. Naturally also the electronic excitation depends on the applied photon energy range. Therefore PES using photons in the ultraviolet regime (UPS) is applied in order to investigate the valence band structure near E_{F}, whereas photons in the x-ray regime (XPS) excite electrons from the core levels. A fact which enables an element specific investigation of chemical composition and bonding characteristics.

Both, XPS and UPS, are frequently applied techniques for the investigation of metal/organic, inorganic/organic and organic/organic interfaces. In this sense XPS is commonly applied to explore molecule-molecule interactions, for example emitter-matrix interactions in emission layers of OLEDs or intermolecular bonding properties, as well as bonding interactions at surfaces and interfaces

[204, 234, 238]. Additionally, XPS is a well-suited experimental tool to look at photo-induced processes, slow chemical reactions or catalytical effects at surfaces [239–241]. UPS, in contrast, is a widely applied technique to investigate all possible mechanisms of ELA, including work function shifts at interfaces and in molecular thin films [204, 238]. It enables experimental access to the energetic position of a molecule's HOMO which permits conclusions about interfacial interactions like charge transfer, band bending and bonding motifs. For metal/organic interfaces and molecular single crystals angle-resolved PES (ARPES) is of crucial significance because it permits access to the dispersion of electronic states demonstrating band formation and delocalization. ARPES can be performed using an angle-resolved analyzer or it can be carried out by changing the emission angle due to sample rotation in front of an analyzer as it is performed in the present case. In doing so, the symmetric dispersion of the Au(111) SS is used to adjust the polar angle zero ($k_\parallel = 0$) which results in a systematic polar angle error of in maximum ±2°. As sketched in figure 3.1 the parallel component of the wave vector k is conserved during the photoemission process ($k_\parallel = k'_\parallel$), whereas the perpendicular component is changed by the work function ($k_\perp \neq k'_\perp$). This facilitates the calculation of the initial wave vector parallel to the surface using the kinetic energy E_{kin} and the emission angle with respect to the surface normal ϕ:

$$k_\parallel = \frac{\sqrt{2m_{\text{e}}E_{\text{kin}}}}{\hbar}\sin(\phi). \tag{3.2}$$

Herein m_{e} represents the electron mass. Assuming a free electron-like dispersion (as has been introduced in section 2.1), the binding energy of an electron in a solid can be accordingly estimated to:

$$E_{\text{Bind}} = E_0 + \frac{\hbar^2 k_\parallel^2}{2m^*} = E_0 + E_{\text{kin}} \cdot \frac{m_{\text{e}}}{m^*} \cdot \sin^2(\phi). \tag{3.3}$$

Yet, PES also underlies some restrictions. For example photo-induced dissociation and other unwanted influences during the measurement procedure are frequently observed as a consequence of required high photon intensities and energies [242–246]. The most essential restriction is the fact that, in principle, PES allows only the excitation of former occupied electronic states. In regard to the unoccupied electronic structure of any kind of material direct PES is blind. This blindness of PES, however, can be overcome by using non-linear optical two-photon photoemission (2PPE). 2PPE gives also access to the unoccupied electronic structure of an investigated material. Moreover, angle- and time-resolved measurements are feasible to look into band formation and delocalization of electronic states but also lifetimes of electronically excited states. This combination of powerful possibilities constitutes 2PPE as an unique experimental tool with increasing importance in the last twenty years [105, 116–118, 153]. Compared to direct PES, the experimental prerequisites are distinctly more challenging since the basic non-linear optical process requires high photon intensities and therefore ultrashort laser pulses.

The present chapter includes a short introduction to 2PPE spectroscopy by amplifying the basic physical principles and the particular experimental setup. Subsequently, the derivation and structure of 2PPE spectra, as well as evaluating processes are presented. Furthermore, the last section offers a short summary of current research activities in the field of metal/organic interfaces using 2PPE spectroscopy which should also reinforce the final results of this thesis.

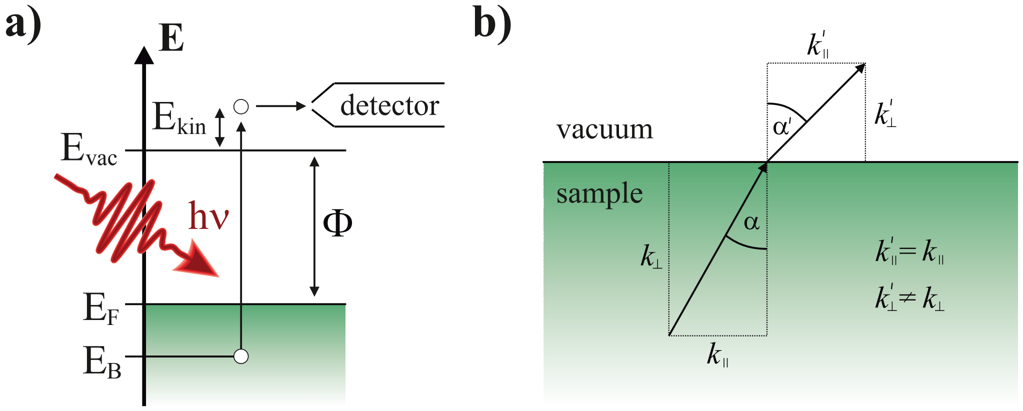

Figure 3.1.: a) Direct photoemission scheme: The electron gets photo-excited above the vacuum level where its kinetic energy is recorded by a detector (e.g. a time of flight spectrometer (TOF)). b) Conditions for emission in off-normal direction: $k_{\|}$ is conserved, whereas $k_{\perp}$ gets changed by the work function.

3.1. Physical Principles of Two-Photon Photoemission

Generally, 2PPE is a pump-probe technique consisting of a two-step process with two consecutive, femtosecond, laser pulses (*pump* pulse and following *probe* pulse) with equal (monochromatic 2PPE, 1C-2PPE) or different (dichromatic 2PPE, 2C-2PPE) photon energies $\mathrm{h}\nu_1$ and $\mathrm{h}\nu_2$. In order to avoid direct photoemission, which has a four times higher cross section, these photon energies are chosen smaller than the sample's work function [247]. Therefore photoemission only takes place through a second-order non-linear optical process in which a first photon excites an electron from an occupied initial (below E_F) to an unoccupied intermediate electronic state (above E_F but below E_vac). A second photon excites the same electron from its unoccupied intermediate state to an unoccupied final state (above E_vac) with energy E_Final. This probing process of the priorly pumped electron can originate from the same pulse, which therefore has the same photon energy, or it comes from a second laser pulse of possibly different photon energy. As a consequence, dichromatic 2PPE can not be separated from monochromatic 2PPE with only one measurement (for zero time-delay). This problem can be solved by a suitable measurement and evaluation procedure (see section 3.3). For the following considerations dichromatic 2PPE is a separated process which can be easily divided from monochromatic 2PPE. It is also worth to mention, that the non-linear optical 2PPE process, in general, is one single quantum mechanical excitation process (for zero time delay). Accordingly, 2PPE is also possible if the unoccupied intermediate electronic state is only virtual and if there is even vanishing DOS. Finally, photo-excited electrons above the E_vac travel to a detector (in this case a *time-of-flight* spectrometer (TOF) assisted by a weak applied electric field) with a characteristic kinetic energy E_kin. Time integration delivers energy-dependent counting rates $N(E_\mathrm{kin})$ collected in typical 2PPE spectra. Figure 3.2 illustrates the origin of a monochromatic 2PPE spectrum with low- and high-energy cutoffs which are also called secondary edge (SE) and Fermi edge (FE), respectively. Electrons whose kinetic energies are just sufficient to overcome the work function can be found at the SE while the FE arises due to photoemission of electrons near E_F. Intensity maxima in 2PPE spectra might have different origins: they can stem from occupied initial, unoccupied intermediate or unoccupied final electronic states. For this reason 2PPE spectra are usually displayed versus the final state energy ($N(E_\mathrm{final})$) in reference to E_F:

$$E_\mathrm{Final} - E_\mathrm{F} = E_\mathrm{kin} + \Phi. \tag{3.4}$$

This energy axis allows the instant reading of the sample's work function which is now the energetic location of the SE. Additionally, the binding energies of initial and intermediate electronic states can be obtained via the subtraction of both, pump and probe photon energies or only the probe photon energy, respectively.

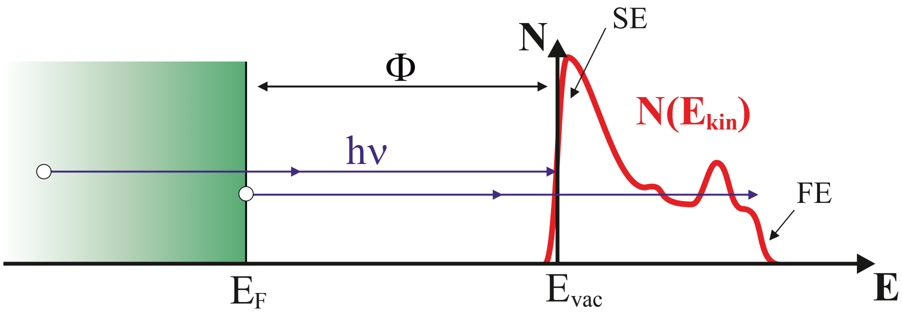

Figure 3.2.: Origin of a monochromatic 2PPE spectrum: The secondary edge (SE) originates from electrons owning just sufficient energy to overcome the work function by adsorption of two photons (hν), whereas electrons stemming from initial states near E_F can be found at the Fermi edge (FE).

An assignment of spectral features in 2PPE spectra to occupied, unoccupied an final electronic states can be achieved by a variation of the applied photon energies, actually performing 2PPE spectroscopy. For monochromatic 2PPE spectroscopy the assignment of spectral features to electronic states is sketched in figure 3.3. Varying the photon energy by Δhν shifts features arising from occupied initial states by 2Δhν because two photons are used for the probing mechanism. Unoccupied intermediate states, on the other hand, are probed (in resonance or indirectly) with only one photon which results in an energetic shift of only 1Δhν. If the spectral feature emerges from an unoccupied final state, two photons are required for the pumping process and consequently there is no energy shift upon photon energy variation (E_kin = const.). Nevertheless, it is important to note at this point that this assignment procedure is not applicable to electronic states owning a dispersion perpendicular to the surface such as bulk states. This is due to the fact that the binding energy of these electronic states is photon energy dependent, since for different photon energies different points in the Brillouin zone are probed.

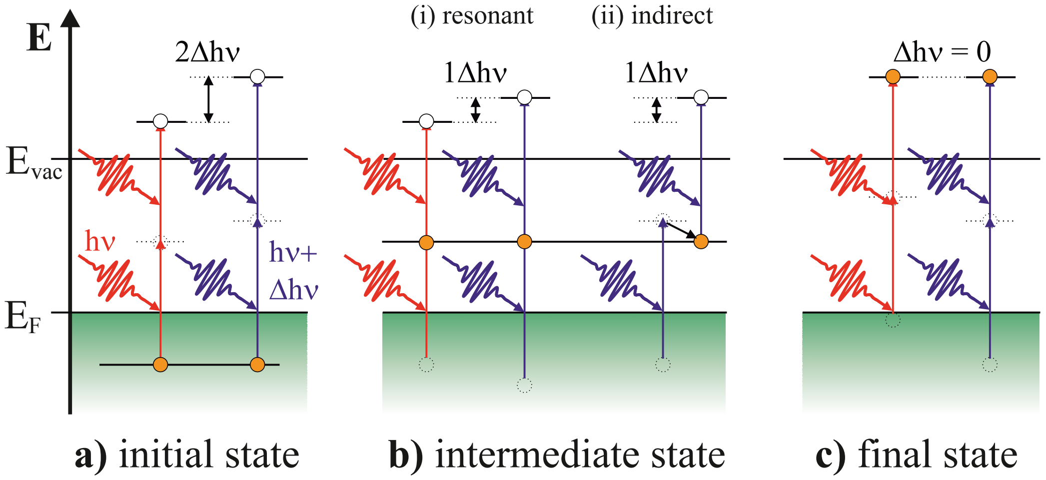

Figure 3.3.: Spectral features in monochromatic 2PPE spectra can be assigned to a) initial, b) intermediate and c) final states due to their energetic shift while performing 2PPE spectroscopy with different photon energies.

Time-resolved Two-Photon Photoemission

Besides angle-resolved 2PPE measurements (AR2PPE), which can be performed and evaluated like ARPES measurements, time-resolved 2PPE (TR2PPE) is a major advantage of this experimental technique. In doing so, femtosecond laser pulses (usually of different photon energies) are separated in space in order to delay the probe pulse with respect to the pump pulse by simple beam path extension. This facilitates the investigation of time-dependent electronic relaxation processes and charge carrier dynamics [122, 184, 248–253].

A variation of time delay results in a delay-dependent countrate at a certain kinetic energy which is also called *cross-correlation* $XC_{\mathrm{E}}(t)$ which implies the transient population of an intermediate electronic state $N(t)$ and the temporal shapes of the used laser pulses $I_i(t)$ (usually assumed to be Gaussian). Hence, this time-dependent countrate can be mathematically described by a convolution:

$$XC_{\mathrm{E}}(t) = (I_1 * I_2 * N)(t) = \int_{-\infty}^{\infty} \int_{-\infty}^{\infty} I_1(x) \cdot N(y-x) \cdot I_2(t-y) \mathrm{d}x \mathrm{d}y. \quad (3.5)$$

Assuming a single exponential decaying transient population of an intermediate state the time-dependent countrate can be expressed using the complementary error function $\mathrm{Erfc}(z) = 1 - \mathrm{Erf}(z)$:

$$XC_{\mathrm{E}}(t) = A \exp\left(\frac{\bar{t}^2 - 2t\tau}{2\tau^2}\right) \mathrm{Erfc}\left(\frac{\bar{t}^2 - 2t\tau}{\sqrt{2}\bar{t}\tau}\right). \tag{3.6}$$

Herein A represents a scaling factor, τ the lifetime of the intermediate state and $\bar{t}$ the average pulse length of both laser pulses (also called cross-correlation). An exhaustive derivation of these formulas can be found in ref. [254].

3.2. Experimental Setup

The present 2PPE setup at the Institute for physical chemistry, Heidelberg, can be roughly divided into two parts: an ultrahigh vacuum (UHV) chamber (base pressure: $5.7 \cdot 10^{-11}$ mbar) and a femtosecond laser system. Since its relocation from Berlin in 2013 no significant modifications have been implemented. This is why the setup description in the present thesis is kept short. A more detailed presentation can be found in refs. [254, 255]. The displayed UHV chamber in figure 3.4 is subdivided into two combined compartments, a preparation and an analysis part, while the sample is mounted on a turnable x-y-z-manipulator including a flow cryostat with resistive heating possibility. This individually allows controllable manipulator-positions for each preparation step or analysis tool. For temperature-controlled measurements the sample is connected via the manipulator to a temperature controller (*LakeShore 340*) which allows a sub-Kelvin temperature control from 40 K when cooled with liquid helium to more than 800 K. A part of the sample holder can be removed in-situ from the cryostat (with a transfer rod) to a sample storage unit or into a load-lock which in combination enables the incomplex removal (insertion) of samples from (into) the UHV chamber without breaking the UHV conditions.

For sample preparation the upper UHV chamber compartment is equipped with a sputter gun (*Specs IQE 11-A*) for ion bombardment with Ar^+, a Knudsen cell evaporator unit (*Kentax TCE-BSC*) in order to prepare thin adsorbate films and a quadrupole mass spectrometer (QMS, *Balzers QMG 112A*). The latter one allows adsorbate composition (fragmentation pattern), residual gas analysis (RGA) and temperature-programmed desorption (TPD) investigations in the range from 1 to 200 amu including adsorbate layer thickness estimations.

For sample characterization and measurement, the lower analysis compartment includes low-energy electron diffraction (LEED) facilities (*Fisons Instruments RVL 900*) and a time-of-flight spectrometer (TOF) with 210 mm drift tube length and acceptance angle of 6°. It determines the kinetic energy E_{kin} of photo-excited electrons indirectly by measuring its flight time passing the drift tube.

For PES and 2PPE measurements laser beams are transmitted through a MgF_2 view-port onto the sample with an angle of 45°. Spatial overlap is arranged with a CCD camera stationed outside the UHV chamber at a position equivalent to the sample position. In order to additionally achieve temporal overlap of two laser pulses, one laser beam is guided onto a reflector mounted on a precision linear stage. While scanning the pump-probe delay, the stage position of temporal overlap can be observed as a huge increase in 2PPE countrate which is correlated to the additive dichromatic 2PPE process.

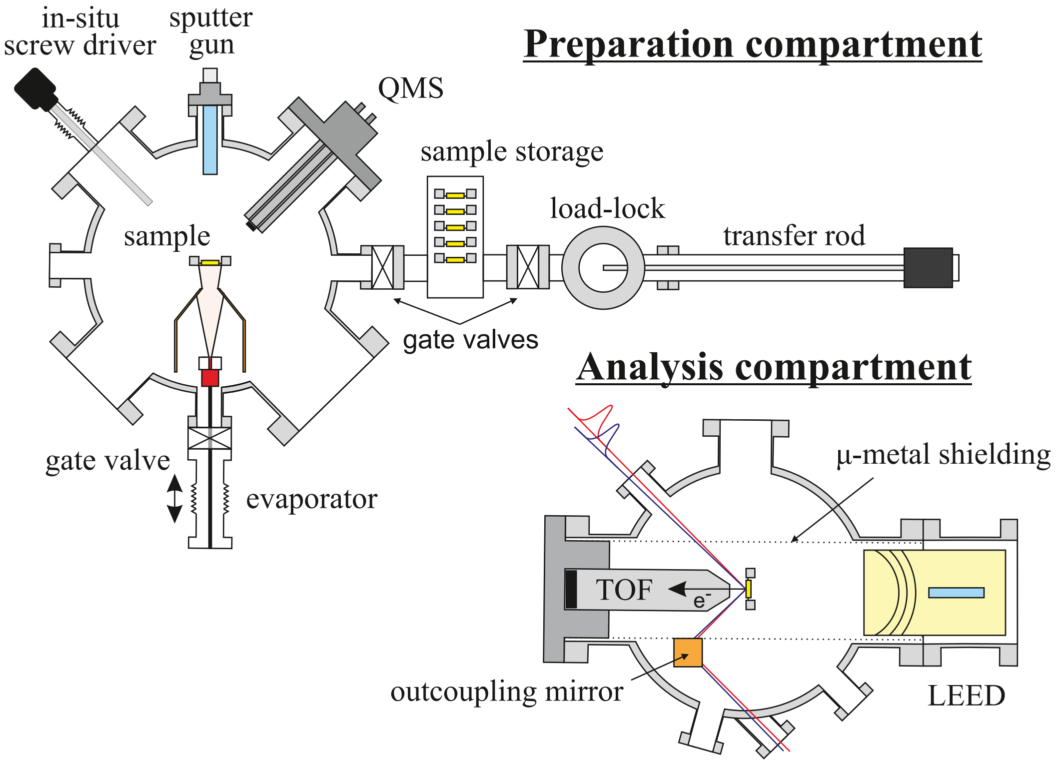

Figure 3.4.: The UHV chamber used in the PES and 2PPE experiments. The preparation compartment is equipped with a sputter gun, a Knudsen cell evaporator and a quadrupole mass spectrometer (QMS). Sample exchange and transfer is enabled by a sample storage and load-lock system to be reached using a transfer rod. The analysis compartment contains a LEED and a TOF shielded from surrounding magnetic and electric fields. Adapted from [255].

Performing 2PPE spectroscopy requires high peak intensities in the photon flux in order to efficiently incite the fundamental non-linear optical process. Therefore ultrashort laser pulses with pulse durations of around 50 fs are produced in a Ti:Sapphire oscillator (*Coherent Mira 900B*) which is pumped by a continuous wave (CW) operating Nd:YAG laser at 532 nm wavelength (*Coherent verdi V18*). For experiments carried out in the present thesis the output wavelength of this oscillator has been centered around 800 nm. Due to the uncertainty principle formulated by Heisenberg in 1927, the limited laser pulse duration is accompanied by a high spectral width, which lies around 30 nm for this setup [256]. The Ti:Sapphire oscillator output pulses are amplified in a regenerative amplifier (*Coherent RegA 9050*) which is pumped by the same Nd:YAG laser. This converts the Ti:Sapphire pulse energies in the order of nJ into more intense pulses with energies in the μJ range. For this purpose several less intense pulses are integrated which reduces the repetition rate from 80 MHz to 300 kHz. As high laser pulse intensities may damage optical components within the regenerative amplifier, the pulses are temporarily stretched before and compressed after the amplification which finally results in infrared (IR) pulses (λ = 800 nm, hν = 1.55 eV) with around 50 fs pulse duration and a spectral resolution below 30 nm.

These output pulses can be used in various ways, either directly for experiments or they can be frequency-doubled using β-barium-borate (BBO) crystals. Twice frequency-doubling the IR beam leads to UV light of 6 to 6.2 eV which can be used for direct photoemission experiments. Additionally, the intense IR pulses can be used to pump an optical parametric amplifier (OPA, *Coherent OPA 9450*) which converts them into pulses of tunable wavelength in the visible regime. The pulses in the visible regime can be converted by another BBO crystal to the corresponding UV wavelengths. Figure 3.5 illustrates a schematic overview of possible beams and combinations. Unless otherwise noted, all applied beams are p-polarized when they are incident on the substrate. Usually monochromatic 2PPE experiments are performed using the frequency doubled visible output of the OPA while dichromatic 2PPE experiments are realized using the visible output in addition to its frequency doubled beam or the frequency doubled visible OPA output and a part of the frequency doubled IR fundamental. In total, the available laser setup covers broad spectral regions between 1.5 and 6.2 eV photon energy.

In order to reduce the temporal width of the laser pulses, which is increased on their way on the optical table by many optical components like lenses, prisms, crystals, etc., prism compressors are installed. Due to a combination of their geometric alignment and the dispersion within the prism material these compressors exhibit a negative dispersion which counters the temporal broadening [257].

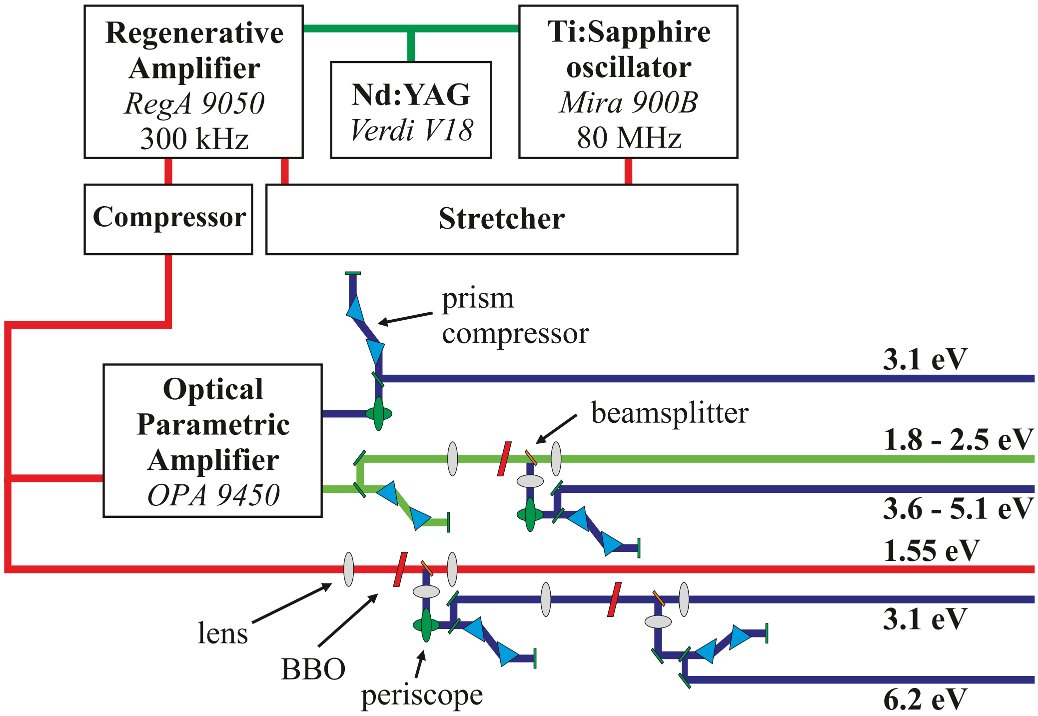

Figure 3.5.: Laser setup used for PES and 2PPE experiments. Pumped by a Nd:YAG laser, a Ti:Sapphire oscillator combined with a regenerative amplifier generates intense IR pulses which can be variously processed for final PES and 2PPE measurements via frequency doubling or by an OPA. Adapted from [258].

Compared to other 2PPE setups found around the world, the herein presented setup has two distinguishing features. The first to mention is the broad spectral range of accessible photon energies for PES and 2PPE investigations which allows a variety of different laser beam combinations and measurement techniques. At this point it is important to underline the possibility of performing 2PPE spectroscopy in order to determine the electronic position and physical origin of detected electrons. An almost unique feature of the present 2PPE setup is the fact that photo-excited electrons are detected by a TOF spectrometer. Compared to hemispherical analyzers, the applied TOF has a slightly lower energy resolution. However, the big advantage of applying a TOF spectrometer is its ability to simultaneously detect electrons of a wider energy range, whereas the pass energy has to be readjusted in hemispherical analyzers. This facilitates measurements with a low photon dose which was proven to be important as photo-induced sample modifications play a crucial role in common PES and 2PPE spectroscopy investigations [242–246].

3.3. Measurement Procedures and Beam Characteristics

Using a TOF spectrometer for electron detection enables the investigation of photo-induced processes like photo damage, photo-induced charge transfer or photo-induced molecular switching as has recently been demonstrated [121, 123, 124, 259–261]. This is usually performed in so-called *illumination series* including up to hundreds of subsequent monochromatic 2PPE measurements with constant laser power at the same spot on the sample held at liquid nitrogen temperature. The photon dose $PD(t)$ can be estimated using the time-averaged laser power P, illumination time t, photon energy $\mathrm{h}\nu$ and spot diameter w (assuming a circular spot):

$$PD(t) = \frac{P \cdot t}{\sqrt{2}\pi \cdot ({}^{w}\!/_{2})^2 \cdot \mathrm{h}\nu}. \tag{3.7}$$

It amounts to up to 10^{20} photons per second and square centimeter. This is why the spatial profile of the laser spot is specified by a CCD camera at a virtual sample position outside the UHV chamber, whereas the time-averaged laser power is measured with a commercial power meter (*Melles Griot*) and the photon energies have been determined with a grating spectrometer. Figure 3.6 shows a typical laser spectrum fitted by a Gaussian for central photon energy and bandwidth determination. It is accompanied by a false color plot of the corresponding beam profile fitted by a 2D Gaussian. In total, the setup has a spectral resolution in the range of 1.7 nm and a spot size of about $125\,\mu\mathrm{m}^2$. In order to obtain the correlated dichromatic 2PPE signal both beams (the UV- as well as the vis-beam) are spatially and temporarily overlapped on the sample which leads to a 2PPE spectrum combining both, the monochromatic 2PPE as well as the correlated dichromatic 2PPE signal. The spectrum which contains all these contributions is also called *consolidated spectrum*.

The usual measurement sequence for spectroscopic investigations includes three successive measurements: a consolidated, a monochromatic 2PPE UV-only and a monochromatic 2PPE Vis-only spectrum, which enables the subtraction of both monochromatic 2PPE spectra from the consolidated spectrum resulting in the correlated dichromatic 2PPE signal. Performing this measurement sequence for different photon energies yields in photon energy dependent spectroscopic investigations for the monochromatic as well as for the correlated dichromatic 2PPE signal, usually called *photon energy series* (1C-PES and 2C-PES, respectively). Choosing the UV photon energy to be below the sample's

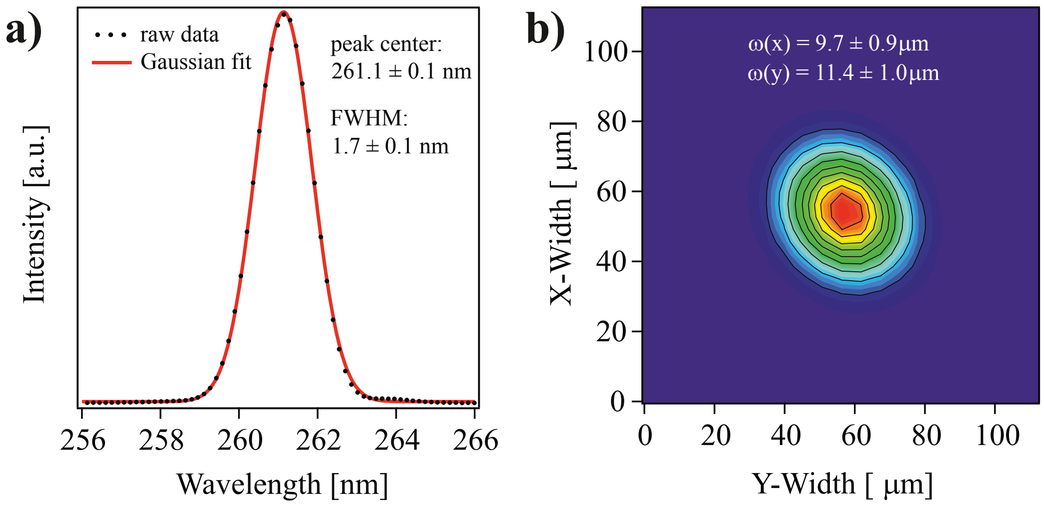

Figure 3.6.: Characterization of the used 2PPE setup: According to the Gaussian fits, the spectral resolution amounts to be 1.7 nm a) and the spot size on the sample is about 125 μm^2 b) (calculated using the full width at half maximum (FWHM) of the beam profile).

work function implies that there is no signal in the monochromatic 2PPE Vis-only spectra according to the fact that the visible photon energy is not sufficient to excite an electron above E_{vac} via a non-linear optical two-photon process.

In total, the spectroscopic investigation of a sample via 2PPE can be presented within an energy diagram in which the energetic position of occupied (initial) and unoccupied (intermediate and final) electronic states is shown relative to E_{F}. For occupied electronic states this energy value is also called *binding energy* ($E_{\mathrm{Bind}} - E_{\mathrm{F}}$), whereas for unoccupied electronic states this energy value is called intermediate state energy ($E_{\mathrm{i}} - E_{\mathrm{F}}$).

3.4. Recent Research on Metal/Organic Interfaces by means of 2PPE

Over the last twenty years, the application of 2PPE has led to interesting results targeting the electronic structure, charge carrier dynamics and photo-induced processes at metal/organic interfaces. The present section shortly summarizes the most important aspects and results in regard to the hereafter presented experimental results of this thesis. As it is not expedient to immerse these topics in much detail, interested readers are referred to the respective literature. Up to the 1990s 2PPE was most commonly applied to study the electronic structure of metal surfaces [153, 247]. In doing so, fundamental understanding was gained in regard to characterize surface states (SSs) and image potential states (IPSs) [152, 158, 262]. Additionally, it turned out that the adsorption of atomic layers has an impact on the energetic position of IPS, their delocalization and their lifetimes [113, 161, 163, 263–272]. The impact of larger molecules adsorbed as dielectric adsorbate layers on metal substrates is still a research field of vital interest. Nonetheless, the focus has moved from pure IPS investigations to dynamical processes like charge carrier or exciton dynamics and photo-induced switching mechanisms in view of possible applications of metal/organic interfaces in organic (opto)electronic devices [107, 114, 123, 182, 249, 259, 260, 273–275]. Beside these dynamical effects, 2PPE also gains importance from its applicability to give an overview of the interfacial electronic structure [118, 253, 276–278]. Recently, metal/organic interfaces have attracted much attention since Temirov *et al.* [66] in 2006 proposed a free electron-like dispersion of an electronic state in an organic monolayer adsorbed on a metal substrate. This observation was interpreted as evidence for adsorbate-induced band formation at metal/organic interfaces indicating possibly enhanced charge injection characteristics into thicker adsorbate layers. Since this initial demonstration of a dispersing adsorbate-induced interface state, paramount academical interest has been evoked by studies revealing new dispersive electronic states at metal/organic interfaces [66, 68, 69, 95, 106, 108, 140, 147, 279–281]. Yet, in most cases (also in case of the initial observation [66]) those designated interface states can be (retrospectively) assigned to SSs of the underlying metal substrate which got energetically shifted due to the interfacial metal-adsorbate interaction.

2PPE experiments play a decisive role in this research field as the SSs of the underlying metal substrates get energetically up-shifted above E_F and therefore can not be detected with common ARPES measurements. Figure 3.7 illustrates the most important findings from 2PPE results concerning a

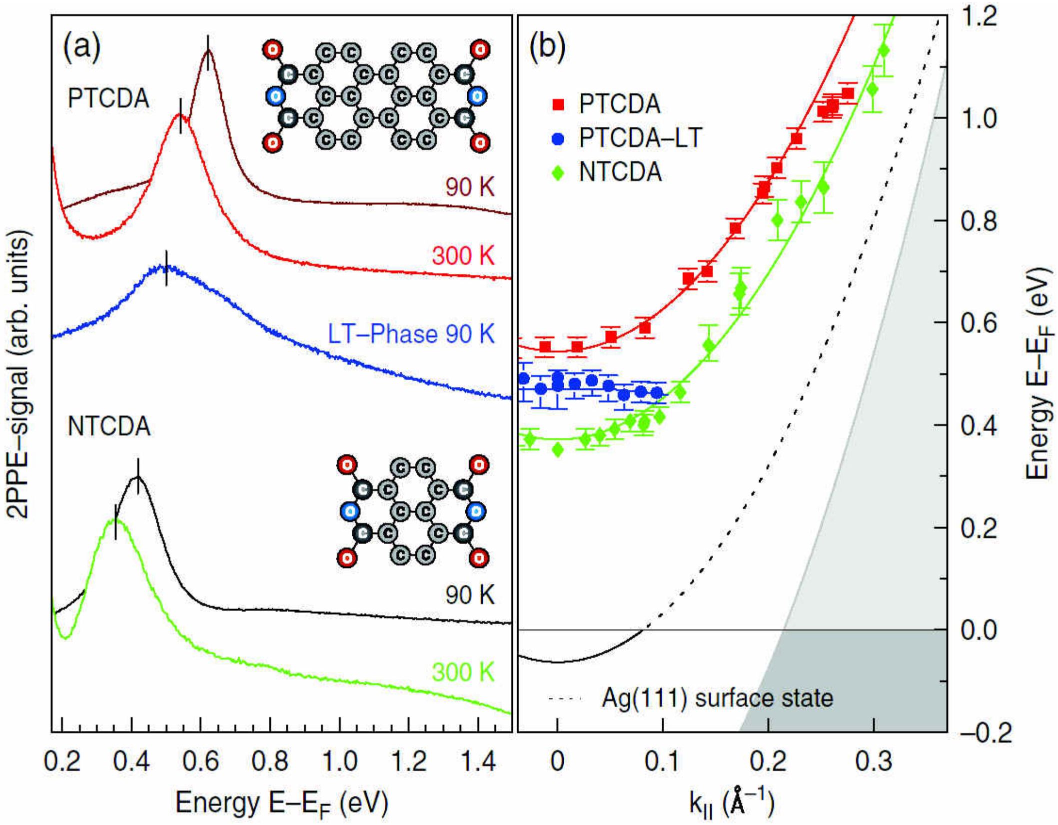

Figure 3.7.: Recent research results for PTCDA adsorbed on Ag(111) studied with energy- and angle-resolved 2PPE. a) Monochromatic UV/UV 2PPE spectra reveal the existence of unoccupied interface states around 0.5 eV above the Fermi edge. b) Angular dependence of the interface state's energetic peak position. For a detailled discussion see [70, 106, 140, 147, 280, 282]. Adopted from ref. [280].

new arising interfacial state at the PTCDA/Ag(111) interface which certainly is the best investigated metal/organic interface with such kind of interface state. Figure 3.7a depicts monochromatic UV-only 2PPE spectra for long-range ordered monolayers of PTCDA (red) and its smaller relative NTCDA (Naphthalene-tetracarboxylic dianhydride, green) adsorbed on a Ag(111) surface at room temperature (light colors) and at 90 K (dark colors). Additionally, a 2PPE spectrum of PTCDA adsorbed in the low-temperature phase is shown in blue. For all three systems monochromatic UV-only 2PPE measurements reveal the existence of an unoccupied interface state around 0.5 eV above the FE (black marks in figure 3.7a). The much broader peak structure for the low-temperature phase grown PTCDA monolayer can be interpreted as a result of reduced geometric ordering at the interface as has been observed in STM investigations [70, 280, 283]. Figure 3.7b illustrates the angular dependent energetic position of the interface state for ordered molecular monolayers adsorbed at room temperature and for the PTCDA low-temperature phase. Moreover, the projected bulk bands of the Ag(111) surface are visualized as gray-shaded area and the dispersing SS of the clean Ag(111) surface is implemented as a black line. The observed interface states of PTCDA and NTCDA adsorbed at room temperature and the SS of the clean Ag(111) surface are characterized by a comparable dispersion which consequently visualize a very similar effective mass of these electronic states. Therefore, subsequent 2PPE studies on these designated interface states at metal/PTCDA interfaces manifest the current interpretation of an adsorbate-induced up-shifted SS [70, 106, 140, 147, 280, 282]. Furthermore, this interpretation is substantiated by different AR2PPE investigations of comparable metal/organic systems with similar up-shifted SS characteristics [68, 108]. Nevertheless, the dream of adsorbate-induced band formation at metal/organic interfaces still exists and is nursed by ARPES results from Wießner *et al.* [69, 281]. These results revealed for the first time substrate-mediated band-dispersion of adsorbate molecule-induced states with very different dispersion characteristics compared to the underlying metal substrate [69, 281]. On account of these results, it is important to preparatorily study the electronic structure and band dispersion of the used metal substrate. Therefore the next chapter explicitly determines the electronic structure and band dispersion at the Au(111) surface.

4. The Electronic Structure of Au(111)

Single-crystal metal surfaces are often applied as substrates for 2PPE investigations as their electronic structure shows easily accessible and intense surface states and image potential states (for details see section 2.2). Due to their strong localization in normal direction to the surface these electronic states are very sensitive to modifications of the surfacial electronic structure. For that reason single-crystal metal surfaces are commonly used to study the impact of molecular adsorption on the surfacial electronic structure via 2PPE including processes like charge delocalization, charge carrier dynamics and photo-switching [116–120, 123]. The Au(111) surface is one of these prototypical metal substrates. Due to its chemical inertness it usually allows 2PPE studies at low-interacting metal/organic interfaces. But in the course of this thesis it will be demonstrated that also an underlying Au(111) surface may have strong influences on the electronic structure of metal/organic interfaces as it was similarly observed for PTCDA adsorbed on silver surfaces (for details see section 3.4).

In order to avoid misassignment and misinterpretation of much more complex results targeting the electronic structure of molecule/Au(111) interfaces and possible adsorbate-induced electronic rearrangements, this chapter introduces the electronic structure of a clean Au(111) surfaces. Starting with a brief overview, the electronic structure around E_F including SS and IPSs is specifically addressed. For later comparison with the electronic structure of metal/organic interfaces the focus especially lies on the dispersion of the SS and IPSs. A following detailed 2PPE study of the particular single-crystal Au(111) surface applied in this thesis demonstrates that this gold sample features all characteristics of a clean Au(111) surface.

Frequently, gold surfaces are used as prototypical conducting substrates and therefore depict model-subjects of intensive surface science investigations since photoemission per se was applied as an experimental tool in order to study the electronic structure of surfaces and interfaces. Gold crystallizes in a face-centered cubic (fcc) lattice which implies a hexagonal structure of the Au(111) surface. Nonetheless, it is energetically favorable for surface atoms of the Au(111) surface to rearrange which results in the so-called herringbone reconstruction [284, 285]. A calculated band structure of the Au(111) surface is presented in figure 4.1 accompanied by a model of the first surface Brillouin zone. At the center of the first Brillouin zone marked with Γ the local band gap between the occupied sp-hybridized band and the first virtual one amounts to 4.6 eV (from −1.09 to 3.51 eV) [286]. In this gap a SS is energetically located below E_F exhibiting a free electron-like dispersion as initially predicted by Tamm and Shockley [132, 133]. The presented calculation fits to experimental derived UPS data as shown in figure 4.1 on the right. Additionally, the occupied sp-hybridized band feature is characterized by a free electron-like dispersion, whereas deeper lying d-bands do not show significant dispersions around the Γ-point [287].

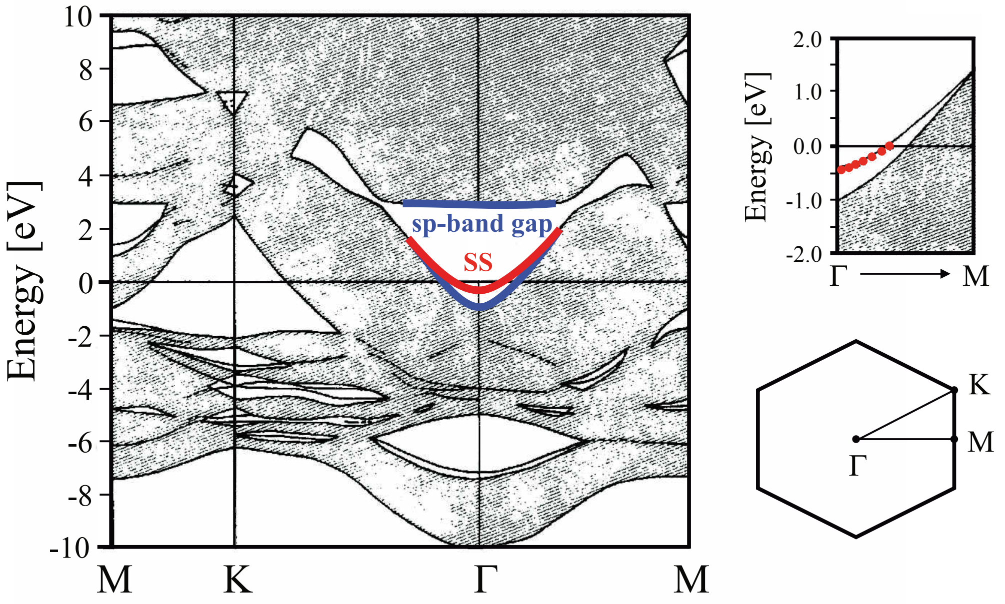

Figure 4.1.: Calculated electronic structure of a Au(111) surface. Around the Brillouin zone center (Γ-point) the occupied sp-hybridized band feature (SP) and the sp-derived SS are characterized by free electron-like dispersions. The graph on the upper right substantiates the calculation by measured data using UPS. The graph on the lower right illustrates the first Brillouin zone of a Au(111) surface. Adapted from [287].

The energetic position and dispersion of SS, the occupied sp-hybridized band feature and of the IPSs as well as the work function of the Au(111) surface represent frequently aimed research topics. Table 4.1 lists the most reasonable results from UPS, STS and 2PPE measurements to give insights into the complex historic path of a transparent verifiable electronic description of the Au(111) surface. For comparison, characteristics from this thesis obtained via

2PPE are specified in the last row. Today high-quality Au(111) surfaces are characterized by a work function about 5.5 eV and a narrow SS energetically located around 0.45 eV below E_F. Surface contamination and adsorption of atoms or molecules usually reduce the work function, broaden and shift the SS towards E_F [138, 139, 142, 143, 288]. However, contamination or molecular adsorption shows only less distinct impact on the respective dispersion of SSs and IPSs. The subsequent detailed specification of the applied Au(111) surface of this thesis demonstrates the high standard of the sample but also enables commensurability with former studies and facilitates the identification of adsorbate-induced changes. The Au(111) surface under investigation was cleaned by several cycles of sputtering (with Ar^+ ions) and subsequent annealing steps at 800 K. LEED investigations reveal the presence of a (111) symmetry. One pattern is exemplarily inset in figure 4.2a. An applied primary energy of 52 eV reveals a six-fold symmetric LEED pattern as predicted for a clean Au(111) surface (shown in figure 4.1). The sample's work function represents another indication for a contamination-free well-defined Au(111) sample. It can be read from the SE of a 2PPE spectrum displayed versus the final state energy referenced to E_F. Figure 4.2a illustrates an exemplary monochromatic 2PPE spectrum of a clean Au(111) surface measured using photons of 4.55 eV photon energy. The experimentally derived work function amounts 5.50 ± 0.02 eV which is at the upper limit of published values (see table 4.1) and satisfactory fits to calculations [286]. Additionally, the shown monochromatic 2PPE spectrum in figure 4.2a exhibits five distinct photoemission peaks which can be assigned to occupied electronic states of the Au(111) surface: three features arise from the bulk d-bands ($\mathrm{D_i}$), one from the occupied sp-band (SP) and the dominant feature can be assigned to the sp-derived Shockley surface state (SS).

Performing a monochromatic photon energy series using UV-light provides access to the binding energy of the assigned electronic states. As illustrated in figure 4.2b the energetic position of the assigned photoemission peaks in monochromatic 2PPE spectra shifts with increasing photon energy as theoretically described in section 3.1. The energetic variation of the designated SS's position tracks the predicted behavior of an occupied electronic state ($\mathrm{m} = 2.0 \pm 0.1$). Nevertheless, this slope evaluation is not possible for electronic bulk states like the SP feature as these states often possess also a dispersion perpendicular to the surface (in $k_\perp$, according to figure 3.1). Figure 4.3 demonstrates this issue by depicting the photon-energy-dependent binding energy of SP measured via 2PPE. The dispersion of SP along the ΓL-line gives also rise to a temperature-dependent measured binding energy [255]. In summary the monochromatic 2PPE photon energy series of a clean Au(111) surface resulted in the assignment of five occupied electronic states: four bulk states

Year	Φ [eV]	E_{SS} [eV]	m^*_{SS} [m_e]	E_{SP} [eV]	m^*_{SP} [m_e]	E_{IPS1} [eV]	m^*_{IPS1} [m_e]
1931 [289]	4.9 ± 0.1						
1966 [290]	5.22 ± 0.05						
1966 [291]	5.45 ± 0.05						
1976 [135]		-0.5 ± 0.1					
1978 [292]	5.26 ± 0.04	-0.45 ± 0.05	0.37 ± 0.05				
1986 [293]						-0.42 ± 0.16	
1986 [294]						-0.6 ± 0.1	1.0 ± 0.2
1987 [295]		-0.41 ± 0.01	0.28 ± 0.01	-0.90 ± 0.03	0.34 ± 0.06		
1995 [296]	5.31	-0.44 ± 0.02				-0.80 ± 0.03	
1995 [297]	5.55 ± 0.03	-0.41 ± 0.03				-0.80 ± 0.03	
1996 [298]		-0.42	0.40				
2003 [288]		-0.49 ± 0.01	0.25 ± 0.01				
2004 [138]	5.36 ± 0.01	-0.47 ± 0.03	0.26 ± 0.01				
2009 [299]		-0.46 ± 0.01	0.23 ± 0.03	-0.90 ± 0.03	0.21 ± 0.01		
2009 [141]		-0.49 ± 0.02	0.26 ± 0.01				
2009 [255]	5.45 ± 0.05	-0.43 ± 0.05	0.29 ± 0.04				
2016 [142]		-0.43 ± 0.01	0.27 ± 0.05				
2016 [143]		-0.47 ± 0.01	0.27 ± 0.02				
2017	5.50 ± 0.02	-0.42 ± 0.03	0.23 ± 0.02	-0.89 ± 0.10	0.39 ± 0.02		

Table 4.1.: Historic path of most reasonable results targeting the electronic structure of a Au(111) surface. The evolution of work function values, binding energies and respective effective masses of SS and the occupied sp-band feature of the Au(111) surface are illustrated in chronological order. For comparison, the last row specifies the characteristics of the herein applied Au(111) surface. Due to the limited photon energy range of the experimental setup it was not possible to detect IPS at the clean Au(111) surface. Their energetic position is listed with respect to the vacuum level.

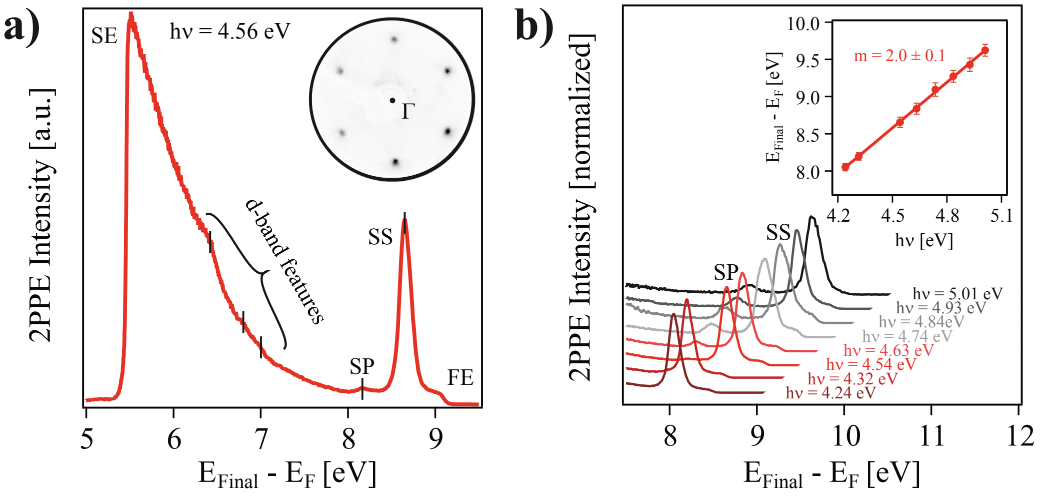

Figure 4.2.: Characterization of a Au(111) surface by means of 2PPE spectroscopy. a) Illustrates a single monochromatic 2PPE spectrum of the Au(111) sample and an inset LEED pattern while b) shows monochromatic 2PPE spectra for several applied photon energies and the resulting photon-energy-dependent energetic position of the SS.

and one surface state. Their binding energies are listed in table 4.2. IPSs of the clean Au(111) surface can not be observed with the applied laser setup as their population with electrons originating from occupied electronic states below E_F requires photon energies near 5 eV.

	Binding Energy [eV]
SS	-0.42 ± 0.03
SP	-0.89 ± 0.10
D1	-2.15 ± 0.03
D2	-2.74 ± 0.03
D3	-3.01 ± 0.03

Table 4.2: Binding energies of electronic states at the Au(111) surface experimentally observed by means of 2PPE spectroscopy. The results for SS and SP fit well to results from literature as reported in table 4.1.

AR2PPE investigations of a sample provide access to electronic states' dispersions in $k_\parallel$. In this thesis the Au(111) surface is mounted enabling AR2PPE measurements along the ΓM-line of the first surface Brillouin zone. Figure 4.4a illustrates normalized monochromatic 2PPE spectra observed using a photon energy of 4.54 eV for polar angles between 30° and $-10°$ slightly displaced to each other in steps of 2°. Besides non-dispersive d-band features near the SE figure 4.4a demonstrates the dispersion of SS, SP and one d-band feature (D). The latter one has been assigned to an occupied d-band feature as it would be located in the sp-band-gap in the unoccupied case.

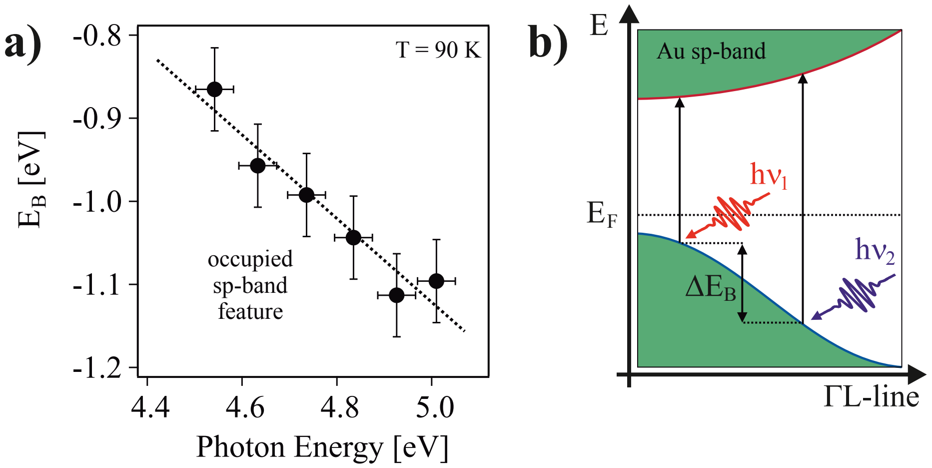

Figure 4.3.: Photon-energy-dependent binding energy of the occupied sp-band feature in 2PPE spectra. a) Demonstrates the increase of determined SP binding energies for increasing photon energy hν (dotted line is a guide to the eye) which can be explained by the excitation of electrons from different points along the ΓL-line (in this context the first Brillouin zone of the gold fcc-crystal is used for allocation). This failure of the necessary condition for possible slope evaluation in 2PPE spectroscopy is visualized in b). Consequently applying this slope evaluation to photoemission peaks in 2PPE spectroscopy holds only for electronic states without dispersion in $k_\perp$, for example surface states or adsorbate-induced electronic states at interfaces.

Furthermore, free electron parabolas visualized in figure 4.4b are fitted to the experimentally determined peak positions of SS and SP. They result in effective masses of $m^*_{\mathrm{SS}} = 0.23 \pm 0.02\,\mathrm{m_e}$ and $m^*_{\mathrm{SP}} = 0.39 \pm 0.02\,\mathrm{m_e}$, respectively. The herein obtained effective masses of SS and SP are consistent with literature findings (see table 4.1). Especially the dispersion of SS was topic of several ARPES studies in the last centuries yielding in an established value of around $0.25\,\mathrm{m_e}$ [138, 141–143, 255, 288, 295, 299]. In contrast, there are only few references for the dispersion of SP [295, 299] which both are matched qualitatively. As visualized in figure 4.1 calculations predict the existence of electron-like dispersing d-band features in gold which qualitatively fits to the herein observed dispersion of D [300–303].

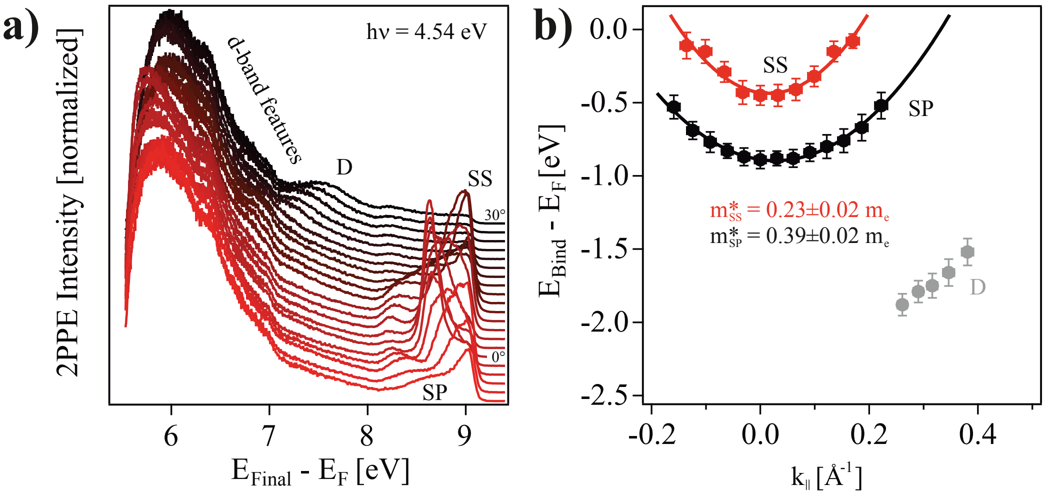

Figure 4.4.: Studying the dispersion of electronic states at the Au(111) surface by means of AR2PPE. a) Displays normalized monochromatic 2PPE spectra for different polar angles between 30° and -10° which have been observed using an applied photon energy of 4.54 eV. b) Peak positions of SS and SP are fitted using free electron parabolas in order to determine an effective mass m*.

5. Studying Metal/Organic Interfaces by means of Temperature - Programmed Desorption

Temperature-programmed desorption (TPD) is a suitable experimental tool to target interfacial processes during the desorption of organic molecules from (metal) surfaces and to determine the binding energy of a molecule adsorbed on an underlying surface [254, 304–308]. In particular TPD is applied in this thesis to determine the coverage or film thickness, respectively. TPD spectra visualize the desorption of adsorbed molecules in terms of a mass fragment intensity measured via QMS in dependence of a linearly increasing substrate temperature (here 1 $^{\mathrm{K}}/_{\mathrm{s}}$). Usually the desorption from the monolayer differs in temperature compared to the desorption of higher lying layers, respectively. A coverage-independent desorption (zero order desorption) is characterized by an exponential increasing QMS intensity for a linearly increasing substrate temperature which is followed by an abrupt decrease when desorption is completed. Contrarily higher intermolecular interactions on the surface usually lead to coverage-dependent desorption temperatures (first or second order desorption). Further experimental and theoretical predictions and descriptions can be found in refs. [305, 309, 310].

The following sections introduce studied organic molecules and the current status of research concerning their adsorption characteristics on a Au(111) surface. All molecules under investigation originate from the research field of donor-acceptor complexes which accompanies the development of organic electronics from the beginning [54, 72, 167, 311]. To the present day charge transfer mechanisms in donor-acceptor complexes and at donor-acceptor interfaces play a crucial role in organic electronic devices (for more information see chapter 2) [41, 44, 48, 82, 83, 174].

5.1. Adsorption and Desorption of TCNQ on Au(111)

Since the early 1960s 7,7,8,8-tetracyanoquinodimethane (TCNQ) is known as a promising acceptor molecule from initial works on donor-acceptor complexes [312–316] (its chemical structure is visualized in figure 5.1a). Especially salts containing TCNQ anion radicals achieved great attention because of their high electrical conductivity [34, 74–76, 80, 175, 317–319]. They were influential in the development of conductive polymers which was honored with the Nobel Prize in Chemistry for A. J. Heeger, A. G. MacDiarmid and H. Shirakawa in 2000 [79, 320]. Due to its famous electron-accepting nature TCNQ is known to be negatively charged on various surfaces, in particular: Ni(111) [321, 322], Cu(100) [102, 323, 324], Cu(111) [325, 326], Ag(100) [324, 327], Ag(111) [327, 328], ITO [329], TiO_2 [330], Graphene [331–333] and PEDOT:PSS [329]. For certain, this list is not complete but illustrates the wide-ranging applicability of TCNQ as electron-accepting dopant.

In contrast to surfaces with lower work function, TCNQ was found to be neutral on Au(111) which makes this interface to a prominent research object [328, 334–336]. STM, STS and XPS investigations suggest a highly ordered network of weakly adsorbed TCNQ molecules on the Au(111) surface which is stabilized by hydrogen bonds [328, 334–336]. An STM image adapted from ref. [328] illustrates the reported one single molecule containing unit cell in figure 5.1c. Additionally, it reveals the persistence of the herringbone reconstruction of the underlying Au(111) surface in figure 5.1b. Its unaffected observation despite adsorption of TCNQ molecules again emphasizes the weakness of the interfacial metal-adsorbate interaction. However, there is computational evidence for a down-bending of cyano-groups which would indicate an interaction stronger than simple physisorption [336]. The reason for a comparatively weak metal-molecule interaction and the missing charge transfer at the TCNQ/Au(111) interface is discussed in section 6.1 by examining the electronic structure of the TCNQ/Au(111) interface.

For the presented experiments in this thesis TCNQ was commercially purchased from TCI[1]. The conditions for thermal evaporation ($p < 3 \cdot 10^{-10}$ mbar, $T_{\text{Doser}} = 388\,\text{K}$) are comparable to literature values [322, 324, 329, 337, 338]. In order to achieve full monolayer coverage the evaporation procedure was performed at a substrate temperature of 300 K, whereas for higher coverages the substrate was cooled with liquid nitrogen. Moreover, a residual gas analysis

---

[1] TCI Deutschland GmbH, Mergenthalerallee 79, 65760 Eschborn, Germany

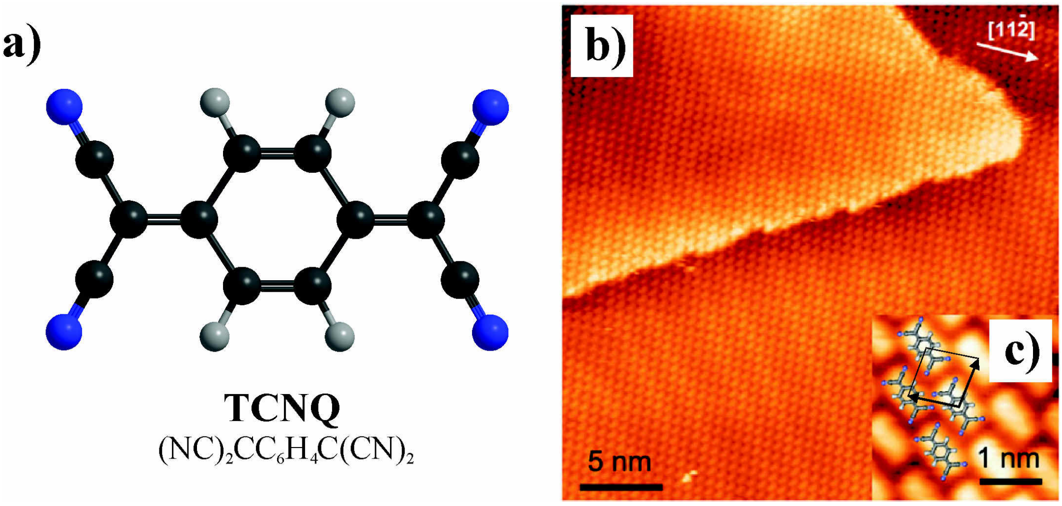

Figure 5.1.: Chemical structure of TCNQ and its adsorption geometry on Au(111). A single TCNQ molecule mainly consists of a central carbon ring and four electron withdrawing cyano groups at its quinoidal extremities a). The accompanying STM image illustrates the persistence of the herringbone reconstruction of the underlying Au(111) surface b) and indicates a monomolecular unit cell c). b) and c) were adapted from ref. [328].

(RGA) was performed to prove the evaporation of intact TCNQ molecules (see appendix B). It additionally allows the verification of the thermally induced desorption of entire molecules from the Au(111) surface. If the spectrum of fragment masses does not vary between the RGA and during TPD measurements the thermal desorption of intact molecules can be assumed. Figure 5.2 depicts TPD measurements for different molecular fragments for the same coverage in a) and for the same molecular fragment but different coverages in b). The former graph indicates that intact TCNQ molecules are thermally desorbed during TPD measurements as the observed molecule fragments coincide with mass fragments from the RGA. Moreover, it visualizes that the molecular fragment $C_{10}N_3^+$ with mass-to-charge ratio of 177 amu features the highest QMS intensity which makes it the best choice for coverage-dependent TPD measurements. Generally these coverage-dependent measurements shown in figure 5.2b display three desorption peaks: a first between 280 K and 340 K (α_1), a second between 300 K and 340 K (α_2) and a third between 390 K and 430 K (α_3). The shape of α_1 is coverage-dependent, whereas α_2 and α_3 saturate at low coverages (or get overgrown by α_1 as visualized for 13 ± 1 ML coverage). According to this behavior, α_1 is assigned to the desorption of higher lying layers, whereas α_2 visualizes desorption of the second and α_3 the desorption of the first layer of TCNQ

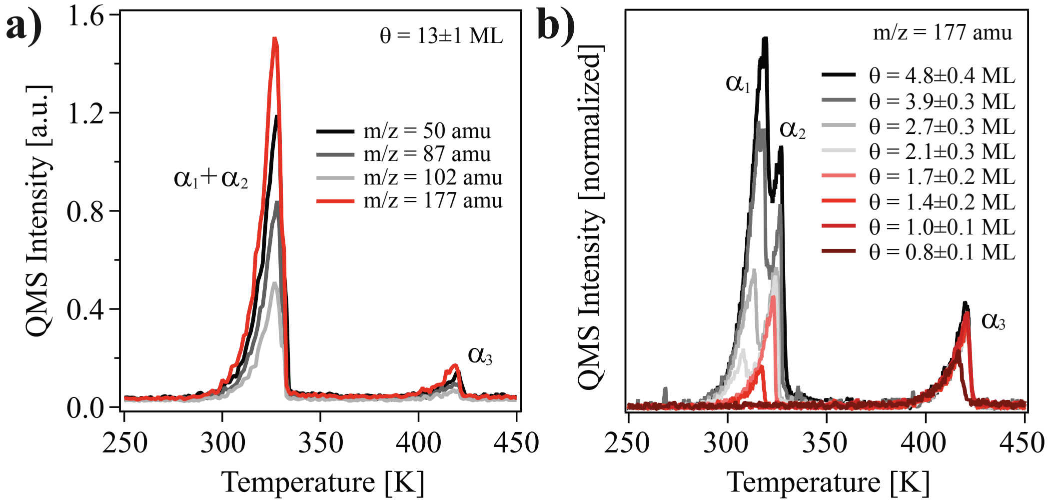

Figure 5.2.: Temperature-programmed desorption spectra of TCNQ intactly adsorbed on Au(111) for different molecular fragments at the same coverage in a) and for the same molecule fragment but different coverages in b).

molecules adsorbed on the Au(111) surface. The first adsorbate layer is also called monolayer (ML). A thermally induced redistribution between α_1 and α_2 was not observed which opposes to a possible assignment of α_2 to a metastable adsorption phase as it was demonstrated for benzene or cyclooctatetraene adsorbed on Ru(001) [339, 340]. Due to their specific desorption temperature ranges the monolayer is stronger bound to the underlying metal surface than the second TCNQ layer to the first and higher lying layers to each other. For increasing metal-molecule distance of course the binding energies of molecules align as soon as the influence of the underlying substrate vanishes. According to this observation, the interfacial metal-molecule interaction is certainly stronger than the intermolecular interaction between TCNQ molecules.
In total, all observed desorption peaks α_i in figure 5.2 noticeably display a very similar shape which can be assigned to zero order desorption. This indicates a coverage-independent molecular desorption and therefore a vanishing intermolecular interaction in higher layers as well as directly at the metal/organic interface. It also suggests a weak interfacial metal-adsorbate interaction. 2PPE investigations shown in figure 5.3 fit to this TPD-derived weak interfacial metal-adsorbate interaction as heating a TCNQ/Au(111) interface up to 600 K leads to an almost complete desorption of TCNQ molecules leaving a fairly clean Au(111) surface without organic molecule residues. More precisely the adsorbate-induced work function change is revoked and the SS is detected at the known energetic position of −0.4 eV. Nevertheless, there are also small

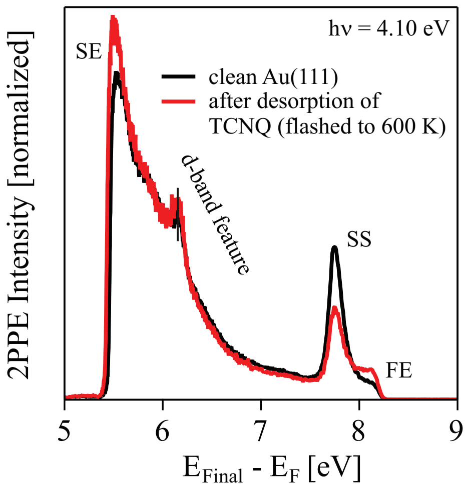

Figure 5.3: Monochromatic 2PPE measurements reveal that annealing a TCNQ covered Au(111) surface up to 600 K leads to an almost complete desorption of TCNQ molecules leaving a fairly clean Au(111) surface.

persisting spectral changes: first of all a decreased SS intensity and an increased DOS just below E_F. The almost complete desorption of TCNQ molecules in TPD measurements indicates the desorption of intact molecules. Assuming such a complete desorption, an integration of the background-corrected QMS intensity $I(T)$ for the observed signals α_i can be used for an estimation of coverage. All TCNQ coverages stated in this thesis were estimated using the following equation:

$$\Theta = \int\limits_{\alpha_1+\alpha_2} I(T)\mathrm{d}T \Big/ \int\limits_{\alpha_3} I(T)\mathrm{d}T + 1. \tag{5.1}$$

A very similar estimation of coverage was performed for the F$_4$TCNQ/Au(111) interface which is discussed in the following section.

5.2. Adsorption Geometry and Desorption Characteristics of F_4TCNQ on Au(111)

Since its first synthesis in the 1970s the quadruple fluorinated TCNQ derivative 7,7,8,8-tetracyano-2,3,5,6-tetrafluoroquinodimethane (F_4TCNQ) is one of the most famous and widely used organic acceptor molecules [316] (its chemical structure is visualized in figure 5.4a. It achieved great attention due to its very high EA (5.20 eV [341]) which makes it applicable for all kinds of organic electronic devices [41, 83, 172, 194, 195, 197]. In particular, F_4TCNQ is applied on one side as an organic dopant to increase the charge carrier density in organic thin films. On the other side it can be used as hole injection layer in organic electronic devices. Like in case of TCNQ, the extraordinary electron-accepting nature of F_4TCNQ leads to the formation of negatively charged molecular species on various surfaces, for example Cu(100) [93, 342], Cu(111) [343, 344], Ag(111) [211, 344], Au(111) [47, 92, 97, 344], ZnO(000$\bar{1}$) [217, 345], diamond (100) [346] and graphene [331, 347–349].

In contrast to the unfluorinated TCNQ, F_4TCNQ was also found to be negatively charged on Au(111) [47, 92, 97, 344]. This fact is usually explained due to the higher EA of F_4TCNQ. STM/STS investigations unveiled a well-defined geometric metal-adsorbate interfacial network at the F_4TCNQ/Au(111) interface. It turned out that at room temperature, F_4TCNQ molecules are two-fold coordinated with Au adatoms segregated from the underlying crystalline metal surface [97]. Figure 5.4 illustrates the molecular structure and adsorption geometry (illustration rendered using VMD 1.9.2 [350]). The geometry is stabilized due to charge transfer from the metal surface to the F_4TCNQ molecule, as also observed for the adsorption of very electronegative atoms [351, 352]. This two-fold coordination destroys the herringbone reconstruction of the underlying Au(111) surface in contrast to its persistence on the TCNQ/Au(111) surface [96, 97, 328, 334]. Furthermore, the reported metal/organic network formation might be accompanied by a down-bending of the cyano-groups as described for F_4TCNQ adsorbed on other metal surfaces [93, 211, 343, 344]. The electronic consequences of this metal/organic network formation and charge transfer type interaction are extensively discussed in section 6.2.

For this thesis F_4TCNQ molecules were commercially purchased from TCI[2]. The conditions for thermal evaporation ($p < 3 \cdot 10^{-10}$ mbar, $T_{\mathrm{Doser}} = 408\,\mathrm{K}$, $T_{\mathrm{S}} = 300\,\mathrm{K}$ or $T_{\mathrm{S}} = 300\,\mathrm{K}$) are similar to literature values [97]. Just as in case of TCNQ, an RGA indicates the evaporation of intact F_4TCNQ molecules (see

---

[2] TCI Deutschland GmbH, Mergenthalerallee 79, 65760 Eschborn, Germany

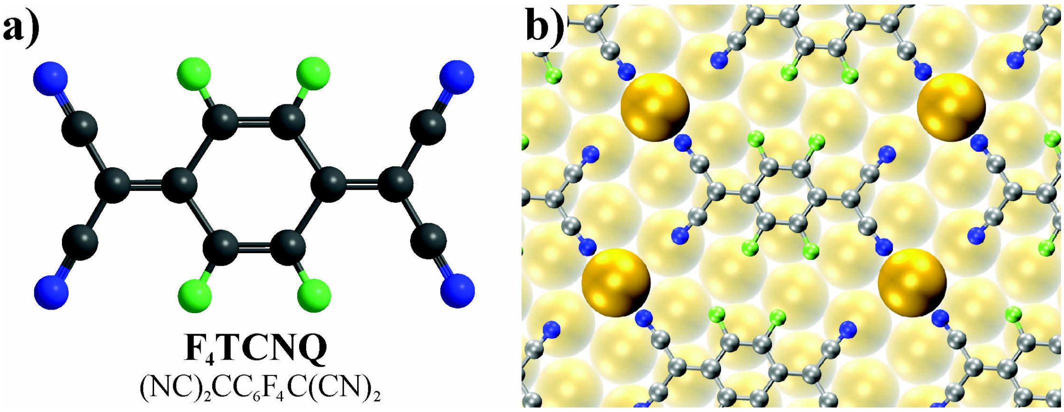

Figure 5.4.: Chemical structure of F_4TCNQ and its adsorption geometry on Au(111). a) F_4TCNQ matches the chemical structure of TCNQ but owning fluorine atoms instead of hydrogen atoms at the central ring. The cyano groups and its quinoidal extremities remain unaffected. b) According to STM investigations, F_4TCNQ molecules are two-fold coordinated with Au adatoms segregated from the underlying crystalline metal surface [97]. The visualization was rendered using VMD 1.9.2 [350].

appendix B). But in contrast to TCNQ which weakly adsorbs on a Au(111) surface, the STM-derived two-fold coordination with Au adatoms and the disappearing herringbone reconstruction of the underlying Au(111) surface are indications for a strong metal-molecule interaction at the F_4TCNQ/Au(111) interface. Consequently, LEED can be used to gain insights into the geometrical structure of the F_4TCNQ/Au(111) interface under investigation. For TCNQ adsorbed on Au(111) such LEED measurements are unemployable due to the incoming electron-induced dissociation. Figure 5.5a visualizes a LEED pattern derived from the F_4TCNQ/Au(111) interface at full monolayer coverage using an electron primary energy of 22 eV. This contrasty pattern fits to a simulated LEED pattern shown in figure 5.5b which is based on the STM-derived adsorption geometry displayed in figure 5.4b. The simulation of this LEED pattern was performed using LEEDpat 4.2 [353].

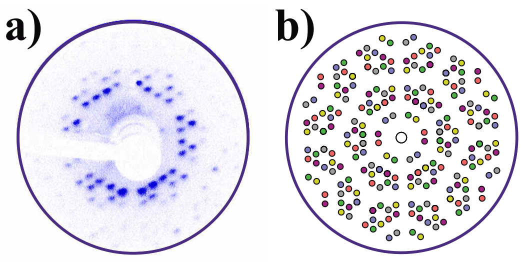

Figure 5.5: LEED pattern of the F_4TCNQ/Au(111) interface at full monolayer coverage (primary energy: 22 eV). The experimentally derived LEED pattern a) can be simulated b) using the STM-derived two-fold coordinated adsorption geometry with monomolecular unit cell. This simulation was performed with LEEDpat 4.2 [353].

It implies the incorporation of six different adsorption domains as expected for an adsorbate with monomolecular unit cell on a six-fold rotational symmetric surface (differently colored in figure 5.4b). The high comparability of measurement and simulation proves that the F_4TCNQ/Au(111) interface features the STM-derived adsorption geometry which involves a charge transfer type interaction and a two-fold coordination of each F_4TCNQ molecule with Au adatoms [97]. As a result the geometric structure of F_4TCNQ molecules adsorbed on a Au(111) surface can be described by a monomolecular unit cell with two lattice vectors b_1 and b_2 in which a_1 and a_2 represent the Au(111) surface unit vectors [97]:

$$\begin{pmatrix} b_1 \\ b_2 \end{pmatrix} = \begin{pmatrix} 5 & 2 \\ 1 & 3 \end{pmatrix} \begin{pmatrix} a_1 \\ a_2 \end{pmatrix}. \tag{5.2}$$

As adsorption and desorption characteristics are correlated, this stronger interfacial interaction in case of F_4TCNQ should also influence the desorption properties. In order to target a verification of this conclusion, an extended TPD analysis of the F_4TCNQ/Au(111) interface was performed. Figure 5.6 illustrates the most important results from TPD measurements. Generally, the observed molecular fragments during TPD measurements match RGA results during the evaporation procedure (comparing results from figure 5.6a to RGA results shown in appendix B). This result suggests the adsorption of intact F_4TCNQ molecules on the Au(111) sample. Moreover, figure 5.6a indicates a similar desorption peak shape for different mass-to-charge ratios from which the molecular fragment CF^+ (m/z = 31 amu) features the highest intensity. Higher lying adsorbed F_4TCNQ layers form a coverage dependent desorption feature between 300 K and 360 K as visualized in figure part b). For F_4TCNQ evaporation onto a Au(111) substrate held at room temperature ($\mathrm{T_S} = 300\,\mathrm{K}$) this signature consists of one single desorption signature β_2. However, for evaporation onto a cooled substrate ($T_\mathrm{S} = 100\,\mathrm{K}$) the desorption of multilayer is divided in two features β_1 and β_2. Figure 5.6c illustrates TPD spectra for F_4TCNQ desorbing from a Au(111) surface formerly evaporated on a substrate held at room temperature ($\mathrm{T_S} = 300\,\mathrm{K}$) or at 100 K. Therefrom β_1 is slightly shifted to lower desorption temperatures compared to β_2 ($\Delta\mathrm{T} \approx 10\,\mathrm{K}$) which points towards an assignment to a less ordered adsorption phase. On basis of TPD measurements at different coverages for both substrate temperatures, β_1 and β_2 can be assigned to two different adsorption phases in higher lying adsorbate layers. Both desorption peaks, β_1 and β_2, are characterized by a zero-order desorption shape indicating a coverage-independent molecular desorption.

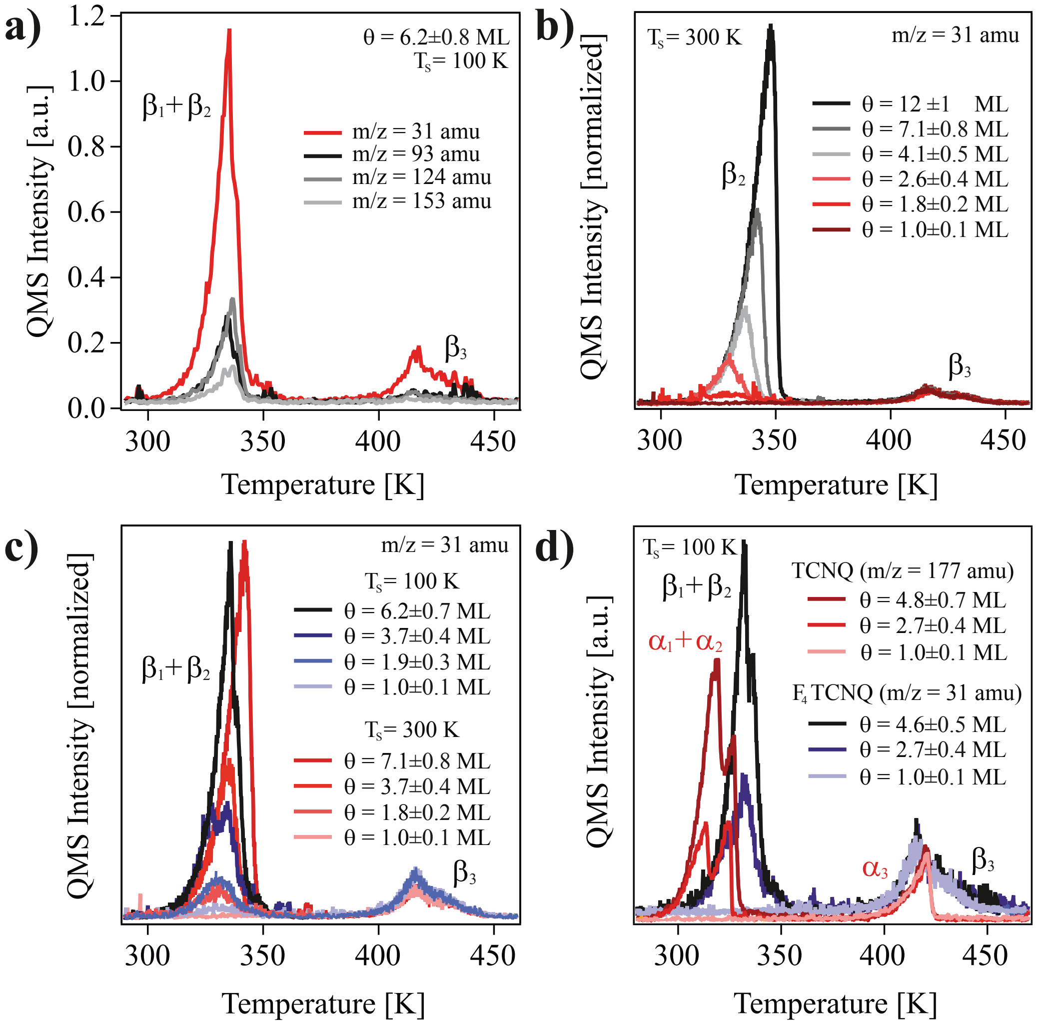

Figure 5.6.: Temperature-programmed desorption spectra of F_4TCNQ intactly adsorbed on Au(111) for different molecular fragments at the same coverage in a) and for the same molecule fragment but different coverages of F_4TCNQ molecules adsorbed on a Au(111) surface hold at room temperature in b). c) Displays different shapes of TPD measurements for evaporation on a Au(111) surface held at room temperature or at $T_S = 100\,$K. A comparison of TPD spectra of TCNQ and F_4TCNQ adsorbed on a Au(111) surface held at $T_S = 100\,$K is shown in d).

Figure 5.6d visualizes differences in the desorption characteristics of TCNQ and F_4TCNQ. As a whole, the desorption characteristics of both molecules adsorbed on a Au(111) surface are very similar. The desorption peak derived from monolayer desorption of F_4TCNQ (β_3) is detected in the same temperature range as the assigned monolayer desorption of TCNQ molecules (α_3). But the desorption of TCNQ in higher lying layers starts at lower temperature than the desorption of F_4TCNQ in higher lying layers. This temperature difference of around 20 K is highly important. It enables the adsorption of thick F_4TCNQ films on a Au(111) surface even held at room temperature, whereas thick films of TCNQ have to be evaporated onto a cooled surface. Particularly, striking differences can be found in the shape of desorption peaks assigned to monolayer desorption (α_3 and β_3). The desorption of a TCNQ monolayer is characterized by a zero-order desorption shape as discussed in section 5.1, whereas F_4TCNQ desorption of the monolayer leads to a much broader second-order-type shape. This distinctly divergent behavior of F_4TCNQ compared to TCNQ adsorbed on a Au(111) surface can be explained due to a much stronger metal-molecule interaction and a dissociative desorption in case of F_4TCNQ. A charge transfer type interaction and a two-fold coordination of each F_4TCNQ molecule with Au adatoms (as stated by STM investigations [97]) implies a higher desorption temperature. But a mutual intermolecular influence at submonolayer coverage leads to a reduction of a single F_4TCNQ molecule's binding energy due to a repulsive intermolecular interaction at the surface. That would explain why the desorption peak maximum β_3 shifts to lower binding energies with increasing submonolayer coverage as suggested from a TPD analysis of different submonolayer coverages. The inset of figure 5.7a visualizes the decreasing desorption temperature with increasing submonolayer thickness or evaporation time, respectively. Film thicknesses above full monolayer coverage do not influence the desorption features of the monolayer. Despite of this stronger metal-molecule interaction, 2PPE measurements reveal a complete desorption of F_4TCNQ molecules from a Au(111) surface without any detectable adsorbate residues by flashing the sample up to 600 K. More precisely the adsorbate-induced work function change is revoked and the SS and SP features of a clean Au(111) surface are detected at known energetic positions and intensities as illustrated in figure 5.7b. This result enables the estimation of the coverage by integrating TPD spectra as previously discussed in case of the TCNQ/Au(111) surface. Conversely, this coverage estimation can not be applied to the Tetrathiafulvalene/Au(111) interface which will be presented and argued in the following section.

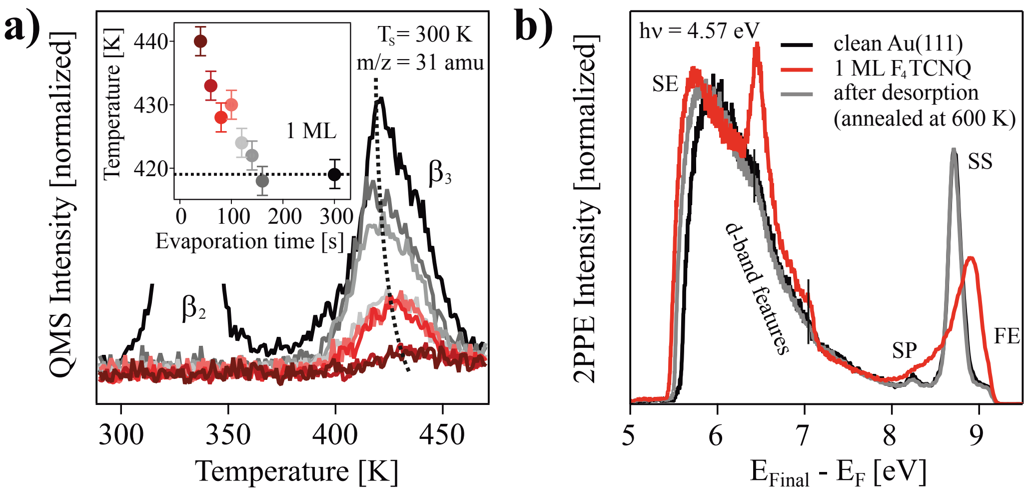

Figure 5.7.: a) Temperature-programmed desorption spectra of different coverages in the submonolayer regime indicate a second-order desorption behavior for F$_4$TCNQ molecules adsorbed in the monolayer on Au(111). The inset and a guide to the eye (dotted line) visualize the decreasing desorption temperature with increasing submonolayer coverage or evaporation time, respectively. b) Monochromatic 2PPE investigations reveal that flashing a F$_4$TCNQ covered Au(111) surface up to 600 K leads to an almost complete desorption of F$_4$TCNQ molecules leaving a fairly clean Au(111) surface without organic molecule residues.

5.3. Adsorption and Desorption of TTF on Au(111)

Tetrathiafulvalene (TTF) is a staple-molecule for the synthesis of a wide bunch of (supra-)molecular architectures with extraordinary electron donating characteristics (its chemical structure is visualized in figure 5.8a [354–365]. Its first synthesis in the early 1970s achieved great attention as it was used in combination with TCNQ for the formation of the first *organic metal*, namely TTF-TCNQ [34, 74–76, 175, 317, 319]. Within such CTCs, TTF usually serves as donating part by transferring a specific amount of negative charge to the participating acceptor molecule (for example TCNQ). Equally this happens on high work function surfaces as for example on Ag [91, 209], Au [91, 94, 209, 329, 366, 367], PEDOT:PSS [329] and ITO [329]. Especially the TTF/Au(111) interface attracted interest since STM investigations exposed an interfacial charge transfer type interaction between adsorbate and underlying metal surface which modulates a long-range repulsive intermolecular interaction [94, 366]. Figure 5.8b depicts an STM image of a small amount of TTF molecules (< 0.1 ML) adsorbed along the fcc sites of a Au(111) herringbone reconstructed surface (adapted from ref. [94]). The displayed self-assembly can be affiliated to a long-range repulsive interaction between positively charged TTF molecules, also known as *Coulomb repulsion* [94]. Additionally, density functional theory (DFT) calculations give evidence for an adsorbate-induced increase of the interfacial DOS [209]. This result implements an electron density smeared out over the entire interface for full monolayer coverage as indicated by an exemplary isodensity plot shown in figure 5.8c [209]. At monolayer coverage, however, STM measurements state a two-molecule containing unit cell as visualized in figure 5.8d [94, 366].

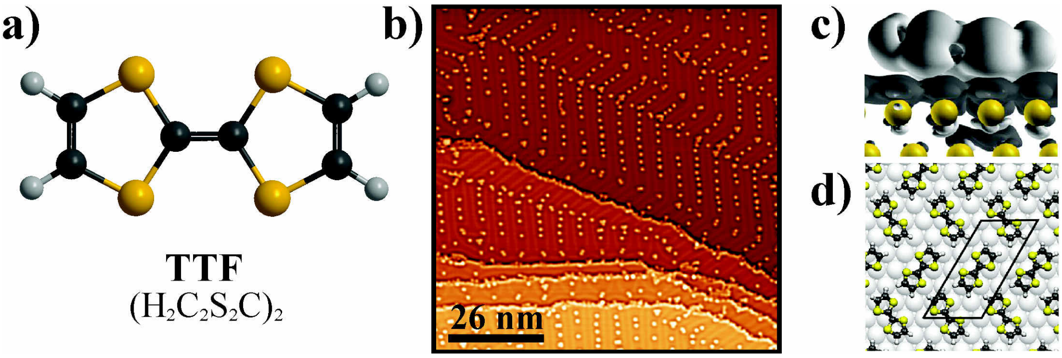

Figure 5.8.: Chemical structure of TTF and its adsorption geometry on Au(111). a) Compared to a simple fulvalene molecule TTF consists of four sulfur atoms replacing carbon atoms. Due to the charge transfer type interaction with an underlying substrate TTF molecules are positively charged and feel a long-range repulsive intermolecular interaction on a Au(111) surface. This leads to a self-assembled molecular arrangement for submonolayer coverage b) (adopted from ref. [94]). But at full monolayer coverage TTF adsorption leads to an electron density smeared out over the entire interface (as indicated by DFT calculations) c) and to the formation of a two-molecule containing unit cell as visualized in d) (adopted from refs. [209] and [366], respectively).

For experiments described in this thesis also TTF molecules were commercially purchased from TCI[3]. TTF molecules are thermally evaporated onto a clean Au(111) substrate which was usually held at room temperature. Generally, the evaporation conditions in this thesis, namely 323 K dosing temperature at increasing base pressure (up to 10^{-8} mbar), conform to literature values [337, 338]. Only targeting higher film thicknesses the substrate was cooled to increase adhesion. Just as for TCNQ and F_4TCNQ, an RGA indicates the evaporation of intact TTF molecules (see appendix B). But in contrast to the former discussed acceptor molecules, TPD spectroscopy of a TTF covered

---

[3] TCI Deutschland GmbH, Mergenthalerallee 79, 65760 Eschborn, Germany

Au(111) surface displays different desorption shapes for different molecule fragments as shown in figure 5.9a. In particular the molecule fragment m/z = 32 amu, which can be assigned to single sulfur atoms, displays a complete diverging behavior. These single sulfur atoms are observed at higher desorption temperatures compared to other mass-to-charge ratios which can be explained by the high sulfur-gold interaction directly at the interface. The difference in desorption temperature proves a dissociative interfacial reaction during the desorption of TTF molecules from a Au(111) surface. According to its high intensity and the consequential detectability of a desorption peak above 300 K desorption temperature, the molecule fragment $C_2SH_2^+$ (m/z = 58 amu) was chosen as the most suitable one for a coverage-dependent TPD investigation.

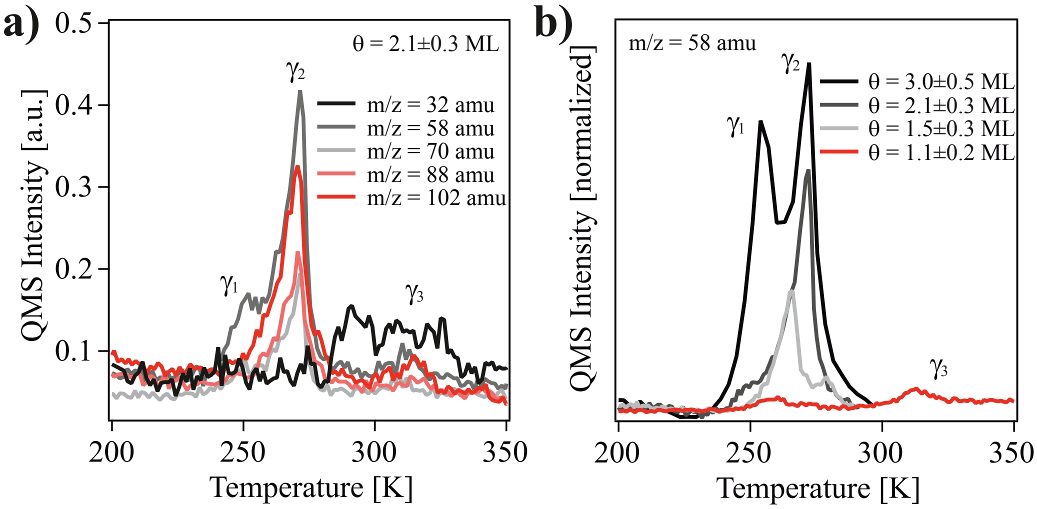

Figure 5.9.: Temperature-programmed desorption spectra of TTF intactly adsorbed on Au(111) for different molecular fragments at the same coverage in a) and for the same molecule fragment but different coverages in b).

Figure 5.9b illustrates such a coverage-dependent measurement in which three desorption peaks γ_i can be found. Both, γ_1 and γ_2, show coverage-dependent intensities according to which they can be assigned to either two different adsorption phases or γ_2 to the desorption of the second adsorbed TTF layer and γ_1 to the desorption of higher lying layers. More or less γ_1 and γ_2 are characterized by a zero-order desorption behavior which suggests the desorption of low intermolecularly interacting molecules. The lack of a charge transfer type interaction, which leads to a repulsive Coulomb-interaction between charged molecules only directly at the TTF/Au(111) interface, particularly explains the low intermolecular interaction in higher lying TTF layers. Contrary, γ_3 saturates for already small evaporation times viz. coverages. That is why it

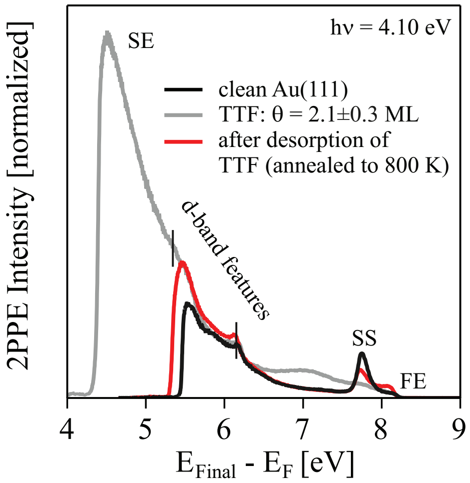

Figure 5.10: Monochromatic 2PPE spectra before and after annealing a TTF covered Au(111) surface up to 800 K and their comparison with a spectrum of a clean Au(111) surface reveals sticking molecular fragments after attempted thermal desorption. This result points towards a dissociative interfacial desorption reaction.

is assigned to the desorption of molecule fragments originating from the TTF monolayer. Nonetheless, it is quite difficult to properly detect γ_3 due to its low intensity which can be explained by a dissociative interfacial desorption reaction. This reaction may imply that the appearance and intensity of some molecule fragments (mass-to-charge ratios) originating from the TTF monolayer distinctly vary in comparison to the characteristics of higher lying layers. Beside that monochromatic 2PPE investigations shown in figure 5.10 verify that even flashing a TTF covered Au(111) surface up to 800 K does not completely remove all molecular residues from the surface. These molecular residues are presumably bound to the Au(111) surface due to strong Au-S-bonds. The adsorbate-induced work function shift is not completely revoked and also the 2PPE intensity just below E_F including the SS does not fit to the 2PPE spectra of a clean Au(111) surface. Molecular residues sticking at the Au(111) surface again indicate a dissociative interfacial desorption reaction whose account surely bases on the strong chemical interaction between gold atoms of the Au(111) surface and sulfur atoms of the adsorbed TTF molecule. Generally, these conclusions render a TPD-derived estimation of molecular coverage impossible as it was performed for TCNQ and F_4TCNQ adsorbed on Au(111). Therefore TTF coverages were estimated using the evaporation time which implies larger estimation errors in comparison to TCNQ and F_4TCNQ coverages.

5.4. Comparing Adsorption and Desorption Characteristics of TCNQ, F_4TCNQ and TTF on Au(111)

Considering the above discussion all three molecules TCNQ, F_4TCNQ and TTF can be evaporated intactly on a Au(111) surface on which they stick and organize in a well-ordered manner (at room temperature). Moreover, the desorption characteristics of higher lying layers are very similar. TPD spectra display a zero-order shape of the desorption peaks which have been assigned to the desorption of higher lying layers. They suggest the desorption of intact molecules from higher lying layers for each of the discussed molecules. Consequently, the impact of the underlying Au(111) substrate becomes only visible for the first adsorbed layer. But there are huge differences concerning the interfacial interaction and the adsorbate's state of charge. TCNQ molecules adsorbed on a Au(111) surface remain neutral and display characteristics of a physisorbed adsorbate: no relevant intermolecular Coulomb interactions, no charge transfer type interaction with the underlying Au(111) surface, unaffected herringbone reconstruction at full monolayer coverage and a complete desorption of probably intact molecules. Its fluorinated derivative F_4TCNQ, however, shows up to be negatively charged in direct contact with a Au(111) surface. In STM investigations this difference is accompanied by a two-fold coordination with Au adatoms and an adsorbate-induced disappearance of the Au(111) herringbone reconstruction [96, 97, 328, 334]. In this thesis TPD investigations suggest a second-order desorption peak shape for desorption of molecules originating from the monolayer which again emphasizes the distinctly higher metal-molecule interaction at the F_4TCNQ/Au(111) interface. Contrary to TCNQ and F_4TCNQ, TTF donates charge to gold and is therefore found to be positively charged on Au(111). According to the performed TPD investigations, a thermally induced dissociative interfacial reaction was supposed which might be induced by a strong gold-sulfur bonding. Thus, in comparison to TCNQ and F_4TCNQ, TTF can not be removed intactly from a Au(111) surface.

This thesis covers three possible charge states of molecular species adsorbed on a Au(111) surface: positively charged (TTF), neutral (TCNQ) and negatively charged (F_4TCNQ). A combined TPD and STM discussion of the adsorption and desorption characteristics demonstrates very different metal-molecule interactions as fundamental basis of these different charge states. The next chapter presents UPS and 2PPE investigations targeting the electronic structure of TCNQ, F_4TCNQ and TTF adsorbed on Au(111).

6. Electronic Structure of the Molecule/Au(111) Interfaces

The interfacial electronic landscape visualizes the most fundamental motives for interfacial metal-molecule interactions and thereby for both, the geometric and electronic arrangement at interfaces. 2PPE represents a powerful experimental tool for the investigation of this electronic perspective on interfacial metal-molecule interactions as it was discussed in section 3.1. This chapter presents 2PPE investigations targeting the electronic structure of TCNQ, F_4TCNQ and TTF adsorbed on Au(111). It provides access to a compact view of the interfacial electronics and unveils the most fundamental motifs of the underlying metal-molecule interactions. Each subsequent presentation of the electronic structure of a metal/organic interface is accompanied by an introducing summary of relevant preknowledge from literature and a conclusive argumentation.

6.1. Interfacial Electronic Structure of TCNQ/Au(111)

STM and TPD investigations (introduced in section 5.1) suggest a weak interfacial metal-molecule interaction and typical physisorption for TCNQ adsorbed on a clean Au(111) surface [328, 334–336]. Whereas on other substrates TCNQ is known to be negatively charged, in particular: Ni(111) [321, 322], Cu(100) [102, 324], Cu(111) [325], Ag(100) [324, 327], Ag(111) [327, 328], ITO [329], TiO_2 [330], Graphene [331–333] and PEDOT:PSS [329]. Studying the interfacial electronic structure of some of these combinations led to a wide-ranging fundamental understanding of interfacial charge transfer type interactions. In case of TCNQ adsorbed on TiO_2 [330], Ag(111) [328], Ag(100) [324] and Cu(100) [323, 324] the LUMO of TCNQ was observed to be located below E_F which can be interpreted as charge transfer from the underlying substrate to the adsorbed TCNQ. Contrary, the LUMO remains unoccupied on Au(111) [328, 334]. As a consequence the neutrality of TCNQ molecules in contact with high work function materials can be traced back to the fact that occupying the LUMO is not energetically favorable in those cases. Generally, this behavior fits well to the ICT model as illustrated in figure 6.1.

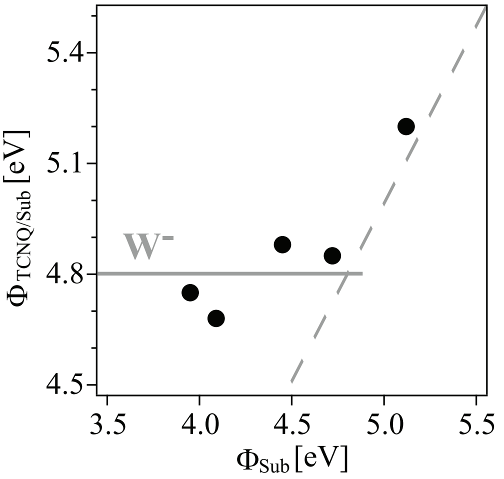

Figure 6.1: Work function data of TCNQ covered substrates visualize a behavior which fits quite well to the ICT model (data taken from ref. [329]). The solid line represents the constant work function range in which $\Phi_{\mathrm{TCNQ/Sub}}$ equals W^-, whereas the dotted line visualizes the line of no work function change (*Schottky-Mott-Limit*).

Here the work function of different TCNQ covered surfaces ($\Phi_{\mathrm{TCNQ/Sub}}$) is plotted versus the work function of the bare substrate (Φ_{Sub}). It visualizes two of three theoretically predicted behaviors as introduced in 2.4.1. Accordingly, the obvious connection between LUMO filling and work function properties can be explained using the ICT model as it was already established for TCNQ [48, 191, 329]. The constant work function range of different TCNQ covered surfaces from figure 6.1 ($\Phi_{\mathrm{TCNQ/Sub}} = 4.8\,\mathrm{eV}$) enables an estimation of the lower pinning level W^- and the Coulomb energy B^-:

$$\mathrm{W}^- = 4.8\,\mathrm{eV} = \mathrm{EA} + \mathrm{B}^-. \tag{6.1}$$

However, this estimation is subject of obvious restrictions as mentioned in section 2.4.1. In literature values for the EA of TCNQ from 2.8 eV to 4.3 eV can be found which would implicate a B^- ranging between 0.5 eV and 2 eV [86, 368–375]. Furthermore, STS measurements of TCNQ adsorbed on a Au(111) surface determined the energetic position of the LUMO to be 0.7 eV above E_{F} which suggests an EA at the upper end of the termed range [334]. In comparison, the IP of TCNQ adsorbed on Au(111) is more or less validated to amount 7.8 eV [86, 329]. In summary, STS, XPS and UPS studies state neutral TCNQ molecules adsorbed on the Au(111) surface [328, 334]. There is no evidence for an interfacial charge transfer type interaction, neither a (partial) occupation of the LUMO nor a work function increase due to an additional negatively charged adsorbate layer.

In this thesis UPS and 2PPE are applied to the TCNQ/Au(111) interface to study the interfacial electronic structure. Recently, STS measurements stated an adsorbate-induced up-shift of the SS which might be explained by an interfacial charge transfer type interaction or a work function change [334]. For validation, figure 6.2 shows results from an ARPES study of the TCNQ/Au(111) interface.

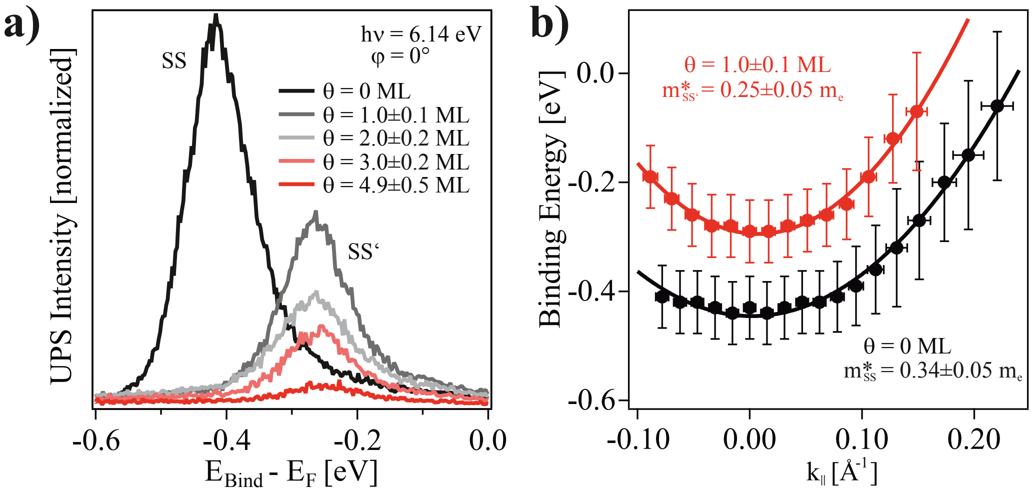

Figure 6.2.: Studying the shifted SS of the TCNQ/Au(111) interface applying ARPES. a) Coverage-dependent photoemission demonstrates an adsorbate-induced energetic up-shift of the SS of 160 ± 30 meV. This shift occurs only for monolayer adsorption, higher layers do not contribute or show any influence but intensity reduction. b) Angle-resolved data unveil a more or less coverage-independent effective mass.

The SS of a clean Au(111) surface was found to be located energetically at $-0.42\pm0.03\,\mathrm{eV}$ below E_F. It possesses a dispersion which can be described by an effective mass of $\mathrm{m}^*_\mathrm{SS} = 0.34\pm0.05\,\mathrm{m_e}$ observed via UPS or $\mathrm{m}^*_\mathrm{SS} = 0.23\pm0.02\,\mathrm{m_e}$ observed via 2PPE (see chapter 4). Moreover, it is known that molecular adsorption may cause an energetic shift of the SS [136, 138–143]. For a TCNQ covered Au(111) surface the shifted SS (SS') is energetically located at $E_\mathrm{B} = -0.26 \pm 0.03\,\mathrm{eV}$ visualizing an energetic shift towards E_F of about $\Delta_\mathrm{SS} = 160 \pm 30\,\mathrm{meV}$. This result fits to the mentioned STS results [334]. Additionally, the performed UPS measurements prove that this shift is only caused by adsorption of the first TCNQ layer. Higher adsorbate layers do not contribute or show any influence but an intensity reduction which characterizes the underlying mechanism to be completely interfacial: The adsorbate-induced energetic up-shift of the SS has to be completely assigned to the metal-molecule interaction directly at the interface. An up-shift of the SS might be accompanied by a work function reduction as the work function represents one side of the potential barrier theoretically describing SSs (see section 2.2). ARPES data at full monolayer coverage depicted in figure 6.2b demonstrate an almost unchanged dispersion and an insignificant reduction of the effective mass compared to the clean Au(111) surface.

In order to substantiate the conclusion drawn from STS, XPS und UPS studies that there is no charge transfer type interaction at the TCNQ/Au(111) interface, 2PPE was applied to investigate the interfacial electronic structure in more detail. Figure 6.3 visualizes monochromatic as well as dichromatic 2PPE spectra and the according slope evaluations from which in total six electronic states (separated from electronic states of the underlying Au(111) surface like d-band features) can be derived, two occupied, three intermediate states and one final state. Their energetic positions with respect to E_F are listed in figure 6.4. 2PPE in general demonstrates an adsorbate-induced work function decrease of $\Delta\Phi = -0.30 \pm 0.05\,\mathrm{eV}$ from $5.50 \pm 0.02\,\mathrm{eV}$ of the clean Au(111) surface to $5.20 \pm 0.05\,\mathrm{eV}$ at full monolayer TCNQ coverage. It can be explained by an interplay between Pauli-repulsion and the molecular dipole perpendicular to the surface (this dipole might be induced due to a down-bending of the molecule's cyano groups) assuming no charge transfer type interfacial interaction (as discussed above). Actually, the observed adsorbate-induced reduction of the work function fits to UPS measurements demonstrating an adsorbate-induced up-shift of SS towards E_F according to theoretical predictions. This up-shift is also observed via 2PPE.

Both, monochromatic and dichromatic 2PPE spectra, demonstrate the existence of an intense 2PPE feature just below E_F which can be assigned due to its slope and energetic position to the shifted SS (SS'). SS' is observed at $-0.26 \pm 0.05\,\mathrm{eV}$ with respect to E_F implying an energetic up-shift of $\Delta_\mathrm{SS} = 160 \pm 30\,\mathrm{meV}$. This experimental result is in agreement with the previously discussed UPS results. In addition to SS', monochromatic 2PPE spectra display a second photoemission feature which shifts with a slope of 2.0 ± 0.1. According to this slope and its energetic position at $-2.48 \pm 0.05\,\mathrm{eV}$ below E_F, this 2PPE feature can be assigned to the HOMO of TCNQ. The concluded IP amounts to $7.7 \pm 0.1\,\mathrm{eV}$ and therefore matches literature values [86, 329]. Unfortunately, the LUMO of TCNQ was not observed via 2PPE which might have several reasons. On one side the required photon energies to probe a formerly pumped LUMO are relatively high and would induce a photoemission signal at the SE of 2PPE spectra. Assuming a low signal intensity as observed for the HOMO-derived signal makes an observation of a LUMO-derived signal in consequence of the exponential-shaped electronic background almost impossible. Beside that the

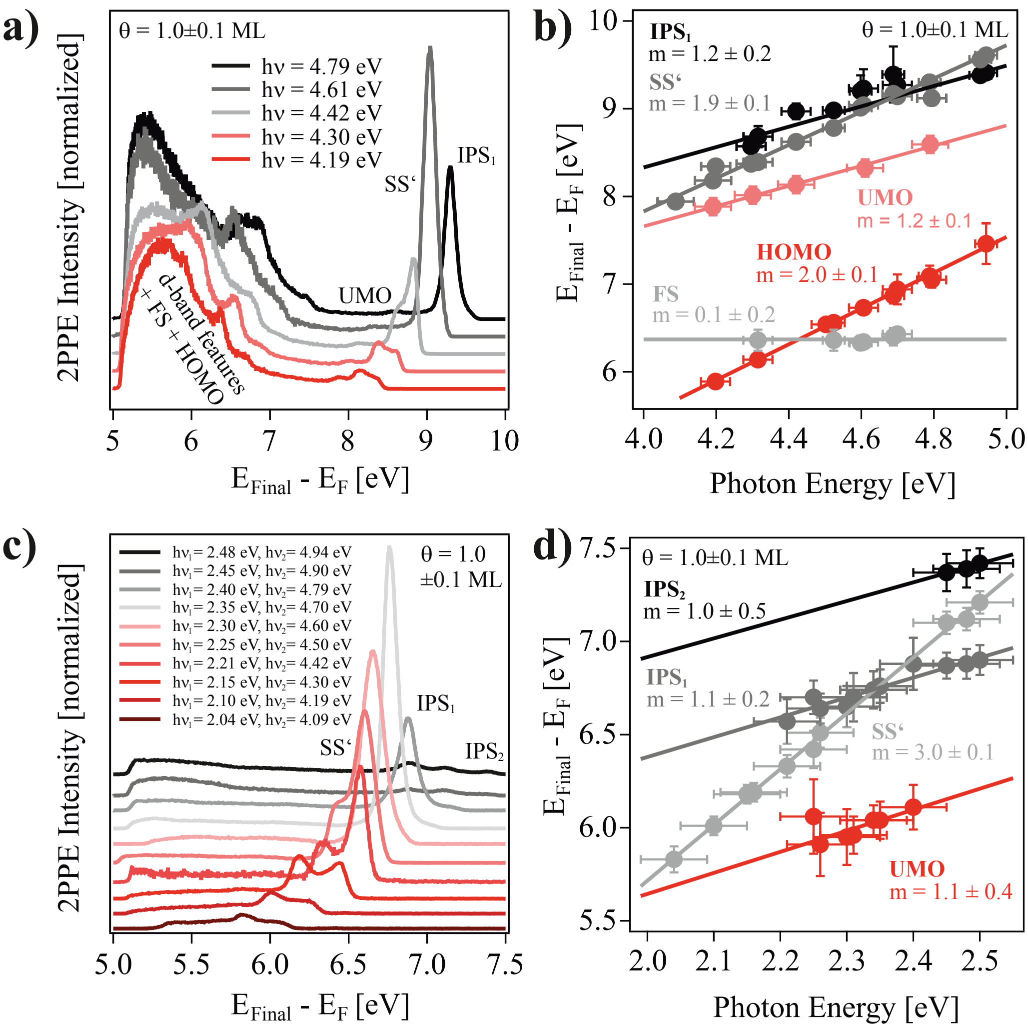

Figure 6.3.: 2PPE spectroscopy study of the TCNQ/Au(111) interface (monolayer coverage). a) Besides d-band features of the underlying Au(111) substrate monochromatic 2PPE spectra display five photoemission features which can be assigned to the HOMO, the shifted Shockley surface state (SS'), an unoccupied molecule-induced electronic state (UMO), the first image potential state (IPS_1) and an unoccupied final state (FS) via a slope evaluation of photon energy dependent measurements in b). c) Dichromatic 2PPE spectra reveal a second image potential state (IPS_2) in addition which only appears for high photon energies as visualized in another slope evaluation of photon energy dependent measurements for the correlated signal in d).

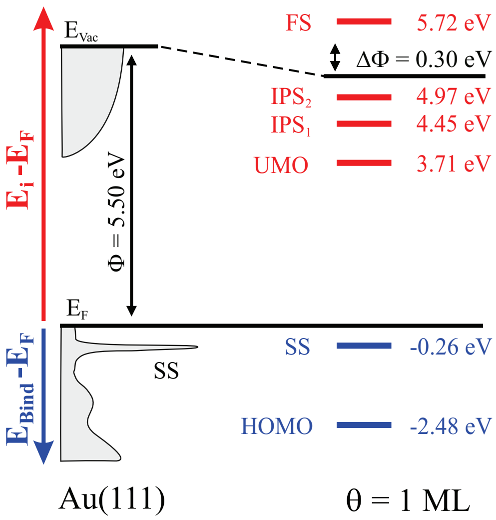

Figure 6.4: Energy level diagram of one monolayer TCNQ adsorbed on a Au(111) surface. The work function is reduced by $\Delta\Phi = 0.30\,\text{eV}$. 2PPE spectroscopy reveals two occupied (blue), three intermediate electronic states and one final state (red). Their energetic positions are given with respect to E_F.

application of such high photon energies provokes photo-induced processes and a modification of the interfacial electronic structure as will be discussed in chapter 7. Another reason for a very low intensity of a LUMO-derived signal in 2PPE spectra might be a small cross section for the pumping process possibly induced by a small wave-function overlap. Monochromatic as well as dichromatic 2PPE spectra display a photoemission feature which can be assigned to an unoccupied molecule-induced electronic state (in the following called unoccupied molecular orbital, UMO). It is energetically located at $3.71 \pm 0.05\,\text{eV}$ above E_F and might arise from a higher lying unoccupied molecular orbital of TCNQ. Figure 6.5 displays an additionally performed AR2PPE measurement. It proves the localized nature of the UMO-derived signal which prevents misassignment to the occupied sp-band feature (SP) of the underlying Au(111) surface (in accordance to the substrate characterization shown in chapter 4) . In addition to HOMO and UMO, monochromatic 2PPE spectra contain a photoemission feature which shows no photon energy dependence (FS, slope m= 0.1 ± 0.2). It can be assigned to an unoccupied final state located at $5.72 \pm 0.05\,\text{eV}$ above E_F which is also derived by a higher lying unoccupied molecular orbital of TCNQ. Beside 2PPE features which can be assigned to adsorbate-induced electronic states, photon-energy series depict two additional peaks shifting across FE. According to their slopes, these signals can be assigned to unoccupied electronic states energetically located at $4.97 \pm 0.05\,\text{eV}$ and $4.45 \pm 0.05\,\text{eV}$ above E_F, respectively. Due to their energetic position relative to E_Vac ($E_\text{IPS1} = -0.75 \pm 0.05\,\text{eV}$ and $E_\text{IPS2} = -0.26 \pm 0.05\,\text{eV}$) these unoccupied electronic states can be assigned to image potential states (IPS$_1$ and IPS$_2$). They are definitely pinned to the

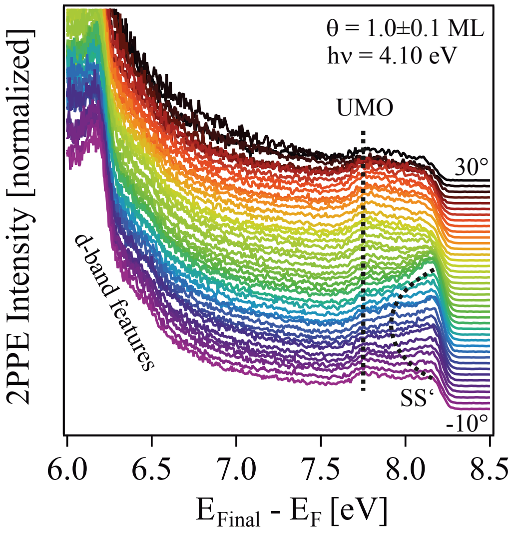

Figure 6.5: AR2PPE measurements display the localized nature of an unoccupied molecule-induced electronic state (UMO) which might arise from a higher lying unoccupied molecular orbital of TCNQ. The shifted SS (SS') displays a dispersion as already shown by UPS measurements.

vacuum level as shown during illumination series targeting the study of photo-induced processes (see chapter 7). Considerably, these photo-induced processes affect angle-resolved investigations which makes a detailed study of the image potential states' dispersions impossible. Nonetheless, their energetic position relative to E_{Vac} indicates a very small quantum defect $a \approx 0.06$ (according to equation 2.11) which fits to the high work function of the sample.

The studied TCNQ/Au(111) interface illustrates the complexity and intricacy of interfacial electronic structures. Altogether, despite of d-band features of the underlying substrate surface, six electronic states have been observed by means of 2PPE and UPS: three molecule-induced electronic states which have been assigned to molecular orbitals of TCNQ, two image potential states and a shifted surface state. As predicted by STS, XPS and UPS studies there are no indications in 2PPE data for a charge transfer type interaction at the TCNQ/Au(111) interface. This conclusion is also substantiated by the slight adsorbate-induced work function reduction. But this total picture changes dramatically for the fluorinated derivative F_4TCNQ on Au(111) as will be shown in the following section.

6.2. Electronic Structure of the F_4TCNQ/Au(111) Interface

In the course of this thesis already TPD measurements revealed that the metal-molecule interactions at the TCNQ/Au(111) and F_4TCNQ/Au(111) interfaces differ substantially. While TCNQ adsorbed on Au(111) should be neutral there are several studies demonstrating a charge transfer type interaction at the F_4TCNQ/Au(111) interface [47, 92, 96, 97, 343, 376]. In particular Koch *et al.* [47] demonstrated via UPS, that the LUMO of F_4TCNQ molecules in direct contact with the Au(111) surface is energetically located below E_F. This first direct evidence of a charge transfer from the Au(111) surface to adsorbed F_4TCNQ molecules was substantiated by subsequent STS measurements and DFT calculations [96, 97, 376]. One further indication for a charge transfer type interaction at the F_4TCNQ/Au(111) interface can be found in extended UPS investigations by Braun *et al.* [48, 101] and their determination of the lower pinning level W^-. Figure 6.6 illustrates the electronic position of the F_4TCNQ's HOMO with respect to E_F and the adsorbate-induced work function change $\Delta\Phi$ as a function of the substrates work function Φ_{Sub}.

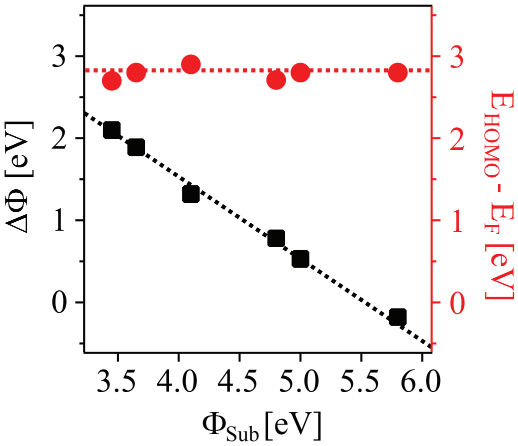

Figure 6.6: The electronic position of the F_4TCNQ's HOMO with respect to E_F (red) and the adsorbate-induced work function change $\Delta\Phi$ as a function of the substrates work function Φ_{Sub} (black) are indicators for a charge transfer type interaction at the F_4TCNQ/Au(111) interface. The fact that the lower pinning level $W^- \approx 5.55\,\text{eV}$ is energetically located below E_F suggests an ICT at the F_4TCNQ/Au(111) interface. Data adopted from ref. [101].

For a substrate's work function of $\Phi_{Sub} = 5.50 \pm 0.02\,\text{eV}$ (as in the present case) and a lower pinning level of approximately 5.55 eV the adsorbate-induced work function change should amount fairly accurate zero. The cancellation of the work function shift induced by Pauli repulsion and the fact that the lower pinning level is energetically located below E_F suggests an ICT at the F_4TCNQ/Au(111) interface. As the EA and IP of F_4TCNQ were determined to be energetically located around 5.2 eV and 8.3 eV, respectively, the Coulomb energy B^- in case of F_4TCNQ adsorbed on Au(111) can be estimated to be smaller than 0.5 eV [101, 341]. This value is explicitly smaller than in case of TCNQ and can be associated to an easier charging of F_4TCNQ molecules [186]. Compared to the TCNQ/Au(111) interface, STS measurements demonstrate again a significant DOS up to 1 eV above E_F [96, 97]. Also these features were assigned to the LUMO of F_4TCNQ which suggests, in combination with the occupied LUMO-derived feature observed via UPS, a hybridized electronic structure directly at the F_4TCNQ/Au(111) interface. Additionally, the SS of the underlying Au(111) surface seems to be quenched in STS spectra [96, 97]. Conclusively, this interface can be described accurately by the ICT model, whereas STS and UPS in combination indicate a hybridized interfacial electronic structure.

Photon energy dependent monochromatic as well as dichromatic 2PPE spectra are visualized in figure 6.7. Despite of d-band features of the Au(111) substrate in total five electronic states can be derived from these data: two occupied, two intermediate states and one final state. Their energetic positions with respect to E_F are listed in figure 6.8. The work function of the F_4TCNQ/Au(111) interface at monolayer coverage amounts to be 5.35 ± 0.02 eV which implies a work function shift of $\Delta\Phi = 0.15 \pm 0.04$ eV. Compared to the TCNQ/Au(111) surface, this down-shift is slightly lower which could be a hint for a higher metal-molecule interaction. In literature a work function of ca. 5.6 eV can be found [47, 101, 344, 377]. According to the ICT model, this value is expected in case of a F_4TCNQ covered surfaces featuring integer charge transfer type interactions [48, 101]. But detailed coverage dependent measurements in this thesis imply an assignment of this value to thicker F_4TCNQ films adsorbed on a Au(111) surface (see chapter 9). So it has to be answered by 2PPE spectroscopy whether there is evidence for an interfacial charge transfer type interaction although the work function shift does not possess the value known from literature.

Considering data from figure 6.7 two occupied electronic states can be derived from 2PPE spectra, energetically located at -2.75 ± 0.05 eV and -0.42 ± 0.07 eV below E_F, respectively. In accordance to literature, the first mentioned state can be assigned to the HOMO of F_4TCNQ (IP = 8.3 eV [101, 341]). The latter can be assigned either to the SS of the Au(111) substrate or to the LUMO-derived occupied state previously observed via UPS [47]. Angle-resolved and coverage-dependent 2PPE results discussed in chapter 9 oppose to a SS assignment. Henceforth this occupied state is consequently assigned to a LUMO-derived state (LUMO*) which gets occupied by electrons from the substrate at the F_4TCNQ/Au(111) interface leading to an energetic position below E_F. Its energetic position fits to results from UPS and DFT calculations [47, 344, 376].

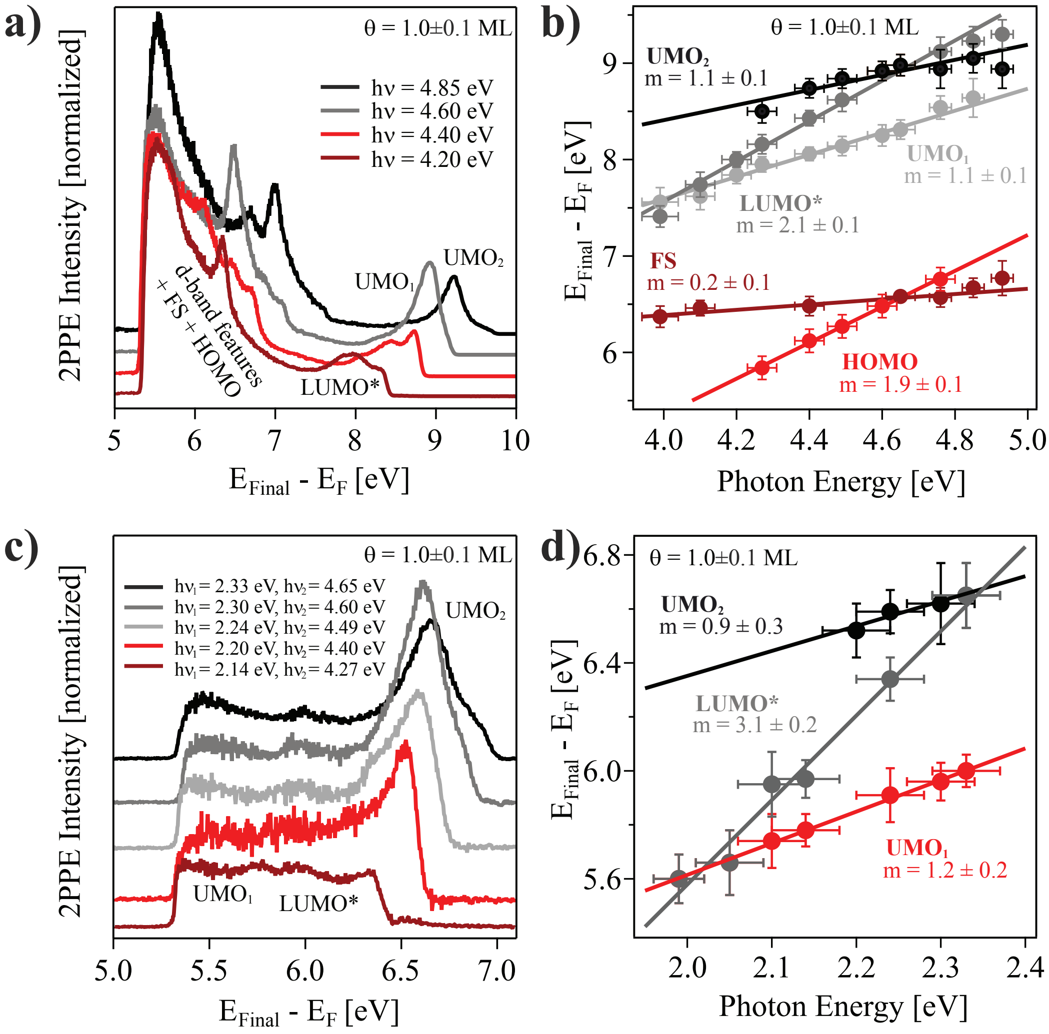

Figure 6.7.: 2PPE spectroscopy study of the F$_4$TCNQ/Au(111) interface (monolayer coverage). a) Besides d-band features of the underlying Au(111) substrate monochromatic 2PPE spectra display five photoemission maxima which can be assigned to the HOMO, a LUMO-derived state (LUMO*), two unoccupied molecule-induced electronic states (UMO$_i$), and an unoccupied final state (FS) via slope evaluation of photon energy dependent measurements in b). c) Dichromatic 2PPE spectra confirm these assignments displaying LUMO*, UMO$_1$ and UMO$_2$ with appropriate slopes in d).

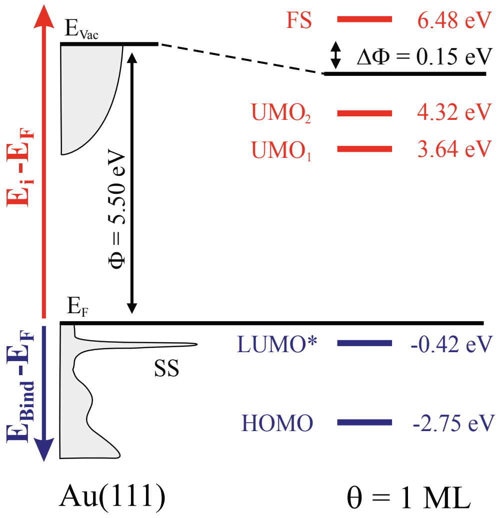

Figure 6.8: Energy level diagram of the F_4TCNQ/Au(111) interface at full monolayer coverage. The work function is reduced by $\Delta\Phi = 0.15\,\text{eV}$. In addition to electronic states of the underlying Au(111) surface 2PPE spectroscopy reveals two occupied (blue) two intermediate states and one final state (red). Their energetic positions are given with respect to E_F.

Additionally to LUMO*, monochromatic as well as dichromatic 2PPE spectra display two 2PPE features which can be assigned by photon energy dependent measurements to intermediate states energetically located at $3.64 \pm 0.03\,\text{eV}$ and $4.32 \pm 0.03\,\text{eV}$ above E_F, respectively. As their energetic position is more than one electron volt below E_Vac both intermediate states can not be assigned to IPSs. Because of this argument both states are assigned to unoccupied molecule-induced electronic states UMO_i. At this point a clear distinction between molecule-induced electronic states originating from molecular orbitals or from interfacial hybrid states is not possible. However, coverage-dependent and angle-resolved 2PPE measurements shown in chapter 9 point towards a molecule-induced UMO_2 without any hybridizational effects with the underlying metal states. Whereas a hybridization involving UMO_1 and LUMO* can not be excluded. Another 2PPE feature which can be assigned to a molecule-induced unoccupied state is energetically located at $6.48 \pm 0.05\,\text{eV}$ above E_F. Due to its high energetic distance to E_F both photons applied in a 2PPE process are used to populate this state which causes its appearance as final state (FS).

Compared to the TCNQ/Au(111) surface, a F_4TCNQ-covered Au(111) surface features no shifted SS (SS') or IPSs which might be also indications for a higher interfacial metal-molecule interaction in case of F_4TCNQ. This interpretation fits perfectly to results from TPD measurements in which F_4TCNQ molecules are comparatively stronger bound to the underlying Au(111) surface. In spite of this significantly higher interfacial metal-molecule interaction, the work function change induced by molecular adsorption is lower for F_4TCNQ than in case of TCNQ at full monolayer coverage. According to that observation, the higher metal-molecule interaction can be associated with a lower work function shift. Again this link can be explained by a charge transfer induced increased interface dipole which almost cancels the Pauli-repulsion-induced work function reduction.

While 2PPE data implicate no indications for a charge transfer type interaction at the TCNQ/Au(111) interface this issue is completely different for its fluorinated derivative. There are several crucial evidences for a charge transfer from a Au(111) surface to adsorbed F_4TCNQ molecules, whereas this interaction is reversed for adsorbed TTF molecules on a Au(111) surface. This makes TTF a perfect counterpart to gain more insights into interfacial charge transfer type interactions via 2PPE.

6.3. Interfacial Electronic Structure of TTF-covered Au(111)

In contrast to the F_4TCNQ/Au(111) interface, a reverse charge transfer from TTF molecules to the gold substrate essentially characterizes the TTF/Au(111) interface [91, 94, 209, 329, 366, 367]. This charge transfer type interaction implies positively charged molecular species on the Au(111) surface which interact via an intermolecular long-range repulsive Coulomb interaction (as discussed in section 5.3). During this thesis TPD measurements revealed a dissociative interfacial desorption reaction of TTF molecules adsorbed on a Au(111) surface (see section 5.3). It might be based on a strong chemical bond between surfacial gold atoms and the sulfur atoms of the adsorbed molecule. In the past the TTF/Au(111) interface led to some contradictious results from an energetic point of view. First to mention there are different published work function values for a thick film of TTF molecules adsorbed on a Au(111) surface. Fraxedas *et al.* [366] demonstrated in 2011 an adsorbate-induced work function decrease to an asymptotic value of 4.9 eV which contrasts to results by Murdey and Salaneck from 2005 [329, 366]. They demonstrated a constant work function value for various TTF-covered substrates which results in an upper pinning level W^+ of 4.2 eV according to the ICT model. Figure 6.9 illustrates this constant work function value in combination with a thickness dependent work function and ionization potential. The latter one indicates band bending in TTF adsorbed on Au(111). Directly at the interface, however, DFT calculations predict the HOMO to be energetically located just below E_F which is difficult to reconcile with the experimental data shown in figure 6.9 [94, 209, 366]. Moreover, these calculations indicate a HOMO occupation below 100 % which fits to the idea of a charge transfer type interaction at the TTF/Au(111) interface. They also explain a high work function decrease due to a charge transfer induced interface dipole and an increased smeared-out electron density directly at the TTF/Au(111) interface [209].

In this thesis a 2PPE study of the TTF/Au(111) interface is performed to gain more insights into the interfacial charge transfer type interaction. In doing so especially the work function and the energetic position of the HOMO constitute important indicators. Additional performed angle-resolved UPS and 2PPE investigations are subject of another detailed analysis which is reported in chapter 9. Nonetheless, compared to previous discussions, this chapter includes also coverage-dependent measurements of the TTF/Au(111) interface due to their key role in the assignment of occupied electronic states. Coverage-dependent UPS data ($h\nu = 6.08$ eV, evaporation onto a substrate held

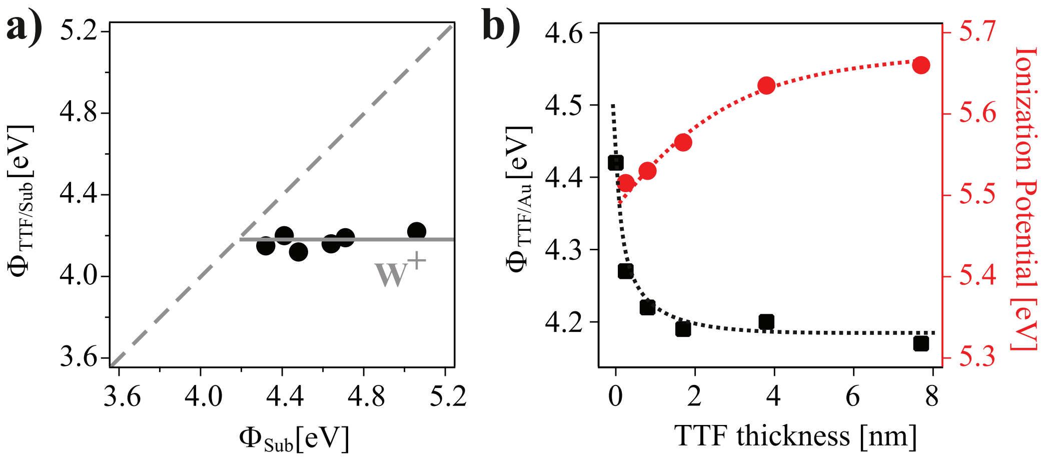

Figure 6.9.: a) UPS data from ref. [329] demonstrate a constant work function for TTF-covered high work function substrates according to the ICT model. The work function of a TTF/Au(111) interface is coverage dependent and decreases asymptotically to 4.2 eV (black data in b)), whereas the ionization potential (IP) shifts to higher values (red data in b)). The latter observation indicates band bending at the TTF/Au(111) interface. Data adopted from ref. [329], dotted lines constitute guides to the eyes.

at 100 K) depicted in figure 6.10a signify an adsorbate-induced work function drop from 5.50 ± 0.02 eV to 4.15 ± 0.04 eV at full monolayer coverage. This observation is in perfect agreement to the work function data of Murdey and Salaneck [329] illustrated in figure 6.9 but oppose to results by Fraxedas *et al.* [366]. In the submonolayer regime UPS data reveal an up-shift and broadening of the Au(111) SS-derived signal. Up to full monolayer coverage it is shifted to its final energetic position just below E_F. According to its disappearance for higher film thicknesses and considering DFT results, this spectral feature can be finally assigned to a hybridized interfacial electronic state derived from the SS of the Au(111) surface and the HOMO [94, 366]. In the following it is called HOMO*. Another interfacial electronic state derived from the TTF molecule's HOMO (HOMO**) is energetically located at 1.6 ± 0.1 eV below E_F. The experimental determined energetic positions of both interface states, HOMO* and HOMO**, fit to predictions made by DFT calculations [94, 366]. But for coverages above one monolayer UPS data indicate an intensity reduction of both 2PPE features which have been assigned to the occupied interface states HOMO* and HOMO**. This behavior might be explained by an additional intermolecular interaction with the second adsorbed layer which leads to an efficient screening or fundamental reorganization of the interfacial electronic structure. TTF molecules in higher adsorbate layers should be neutral due to their higher distance to the Au(111) surface. Therefore a huge intensity increase

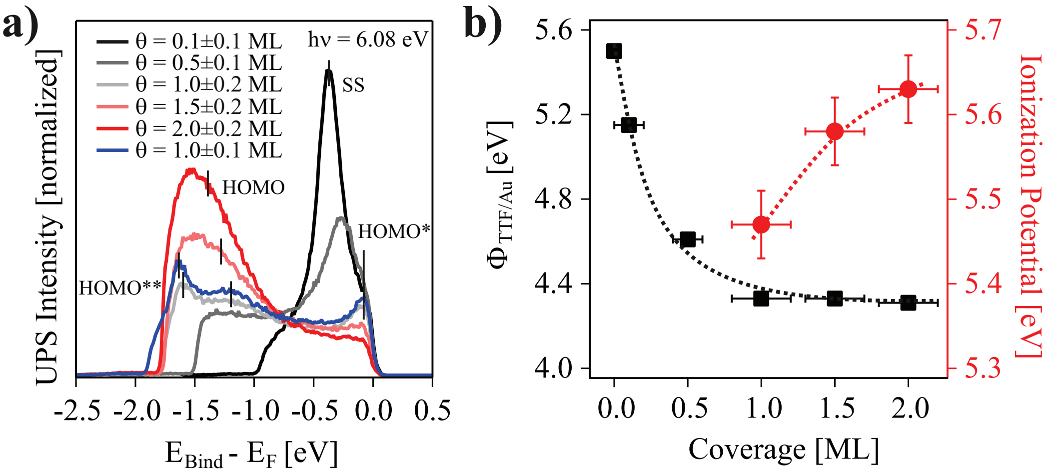

Figure 6.10.: a) Coverage-dependent UPS investigations demonstrate a huge adsorbate-induced work function decrease (SE of each spectrum) up to full monolayer coverage and additionally, they demonstrate the appearance of two occupied HOMO-derived interface states (HOMO* and HOMO**). Evaporation onto a substrate held at room temperature results in a slightly lower work function of $4.15 \pm 0.04\,\text{eV}$ (blue line) and a more distinct photoemission peak appearance in comparison to TTF films evaporated onto a substrate held at 100 K (the usual case). For higher coverages the HOMO of non-interacting TTF molecules is observed. b) Its coverage-dependent binding energy in combination with an almost constant work function value for higher coverages indicates band bending at the TTF/Au(111) interface in total agreement with previously reported results [329].

below $-1.0\,\text{eV}$ binding energy for higher film thicknesses can be associated with the HOMO of neutral TTF molecules. Presumably for full monolayer coverage the 2PPE feature energetically located at $-1.2 \pm 0.1\,\text{eV}$ below E_F can be also assigned to the HOMO of uncharged TTF molecules which implies a thickness-dependent binding energy. This coverage-dependent binding energy shift of neutral TTF molecules' HOMO from $-1.2 \pm 0.1\,\text{eV}$ to almost $-1.6 \pm 0.1\,\text{eV}$ evidences band bending at the TTF/Au(111) interface as visualized in figure 6.10b. It was previously reported by Murdey and Salaneck [329].

Evaporation onto a substrate held at room temperature results in a comparatively slightly lower work function of $4.20 \pm 0.04\,\text{eV}$ and more distinct 2PPE feature appearance at full monolayer coverage (blue line in figure 6.10a). This observation might be related to a higher adsorbate diffusion which usually leads to a higher degree of ordering and accordingly to sharper and more intense spectral features.

Figure 6.11 presents monochromatic as well as dichromatic 2PPE spectra and photon energy dependent data. Monochromatic spectra are depicted in an adequate final state energy sequence to visualize 2PPE features near FE.

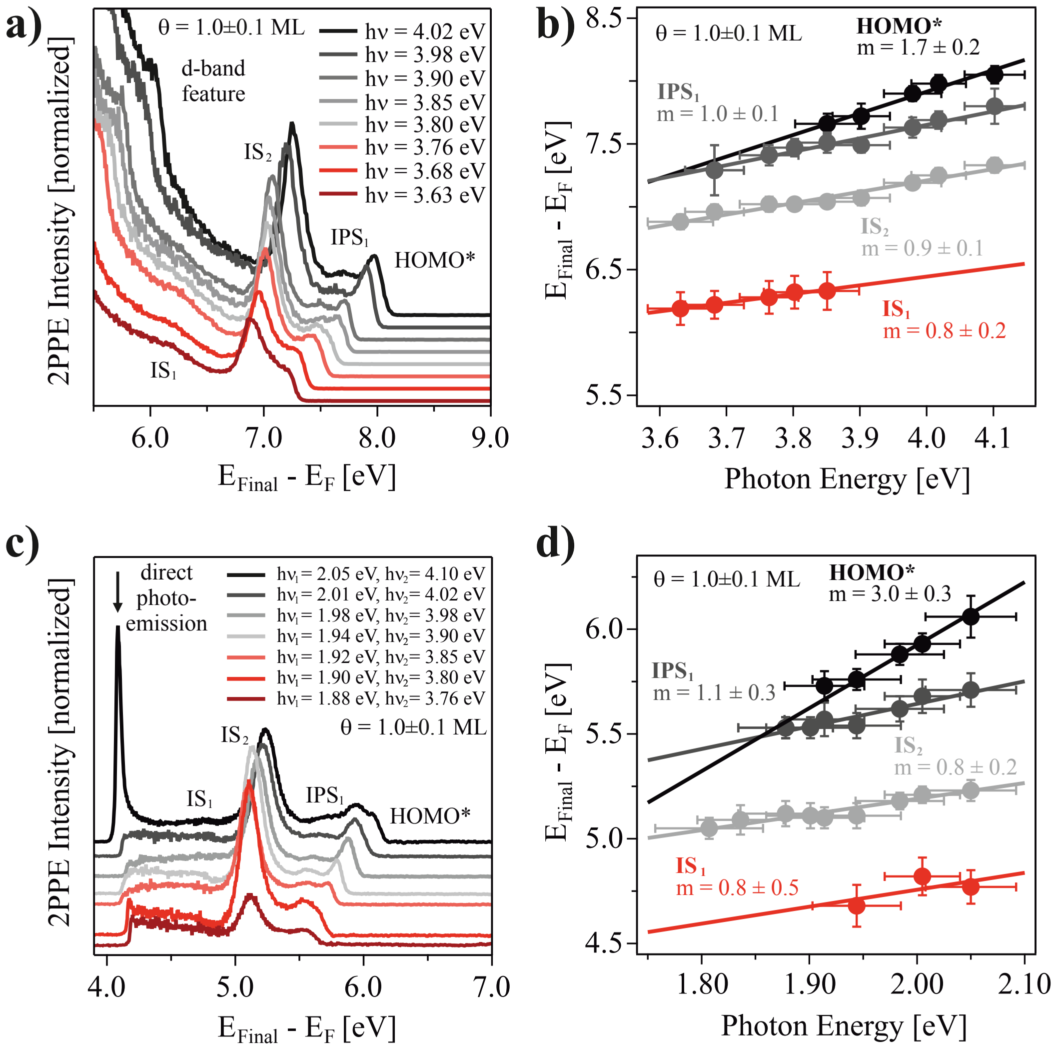

Figure 6.11.: 2PPE spectroscopy study of the TTF/Au(111) interface (monolayer coverage). Besides d-band features of the underlying Au(111) substrate, monochromatic 2PPE spectra illustrated in a) display four photoemission maxima which can be assigned to a HOMO-derived occupied electronic state (HOMO*), two unoccupied interfacial electronic states (IS_i) and one image potential state (IPS_1) via slope evaluation of photon-energy-dependent measurements in b). c) Dichromatic 2PPE spectra confirm these assignments displaying HOMO*, IS_1, IS_2 and IPS_1 with appropriate slopes in d).

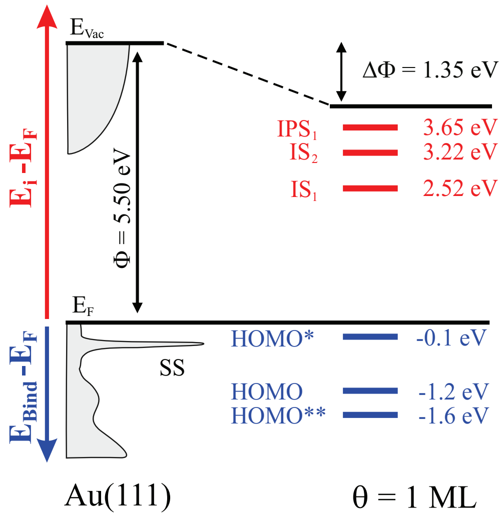

Figure 6.12: Energy level diagram of the TTF/Au(111) interface at full monolayer coverage. The work function is reduced by $\Delta\Phi = 1.35$ eV. In addition to electronic states of the Au(111) surface, UPS in combination with 2PPE spectroscopy reveals three occupied (blue) and three unoccupied electronic states (red). Their energetic positions are given with respect to E_F.

Without exception deeper lying features can be assigned to d-band features of the Au(111) surface. In total, 2PPE results end up in the observation of one initial and three unoccupied molecule-induced electronic states. Their energetic positions combined with so far presented UPS results are listed in an energy diagram (figure 6.12). 2PPE spectra give evidence for an occupied molecule-induced electronic state just below E_F. This energetic position enables an assignment to the HOMO-derived occupied electronic state HOMO* consistent with the presented UPS results. Beside that 2PPE data display three additional features which can be assigned to unoccupied intermediate states. First to mention a state energetically located at 3.65 ± 0.05 eV above E_F which features a very low intensity. Due to its energetic position it is assigned to an IPS (IPS_1). Its low intensity permits no subsequent angle-resolved investigations that is why an assignment to an interfacial unoccupied electronic state is also possible. Both additionally observed unoccupied intermediate states (IS_1 and IS_2) demonstrate an intensity reduction caused by the adsorption of more than one monolayer TTF molecules as illustrated in figure 6.13. As these unoccupied states can not be assigned to IPS, due to their energetic position relative to E_{Vac}, both states are assigned to unoccupied interface states. The occurrence of both observed unoccupied interfacial states can be explained by a hybridized electronic structure directly at the TTF/Au(111) interface which is also responsible for the HOMO-derived occupied hybrid states HOMO* and HOMO**. Nevertheless, it is difficult to find an explanation for its complete disappearance after the adsorption of only a second TTF layer. A very efficient screening of the interfacial electronic structure by further adsorbate layers might be possible. An alternative might be a geometric rearrangement of the first adsorbed TTF layer due to the adsorption of higher layers which would also imply a complete rearrangement of the interfacial electronic structure. Moreover, coverage-dependent 2PPE data visualized in figure 6.13 demonstrate a huge intensity increase at 6.5 to 7.0 eV final state energy. It can be associated with the HOMO signature of neutral TTF molecules adsorbed in the second layer as already noticed in UPS measurements.

Compared to the F_4TCNQ/Au(111) interface, the TTF/Au(111) interface is characterized by a charge transfer type interaction in which TTF molecules donate charge to the gold surface in terms of a HOMO-derived electronic hybrid state which is energetically located just at E_F. DFT calculations also confirm a partial depletion of HOMO* which fits to the overall charge transfer type interaction at the TTF/Au(111) interface. This interfacial charge donation from the first adsorbed TTF layer to the metal substrate causes an interface dipole which lowers the substrate's work function in addition to Pauli repulsion. Whereas the adsorbate-induced work function shift $\Delta\Phi$ can be explained using the ICT model, energy-resolved and coverage-dependent 2PPE data suggest an interfacial hybridization. In total three occupied and three unoccupied electronic states were observed in UPS and 2PPE measurements at the TTF/Au(111) interface. Amongst those states there are at least four interfacial electronic states with possible metal-molecule hybrid character: HOMO**, HOMO*, IS_1 and IS_2. In chapter 9 this hybrid character is confirmed by means of angle-resolved UPS and 2PPE measurements revealing band formation at the TTF/Au(111) interface.

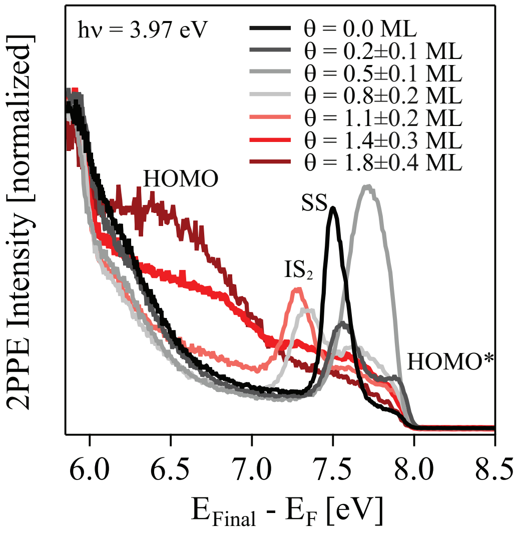

Figure 6.13: Coverage-dependent 2PPE data of TTF adsorbed on a Au(111) surface demonstrate a complex interfacial electronic structure. For coverages above 1 ML interfacial electronic states get reduced in their intensity. This process is completed for two monolayer coverage which might indicate a very efficient screening by the second adsorbate layer or an structural rearrangement of the first adsorbed TTF layer due to the adsorption of higher layers.

6.4. Comparing Electronic Structures of the Investigated Metal/Organic Interfaces

Considering all presented results from this chapter enables a fundamental understanding of the interplay between molecular ordering, electronic states just below E_F and a charge transfer type interaction at metal/organic interfaces. In case of TCNQ adsorbed on a Au(111) surface, a well-defined geometric structure was found via STM studies [328, 334–336]. Performed TPD measurements suggest a weak metal-molecule interaction and thus physisorption as discussed in section 5.1. Neither UPS, 2PPE nor STS data give evidence for an interfacial hybridization or evidence for charged molecular species in direct contact with the Au(111) surface. Nevertheless, there is an occupied electronic state just below E_F which can be assigned to the Au(111) SS shifted towards E_F. This picture dramatically changes for the F_4TCNQ/Au(111) interface.
Also F_4TCNQ adsorbs in a well-defined geometric structure but already STM and TPD measurements introduced in section 5.2 emphasize a higher metal-molecule interaction [96, 97, 328, 334]. In contrast to TCNQ/Au(111), UPS and 2PPE measurements unveil an electronic structure of the F_4TCNQ/Au(111) interface which proves an interfacial charge transfer type interaction. Also this metal/organic interface features an occupied electronic state just below E_F which in this case can be assigned to a LUMO-derived electronic state. This result implies a LUMO occupation which ends up in a metal to molecule electron transfer. Accordingly, F_4TCNQ molecules in direct contact with a Au(111) surface are negatively charged, whereas TCNQ molecules stay neutral.
A reverse charge transfer type interaction was found at the TTF/Au(111) interface. Here STM studies uncover a long-range repulsive intermolecular adsorbate interaction and TPD measurements suggest a dissociative desorption reaction [94, 366]. Moreover, UPS and 2PPE data display an molecule-induced occupied electronic state at E_F which in this case can be assigned to a HOMO-derived electronic state. This observation is equivalent to a partial depopulation of the HOMO which implies an electron transfer from the molecule to the metal substrate. Consequently, the long-range repulsive intermolecular interaction between TTF molecules adsorbed on a Au(111) surface can be ascribed to a Coulomb-type interaction between positively charged molecular species.
Table 6.1 presents a brief overview of the results discussed in this chapter and visualizes the essential differences. As discussed for the individual metal/organic interfaces, respectively, the ICT model is applicable for each of the observed adsorbate-induced work function shifts observed at these interfaces. According to the ICT model, TTF is positively charged, F_4TCNQ is negatively charged

and TCNQ stays neutral adsorbed on a clean Au(111) surface. This statement perfectly agrees with UPS and 2PPE results, especially derived work function values of this thesis. However, in case of TTF and F$_4$TCNQ adsorbed on Au(111) there are indications pointing towards significant hybridization.

	TCNQ/ Au(111)	**F$_4$TCNQ/ Au(111)**	**TTF/ Au(111)**
Well-defined geometric structure	✓	✓	✓
Charge transfer type interaction	✗	✓	✓
Occupied state just below E_F	SS‘	LUMO*	HOMO*
Molecule‘s charge state	✗	⊖	⊕
ICT model applicable	✓	✓	✓
Metal-molecule hybridization	✗	✓	✓

Table 6.1.: Comparing the discussed interfacial electronic structures. This brief overview of presented experimental results and conclusions from this chapter enables a fundamental understanding of the interplay between molecular ordering, electronic states just below E_F and a charge transfer type interaction at metal/organic interfaces.

7. Photo-Induced Charge Transfer at the TCNQ/Au(111) Interface

From a phenomenological point of view the most appropriate argument for an extended analysis and characterization of photo-induced processes is their possible field of application in organic electronic devices like organic solar cells, sensors or switches [22, 123, 180, 378–381]. The functionality of these devices is based on photo-induced processes like photoisomerization, photo-induced charge transfer and photo-induced charge separation which might be the reason for the wide-ranging application of light-using experimental methods in this research field. Particularly, time-resolved experimental tools provide unique insights into the physics of organic semiconductors and of metal/organic interfaces as they can trace the chain of consequences initially triggered by the adsorption of one photon.

In this chapter a photo-induced process occurring at the TCNQ/Au(111) interface is presented and characterized by means of 2PPE. Its subsequent analysis suggests a photo-induced charge transfer at the TCNQ/Au(111) interface. This charge transfer from the metal substrate to the molecule would dramatically increase the concentration of negatively charged molecular species directly at the interface. However, this would have also impact on the work function of the sample. In fact there are inconsistent work function values (or adsorbate-induced work function changes) for the TCNQ/Au(111) interface reported in UPS studies which were interpreted as hints towards or against an interfacial charge transfer type interaction [44, 328, 329, 374]. As stated in section 6.1 there are no indications in the displayed 2PPE data for such an interfacial interaction. Admittedly, these data were measured within an illumination time of 10 s per spot which signifies the just acceptable photon dose for an unaffected 2PPE spectrum before photo-induced modifications occur. Figure 7.1 visualizes the evolution of monochromatic 2PPE data towards longer illumination times viz. higher photon doses for 4.75 eV photon energy. The spectra were taken within an illumination time of 10 s each in a subsequent order on the same spot (so-called illumination series) in order to study photo-induced modifications in more depth. For illustrative purposes only every tenth spectrum is shown. Figure 7.1b-d illustrate photo-induced spectral changes in more detail as they will be discussed in the following.

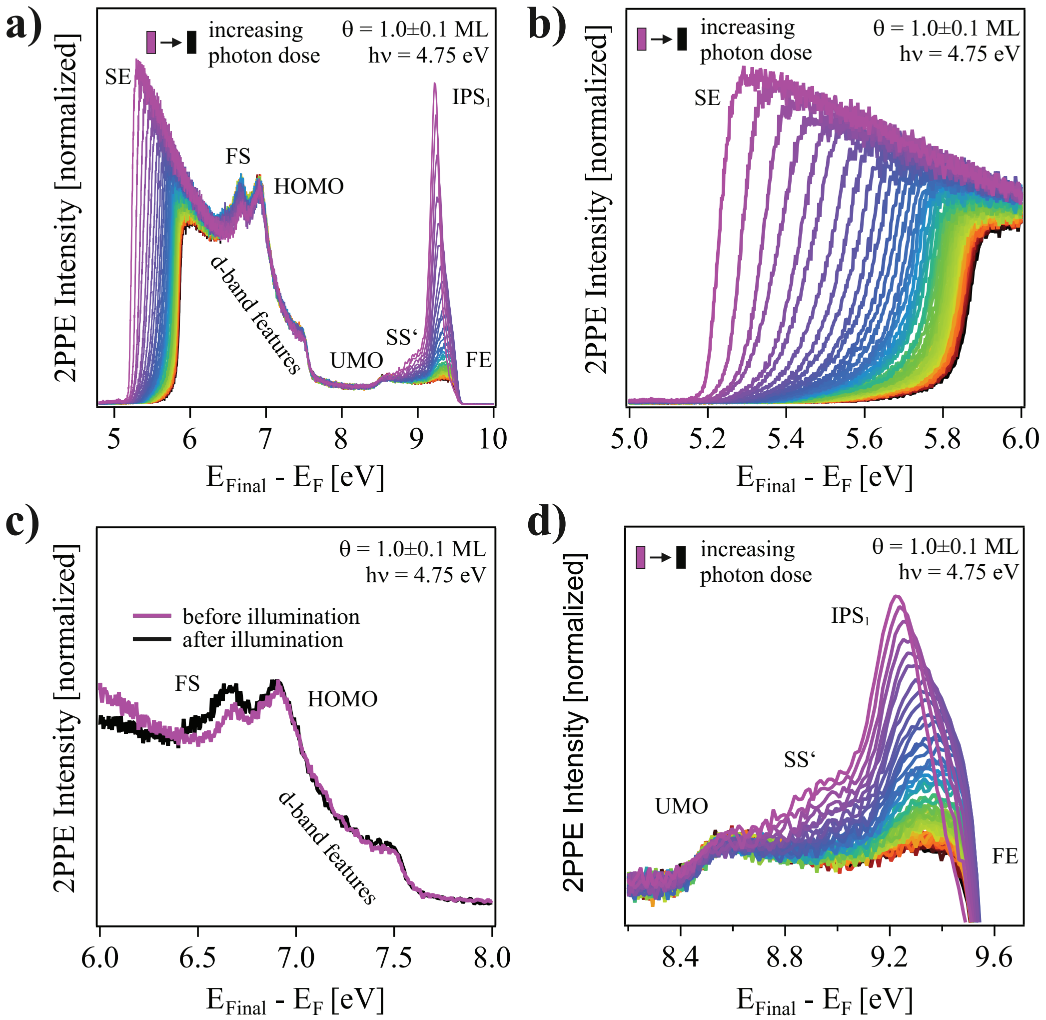

Figure 7.1.: Visualizing photo-induced modifications in monochromatic 2PPE spectra of the TCNQ/Au(111) interface via an illumination series. An overview of photo-induced spectral modifications is shown in a). b) Displays the photo-induced shift of the SE in more detail which later-on serves as indication for a subsequent characterization. c) And d) depict selected spectral ranges demonstrating the constant energetic position and 2PPE intensity of the HOMO, UMO and d-band derived features, the quenching of the shifted SS (SS') and an intensity increase of the FS-derived signature. The energetic shift of IPS_1 can be explained due to its pinning to E_{Vac}.

Out of all observed spectral changes the photo-induced shift of the SE might be the most obvious and remarkable aspect. As visualized in figure 7.1b the SE viz. the sample's work function increases from $5.20 \pm 0.05\,\mathrm{eV}$ up to a saturation limit at $5.85 \pm 0.05\,\mathrm{eV}$. This exponential increase serves further on as measure for a quantitative characterization of this photo-induced process. The photo-induced energetic up-shift of a 2PPE signature which was assigned to IPS_1 is related to the work function change as IPSs are generally pinned to E_{Vac}. Its pinning to E_{Vac} is the ultimate argument for its correct assignment. For long illumination times or high photon doses, respectively, IPS_1 shifts across FE as the applied pump photon energy is insufficient to excite an electron into this unoccupied electronic state. Interestingly, IPS_1 is the only electronic state at the TCNQ/Au(111) interface which gets energetically shifted during an illumination series. All other 2PPE features are found to be located at constant energetic positions relative to E_{F}. This especially holds for 2PPE peaks which can be assigned to molecule-derived electronic states like HOMO, UMO and FS. Additionally, only FS and SS' display a photo-induced 2PPE signal intensity variation. Figure 7.1c demonstrates the slight intensity increase of the FS-derived feature after a sufficient illumination for a saturated work function shift. The intensity increase of the FS-derived 2PPE feature might be explained by a reduced energetic distance to E_{Vac}, as the sample's work function gets increased by illumination as well, which presumably leads to an increased probability of presence in this electronic state. Conversely, the 2PPE feature which was assigned to SS' gets suppressed for long illumination times as illustrated in figure 7.1d.

In the following these photo-induced spectral changes and unaffected molecule-derived spectral features are used for a subsequent discussion of possible underlying physical processes. While considering only the photo-induced work function increase in total four different physical phenomenons may serve as an adequate reason for this observation. i) First to mention a photo-induced degradation or photodissociation which might lead to the formation of dipolar molecule fragments. These dipolar fragments may then influence the work function [244, 382–384]. ii) A second explanation for a photo-induced work function variation might be a structural rearrangement of dipolar molecules as it is also observed for thicker films by erasing a so-called *giant surface potential* [219, 220, 385]. In this case a formerly to some degree ordered molecular structure gets randomized by UV irradiation. iii) The third physical reason which has to be considered is an intermolecular chemical reaction like polymerization or photoisomerization which entails a work function change due to generated molecular radicals on the surface [124, 261, 321, 386, 387]. iv) The fourth physical reason which has to be mentioned here is a photo-induced charge transfer type interaction. Such a photo-induced charge transfer usually implies a very temporary excited molecule-induced state which decays on pico- or femtosecond timescale [105, 120, 182, 184, 276, 388]. Nevertheless, there are cases in which photo-induced charge transfer states are stabilized and can be used for an efficient charge separation [173, 174, 180, 389–391].

For a detailed discussion and final assignment of the presented photo-induced process at the TCNQ/Au(111) interface all addressed spectral changes have to be taken into account. First of all the unmodified energetic position of adsorbate-derived 2PPE features (relative to E_F) is suitable for an initial selection. As intermolecular or intramolecular chemical reactions as well as photo-induced decomposition would comprise a modification of the electronic structure approaches i) and iii) have to be rejected. The quenching of SS is conceivable for both photo-induced rearrangement or charge transfer. In case of rearrangement the quenching might be explained by an increased metal-molecule interaction [392–395]. Whereas an adsorbate-induced quenching of the SS due to an interfacial hybridization was presented for the F_4TCNQ/Au(111) interface in the course of this thesis (see section 6.2 and later on chapter 9). TCNQ is a flat symmetric molecule which possesses almost no intrinsic molecular dipole. Therefore the observed photo-induced work function shift can not be explained by a pure molecular rearrangement at the interface. Especially a photo-induced molecular rearrangement of flat-lying TCNQ molecules (as they were observed via STM measurements [328, 334]) in an up-right position would result in free Au(111) places which should be observable due to an increased SS intensity. While the SS-derived signature gets quenched by illumination a photo-induced substantial molecular rearrangement has to be excluded. Even though a down-bending of cyano groups of flat lying molecules might have some impact. It is known that for F_4TCNQ molecules adsorbed on Cu(100) this down-bending of cyano groups is thermally activated and leads to a work function decrease due to a back donation of electrons to the substrate [93]. A similar down-bending of cyano groups is a possible feature but not indispensable for describing the photo-induced modifications at the TCNQ/Au(111) interface via a light-triggered charge transfer type interaction. Solely an interfacial charge transfer remains as adequate reason which implies a work function increase due to the formation of a negatively charged interfacial layer. This negatively charged layer consequently prevents electrons from leaving the surface. Considering all described photo-induced modifications of the electronic structure at the TCNQ/Au(111) interface, the most convenient explanation is a photo-induced interfacial charge transfer type interaction which might be accompanied by a down-bending of cyano groups.

Unfortunately, it is not possible using 2PPE or UPS to gain more insights into the adsorption geometry of TCNQ on Au(111) and a possible down-bending of the molecule's cyano groups as obtained via HREELS in case of F_4TCNQ on Cu(100) [93]. Nevertheless, Katayama *et al.* [93] demonstrated also a thermal activation of this down-bending of the cyano groups and the accompanying charge back donation to the underlying metal substrate. In order to investigate a possibly similar thermal influence on the photo-induced spectral changes at the TCNQ/Au(111) interface, figure 7.2a displays selected annealing steps and their specific induced work function back-shifts towards the original value of an unilluminated spot.

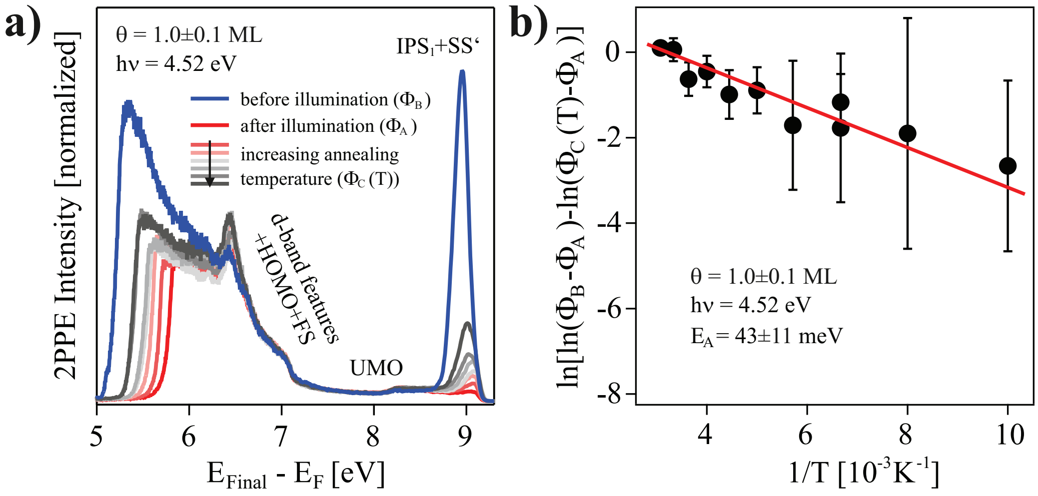

Figure 7.2.: a) The photo-induced work function shift as well as all other spectral changes at the TCNQ/Au(111) interface can be reversed by a thermally induced process. An Arrhenius-like behavior of the thermally induced work function back-shift is illustrated in b). It enables an estimation of the activation energy E_A of the reverse process to 43±11 meV or 4.2±1.1 kJ/mol, respectively. At this point Φ_A constitutes the work function after saturating illumination, Φ_B represents the work function of the unilluminated spot and Φ_C depicts the sample's work function after annealing.

The thermal annealing steps lasted 10 min each at different temperatures ranging from 100 K to 325 K. In each case the thermal influence was checked on a former sufficiently illuminated spot. Generally, the thermally induced work function back-shift increases with increasing annealing temperature. Especially annealing at higher temperatures demonstrates the reversibility of all described photo-induced modifications in 2PPE spectra. As illustrated in an Arrhenius-plot (figure 7.2b) the thermally induced work function back-shift of former sufficiently illuminated spots at the TCNQ/Au(111) interface signifies an Arrhenius-like behavior. For this graph the work function of the illuminated spot before

(Φ_A) and after an annealing step (Φ_B) is compared with the work function of an unilluminated spot (Φ_C). A linear behavior, as illustrated in figure 7.2b, substantiates a full thermal reversibility of the photo-induced modifications and results in an activation energy (E_A) of 43 ± 11 meV (4.2 ± 1.1 $^{\mathrm{kJ}}/_{\mathrm{mol}}$). This calculation was performed as discussed in ref. [124] and results in a value which can be associated to a thermally induced transfer to the initial state. Presumably, its low magnitude is favored by the substrate temperature difference while molecular adsorption (300 K) and illumination (100 K).

After the assignment of the observed photo-induced modifications in 2PPE spectra to a photo-induced interfacial charge transfer the subject of the following part is its physical excitation process. For this purpose the photo-induced work function shift was chosen as measure for a photon energy dependent study. In order to gain additional insights into the efficiency of this process, the photo-induced work function change was plotted versus the photon dose (PD, number of incoming photons) as visualized for four different photon energies in figure 7.3a. It can be noticed that the photo-induced work function shift follows an asymptotic behavior which starts at $\Phi_B = 5.20 \pm 0.05$ eV and saturates at a constant value of $\Phi_A = 5.85 \pm 0.05$ eV. The following saturation function was used to fit this behavior and to determine an effective cross section σ:

$$\Phi = \Phi_B + \Delta\Phi \exp(-\sigma \cdot \mathrm{PD}). \tag{7.1}$$

Figure 7.3a illustrates this fit for four different photon energies which prove a monoexponential behavior. Interestingly, for increasing photon energies the cross section also increases which is visualized in figure 7.3b. Beside that there is a photon energy threshold which amounts to be 4.25 ± 0.05 eV up to which no photo-induced charge transfer occurs at the TCNQ/Au(111) interface. Above this threshold the cross section exponentially increases up to around 10^{-21} cm^2 for a photon energy of 5 eV. In addition, figure 7.3c demonstrates that there is no power density dependence of the cross section for a given photon energy which, in contrast, would exist for a non-linear two-photon process. This result is supported by illumination experiments using an external pulsed laser source shown in appendix C. Another result is illustrated in figure 7.3d. By randomized repeated illumination series at constant photon energy the cross section was found to depend on the polar angle (ϕ) of the sample.

According to these results, the photo-induced charge transfer at the TCNQ/Au(111) interface is a single-photon-derived process with a threshold which amounts to be 4.25 ± 0.05 eV. But this threshold energy is higher than the HOMO-LUMO gap (around 3.2 eV, from combined STS and 2PPE results

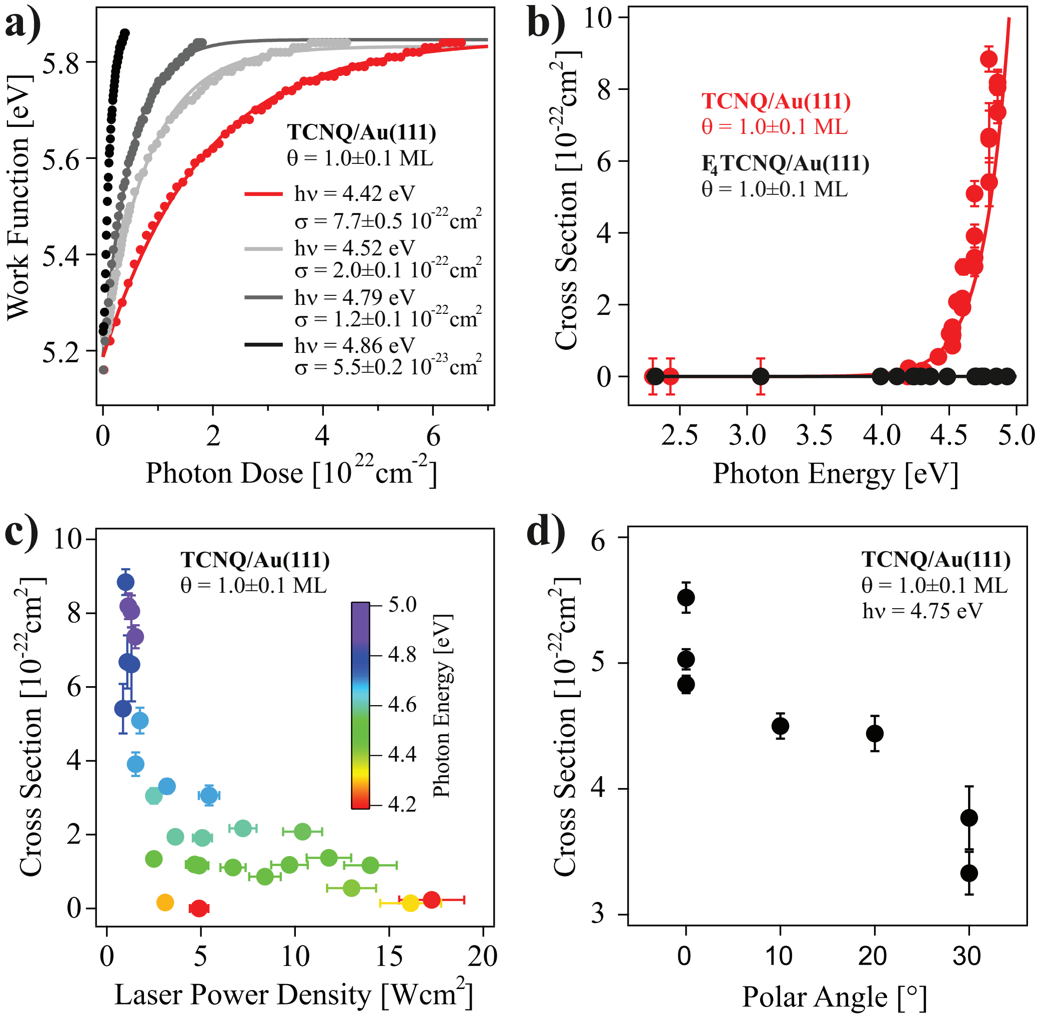

Figure 7.3.: Characterizing the demonstrated photo-induced spectral modifications by monitoring the work function change at full monolayer TCNQ coverage. a) Illustrates the monoexponential behavior of the work function shift and a strong photon energy dependence. This strong photon energy dependence indicates a threshold at 4.25±0.07 eV as visualized in b). In case of F$_4$TCNQ such a photo-induced effect was not observed. c) Demonstrates a power-density independent cross section, whereas an angular dependence is shown in d).

[334]) or the energetic position of the LUMO relative to E_F (around 0.7 eV [334]). As this threshold fits adequately to the intermediate state energy of IPS$_1$, the photo-induced interfacial charge transfer type interaction might be driven by the population of IPSs which is followed by an electron transfer into TCNQ molecules at the interface. Nevertheless, also a direct photo-induced population of a molecule-induced anionic state seems possible. Unfortunately, it was impossible to monitor the transferred electron in TCNQ molecules or the appearance of anion states at the TCNQ/Au(111) interface with the available 2PPE setup. Photon energies below 4.25 ± 0.05 eV are not sufficient to trigger the suggested photo-induced charge transfer mechanism which might correlate to the fact that these photon energies are not sufficient to excite an electron from an initial state below E_F to IPSs. The observed angular dependence of the cross section serves as another hint towards an image potential driven charge transfer type interaction as the dispersion of IPS$_1$ leads to an angle-dependent intermediate state energy of IPS$_1$. This angular dependence results in an increased threshold value for higher polar angles implying a decreasing cross section for increasing polar angles at a constant photon energy as displayed in figure 7.3d.

Figure 7.4 summarizes the photo-induced spectral changes in an energy diagram. Considering all reported results this chapter suggests that the described photo-induced charge transfer type interaction at the TCNQ/Au(111) interface is triggered by a photon-induced population of IPSs followed by an electron transfer into TCNQ molecules. Possibly this photo-induced charge transfer at the TCNQ/Au(111) interface is stabilized due to the strong electron-accepting

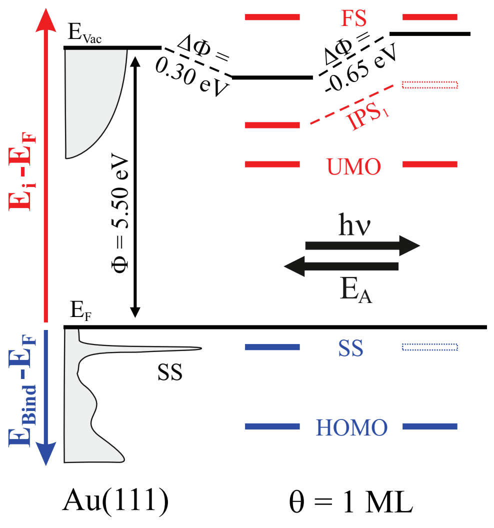

Figure 7.4: Summarizing photo-induced spectral changes and their thermal reversibility in an energy diagram. A detailed listing and discussion of these spectral changes and possible underlying physical processes can be found in the text.

nature of TCNQ (according to its high EA [86, 372–375]). The herein presented results indicate that the corresponding photo-induced modifications are completely reversible due to thermal annealing. Therefore, analogous to F_4TCNQ adsorbed on Cu(100), it might be possible that the photo-induced charge transfer at the TCNQ/Au(111) interface is correlated with an uplifting of formerly down-bended cyano groups [93]. For this special photo-induced process mainly two applications seem possible: The application as photosensitive hole injection layer and the utilization as organic UV-radiation sensor. Both possibilities would immensely profit from the full thermal reversibility of photo-induced processes. Comparing F_4TCNQ with its unfluorinated derivative TCNQ adsorbed on a clean Au(111) surface there is no photo-induced process as visualized in figure 7.3b. This is due to the fact that F_4TCNQ is found to be already negatively charged on the Au(111) surface as demonstrated in section 6.2.

8. Extended Space Charge Region and Unoccupied Band Formation in Epitaxial F_4TCNQ Films

The generation and control of molecular ordering and self-organization at metal/organic interfaces and within thin molecular films emerged as a key step in the engineering of organic (opto)electronic devices [1, 396, 397]. Its strong impact on charge carrier transport makes molecular ordering and self-organization to easily accessible adjustment screws for device performance optimization [52, 53, 398]. Charge transport in organic semiconducting materials can be described either by thermally activated hopping of charge carriers or via band transport. In comparison, the latter one usually leads to much higher charge carrier mobilities and conductivities [25, 40, 64, 398–400]. Admittedly both, band formation and band transport, are only possible in well-ordered crystal-like extended molecular arrangements. For instance band transport was recently demonstrated in extended aromatic π-systems in which π-stacking results in an ordered molecular structure followed by molecular orbital hybridization [59–61, 401, 402]. Moreover, band formation was observed at metal/organic interfaces where delocalized substrate bands hybridize with localized molecular orbitals [66, 68–70, 95, 106]. Nonetheless, these interfacial bands can not exist in thicker adsorbate films due to a decreasing wave function overlap.

During this thesis F_4TCNQ was found to grow in epitaxial well-ordered molecular film structures on Au(111) surfaces. This chapter presents a first determination of the geometrical and electronic structure of these well-ordered F_4TCNQ films by means of LEED and AR2PPE. Coverage-dependent 2PPE measurements demonstrate the coverage-independent well-defined electronic position of molecule-induced electronic states and the formation of an extended space charge region. Whereas angle-resolved 2PPE clarifies band formation in epitaxial well-ordered F_4TCNQ films and states the first time observation of an unoccupied band dispersion in a molecular crystal-like film.

The geometric arrangement of F_4TCNQ molecules adsorbed on Au(111) surfaces was subject of several STM investigations as discussed in section 5.2 [96, 97]. They demonstrate an adsorption structure at full monolayer coverage which is characterized by an unit cell containing one single molecule. This adsorption structure is supported via coordination to gold adatoms [97]. In contrast, single-crystals grown from dry acetonitrile feature an unit cell comprising four molecules [64, 97, 403]. Intuitively one would assume a F_4TCNQ growth on Au(111) surfaces which transitions from a monomolecular unit cell directly at the interface into the common molecular packing structure in solution-processed F_4TCNQ single-crystals. However, comparing LEED pattern for a sample at full monolayer coverage and a 20 ± 3 ML thick film shown in figure 8.1 indicates an almost unchanged geometric structure.

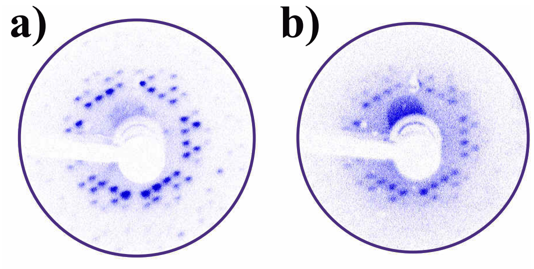

Figure 8.1: LEED pattern of the F_4TCNQ/Au(111) interface at full monolayer coverage a) and for an epitaxial 20 ± 3 ML thin F_4TCNQ film grown on a Au(111) surface held at room temperature b) (primary energy: 22 eV). A comparison indicates an almost unchanged geometric structure.

Consequently, the crystalline structure of F_4TCNQ films grown by thermal evaporation of molecules onto a Au(111) surface held at room temperature is strongly correlated to the molecular adsorption geometry at the interface. Thus in the present case, F_4TCNQ was found to grow in a well-ordered epitaxial fashion which results in a crystalline molecular structure with only one molecule per unit cell. Note, that such a crystalline structure with monomolecular primitive unit cell is very uncommon for organic molecular crystals [64, 404].

Performing 2PPE at different film thicknesses enables experimental access to the transition from the F_4TCNQ/Au(111) interfacial electronic structure to the electronic structure in epitaxial F_4TCNQ films. Figure 8.2a illustrates 2PPE spectra of different thick epitaxial F_4TCNQ films grown on Au(111). For all depicted coverages five 2PPE features are observed which can be assigned to molecule-induced electronic states, according to findings from section 6.2. Unexpectedly, the energetic position, intensity, and width of all observed spectral features does not change with increasing coverage. The thickness-independent intensity and width of 2PPE features can be ascribed to the well-ordered molecular structure in the epitaxial F_4TCNQ films as geometric disorder usually leads to an energetic broadening and intensity decrease. A constant energetic position of 2PPE features suggests that no decoupling effects between metal bands

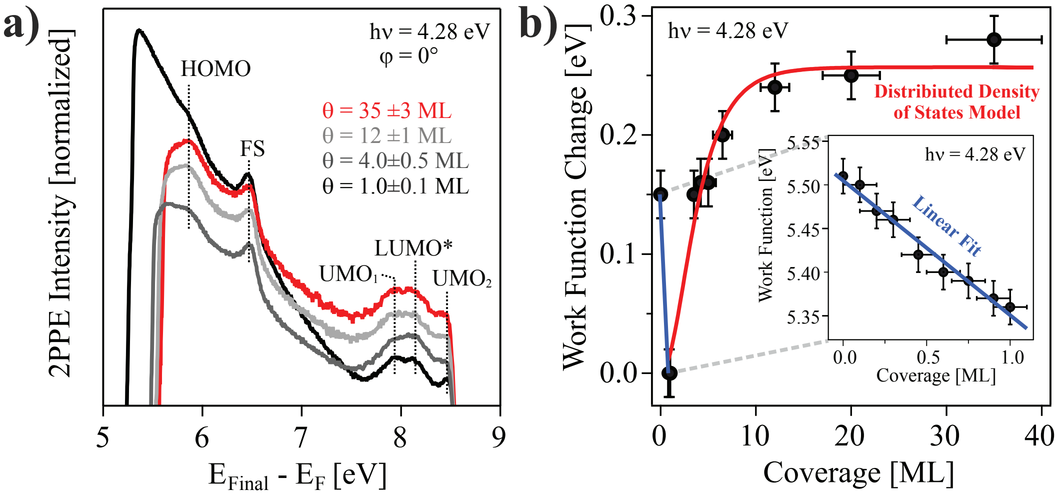

Figure 8.2.: a) Monochromatic 2PPE spectra of different F_4TCNQ film thicknesses grown on Au(111). b) Work function changes as a function of coverage. In the submonolayer regime the work function change was fitted linearly (blue), whereas for higher thicknesses the distributed density of states model [218] (red) was used.

and adsorbate-induced electronic states occur like, for example, band bending as discussed in section 2.5.2. At first glance this result contradicts to the established charge transfer type interaction at the F_4TCNQ/Au(111) interface which should have impact on the interfacial electronic structure [47, 92, 344]. But such an influence is only observed in a thickness-dependent work function change illustrated in figure 8.2b. In the submonolayer regime the work function decreases linearly from 5.50 ± 0.02 eV, the value of the clean Au(111) surface, to 5.35 ± 0.02 eV (as inset in figure 8.2b) as consequence of an interplay between Pauli-repulsion and charge transfer induced dipole formation. The linearity of this adsorbate-induced work function shift might be explained by two scenarios. On one side a linear work function shift can be explained by island-like film growth [344]. Alternatively, for increasing coverage, a repulsive intermolecular interaction would lead to a gradual decrease in the average interspace between the adsorbate molecules [344]. The latter argumentation fits to the second-order desorption shape shown by TPD measurements in section 5.2 for F_4TCNQ desorption in the submonolayer regime. In combination both results suggest a repulsive intermolecular interaction between F_4TCNQ molecules adsorbed on a Au(111) surface. Comparing this conclusion with an analog observation for TTF adsorbed on Au(111) via STM, this repulsive intermolecular interaction can be traced back in both cases to an interfacial charge transfer type interaction which implies a Coulomb-repulsion between charged molecular species [94].

For F_4TCNQ coverages above one monolayer the work function rises asymptotically to 5.60 ± 0.02 eV. This limit is even larger than the work function of the clean Au(111) substrate and was reported for various F_4TCNQ covered surfaces [48, 101]. As interfacial effects should not contribute for thicker F_4TCNQ films, this observation can be assigned to the formation of a space charge region. The formation of such a region is usually discussed in combination with band bending to describe the transition from interfacial to the bulk electronic structure [217, 230, 308, 405]. But in the present case the energetic position of molecule-induced electronic states relative to E_F was found to be constant which excludes an explanation via band bending. Nonetheless, the asymptotic work function increases up to ca. 15 ML film thickness is a strong indication for additional charges in higher adsorbate layers. Presumably, the supply of negative charge carriers from the underlying Au(111) substrate leads to the transport of a specific amount of negative charges to higher adsorbate layers. This effect might be facilitated by the high molecular ordering and the small-dimensioned unit cell in epitaxial F_4TCNQ films grown on Au(111) surfaces. Recently, exceptional transport properties in difluoro-tetracyanoquinodimethane (F_2TCNQ) single crystals were attributed to a comparable crystal structure with a primitive unit cell containing only one molecule [64]. Considering all arguments, the extended space charge region in epitaxial F_4TCNQ films grown on Au(111) surfaces might be explained by a film thickness-dependent charge carrier concentration. These charges originally stem from a charge transfer type interaction directly at the F_4TCNQ/Au(111) interface. The driving force for this efficient charge transport to higher lying layers is the very high electron affinity of the F_4TCNQ molecule which is supported by a well-ordered molecular structure and a small-dimensioned primitive unit cell.

Phenomenologically, the work function increase in epitaxial F_4TCNQ films as a function of coverage can be fitted using a simplified distributed density of states model introduced by Mankel *et al.* [218]. This model describes the charge carrier concentration in an organic semiconductor film in dependence of the distance to the interface using a constant density of states DOS(E) as discussed in section 2.5.2. In the present case a DOS value of around $10^{20}\,\mathrm{cm}^{-3}\mathrm{eV}^{-1}$ has been derived. Recently, a similar value was found for a well-ordered semiconducting polymer adsorbed on a gold surface, whereas different organic semiconductor thin films adsorbed on inorganic, non-metallic substrates demonstrate a lower DOS [55, 218]. Interestingly, in all these different systems the work function change saturates already at low coverages (2 to 3 ML). In contrast, the space charge region in epitaxial F_4TCNQ films grown on Au(111) surfaces is much more extended and goes up to ca. 15 ML film thickness.

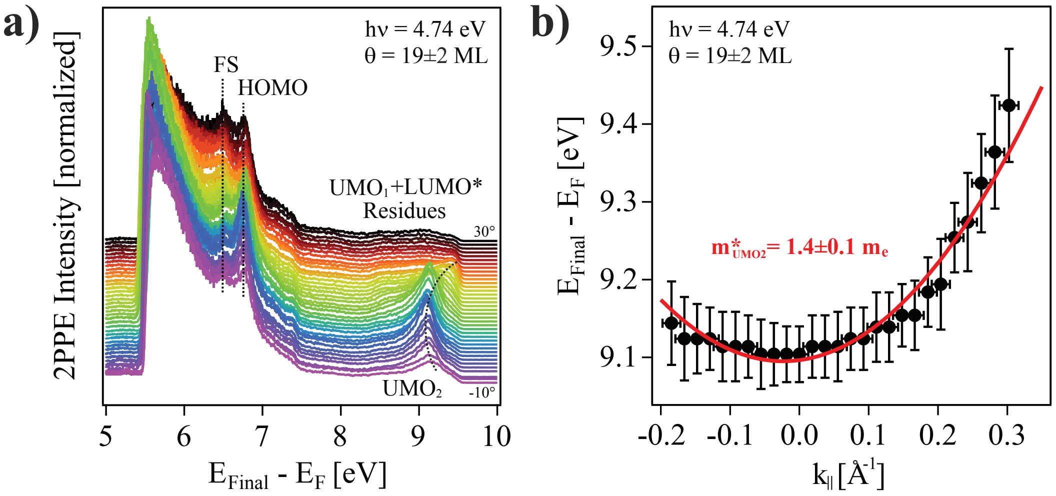

Figure 8.3.: a) AR2PPE spectra recorded with a photon energy of 4.74 eV demonstrate the dispersion of UMO_2 in epitaxial F_4TCNQ films grown on a Au(111) surface. b) The dispersion of UMO_2 can be fitted by a free electron parabola which results in an effective mass of $m^* = 1.4 \pm 0.1\,m_e$.

F_4TCNQ adsorbed on metal electrodes was successfully applied as hole injection layer in organic (opto)electronic devices [47, 377, 406, 407]. So far this applicability was explained due to the increased electrode's work function and the accompanying reduction of the hole injection barrier into the device. Results discussed in this chapter point towards a much more complex interplay between interfacial charge transfer type interaction and molecular ordering as motive for efficient charge transport from a Au(111) surface into thin F_4TCNQ films. In order to gain more information about the effective charge transport in epitaxial F_4TCNQ films, AR2PPE measurements were performed for a 19 ± 2 ML thick film. However, AR2PPE probes the dispersion of electronic states or bands parallel to the surface ($k_{\|}$), whereas $k_{\perp}$ is the needed value for explaining the charge transport from the interface into epitaxial F_4TCNQ films. Nevertheless, band formation in the direction parallel to the surface may suggest also band formation perpendicular to the surface. Figure 8.3a visualizes the addressed AR2PPE data. Indeed, the unoccupied molecule-induced electronic state UMO_2 exhibits an angular dependent energetic shift, whereas both, the HOMO and FS, remain localized. Evaluating the dispersion of UMO_2 using a parabolic fit as shown in figure 8.3b results in an effective mass of $m^* = 1.4 \pm 0.1m_e$ which substantiates a quasi free electron behavior. Conclusively, the performed AR2PPE measurement unveils band formation in epitaxial F_4TCNQ films grown on a Au(111) surface. Such band formation has been reported for the occupied electronic regime of molecular crystals [59–61, 401, 402], but to date an experimental proof of unoccupied molecular band formation in organic molecular crystals is still missing. The surprising band formation in epitaxial F_4TCNQ films has to be allocated to a hybridization of neighboring molecules' unoccupied molecular orbitals. The herein gained fundamental understanding of the interplay between interfacial charge transfer, band formation and an extended space charge region may be used to optimize the hole injection via an application-adjusted thickness modification of an epitaxial F_4TCNQ film grown on metal electrodes in organic (opto)electronic devices.

Unoccupied band formation in epitaxial F_4TCNQ films presented in this chapter serves as definite indication for an intermolecular hybridization. Due to the film thickness-independent geometric ordering in F_4TCNQ adsorbed on a Au(111) surface this hybridization might be also expected directly at the F_4TCNQ/Au(111) interface. The following chapter therefore presents and discusses AR2PPE measurements of the F_4TCNQ/Au(111) interface as well as of the TTF/Au(111) interface. Interestingly, both charge transfer characterized metal/organic interfaces feature band formation in the occupied as well as the unoccupied electronic region.

9. Band Formation at Metal/Organic Interfaces with Charge Transfer Type Interaction

Obviously, charge transport plays a crucial role in any kind of molecule-based (opto)electronic devices. It can be described via a thermally activated hopping transport in pure organic thin films, while its induced conductivity especially depends on the intermolecular orbital overlap [40, 42, 408]. Notwithstanding, amorphous molecular thin films feature a much smaller conductivity than well-ordered molecular structures which can be associated with band formation in molecular crystals [40, 167]. Nonetheless, in particular metal/organic interfaces are crucial regarding the charge transport properties in an entire molecule-based (opto)electronic device [44, 46, 48, 54, 56]. At these interfaces charges have to be transferred from metallic electrodes into organic thin films in which they can participate in transport mechanisms. In order to overcome possible transferring embarrassments like low interfacial electron density overlap or a significant hole injection barrier, band formation at metal/organic interfaces recently attracted much interest [68–70, 95]. It is known that the interaction between delocalized metal bands and localized molecular orbitals can give rise to new delocalized interfacial hybrid bands. Oftentimes, the degree of dispersion of these interfacial hybrid bands is strongly dominated by the participating metal band as they possess similar effective masses [66, 70]. Up to date, the PTCDA/Ag(110) interface and its derivative NTCDA/Ag(110), respectively, are the only cases in which this linkage does not hold [69, 281]. For these interfaces it has been proposed that the LUMO (located below E_F) hybridizes with the delocalized metal sp-states [69, 281]. Interfacial hybridization certainly implies a strong metal-molecule interaction which makes charge transfer characterized metal/organic interfaces suitable to investigate interfacial band formation.

During this thesis, the F_4TCNQ/Au(111) interface as well as the TTF/Au(111) interface were found to be such charge transfer characterized metal/organic interfaces. According to the adsorbate-induced work function changes at both interfaces, the charge transfer type interaction can be explained by the ICT model. Nonetheless, both analyzed interfacial electronic structures give occasion to a possible interfacial hybridization [94, 209, 343, 344]. Interfacial hybridization, however, might be connected to interfacial band formation. That is why ARPES and AR2PPE were applied to study possible band formation at these charge transfer characterized metal/organic interfaces.

Figure 9.1 visualizes ARPES data of a TTF/Au(111) interface at different coverages. As previously discussed in section 6.3 this interface is characterized by an electron transfer from the molecule to the metal surface. For a clean Au(111) surface, as shown in figure 9.1a, the metal surface's SS is observed at its well-known binding energy of $-0.42 \pm 0.03\,\mathrm{eV}$. Using ARPES data the Au(111) SS's dispersion can be calculated to an effective mass of $0.5 \pm 0.02\,\mathrm{m_e}$ as illustrated in figure 9.2. This value is in accordance with previously presented AR2PPE results (see chapter 4). Increasing the TTF coverage to $0.5 \pm 0.1\,\mathrm{ML}$ leads to a broadening and energetic shift of this photoemission signature towards E_F. As already discussed in section 6.3 this adsorbate-induced energetic shift is attributed to a hybridization of the SS with the HOMO of the molecule in accordance to DFT calculations [94, 209]. Following this argumentation, the adsorbate-induced shifted SS-derived photoemission signature is declared as HOMO* in figure 9.1b. The adsorption of additional TTF molecules up to full monolayer coverage effects a further continuing energetic shift of HOMO* towards E_F. For submonolayer coverage as well as for full monolayer coverage the interfacial hybrid state HOMO* is characterized by a SS-like dispersion which, unfortunately, is not evaluable in case of full monolayer coverage due to its energetic position just below E_F. Figure 9.2 illustrates this comparison. Besides the energetic shift of HOMO* towards E_F, an increasing coverage also implies a work function decrease (as previously discussed in section 6.3). This enables the observation of two additional photoemission signatures for full monolayer coverage as visualized in figure 9.1c. While HOMO** can be assigned to a second HOMO-derived interfacial hybrid state, according to DFT calculations [94, 209], the HOMO of neutral, non-interacting TTF molecules can be additionally observed. The HOMO-derived photoemission peak features band bending for increasing TTF film thickness (as discussed in section 6.3) but no dispersion. In contrast, the second HOMO-derived interfacial hybrid state HOMO** exhibits a distinct electron-like dispersion. It can be described using a free electron parabola and an effective mass which amounts to be $0.8 \pm 0.1\,\mathrm{m_e}$. According to the determined dispersions of the interfacial HOMO-derived hybrid bands HOMO* and HOMO** shown in figure 9.2, both are characterized by free electron-like dispersions. However, for $2.0 \pm 0.4\,\mathrm{ML}$ TTF coverage both interfacial hybrid states, HOMO* and HOMO**, are reduced in their intensity (as already discussed in section 6.3). Only the localized HOMO

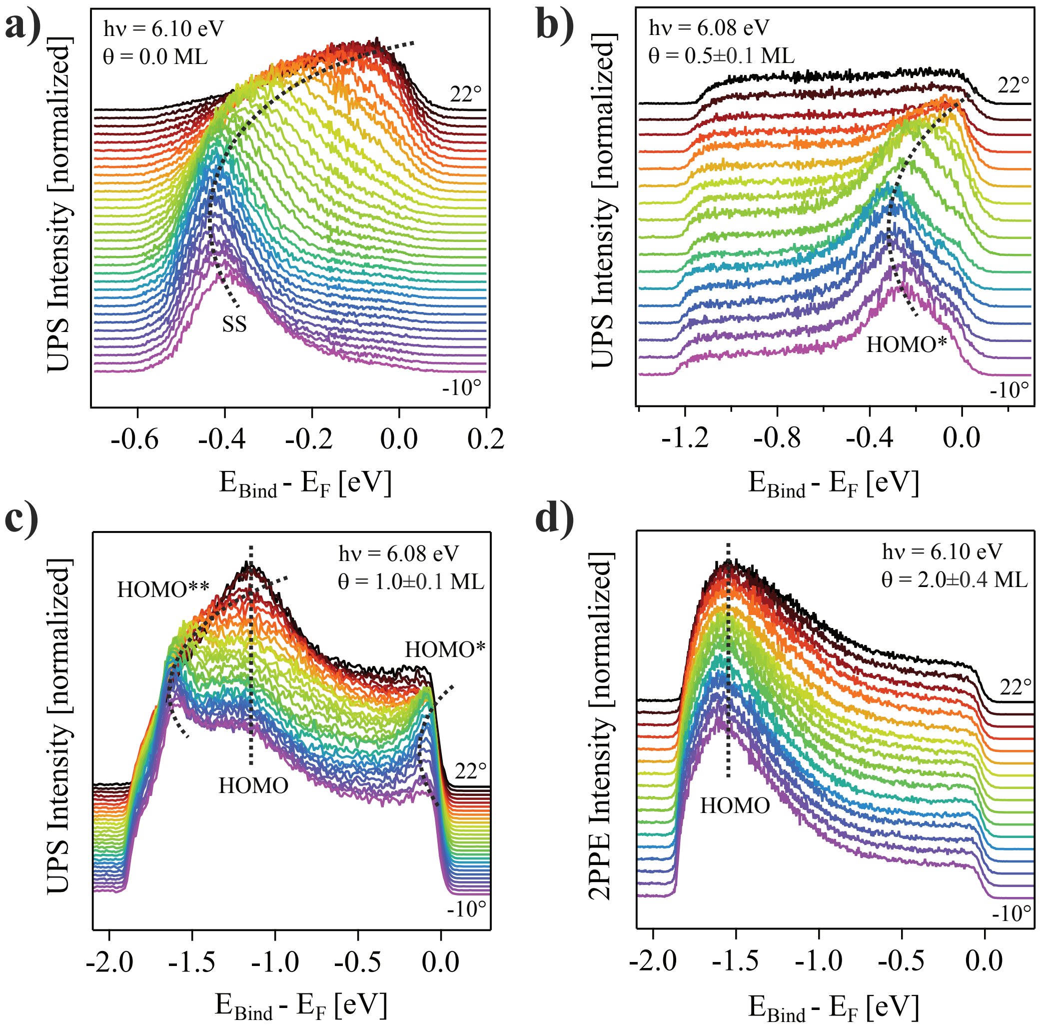

Figure 9.1.: ARPES data of a TTF/Au(111) interface for different coverages: a) clean Au(111) surface, b) 0.5 ± 0.1 ML, c) 1.0 ± 0.1 ML and d) 2.0 ± 0.4 ML. The two HOMO-derived interfacial hybrid states HOMO* and HOMO** are characterized by an electron-like dispersion, whereas the HOMO of neutral, non-interacting TTF molecules is localized. Black dotted lines depict guides to the eyes in order to underline the dispersion of HOMO* and HOMO**.

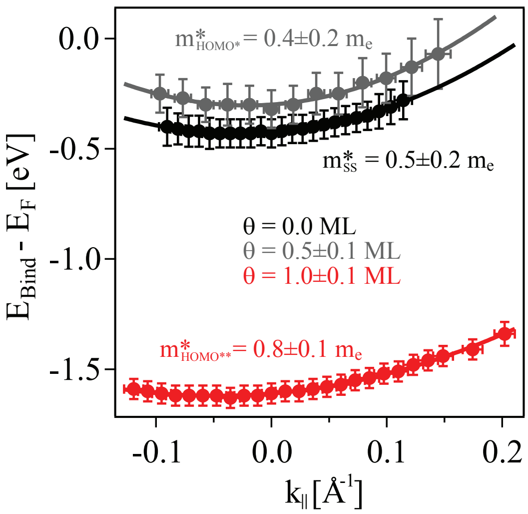

Figure 9.2: Coverage-dependent dispersion of HOMO-derived interfacial states (HOMO* and HOMO**) at the TTF/Au(111) interface. For comparison, the SS dispersion of the clean Au(111) is added to the graph. Both HOMO-derived interface states are characterized by a free electron-like dispersion

of neutral, non-interacting TTF molecules is still observed at slightly shifted binding energy ($-1.5 \pm 0.1\,\mathrm{eV}$) due to band bending.

Hitherto presented ARPES data definitely reveal the delocalization of charge carriers at the TTF/Au(11) interface. As the related delocalized hybrid states exist only directly at the interface the term interfacial band formation is appropriate. These interfacial hybrid bands rise because of a strong metal-molecule interaction which is accompanied by an efficient charge transfer from the molecule into the metal substrate. It is also worth to mention at this point that the observed interfacial hybrid band formation is in full agreement with DFT calculations predicting an equivalent "additional electron density buildup smeared out over the whole metal surface" (O. T. Hofmann, [209], page 20361). In the following, subsequent AR2PPE investigations confirm that this interfacial band formation can be also observed for the unoccupied energetic region above E_F. Monochromatic AR2PPE data shown in figure 9.3 reinforce the dispersion of the HOMO-derived interfacial hybrid state HOMO* for full monolayer coverage. In addition, these data expose an angle-dependent energetic shift of the unoccupied interface state IS_2. Also this dispersion can be described using a parabolic fit which results in an effective mass of $0.8 \pm 0.1\,\mathrm{m_e}$. Interestingly, this value equalizes the effective mass evaluated for the HOMO-derived interfacial hybrid state HOMO**. Conclusively, the presented results targeting the dispersion of the interfacial (hybrid) states HOMO*, HOMO** and IS_2 reveal an interfacial charge carrier delocalization (in $k_{\|}$) directly at the TTF/Au(111) interface. Importantly, the degree of dispersion of these electronic states is not dominated by the metal bands as the dispersion of these states does not

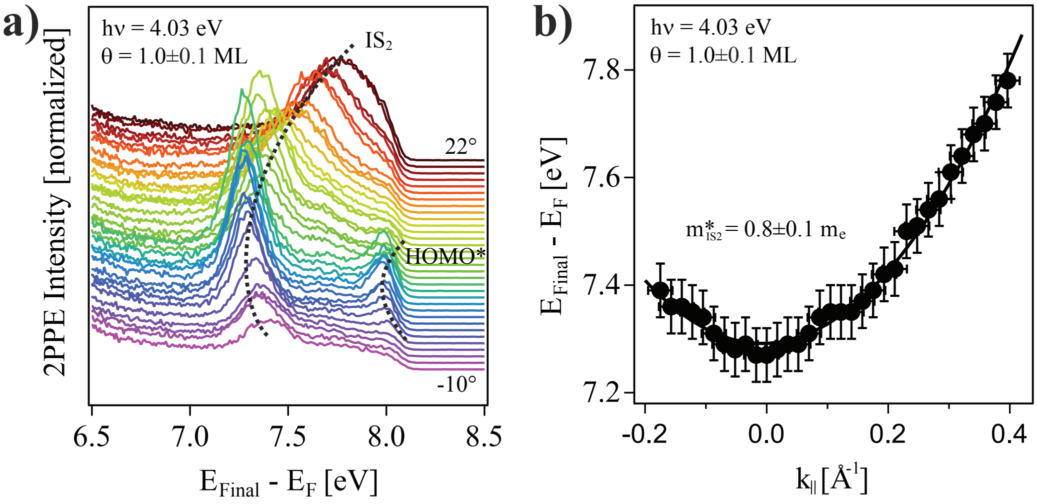

Figure 9.3.: a) Monochromatic AR2PPE data unfold the dispersion of the interfacial electronic state IS_2 at the TTF/Au(111) interface at full monolayer coverage. b) This dispersion results in an effective mass amounting $0.8 \pm 0.1\,m_e$ which equalizes the effective mass evaluated for the HOMO-derived interfacial hybrid state HOMO**.

equalize the dispersion of the underlying Au(111) SS. Convincingly, the dispersion of the interfacial (hybrid) states HOMO*, HOMO** and IS_2 illustrates the hybridization-induced delocalization of charge carriers at the TTF/Au(111) interface. Up to date, the TTF/Au(111) interface is the first interface at which band formation in the unoccupied energetic region was observed. Moreover, the experimental results of this chapter may establish for the first time a link between charge transfer, hybridization and band formation at metal/organic interfaces.

In order to gain more insights into this linkage also the F_4TCNQ/Au(111) interface was investigated by means of AR2PPE. Compared to TTF/Au(111), the F_4TCNQ/Au(111) interface is characterized by an electron transfer from the metal substrate into the molecule. Nonetheless, analyzing the electronic structure of the F_4TCNQ/Au(111) interface by means of 2PPE and DFT calculations again points towards a significant interfacial hybridization (for details see chapter 6) [343, 344]. Figure 9.4 shows AR2PPE data of a F_4TCNQ/Au(111) interface at full monolayer coverage for two different photon energies, 4.74 eV and 4.00 eV, respectively. In an overview, figure 9.4a visualizes that the adsorbate-induced 2PPE features which were assigned to a FS and the HOMO of F_4TCNQ do not show any angular dependence. So again the HOMO is localized in the direction parallel to the surface ($k_{\|}$) as previously observed also for thicker epitaxial F_4TCNQ films (see chapter 8). Otherwise, UMO_2 is characterized

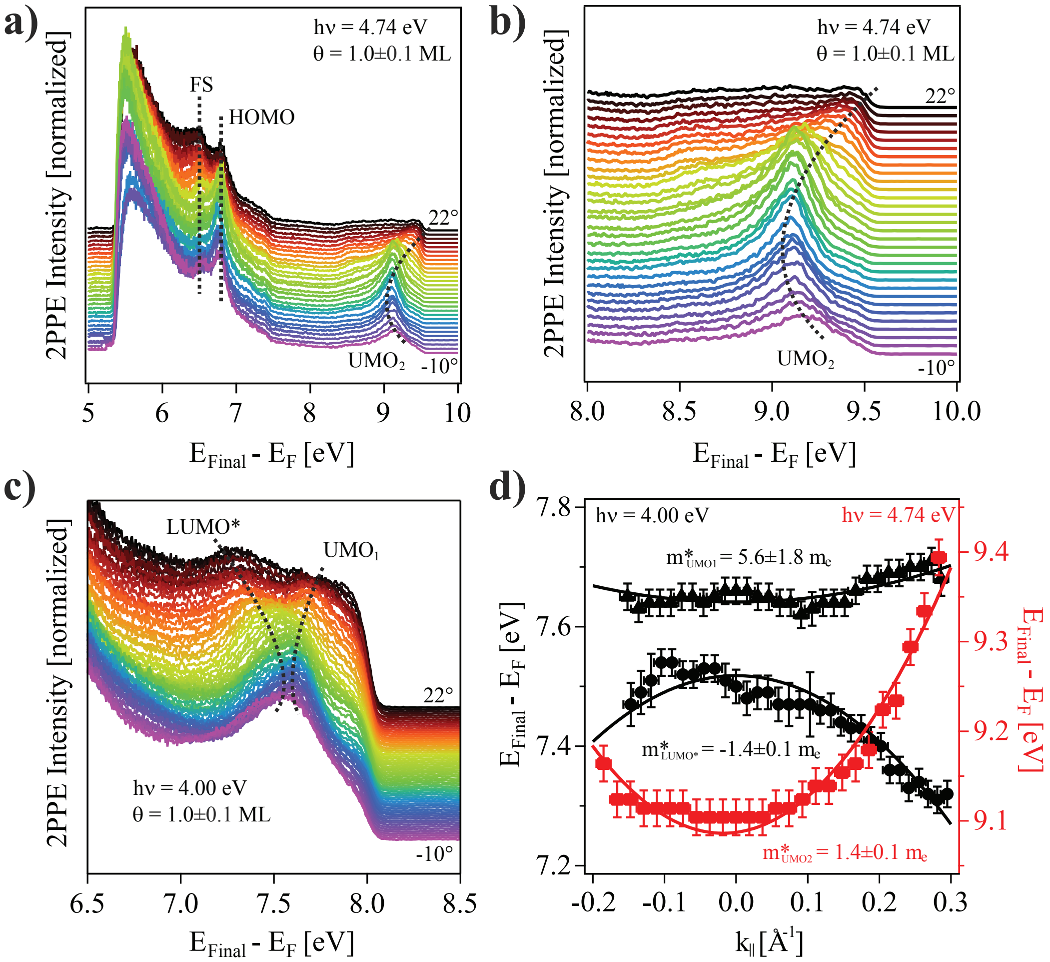

Figure 9.4.: Monochromatic AR2PPE data for two different photon energies, 4.74 eV (overview in a) and zoomed presentation in b)) and 4.00 eV (zoomed presentation in c)), respectively, reveal band formation directly at the F_4TCNQ/Au(111) interface. The dispersions of LUMO*, UMO_1 and UMO_2 are evaluated in d). Black dotted lines depict guides to the eyes in order to underline these dispersions.

by an electron-like dispersion as illustrated in more detail in figure 9.4b. This electron-like dispersion of UMO_2 was also observed in thicker epitaxial F_4TCNQ films (see chapter 8). Its energetic position and effective mass perfectly matches for full monolayer coverage and 19 ± 2 ML film thickness as depicted in figure 9.5a.

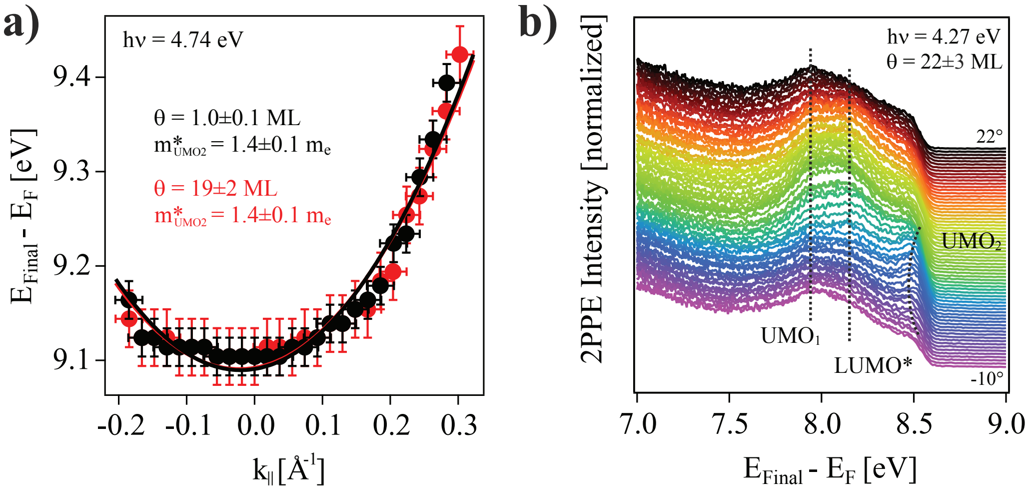

Figure 9.5.: a) Comparing the energetic position and dispersion of UMO_2 for 1 ML and 19 ± 2 ML film thickness. b) In an epitaxial F_4TCNQ film of 22 ± 3 ML thickness LUMO* as well as UMO_1 are still located at the known energetic positions but possess no dispersions.

But for lower photon energies, i.e. 4.00 eV, which are insufficient to populate UMO_2, less intense UMO_1 and LUMO* derived 2PPE maxima can be observed as shown in figure 9.4c. In these measurements both signatures show a significant angle-dependent energetic position. Evaluating these angular dependency as illustrated in 9.4d leads to an electron-like dispersion of UMO_1 with an effective mass amounting $5.6 \pm 1.8\, m_e$, whereas LUMO* displays a reverse hole-like dispersion with an effective mass amounting $-1.4 \pm 0.1\, m_e$. For 4.00 eV photon energy the respective peak positions were fitted using a pair of Gaussians as detailed in appendix E. In contrast to UMO_2, UMO_1 and LUMO* lose their delocalized character in thicker epitaxial F_4TCNQ films as indicated by a monochromatic AR2PPE study at 4.27 eV for a 22 ± 3 ML thick film shown in figure 9.5b.

The presented AR2PPE data demonstrate that UMO_1 and LUMO* feature a dispersion parallel to the surface ($k_{||}$) directly at the F_4TCNQ/Au(111) interface. Interestingly, this dispersion is quenched for 22 ± 3 ML film thickness as shown in figure 9.5b. In contrast, UMO_2 is characterized by an electron-like dispersion which is almost the same at the interface and in epitaxial films. As a consequence it can be concluded that UMO_2 gains its delocalized character from an intermolecular hybridization without any impact of the Au(111) substrate while the degree of delocalization of UMO_1 and LUMO* strongly depends on the metal-molecule hybridization directly at the interface. Apart from that, the HOMO displays no dispersion which emphasizes its localized character directly at the F_4TCNQ/Au(111) interface as well as in epitaxial thin films.

In summary, the performed AR2PPE study of the F_4TCNQ/Au(111) interface gives rise to in general three different angle-dependent variations of 2PPE features' energetic locations at metal/organic interfaces: localization (no dispersion, i.e. HOMO), electron-like dispersion (UMO_1 and UMO_2) and hole-like dispersion (LUMO*). According to unpublished DFT calculations by O. T. Hofmann (TU Graz), the hole-like dispersion of LUMO* might originate from a decreasing bonding character along the $\Gamma - K$ direction of this in Γ antibonding interfacial hybrid state [409]. Up to now PTCDA/Ag(110) is the only interface at which a hole-like dispersion of a LUMO-derived photoemission signature located below E_F has been reported [69]. Both, the range of binding energy variation and the angular dependence of the binding energy itself are similar for PTCDA/Ag(110) as well as for F_4TCNQ/Au(111).

Moreover, the before-mentioned three different angle-dependent variations of 2PPE features' energetic locations at metal/organic interfaces can be also classified into three different hybrid state categories, namely localization (no hybridization), intermolecular hybridization and interfacial hybridization. Localized electronic states without significant dispersion are the common case for amorphous organic semiconductor thin films as less molecular ordering and/or slight molecular orbital overlap impedes a hybridization of electronic states. For comparison intermolecular hybridization describes the hybridization of equivalent molecular orbitals of neighboring molecules. In this case a well-ordered geometric structure and a sufficient molecular orbital overlap might lead to molecular band formation as previously presented for an epitaxial F_4TCNQ film (see chapter 8). In contrast, in case of interfacial hybridization electronic states of the adsorbate hybridize with bands of the underlying metal substrate. At the presented F_4TCNQ/Au(111) interface electronic states from each of these three categories were observed which in fact is unique per se. In detail, the HOMO can be assigned to a localized molecule-induced state while UMO_2 represents the only intermolecular hybrid state which is signified by a comparable dispersion in epitaxial films as well as directly at the F_4TCNQ/Au(111) interface. Certainly, UMO_1 and LUMO* are also characterized by significant dispersions directly at the interface but these dispersions vanish for increasing coverage. That is why both, UMO_2 as well as LUMO*, are assigned to interfacial hybrid bands which lose their hybrid character for higher film thicknesses. Alone their dispersion directly at the F_4TCNQ/Au(111) interface is induced by the strong metal-molecule interaction, whereas their energetic position surprisingly does not significantly change (as discussed in chapter 8).

Altogether hybridization at both charge transfer characterized metal/organic interfaces, TTF/Au(111) as well as F_4TCNQ/Au(111), gives rise to dispersive interfacial hybrid states and thus to charge carrier delocalization parallel to the surface. The presented results suggest that interfacial hybridization, interfacial band formation and interfacial charge transfer are strongly correlated. For both investigated metal/organic interfaces the discussed ARPES and AR2PPE measurements depict that interfacial hybridization implies a redistribution of the interfacial electronic structure and accordingly of the charge carrier density which in case of interfacial hybrid bands is delocalized at least parallel to the surface. The redistributed charge carrier density in combination with hybrid bands crossing E_F presumably determines the amount of transferred charge at an hybrid interface and is therefore significant for the population or depopulation of a metal/organic interface with charges. Prospectively, charge transfer at metal/organic interfaces may serve as a sufficient prerequisite to possibly observe an underlying hybridization and/or band formation. For a future investigation of interfacial band formation one should therefore focus on charge transfer characterized metal/organic interfaces.

10. Adsorbate-Supported Relaxation Dynamics of Hot Electrons at Metal/Organic Interfaces

The predominant step in photochemical reactions at metal surfaces is the generation of photo-excited “hot” electrons in the metal which may attach to an adsorbate and may lead to photochemical reactions (femto-chemistry). As TR2PPE is the method of choice providing direct access to the lifetime of these hot electrons, the following chapter deals with the impact of adsorbates and interfacial charge transfer on the hot electron’s lifetime. Understanding the dynamics of optically excited electrons in metals is the prerequisite for their application in (opto) electronic devices as the transient behavior of (photo)excited “hot” electrons is crucial for charge transport and chemical reactions [410–413]. Therefore a detailed and quantitative knowledge of interfacial hot electron relaxation phenomena can be used for technological engineering in solid-state physics and surface chemistry [411, 413]. In this relation an increased hot electron lifetime generally results in an enhanced probability of their participation in charge transport mechanisms or chemical reactions. Basically, the lifetime of (photo)excited hot electrons in noble metals is determined by the excitation energy, electronic band structure, spin polarization, dimensionality or film thickness, respectively, and sample morphology [414–420]. Contributing relaxation mechanisms might be scattering events with excited holes, other “cold” electrons (energetically located just below E_F), phonons, plasmons, defects or impurities, hot electron diffusion and the repopulation of lower excited states by secondary electrons [411, 413, 414, 417]. Generally, hot electron lifetimes are observed up to 600 fs at very low intermediate state energies $E_\mathrm{i} - \mathrm{E_F}$ [421] which makes TR2PPE the perfect experimental tool to study hot electron lifetimes at metal/organic interfaces.

Several TR2PPE studies have shown that the relaxation of hot electrons at metal surfaces is dominated by inelastic electron-electron scattering for low excitation energies, high phase space ($E_\mathrm{i} - \mathrm{E_F} > 0.5\,\mathrm{eV}$) and low hot electron density [411, 413, 414]. Assuming a free electron-like behavior, the inelastic electron-electron scattering rate can be described by the Landau theory of Fermi liquids (FLT) from which the lifetime of hot electrons τ_{FLT} can be calculated to [411, 413, 422]:

$$\tau_{\text{FLT}} = \tau_0 \cdot \frac{E_{\text{F}}^2}{(E_{\text{i}} - \text{E}_{\text{F}})^2}. \tag{10.1}$$

Herein the prefactor τ_0 is mainly determined by the electron density. Deductively, the available phase space strongly determines the lifetime of hot electrons which tends to infinity for an infinitesimal small intermediate state energy as hot electrons can scatter only into lower lying unoccupied electronic states. Especially for small intermediate state energies, experiments observed a significant deviation from FLT which can be assigned to a different secondary decay channel or a combination of additional decay channels. Conclusively, the lifetime of hot electrons τ can be modeled using a scaling factor z and a second (effective) decay constant τ_1 [417, 423]:

$$\frac{1}{\tau} = \frac{1}{\tau_1} + \frac{1}{z \cdot \tau_{\text{FLT}}}. \tag{10.2}$$

This model was demonstrated to adequately describe experimental data of ultrafast hot electron dynamics in single-crystal Au(111) films [423]. Due to the high work function of a clean Au(111) surface and the limited photon energy range of the used femtosecond laser setup, it was not possible to study hot electron dynamics of a clean Au(111) surface during this thesis. Fortunately, as discussed in section 6.3, TTF adsorption lowers the surface work function to 4.15 ± 0.04 eV which in turn enables the study of hot electron dynamics at the TTF/Au(111) interface. Figure 10.1a displays a two-dimensional representation of TR2PPE measurements at full monolayer TTF coverage. In such representations the normalized correlated dichromatic 2PPE signal at a given finale state energy (left axis) or intermediate state energy (right axis) with respect to E_{F} is plotted as a function of pump-probe delay. Positive pump-probe delays imply that the probe pulse (here $\text{h}\nu_1 = 4.01$ eV) reaches the sample after the pump pulse (here $\text{h}\nu_2 = 3.09$ eV). At full monolayer coverage the interface state IS_2 shows no significant lifetime while in the region towards the SE at 4.15 ± 0.04 eV final state energy or 0.00 ± 0.04 eV intermediate state energy, respectively, long living electrons can be observed in an extended energy range of about 1 eV. Additionally, this two-dimensional representation already visualizes that for decreasing intermediate state energy or phase space, respectively, the lifetime of these electrons increases. Because of this behavior these long-living electrons can be assigned to hot electrons at the TTF/Au(111) interface. Figure 10.1b illustrates this two-dimensional representation for 2.0 ± 0.5 ML and 3.0 ± 0.8 ML

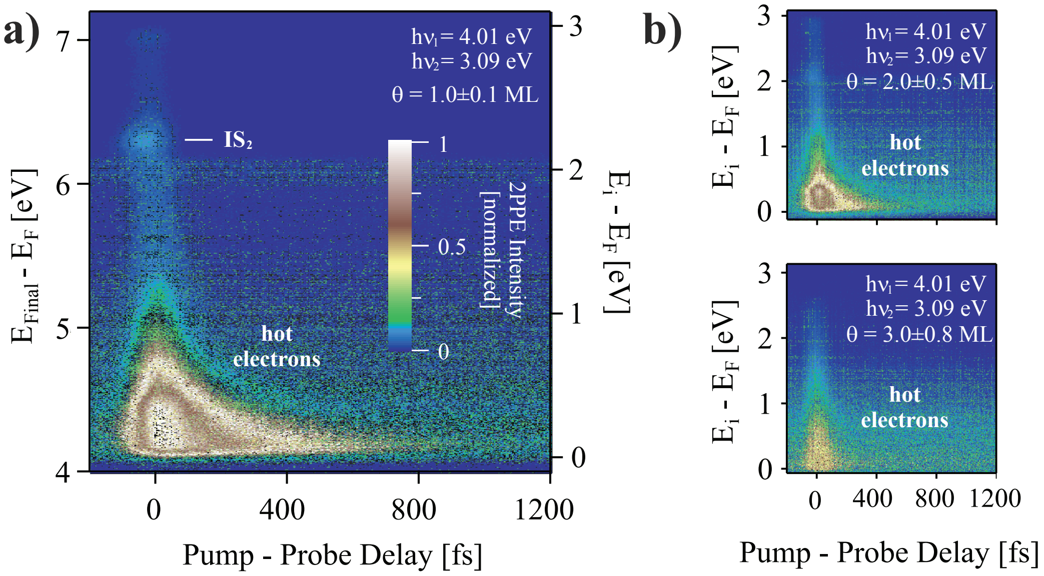

Figure 10.1.: Time-resolved 2PPE measurements of the TTF/Au(111) interface at different coverages. a) At 1.0 ± 0.1 ML coverage hot electrons can be observed in an extended energy range of about 1 eV. With decreasing intermediate state energy the lifetime of hot electrons is increased up to some hundred fs, whereas the unoccupied interfacial electronic state IS$_2$ features no significant lifetime. b) The adsorption of a second and a third layer of TTF molecules has no significant impact on hot electron lifetimes at the TTF/Au(111) interface.

TTF coverage, respectively, applying the same photon energies. For both coverages the 2PPE intensity near the secondary edge decreases but features a comparable pump-probe delay dependency. This observation demonstrates that the adsorption of a second and a third layer of TTF molecules has no significant impact on hot electron lifetimes at the TTF/Au(111) interface.

In order to study the lifetime of hot electrons at the TTF/Au(111) interface in more detail, figure 10.2a depicts the cross-correlation curves averaged for a 0.1 eV broad intermediate state energy range each. The averaged cross-correlation curves were fitted using a monoexponential decay function (see equation 3.6). These fits reveal that the cross correlation can be fitted using one single exponential decay and that the lifetime of hot electrons increases for decreasing intermediate state energy. Figure 10.2b visualizes the energy-dependent lifetime of hot electrons at the TTF/Au(111) interface for 1.0 ± 0.1 ML as well as for 2.0 ± 0.5 ML coverage. Moreover, data of hot electron dynamics in single-crystal Au(111) films from ref. [423] are enclosed for comparison. As discussed before, these hot electron dynamics in single-crystal Au(111) films can be described using equation 10.2 while an interpretation as pure Fermi liquid fails [423].

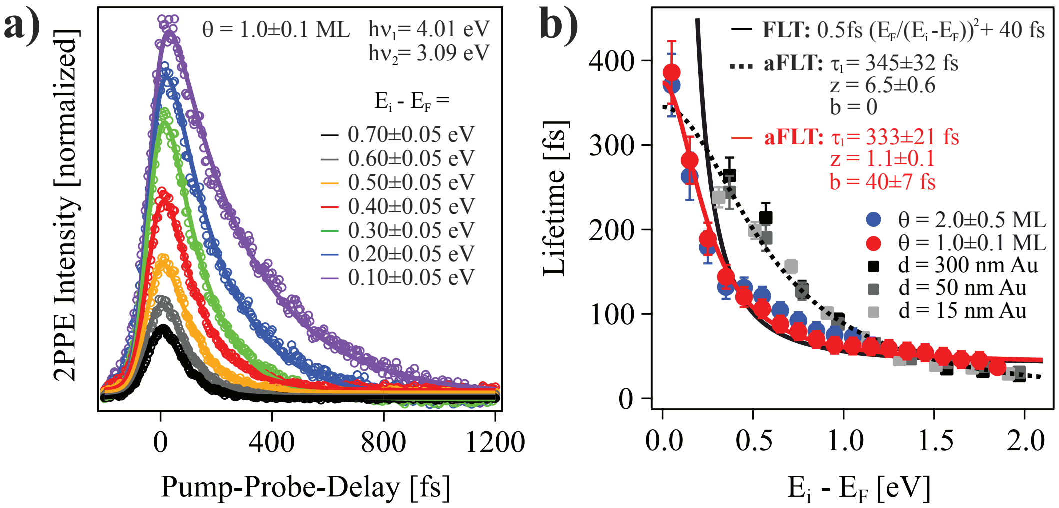

Figure 10.2.: Characterizing hot electron dynamics at the TTF/Au(111) interface. a) Averaged cross-correlation curves for different intermediate state energies fitted by a monoexponential decay function. b) Energy-dependence of hot electron lifetimes for the TTF/Au(111) interfaces and single-crystal Au(111) films (data adopted from ref. [423]).

The presented hot electron dynamics at the TTF/Au(111) interface and in single-crystal Au(111) films coincidence for high intermediate state energies ($((E_\mathrm{i} - \mathrm{E_F}) > 0.9\,\mathrm{eV})$, whereas for low intermediate state energy significant differences occur. Generally, the hot electron dynamics at the TTF/Au(111) interface are characterized by a steeper lifetime increase up to almost 400 fs for an infinitesimal intermediate state energy which includes lower lifetimes in the range from 0.3 eV to 0.9 eV. Above 0.4 eV intermediate state energy hot electron lifetimes at the TTF/Au(111) interface can be adequately described using FLT and a constant background $b = 40$ fs. Including a scaling factor z and a decay constant τ_1 also the data region below 0.4 eV intermediate state energy can be sufficiently described. From this applied FLT fit (aFLT) the second decay constant τ_1 can be estimated to amount 333 ± 21 fs. This value is consistent with a reported decay constant on single-crystal Au(111) films (the corresponding aFLT-fit is also depicted in figure 10.2b) [423]. As hot electron diffusion into the bulk usually plays a minor role [418, 420, 423, 424] this second decay channel for hot electrons is usually assigned to electron-phonon scattering on a sub-picosecond time scale [423, 425–428]. Electron-phonon scattering per se is not influenced by the interfacial electronic structure as phonons describe a solid state phenomenon. Contradictory, it will be shown in the following that hot electron dynamics at the TTF/Au(111) interface strongly depend on the interfacial electronic structure which excludes in this special case an electron-phonon scattering assisted decay. Regarding the scaling factor z in performed aFLT-fits, polycrystalline Au(111) films possess a medium single digit value [423, 425, 426], whereas for the TTF/Au(111) interface z is close to one. As z gives more weight on the second decay channel (τ_1) a value close to one proves the ideal FLT-conform behavior of the investigated TTF/Au(111) surface for intermediate state energies above 0.3 eV.

Collectively, the presented results suggest a negligible impact of TTF adsorption on hot electron lifetimes at a Au(111) surface. This finding is quite surprising as the electronic band structure around E_F should influence the hot electron lifetimes at metal surfaces [156, 429, 430]. But TTF adsorption leads to a minor effect on hot electron dynamics at a Au(111) surface, in comparison to polycrystalline Au(111) films, despite of the presented interfacial band formation and charge transfer type interaction at the TTF/Au(111) interface (for details see chapter 9). So in this special case a fundamental modification of the interfacial electronic structure has no impact on the hot electron dynamics. In order to understand this observation, one layer TCNQ was additionally evaporated onto a fully covered TTF/Au(111) interface. Due to its high EA, TCNQ adsorption should influence the ultrafast hot electron dynamics at the TTF/Au(111) interface by a possible adsorbate-induced rearrangement. Annealing at 370 K leads to a structural and electronic reorganization and the desorption of non-surface-bound TTF and TCNQ molecules (see appendix F) which presumably results in a single molecular layer of mixed TTF/TCNQ complexes adsorbed on the Au(111) substrate (from now on called TCNQ/TTF/Au sample). In order to prove the impact of this molecular reorganization on hot electron lifetimes, the evaporation sequence was reversed: first a TCNQ monolayer was prepared and annealed to 370 K, then TTF was additionally dosed on top and subsequently annealed at 300 K which again led to a structural and electronic reorganization and the desorption of non-surface-bound TTF and TCNQ molecules. From now on this sample is called TTF/TCNQ/Au. Both samples, TCNQ/TTF/Au and TTF/TCNQ/Au, are characterized by a very similar electronic structure (see appendix F). This includes a similar work function of about 4.80 ± 0.10 eV and the observation of a broad unoccupied electronic state energetically located around 0.85 ± 0.12 eV below E_Vac which can be assigned to the first image potential state (IPS$_1$), according to AR2PPE investigations (see appendix F). Unfortunately, the exact chemical composition of both samples is unknown, but it can be assumed due to the similar electronic structure that both samples consist of a comparable single layer of mixed TTF/TCNQ molecules on a Au(111) surface.

Figure 10.3 illustrates for both samples a two-dimensional representation of TR2PPE measurements and cross-correlation curves averaged for 0.1 eV intermediate state energy steps each. For these time-resolved measurements the applied photon energies were 2.39 eV and 4.79 eV, respectively, in order to probe again photo-excited electrons directly above E_{F}. Also in this case positive pump-probe delays imply that the probe pulse ($\mathrm{h}\nu_1 = 4.79\,\mathrm{eV}$) reaches the sample after the pump pulse ($\mathrm{h}\nu_2 = 2.39\,\mathrm{eV}$). TR2PPE measurements of both mixed layer samples shown in figure 10.3a and c reveal similar hot electron dynamics. As previously performed for the TTF/Au(111) interface, the cross-correlation curves averaged for 0.1 eV intermediate state energy steps are illustrated in figure 10.3b and d to characterize the hot electron dynamics at these mixed layer interfaces in more depth. Also for the mixed layer the averaged cross-correlation curves can be fitted by a monoexponential decay function. Figure 10.4 visualizes the resulting intermediate state energy dependent lifetimes for TCNQ/TTF/Au and TTF/TCNQ/Au in comparison to hot electron dynamics at the TTF/Au(111) interface. For intermediate state energies above 0.5 eV hot electron dynamics at mixed layer covered Au(111) surfaces coincide with hot electron lifetimes at the TTF/Au(111) interface and at single-crystal Au(111) films (see figure 10.2b). As previously discussed these lifetimes are in full agreement with FLT which suggests an electron-electron scattering assisted decay of hot electrons in this energy range. In contrast, for intermediate state energies below 0.5 eV the hot electron dynamics at mixed layer covered Au(111) surfaces strongly differ from hot electron lifetimes at the TTF/Au(111) interface or at single-crystal Au(111) films. Also in case of low intermediate state energies the hot electron dynamics at mixed layer covered Au(111) surfaces can be adequately described using FLT (without any modification), whereas hot electron lifetimes at the TTF/Au(111) interface have to be described using an additional decay channel. Therefore the intermixture of TCNQ and TTF molecules adsorbed in a single layer on a Au(111) surface quenches this additional decay channel. Due to its dependence on the interfacial structure this decay channel at the TTF/Au(111) interface can not be assigned to hot electron dissociation or electron-phonon scattering. So the ultrafast hot electron dynamics at the TTF/Au(111) interface might be explained by a phase space argument. Hybrid band formation at the charge transfer characterized TTF/Au(111) interface leads to the formation of an increased density of occupied and unoccupied electronic states near E_{F}. This increased DOS near E_{F} can be interpreted as an increased amount of available scattering partners as well as an increased phase space as discussed for hot electron dynamics in transition metals [411]. Both effects enable a fast electron-electron scattering assisted hot electron relaxation also for low intermediate state energies at the TTF/Au(111)

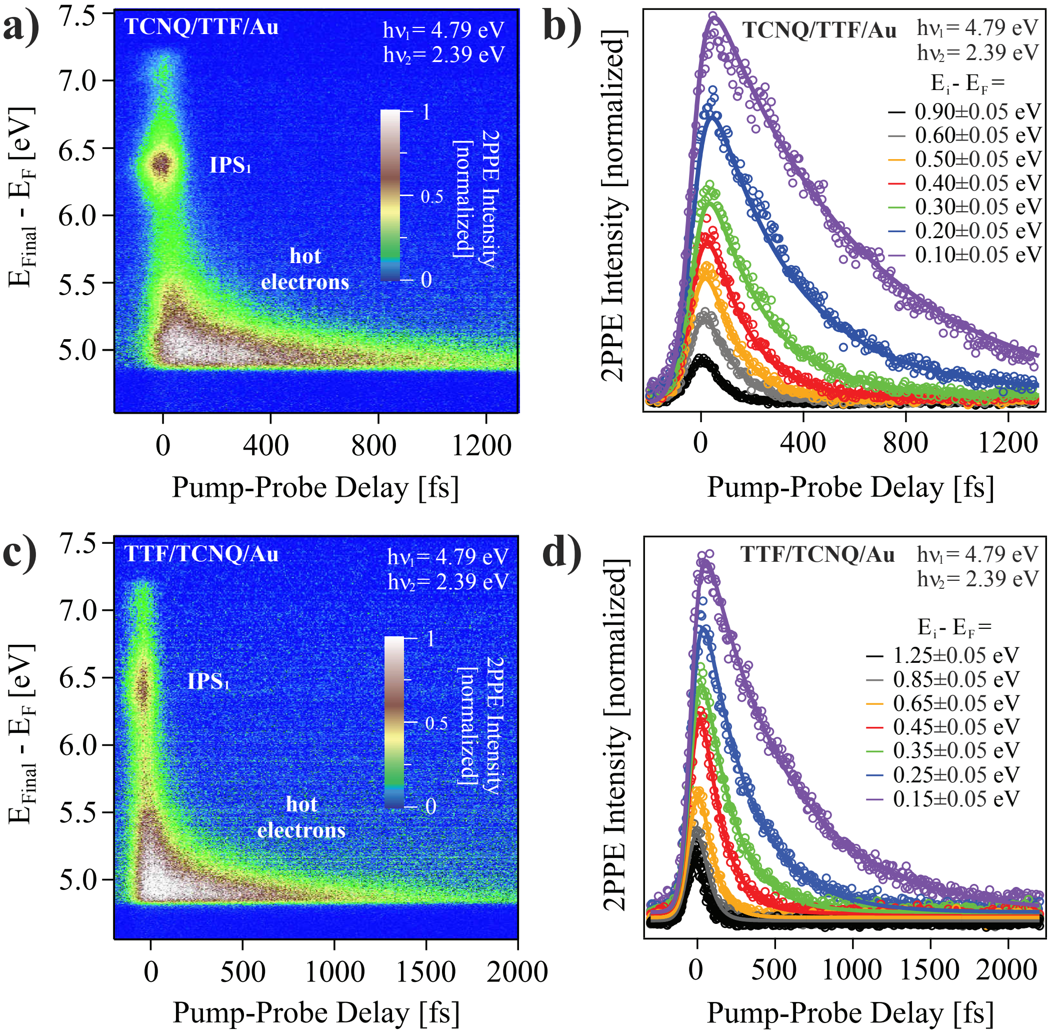

Figure 10.3.: Characterizing hot electron dynamics of a Au(111) surface covered with a mixed TTF/TCNQ layer prepared in different evaporation sequences. a) And c) visualize two-dimensional representations of TR2PPE measurements for TCNQ/TTF/Au and TTF/TCNQ/Au, respectively. b) And d) illustrate cross-correlation curves averaged for 0.1 eV intermediate state energy steps fitted by a monoexponential decay function.

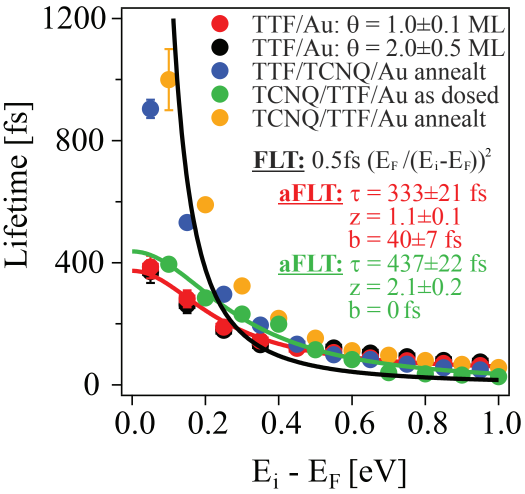

Figure 10.4: Resulting intermediate state energy-dependent lifetimes for TCNQ/TTF/Au and TTF/TCNQ/Au samples in comparison to hot electron dynamics at the TTF/Au(111) interface. Whereas hot electron dynamics at the mixed layer samples can be described by pure FLT, the hot electron lifetimes at the TTF/Au(111) interface follow the applied FLT model (equation 10.2) incorporating a second decay channel.

interface. In contrast, an intercalation of additional TCNQ molecules into the first adsorbed layer, which can be traced by TPD measurements (shown in appendix F), disturbs the well-defined geometric and electronic structure at the TTF/Au(111) interface. This electronic disorder leads to a strong increase of hot electron lifetimes especially for low intermediate state energies. The reversibility of the dosing sequence has no effect on hot electron lifetimes which can be quoted as an additional argument for increased hot electron lifetimes due to TCNQ intercalation at the TTF/Au(111) interface.

The herein presented TR2PPE results suggest an adsorbate-supported hot electron relaxation at the TTF/Au(111) interface which is characterized by hot electron lifetimes up to almost 400 fs for infinitesimal small intermediate state energies. However, these results contrast to FLT which predicts infinity lifetime for infinitesimal small intermediate state energies. The short lifetimes at the TTF/Au(111) interface can be explained by an adsorbate-induced increase of the interfacial density of occupied and unoccupied electronic states around E_F as discussed in terms of band formation in chapter 9. Especially for very low intermediate state energies ($(E_\mathrm{i} - \mathrm{E_F}) < 0.3\,\mathrm{eV}$) this increase of the interfacial DOS leads to an increased scattering rate and an increased phase space which in turn results in limited hot electron lifetimes. An intercalation of TCNQ molecules disturbs the well-defined geometric and electronic structure at the interface which results in a decrease of the adsorbate-induced interfacial DOS near E_F and consequently in an increase of hot electron lifetimes especially for low intermediate state energy.

11. Conclusion and Outlook

Within the scope of this thesis ultraviolet photoemission spectroscopy (UPS) and two-photon photoemission (2PPE) were applied to study the electronic structure of three different metal/organic interfaces. In combination the gained insights led to a detailed understanding of correlations between charge transfer, hybridization and band formation at metal/organic interfaces.

In order to ensure a reproducible preparation of these interfaces, the desorption characteristics of TCNQ, F_4TCNQ and TTF formerly evaporated on a clean Au(111) surface were preparatory studied by means of temperature-programmed desorption (TPD). These investigations gave indirect access to intermolecular and adsorbate/substrate interactions in the respective first adsorbate layer. The obtained TPD data suggest a charge transfer type interaction at the F_4TCNQ/Au(111) interface due to an observed repulsive, presumably Coulombic intermolecular interaction as it was previously reported for the TTF/Au(111) interface [94]. In contrast, there is no evidence for such an intermolecular interaction at the TCNQ/Au(111) interface which points towards neutral molecules in the first adsorbed layer.

It was the primary goal of this thesis to gain an overall picture of the electronic structure at metal/organic interfaces which feature a charge transfer type interaction. The adsorbate-induced work function changes at the TCNQ/Au(111), the F_4TCNQ/Au(111) as well as the TTF/Au(111) interface revealed, according to the integer charge transfer model, that these three metal/organic interfaces cover three possible charge states of the adsorbed molecules on a Au(111) surface: neutral (TCNQ), negatively charged (F_4TCNQ) and positively charged (TTF). In case of the F_4TCNQ/Au(111) interface this result is supported by the energetic position of a lowest unoccupied molecular orbital derived occupied electronic state below the Fermi energy which suggests an electron transfer from the metal surface into the molecule. Contrary, the TTF/Au(111) interface features a highest occupied molecular orbital derived electronic state directly at the Fermi energy which indicates an electron transfer from the adsorbate into the gold substrate. For both, F_4TCNQ/Au(111) and TTF/Au(111), energy-resolved and coverage-dependent 2PPE data point towards possible hybridization between metal bands and molecular electronic states, whereas in first instance, the electronic structure of the TCNQ/Au(111) interface displays no indications for a charge transfer type interaction. However, 2PPE investigations revealed photo-induced spectral changes at the TCNQ/Au(111) interface which indicate a photo-induced charge transfer type interaction at this interface as well. Its characterization using the photo-induced work function increase as measure suggests an image potential assisted population of the anion state and a temperature-dependent back transfer to the initial state. Presumably, the anionic molecule state is stabilized due to the strong electron accepting nature of TCNQ.

In advance of investigating the electronic structure of the F_4TCNQ/Au(111) interface, low-energy electron diffraction (LEED) demonstrate epitaxial F_4TCNQ growth. 2PPE measurements showed that this epitaxial film growth is accompanied by a coverage-independent electronic structure but also by a coverage-dependent work function change. The asymptotic work function evolution for film thicknesses above one monolayer can be assigned to the formation of a space charge region. Presumably, it is generated by a specific amount of F_4TCNQ anions which are formed due to the transport of electrons from the F_4TCNQ/Au(111) interface also to higher adsorbate layers. Therefore the driving force for this observation might be efficient charge transport to higher lying adsorbate layers due to the very high electron affinity of F_4TCNQ molecules which is supported by a well-ordered molecular structure and a small-dimensioned primitive unit cell. In this context, subsequent angle-resolved two-photon photoemission (AR2PPE) measurements substantiate efficient charge transport in epitaxial F_4TCNQ films by the observation of intermolecular hybridization and band formation.

In the course of this thesis angle-resolved photoemission (ARPES) and AR2PPE exposed band formation and thus charge carrier delocalization parallel to the surface at both, the F_4TCNQ/Au(111) as well as the TTF/Au(111) interface. Whereas the latter one is characterized by three interfacial hybrid bands which are only observed directly at the metal/organic interface, the F_4TCNQ/Au(111) interface constitutes the first metal/organic hybrid interface at which both, interfacial hybrid states and intermolecular hybrid states, can be simultaneously observed. Moreover, all experimentally observed dispersions do not match the characteristic effective mass of the Shockley surface state (SS) of the Au(111) surface. Up to date PTCDA/Ag(110) and NTCDA/Ag(110), respectively, are the only metal/organic interfaces in which the dispersion of hybrid bands is not equal to the dispersion of the metal substrate's SS. The herein presented results strongly suggest a correlation between hybridization, band formation and charge transfer at metal/organic interfaces. Generally, interfacial hybridization implies a redistribution of the interfacial charge carrier density which in case of band formation is delocalized at least parallel to the surface. Additionally, the hybridization induced charge carrier redistribution in combination with hybrid bands crossing the Fermi energy presumably determines the transferred amount of charge at the interface. Therefore charge transfer may prospectively serve as sufficient prerequisite to observe underlying hybridization and/or band formation at well-ordered metal/organic interfaces.

The last part of this thesis deals with hot electron dynamics of adsorbate-covered Au(111) surfaces. Time-resolved two-photon photoemission (TR2PPE) data display hot electron relaxation at the TTF/Au(111) interface with lifetimes of up to 400 fs for infinitesimal intermediate state energies, whereas a TTF/TCNQ mixed layer adsorbed on Au(111) features hot electron lifetimes up to 1000 fs in agreement with Fermi liquid theory (FLT). Especially for low intermediate state energies the ultrashort electron lifetimes at the TTF/Au(111) interface can be explained by a reduced phase space which is provoked by the adsorbate-induced interfacial density of electronic states around the Fermi energy. An intercalation of TCNQ molecules disturbs this well-defined interfacial electronic structure which therefore leads to an increase of hot electron lifetimes. Consequently, this thesis also demonstrates the impact of interfacial hybridization on hot electron lifetimes at metal/organic interfaces.

Prospectively, the herein presented results may lead to subsequent fundamental insights into the impact of the electronic structure at metal/organic interfaces on organic (opto)electronic device functionalities and performances. For instance, the prevalent application of F_4TCNQ as hole injection layer on gold electrodes has to be discussed from now on in terms of interfacial hybridization, band formation and charge transfer. In this context, subsequent studies at organic electronic devices with well-defined metal/organic interfaces would substantiate the gained fundamental conclusions. Similarly, the photo-induced charge transfer at the TCNQ/Au(111) interface might be tested to be applicable as UV-radiation sensitive organic electronic device. In future, the herein achieved detailed understanding of correlations between charge transfer, band formation and hot electron lifetimes at well-defined metal/organic interfaces can be used to choose and prepare appropriate metal/organic interfaces for the study of interfacial hybridization, band formation, charge transfer and adsorbate-supported hot electron lifetimes.

A. List of Acronyms

1C	one color
1C-2PPE	one color two-photon photoemission
1C-PES	one color photon energy series
2C	two color
2C-2PPE	two color two-photon photoemission
2C-PES	two color photon energy series
2D	two-dimensional
2PPE	two-photon photoemission
3D	three-dimensional
aFLT	applied Landau theory of Fermi liquids
AR2PPE	angle-resolved two-photon photoemission
ARPES	angle-resolved photoemission spectroscopy
BBO	beta-barium-borate
CBM	conduction band minimum
CNL	charge neutrality level
CTC	charge transfer complex
CW	continious wave
DFT	density functional theory
DOS	density of states
EA	electron affinity
ELA	energy level alignment
F_2TCNQ	difluoro-tetracyanoquinodimethane
F_4TCNQ	tetrafluoro-tetracyanoquinodimethane
fcc	face-centered cubic
FE	Fermi edge
FLA	Fermi level alignment
FLT	Landau theory of Fermi liquids
FWHM	full width at half maximum
HCT	hybrid charge transfer
HOMO	highest occupied molecular orbital
HREELS	high-resolution electron energy loss spectroscopy
ICT	integer charge transfer

IP	ionization potential
IPS	image potential state
IR	infrared
IS	interface state
LEED	low-energy electron diffraction
LUMO	lowest unoccupied molecular orbital
ML	monolayer
NTCDA	naphthalene-tetracarboxylic dianhydride
OLED	organic light emitting diode
OPA	optical parametric amplifier
PES	photoemission spectroscopy
PTCDA	perylenetetracarboxylic dianhydride
QMS	quadrupol mass spectrometer
RGA	residual gas analysis
SE	secondary edge
SS	Shockley surface state
STM	scanning tunneling microscope
STS	scanning tunneling spectroscopy
TCNQ	tetracyanoquinodimethane
TOF	time-of-flight spectrometer
TPD	temperature-programmed desorption
TR2PPE	time-resolved two-photon photoemission
TTF	tetrathiafulvalene
UHV	ultra-high vacuum
UMO	unoccupied molecular orbital
UPS	ultraviolet photoemission spectroscopy
UV	ultraviolet
VLA	vacuum level alignment
XPS	x-ray photoemission spectroscopy

B. Residual Gas Analysis

A residual gas analysis (RGA) is a common tool to study the chemical composition of the residual gas in a UHV-chamber. For this purpose a mass spectrometer (*Balzers QMG 112A*) is used to record a fragmentation pattern with ranging mass-to-charge ratios from 0 to 200 amu. The residual gas in the applied UHV-chamber contains typical air composites like N_2, CO_2 and H_2O as shown in figure B.1a. Moreover, there is no significant signal for $^{m}/_{z} > 50$ amu which demonstrates the cleanliness of the apparatus. Only a negligible contamination with chlorine is noted which in this special case originates from the previous evaporation of chlorine-containing molecules.
During the thermal evaporation of organic molecules RGA is used to determine detectable molecular fragments for subsequent TPD (spectroscopy) investigations. Generally, the detection process in QMS requires the ionization of molecules which may lead to dissociation into small molecular fragments and consequently to a characteristic fragmentation pattern. For all herein introduced molecules the molar mass is above 200 $^{g}/_{mol}$ which is the upper limit of the applied QMS detection range. Therefore the singly ionized intact molecules $TCNQ^+$, F_4TCNQ^+ and TTF^+ can not be observed in this thesis. Compared to the fragmentation pattern of the residual gas in the UHV-chamber (without evaporation), the illustrated patterns during the evaporation of TCNQ, F_4TCNQ and TTF display various additional mass intensities as shown in figure B.1. These additional mass intensities can be assigned to molecular fragments listed in table B.1.

The following mass-to-charge ratios were chosen for a subsequent TPD analysis: $^{m}/_{z} = 178$ amu for TCNQ, $^{m}/_{z} = 31$ amu for F_4TCNQ and $^{m}/_{z} = 58$ amu for TTF. As long as the mass fragments in RGA, while evaporation and in TPD spectroscopy, coincidence, it is common to assume the desorption of intact molecules from the surface. This can be confirmed by 2PPE measurements of the underlying metal surface after desorption of molecules as shown in chapter 6.

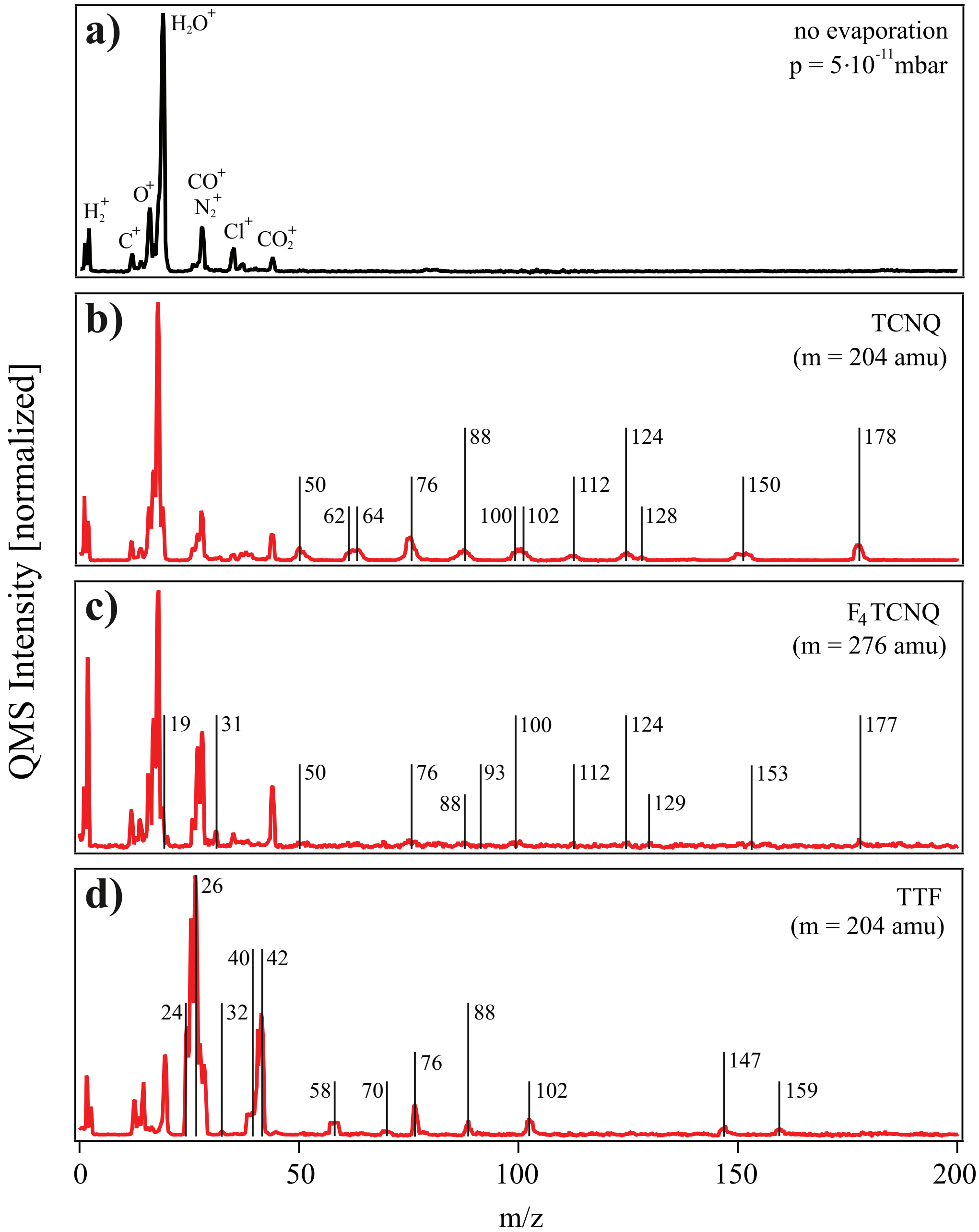

Figure B.1.: Residual gas analysis while evaporation delivers fragmentation pattern of TCNQ b), F_4TCNQ c) and TTF d) which can be compared to the residual gas in the UHV-chamber without evaporation a). The applied mass spectrometer allows the detection of several molecular fragments up to 200 amu in each case. An possible assignment of observed fragments is shown in table B.1.

	fragment mass [amu]	**chemical assignment**
TCNQ	50	C_3N^+
($C_{12}N_4H_4$)	62	C_4N^+
m = 204 amu	64	$C_3N_2^+$
	76	$C_4N_2^+$, $C_6H_4^+$
	88	$C_5N_2^+$, $C_7H_4^+$
	102	$TCNQ^{++}$, $C_7NH_4^+$
	112	$C_9H_4^+$
	124	$C_{10}H_4^+$
	128	$C_9NH_4^+$
	150	$C_{10}N_2H_4^+$
	178	$C_{11}N_3H_4^+$
F_4TCNQ	19	F^+
($C_{12}N_4F_4$)	31	CF^+
m = 276 amu	50	C_3N^+
	76	$C_4N_2^+$
	88	$C_5N_2^+$
	93	C_5NF^+
	100	$C_6N_2^+$
	112	$C_7N_2^+$
	124	$C_8N_2^+$
	129	$C_6F_3^+$
	153	$C_8F_3^+$
	177	$C_{10}F_3^+$
TTF	24	C_2^+
($C_6S_4H_4$)	26	$C_2H_2^+$
m = 204 amu	32	S^+
	40	C_2O^+
	42	$C_2H_2O^+$
	58	$C_2SH_2^+$
	70	$C_3SH_2^+$
	76	CS_2^+
	88	$C_2S_2^+$
	102	TTF^{++}, $C_3S_2H_2^+$
	147	$C_4S_3H_3^+$
	159	$C_5S_3H_3^+$

Table B.1.: A residual gas analysis delivers detectable molecule fragment masses while evaporation of TCNQ, F_4TCNQ and TTF. These masses can be possibly assigned to the here listed molecule fragments.

C. Illuminating the TCNQ/Au(111) Interface with an External Laser Source

In chapter 7, presented results strongly indicate a photo-induced interfacial charge transfer type interaction at the TCNQ/Au(111) interface. Unfortunately the spot-size in 2PPE measurements is very low (see section 3.3) which prevents the investigation of photo-induced modifications using TPD. In order to overcome this difficulty an upscaling was tried using an external laser source (Surelite II, Continuum, USA) borrowed from the research group of Prof. Petra Panak[1]. Its photon energy and output power ($h\nu_2 = 4.66\,\mathrm{eV}$, $P = 6.5 \pm 0.5\,\mathrm{mW}$) matches the specifications of the applied 2PPE setup. In compliance with a photon energy dependent series of illumination experiments discussed in chapter 7 a higher photon energy about 5 eV would be great for pursuing upscaling attempts. In order to achieve upscaling using this available light source, the illumination spot of the external laser beam was chosen to have a larger diameter than the measurement spot for 2PPE which in the end led to a low photon dose per time interval (approximately twenty times lower than in respective 2PPE experiments). Using a photon energy of 4.13 eV for 2PPE measurements ($h\nu_1$) which is not sufficient to trigger a photo-induced charge transfer at the TCNQ/Au(111) interface enables the possibility to study the influence of irradiation with the external laser source by means of 2PPE. Figure C.1 illustrates the photo-induced work function change of the TCNQ/Au(111) interface as a function of illumination time with the external laser. Due to the low photon dose per time interval, illumination for several minutes induces a small work function change. However, a saturated photo-induced work function change, as achieved via illumination series using 2PPE (see chapter 7), was not approachable. Nevertheless, subsequent annealing steps revealed a full reversibility of photo-induced spectral modifications which in accordance to 2PPE investigations can be traced back to the identical

---

[1] Prof. Petra Panak, Radiochemistry Research Group, Physikalisch-Chemisches Institut, Ruprecht-Karls-Universität Heidelberg

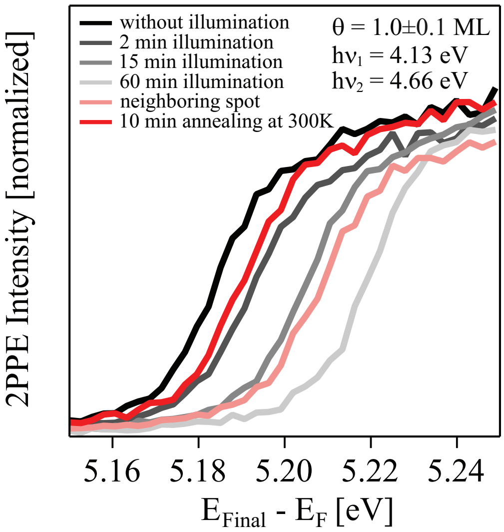

Figure C.1: Illuminating the TCNQ/Au(111) interface with an external laser source ($h\nu = 4.66\,\mathrm{eV}$) leads to identical photo-induced spectral changes as observed by means of 2PPE as they were presented in chapter 7. However the photon dose for illumination in this experiment is comparably low which results in higher illumination times to visualize a photo-induced charge transfer at the TCNQ/Au(111) interface. A subsequent annealing demonstrates the full thermal reversibility.

physical process: a photo-induced charge transfer at the TCNQ/Au(111) interface. In summary, two important findings can be derived from this additional illumination experiment with an external laser source. First to mention, it was possible to upscale the photo-induced modifications which enables subsequent experiments via TPD, STM or HREELS. A second conclusion can be driven from the fact that the applied external laser source features pulses in the nanosecond range, whereas 2PPE was performed using femtosecond laser pulses. As both light sources cause a photo-induced charge transfer at the TCNQ/Au(111) interface with comparable photon doses a non-linear optical process for its stimulation can be excluded. Consequently, the photo-induced charge transfer at the TCNQ/Au(111) interface is a single photon triggered process.

D. Monochromatic 2PPE Spectra of the F$_4$TCNQ/Au(111) Interface for Submonolayer Coverages

During he discussion of the coverage-dependent work function change in epitaxial F$_4$TCNQ films grown on Au(111) surfaces in chapter 8, a linear work function decrease for increasing submonolayer coverage was visualized. This slight linear work function decrease (from 5.50 ± 0.02 eV to 5.35 ± 0.02 eV) was assigned to an interplay between Pauli-repulsion and charge transfer induced interface dipole. The latter one entails an intermolecular repulsive interaction in full conformance with TPD results in the submonolayer regime (discussed in section 5.2). As a consequence a gradual decrease in the average interspace between the adsorbed molecules should be involved for increasing submonolayer coverage. This appendix illustrates 2PPE data for different submonolayer coverages in figure D.1 to demonstrate the evolution of 2PPE features up to 1 ML coverage. 2PPE signatures which were assigned to adsorbate-induced electronic states like FS, UMO$_1$ and UMO$_2$ experience an intensity increase

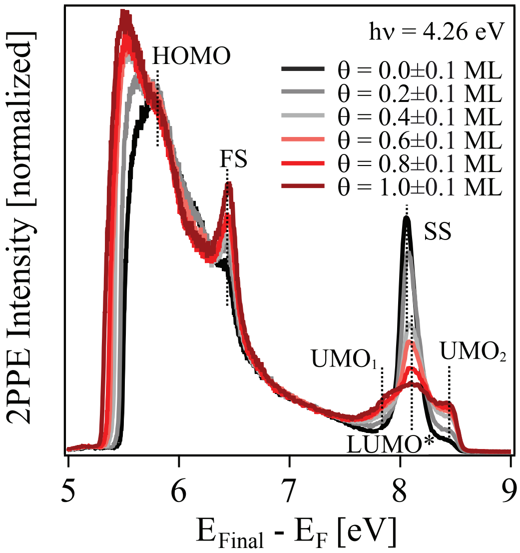

Figure D.1: 2PPE spectra of the F$_4$TCNQ/Au(111) interface for increasing submonolayer coverage. While the work function decreases with increasing coverage molecule-induced electronic states rise in intensity and the Au(111)-derived SS gets quenched.

with increasing coverage, whereas the Au(111)-derived SS gets quenched up to a coverage of 1 ML. Both evolutions can be assigned to an increasing number of adsorbed F_4TCNQ molecules on the Au(111) substrate which implies an increasing molecule packing density and intensity of electronic states. Therefore the gradual quenching of SS and the intensity increase of molecule-induced 2PPE features indicate a gradual interspace-reduction between the adsorbed molecules. This argumentation is consistent with the noticed intermolecular repulsive interaction of adsorbed molecules directly at the interface which was concluded from TPD results in the submonolayer regime and from the linearity of the adsorbate-induced work function decrease for increasing submonolayer coverage.

E. Fitting Electronic State Dispersions at the F_4TCNQ/Au(111) Interface

This appendix illustrates the detailed fitting results of monochromatic AR2PPE data at 4.01 eV photon energy for the F_4TCNQ/Au(111) interface at full monolayer coverage. Fitting was applied to 32 2PPE spectra taken at different polar angles between 21° and -10° in the spectral range between 7.0 eV and 7.9 eV. The procedure contains two Gaussians of variable width, intensity and energetic position which can be assigned to LUMO* and UMO_1. Figure E.1 displays nine exemplarily 2PPE spectra taken at different polar angles (black lines). The total fit including a linear background and the two Gaussians is represented in red, whereas the two single Gaussians used in the fitting procedure are shown in dark blue (peak width $\omega_1 \approx 0.2$ eV) and light blue (peak width $\omega_2 \approx 0.1$ eV). The angle-dependent energetic positions of both electronic states in the displayed 2PPE spectra demonstrate band formation at the F_4TCNQ/Au(111) interface which also entails the decrease of electronic state intensities for higher polar angles due to an almost resonant excitation around 0°. The peak positions from this fitting were used to visualize the dispersion of LUMO* and UMO_1 directly at the F_4TCNQ/Au(111) interface in chapter 9.

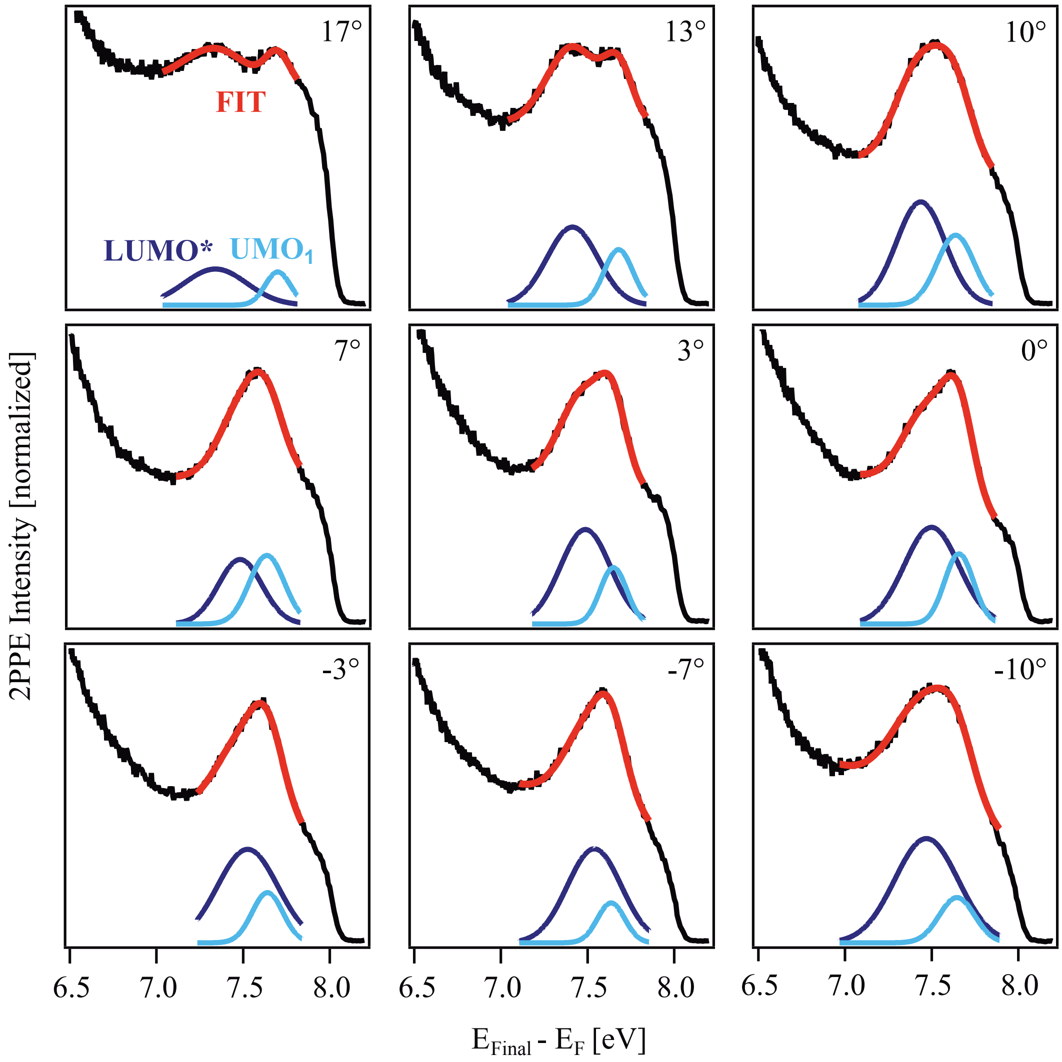

Figure E.1.: Detailed results from fitting AR2PPE data (monochromatic, hν = 4.01 eV, θ = 1 ML) of the $F_4TCNQ/Au(111)$ interface. Fits (in red) contain two Gaussians of constant width which can be assigned to LUMO* (dark blue) and UMO$_1$ (light blue). The peak positions from this fitting were used to visualize the dispersion of LUMO* and UMO$_1$ directly at the $F_4TCNQ/Au(111)$ interface in chapter 9.

F. Investigating the Electronic Structure in a TTF/TCNQ Mixed Layer on Au(111)

TTF/TCNQ mixed layers adsorbed on Au(111) are investigated with special view on their hot electron dynamics in chapter 10. This appendix contains a description of their preparation and a compact view on their electronic structure. Figure F.1 illustrates TPD measurements during the preparation procedure which consists of two evaporation and annealing steps each.

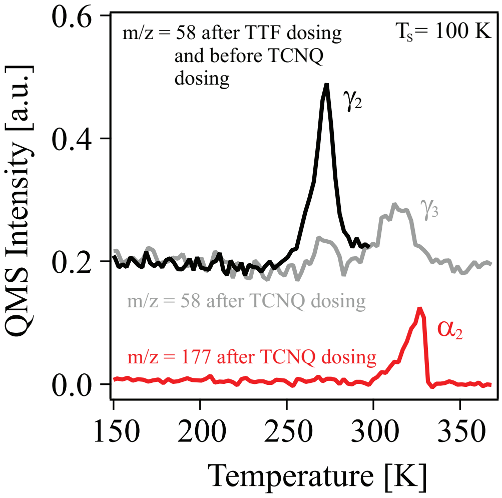

Figure F.1: TPD measurements tracing the mixed layer formation of TCNQ/TTF/Au. After TTF evaporation and annealing up to 300 K molecules from higher layers desorb (γ_2) which results in a well-defined TTF/Au(111) interface of 1 ML coverage. Subsequent TCNQ adsorption and annealing to 370 K leads to TCNQ intercalation into the TTF monolayer which can be concluded from TTF desorption of the monolayer (γ_3) accompanied by TCNQ desorption from higher layers (α_2).

First, TTF molecules are dosed on a clean Au(111) surface held at $T_S = 100$ K which afterwards is heated to 300 K in order to thermally desorb TTF molecules which are not in direct contact with the Au(111) substrate. The desorption of these TTF molecules in higher lying layers can be traced by TPD as visualized in figure F.1 (black data). In combination this first evaporation and annealing step leads to a coverage of 1 ML TTF. Subsequent TCNQ evaporation leads to the adsorption of TCNQ molecules onto this TTF/Au(111) interface held at $T_S = 100$ K. At first glance an intercalation of TCNQ molecules into the TTF monolayer can be excluded from the fact that the TCNQ adsorption onto a TTF-covered Au(111) held at $T_S = 100\,K$ only moderately affects the hot electron dynamics of the underlying TTF/Au(111) interface as proven by TR2PPE data shown in figure F.2a and further on evaluated using an aFLT fit as depicted in figure F.3 (green line).

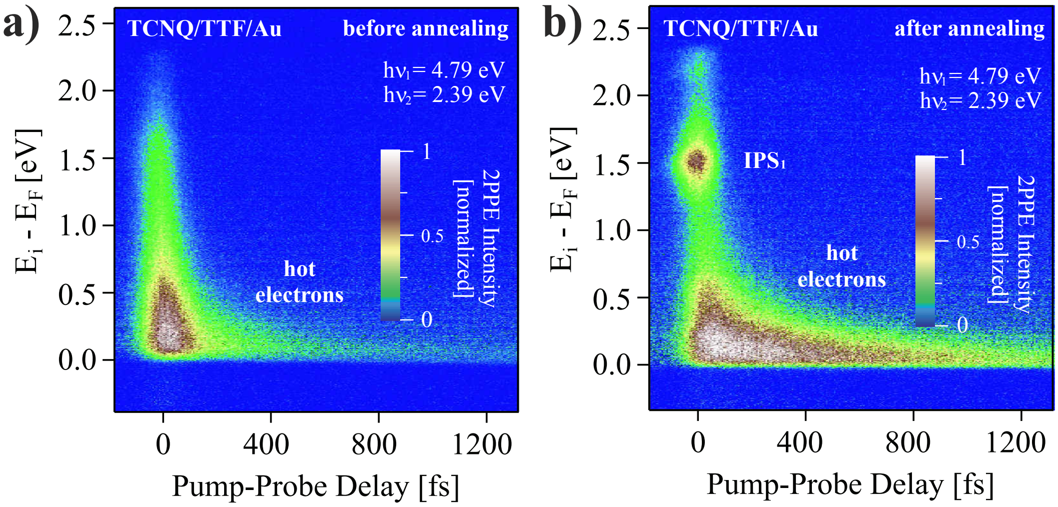

Figure F.2.: Two-dimensional representations of TR2PPE measurements for a TCNQ-covered TTF/Au(111) interface with 1 ML coverage before a) and after the second annealing step (up to 370 K) b).

According to this fit, the maximum lifetime of photo-excited hot electrons at infinitesimal intermediate state energy is 437 ± 22 fs. A subsequent annealing step to 370 K, which was originally performed to desorb TCNQ molecules from higher lying layers, leads to the desorption of TCNQ molecules and non-surface-bound TTF molecules as it can be traced by TPD measurements (see figure F.2 gray and red data). From this observation a thermally induced intercalation of TCNQ molecules into the TTF monolayer on Au(111) has to be considered as in turn TTF molecules desorb from the former monolayer (desorption peak γ_3). Conclusively after the second evaporation and annealing sequence the Au(111) surface is presumably covered by a mixed layer of TTF and TCNQ molecules. However, this TCNQ intercalation disturbs the well-defined electronic structure at the TTF/Au(111) interface as discussed in chapter 10. As this well-defined interfacial electronic structure is the prerequisite argument for ultrafast hot electron dynamics at the TTF/Au(111) interface, hot electron lifetimes get increased due to TCNQ intercalation as shown by TR2PPE data in figure F.2b. According to Fermi liquid theory, TCNQ intercalation consequently increases hot electron lifetimes for infinitesimal intermediate state energies up to about 1000 fs as visualized in figure F.3. Interestingly, comparable hot electron life-

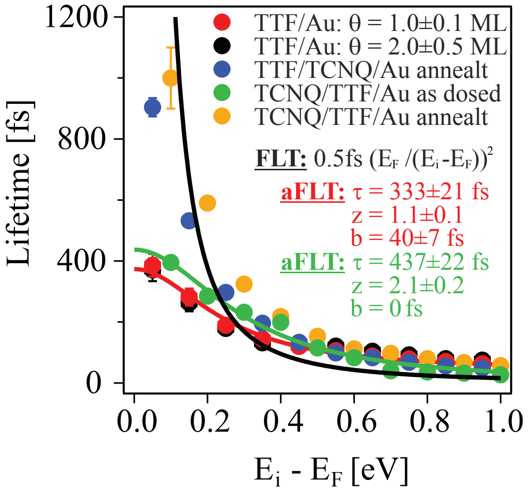

Figure F.3: Resulting intermediate state energy dependent lifetimes for TCNQ/TTF/Au (before and after the second annealing step up to 370 K) and TTF/TCNQ/Au samples in comparison to hot electron dynamics at the TTF/Au(111) interface.

times can be achieved for a TCNQ/Au(111) sample with intercalated TTF molecules by inverting the evaporation and annealing sequence.

In order to further study the electronic structure of these mixed layer interfaces in more depth, dichromatic 2PPE spectra for different photon energies are shown in figure F.4. Both mixed layer samples (TCNQ/TTF/Au andTTF/TCNQ/Au) feature comparable work function values of 4.80 ± 0.10 eV. Moreover, dichromatic 2PPE spectra display two photoemission features which can be assigned to unoccupied image potential states (IPS$_1$ and IPS$_2$) energetically located around 0.85 ± 0.12 eV below the vacuum energy according to photon-energy dependent data (see figure F.4c). AR2PPE results additionally support this assignment due to exposing a free electron-like dispersion of IPS$_1$ for both mixed layer interfaces.

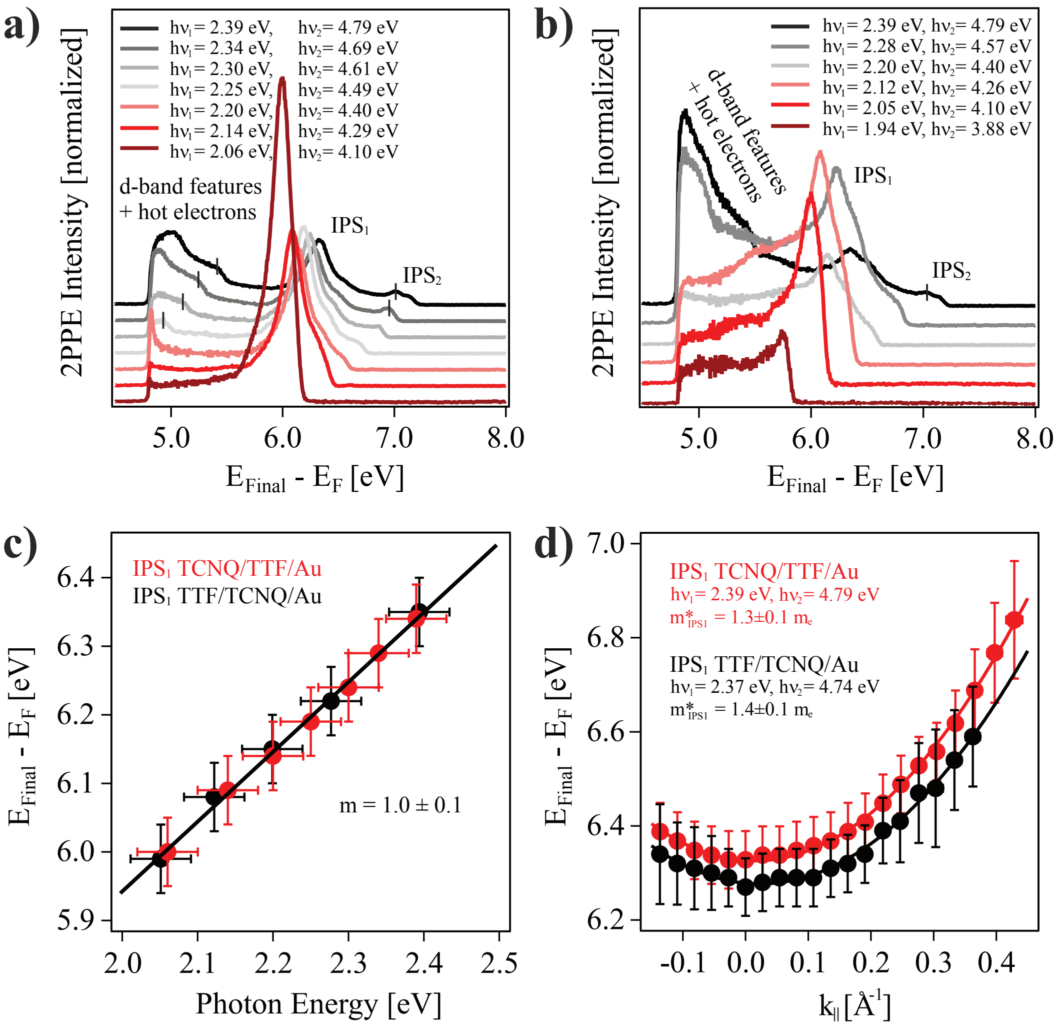

Figure F.4.: 2PPE spectroscopy study of TCNQ/TTF/Au and TTF/TCNQ/Au samples, prepared as described in chapter 10. a) Dichromatic 2PPE data of the TCNQ/TTF/Au sample as well as of the TTF/TCNQ/Au sample b) display two photoemission features which can be assigned to image potential states (IPS_1 and IPS_2) according to photon-energy-dependent data shown in c). d) AR2PPE data unveil the free electron-like dispersion of IPS_1 for both mixed layer interfaces.

Bibliography

[1] S. R. Forrest. The path to ubiquitous and low-cost organic electronic appliances on plastic. *Nature*, 428(6986):911–918, 2004.

[2] L. Zhou, A. Wanga, S.-C. Wu, J. Sun, S. Park, and T. N. Jackson. All-organic active matrix flexible display. *Applied Physics Letters*, 88(8), 2006.

[3] T. Sekitani, H. Nakajima, H. Maeda, T. Fukushima, T. Aida, K. Hata, and T. Someya. Stretchable active-matrix organic light-emitting diode display using printable elastic conductors. *Nature Materials*, 8(6):494–499, 2009.

[4] S. Reineke, F. Lindner, G. Schwartz, N. Seidler, K. Walzer, B. Lüssem, and K. Leo. White organic light-emitting diodes with fluorescent tube efficiency. *Nature*, 459(7244):234–238, 2009.

[5] C. W. Tang and S. A. VanSlyke. Organic electroluminescent diodes. *Applied Physics Letters*, 51(12):913–915, 1987.

[6] J. H. Burroughes, D. D. C. Bradley, A. R. Brown, R. N. Marks, K. Mackay, R. H. Friend, P. L. Burns, and A. B. Holmes. Light-emitting diodes based on conjugated polymers. *Nature*, 347(6293):539–541, 1990.

[7] M. A. Baldo, D. F. O'Brien, Y. You, A. Shoustikov, S. Sibley, M. E. Thompson, and S. R. Forrest. Highly efficient phosphorescent emission from organic electroluminescent devices. *Nature*, 395(6698):151–154, 1998.

[8] H. Sirringhaus, N. Tessler, and R. H. Friend. Integrated optoelectronic devices based on conjugated polymers. *Science*, 280(5370):1741–1744, 1998.

[9] R. H. Friend, R. W. Gymer, A. B. Holmes, J. H. Burroughes, R. N. Marks, C. Taliani, D. D. C. Bradley, D. A. Dos Santos, J.-L. Brédas, M. Logdlund, and W. R. Salaneck. Electroluminescence in conjugated polymers. *Nature*, 397(6715):121–128, 1999.

[10] B. W. D'Andrade and S. R. Forrest. White organic light-emitting devices for solid-state lighting. *Advanced Materials*, 16(18):1585–1595, 2004.

[11] Z. B. Wang, M. G. Helander, J. Qiu, D. P. Puzzo, M. T. Greiner, Z. M. Hudson, S. Wang, Z. W. Liu, and Z. H. Lu. Unlocking the full potential of organic light-emitting diodes on flexible plastic. *Nature Photonics*, 5(12):753–757, 2011.

[12] J. Lee, H.-F. Chen, T. Batagoda, C. Coburn, P. I. Djurovich, M. E. Thompson, and S. R. Forrest. Deep blue phosphorescent organic light-emitting diodes with very high brightness and efficiency. *Nature Materials*, 15(1):92–98, 2016.

[13] G. A. Chamberlain. Organic solar cells: A review. *Solar Cells*, 8(1):47–83, 1983.

[14] C. W. Tang. Two-layer organic photovoltaic cell. *Applied Physics Letters*, 48(2):183–185, 1986.

[15] D. Wöhrle and D. Meissner. Organic solar cells. *Advanced Materials*, 3(3):129–138, 1991.

[16] C. J. Brabec, N. S. Sariciftci, and J. C. Hummelen. Plastic solar cells. *Advanced Functional Materials*, 11(1):15–26, 2001.

[17] H. Hoppe and N. S. Sariciftci. Organic solar cells: An overview. *Journal of Materials Research*, 19:1924–1945, 2004.

[18] S. Günes, H. Neugebauer, and N. S. Sariciftci. Conjugated polymer-based organic solar cells. *Chemical Reviews*, 107(4):1324–1338, 2007. PMID: 17428026.

[19] G. Li, R. Zhu, and Y. Yang. Polymer solar cells. *Nature Photonics*, 6(3):153–161, 2012.

[20] Z. He, C. Zhong, S. Su, M. Xu, H. Wu, and Y. Cao. Enhanced power-conversion efficiency in polymer solar cells using an inverted device structure. *Nature Photonics*, 6(9):591–595, 2012.

[21] L. Li, F. Zhang, J. Wang, Q. An, Q. Sun, W. Wang, J. Zhang, and F. Teng. Achieving EQE of 16,7% in P3HT:PC71BM based photodetectors by trap-assisted photomultiplication. *Scientific reports*, 5, 2015.

[22] D. M. DeLongchamp. Organic photovoltaics. In *Semiconductor Materials for Solar Photovoltaic Cells*, pages 169–196. Springer, 2016.

[23] A. Dodabalapur, L. Torsi, and H. E. Katz. Organic transistors: Two-dimensional transport and improved electrical characteristics. *Science*, 268(5208):270–271, 1995.

[24] G. Horowitz. Organic field-effect transistors. *Advanced Materials*, 10(5):365–377, 1998.

[25] C. D. Dimitrakopoulos and D. J. Mascaro. Organic thin-film transistors: A review of recent advances. *IBM Journal of Research and Development*, 45(1):11–27, 2001.

[26] H. Sirringhaus. Device physics of solution-processed organic field-effect transistors. *Advanced Materials*, 17(20):2411–2425, 2005.

[27] T. Sekitani, U. Zschieschang, H. Klauk, and T. Someya. Flexible organic transistors and circuits with extreme bending stability. *Nature Materials*, 9(12):1015–1022, 2010.

[28] L. Torsi, M. Magliulo, K. Manoli, and G. Palazzo. Organic field-effect transistor sensors: a tutorial review. *Chemical Society Reviews*, 42:8612–8628, 2013.

[29] B. H. Cumpston, S. P. Ananthavel, S. Barlow, D. L. Dyer, J. E. Ehrlich, L. L. Erskine, A. A. Heikal, S. M. Kuebler, I.-Y. S. Lee, D. McCord-Maughon, J. Qin, H. Röckel, X.-L. Rumi, M.and Wu, S. R. Marder, and J. W. Perry. Two-photon polymerization initiators for three-dimensional optical data storage and microfabrication. *Nature*, 398(6722):51–54, 1999.

[30] L. P. Ma, J. Liu, and Y. Yang. Organic electrical bistable devices and rewritable memory cells. *Applied Physics Letters*, 80(16):2997–2999, 2002.

[31] S. Möller, C. Perlov, W. Jackson, C. Taussig, and S. R. Forrest. A polymer/semiconductor write-once read-many-times memory. *Nature*, 426(6963):166–169, 2003.

[32] C. W. Chu, J. Ouyang, J.-H. Tseng, and Y. Yang. Organic donor-acceptor system exhibiting electrical bistability for use in memory devices. *Advanced Materials*, 17(11):1440–1443, 2005.

[33] Y. Guo, C. Di, S. Ye, X. Sun, J. Zheng, Y. Wen, W. Wu, G. Yu, and Y. Liu. Multibit storage of organic thin-film field-effect transistors. *Advanced Materials*, 21(19):1954–1959, 2009.

[34] A. F. Garito and A. J. Heeger. Design and synthesis of organic metals. *Accounts of Chemical Research*, 7(7):232–240, 1974.

[35] J. M. Tour. Molecular electronics. synthesis and testing of components. *Accounts of Chemical Research*, 33(11):791–804, 2000.

[36] J. E. Anthony. The larger acenes: Versatile organic semiconductors. *Angewandte Chemie International Edition*, 47(3):452–483, 2008.

[37] W. Wu, Y. Liu, and D. Zhu. π-conjugated molecules with fused rings for organic field-effect transistors: design, synthesis and applications. *Chemical Society Reviews*, 39:1489–1502, 2010.

[38] A. Mishra and P. Bäuerle. Small molecule organic semiconductors on the move: Promises for future solar energy technology. *Angewandte Chemie International Edition*, 51(9):2020–2067, 2012.

[39] A. B. Kaiser. Electronic transport properties of conducting polymers and carbon nanotubes. *Reports on Progress in Physics*, 64(1):1, 2001.

[40] N. Karl. Charge carrier transport in organic semiconductors. *Synthetic Metals*, 133–134:649–657, 2003. Proceedings of the Yamada Conference LVI. The Fourth International Symposium on Crystalline Organic Metals, Superconductors and Ferromagnets (ISCOM 2001).

[41] K. Walzer, B. Maennig, M. Pfeiffer, and K. Leo. Highly efficient organic devices based on electrically doped transport layers. *Chemical Reviews*, 107(4):1233–1271, 2007. PMID: 17385929.

[42] V. Coropceanu, J. Cornil, D. A. da Silva Filho, Y. Olivier, R. Silbey, and J.-L. Brédas. Charge transport in organic semiconductors. *Chemical Reviews*, 107(4):926–952, 2007. PMID: 17378615.

[43] B. Lüssem, C.-M. Keum, D. Kasemann, B. Naab, Z. Bao, and K. Leo. Doped organic transistors. *Chemical Reviews*, 116(22):13714–13751, 2016.

[44] H. Ishii, K. Sugiyama, E. Ito, and K. Seki. Energy level alignment and interfacial electronic structures at organic/metal and organic/organic interfaces. *Advanced Materials*, 11(8):605–625, 1999.

[45] X. Zhou, J. Blochwitz, M. Pfeiffer, A. Nollau, T. Fritz, and K. Leo. Enhanced hole injection into amorphous hole-transport layers of organic light-emitting diodes using controlled p-type doping. *Advanced Functional Materials*, 11(4):310–314, 2001.

[46] J. C. Scott. Metal-organic interface and charge injection in organic electronic devices. *Journal of Vacuum Science & Technology A*, 21(3):521–531, 2003.

[47] N. Koch, S. Duhm, J. P. Rabe, A. Vollmer, and R. L. Johnson. Optimized hole injection with strong electron acceptors at organic-metal interfaces. *Physical Review Letters*, 95:237601, 2005.

[48] S. Braun, W. R. Salaneck, and M. Fahlman. Energy-level alignment at organic/metal and organic/organic interfaces. *Advanced Materials*, 21(14-15):1450–1472, 2009.

[49] C. E. Small, S.-W. Tsang, J. Kido, S. K. So, and F. So. Origin of enhanced hole injection in inverted organic devices with electron accepting interlayer. *Advanced Functional Materials*, 22(15):3261–3266, 2012.

[50] A. Kumatani, Y. Li, P. Darmawan, T. Minari, and K. Tsukagoshi. On practical charge injection at the metal/organic semiconductor interface. *Scientific Reports*, 3:1026–, 2013.

[51] M. Oehzelt, N. Koch, and G. Heimel. Organic semiconductor density of states controls the energy level alignment at electrode interfaces. *Nature Communications*, 5:4174–, 2014.

[52] D. J. Gundlach, Y. Y. Lin, T. N. Jackson, S. F. Nelson, and D. G. Schlom. Pentacene organic thin-film transistors-molecular ordering and mobility. *IEEE Electron Device Letters*, 18(3):87–89, 1997.

[53] H. Sirringhaus, P. J. Brown, R. H. Friend, M. M. Nielsen, K. Bechgaard, B. M. W. Langeveld-Voss, A. J. H. Spiering, R. A. J. Janssen, E. W. Meijer, P. Herwig, and D. M. de Leeuw. Two-dimensional charge transport in self-organized, high-mobility conjugated polymers. *Nature*, 401(6754):685–688, 1999.

[54] N. Koch. Organic electronic devices and their functional interfaces. *ChemPhysChem*, 8(10):1438–1455, 2007.

[55] Q. Bao, S. Fabiano, M. Andersson, S. Braun, Z. Sun, X. Crispin, M. Berggren, X. Liu, and M. Fahlman. Energy level bending in ultrathin polymer layers obtained through langmuir-shaefer deposition. *Advanced Functional Materials*, 26(7):1077–1084, 2016.

[56] D. Cahen, A. Kahn, and E. Umbach. Energetics of molecular interfaces. *Materials Today*, 8(7):32–41, 2005.

[57] J. Hwang, A. Wan, and A. Kahn. Energetics of metal-organic interfaces: New experiments and assessment of the field. *Materials Science and Engineering: R: Reports*, 64(1-2):1–31, 2009.

[58] S. Hasegawa, T. Mori, K. Imaeda, S. Tanaka, Y. Yamashita, H. Inokuchi, H. Fujimoto, K. Seki, and N. Ueno. Intermolecular energy-band dispersion in oriented thin films of bis(1,2,5-thiadiazolo)-p-quinobis(1,3-dithiole) by angle-resolved photoemission. *The Journal of Chemical Physics*, 100(9):6969–6973, 1994.

[59] N. Koch, A. Vollmer, I. Salzmann, B. Nickel, H. Weiss, and J. P. Rabe. Evidence for temperature-dependent electron band dispersion in pentacene. *Physical Review Letters.*, 96:156803, 2006.

[60] G. Koller, S. Berkebile, M. Oehzelt, P. Puschnig, C. Ambrosch-Draxl, F. P. Netzer, and M. G. Ramsey. Intra- and intermolecular band dispersion in an organic crystal. *Science*, 317(5836):351–355, 2007.

[61] S. Machida, Y. Nakayama, S. Duhm, Q. Xin, A. Funakoshi, N. Ogawa, S. Kera, N. Ueno, and H. Ishii. Highest-occupied-molecular-orbital band dispersion of rubrene single crystals as observed by angle-resolved ultraviolet photoelectron spectroscopy. *Physical Review Letters*, 104:156401, 2010.

[62] H. Ding, C. Reese, A. J. Mäkinen, Z. Bao, and Y. Gao. Band structure measurement of organic single crystal with angle-resolved photoemission. *Applied Physics Letters*, 96(22), 2010.

[63] N. W. Ashcroft and D. N. Mermin. *Festkörperphysik*. Oldenbourg Wissenschaftsverlag, 2012.

[64] Y. Krupskaya, M. Gibertini, N. Marzari, and A. F. Morpurgo. Band-like electron transport with record-high mobility in the TCNQ family. *Advanced Materials*, 27(15):2453–2458, 2015.

[65] H. Yamane and N. Kosugi. Systematic study on intermolecular valence-band dispersion in molecular crystalline films. *Journal of Electron Spectroscopy and Related Phenomena*, 204, Part A:61–67, 2015. Organic Electronics.

[66] R. Temirov, S. Soubatch, A. Luican, and F. S. Tautz. Free-electron-like dispersion in an organic monolayer film on a metal substrate. *Nature*, 444(7117):350–353, 2006.

[67] E. Annese, J. Fujii, C. Baldacchini, B. Zhou, C. E. Viol, I. Vobornik, M. G. Betti, and G. Rossi. Molecular charge distribution and dispersion of electronic states in the contact layer between pentacene and Cu(119) and beyond. *Physical Review B*, 77:205417, 2008.

[68] B. W. Heinrich, L. Limot, M. V. Rastei, C. Iacovita, J. P. Bucher, D. M. Djimbi, C. Massobrio, and M. Boero. Dispersion and localization of electronic states at a ferrocene/Cu(111) interface. *Physical Review Letters*, 107:216801, 2011.

[69] M. Wießner, J. Ziroff, F. Forster, M. Arita, K. Shimada, P. Puschnig, A. Schöll, and F. Reinert. Substrate-mediated band-dispersion of adsorbate molecular states. *Nature Communications*, 4:1514–, 2013.

[70] M. Marks, A. Schöll, and U. Höfer. Formation of metal-organic interface states studied with 2PPE. *Journal of Electron Spectroscopy and Related Phenomena*, 195:263–271, 2014.

[71] G. Vasseur, Y. Fagot-Revurat, M. Sicot, B. Kierren, L. Moreau, D. Malterre, L. Cardenas, L. Cardenas, J. Lipton-Duffin, F. Rosei, M. Di Giovannantonio, G. Contini, P. Le Fevre, F. Bertran, L. Liang, V. Meunier, and D. F. Perepichka. Quasi one-dimensional band dispersion and surface metallization in long-range ordered polymeric wires. *Nature Communications*, 7:–, 2016.

[72] M. Pope, H. P. Kallmann, and P. Magnante. Electroluminescence in organic crystals. *The Journal of Chemical Physics*, 38(8):2042–2043, 1963.

[73] W. Helfrich and W. G. Schneider. Recombination radiation in anthracene crystals. *Physical Review Letters*, 14:229–231, 1965.

[74] J. Ferraris, D. O. Cowan, V. Walatka, and J. H. Perlstein. Electron transfer in a new highly conducting donor-acceptor complex. *Journal of the American Chemical Society*, 95(3):948–949, 1973.

[75] L. B. Coleman, M. J. Cohen, D. J. Sandman, F. G. Yamagishi, A. F. Garito, and A. J. Heeger. Superconducting fluctuations and the peierls instability in an organic solid. *Solid State Communications*, 12(11):1125–1132, 1973.

[76] D. E. Schafer, F. Wudl, G. A. Thomas, J. P. Ferraris, and D. O. Cowan. Apparent giant conductivity peaks in an anisotropic medium: TTF-TCNQ. *Solid State Communications*, 14(4):347–351, 1974.

[77] M. J. Cohen, L. B. Coleman, A. F. Garito, and A. J. Heeger. Electrical conductivity of tetrathiofulvalinium tetracyanoquinodimethan (TTF) (TCNQ). *Physical Review B*, 10:1298–1307, 1974.

[78] H. Shirakawa, E. J. Louis, A. G. MacDiarmid, C. K. Chiang, and A. J. Heeger. Synthesis of electrically conducting organic polymers: halogen derivatives of polyacetylene, (CH). *Journal of the Chemical Society, Chemical Communications*, pages 578–580, 1977.

[79] C. K. Chiang, C. R. Fincher, Y. W. Park, A. J. Heeger, H. Shirakawa, E. J. Louis, S. C. Gau, and A. G. MacDiarmid. Electrical conductivity in doped polyacetylene. *Physical Review Letters*, 39:1098–1101, 1977.

[80] J. B. Torrance. The difference between metallic and insulating salts of tetracyanoquinodimethone (TCNQ): how to design an organic metal. *Accounts of Chemical Research*, 12(3):79–86, 1979.

[81] H. Shirakawa. The discovery of polyacetylene film: The dawning of an era of conducting polymers (nobel lecture). *Angewandte Chemie International Edition*, 40(14):2574–2580, 2001.

[82] B. Lüssem, M. Riede, and K. Leo. Doping of organic semiconductors. *physica status solidi (a)*, 210(1):9–43, 2013.

[83] I. Salzmann and G. Heimel. Toward a comprehensive understanding of molecular doping organic semiconductors (review). *Journal of Electron Spectroscopy and Related Phenomena*, 204, Part A:208–222, 2015. Organic Electronics.

[84] S. T. Lee, Y. M. Wang, X. Y. Hou, and C. W. Tang. Interfacial electronic structures in an organic light-emitting diode. *Applied Physics Letters*, 74(5):670–672, 1999.

[85] N. Koch, A. Kahn, J. Ghijsen, J.-J. Pireaux, J. Schwartz, R. L. Johnson, and A. Elschner. Conjugated organic molecules on metal versus polymer electrodes: Demonstration of a key energy level alignment mechanism. *Applied Physics Letters*, 82(1):70–72, 2003.

[86] A. Kahn, N. Koch, and W. Gao. Electronic structure and electrical properties of interfaces between metals and pi-conjugated molecular films. *Journal of Polymer Science Part B: Polymer Physics*, 41(21):2529–2548, 2003.

[87] B. de Boer, A. Hadipour, M. M. Mandoc, T. van Woudenbergh, and P. W. M. Blom. Tuning of metal work functions with self-assembled monolayers. *Advanced Materials*, 17(5):621–625, 2005.

[88] I.-H. Hong, M.-W. Lee, Y.-M. Koo, H. Jeong, T.-S. Kim, and O.-K. Song. Effective hole injection of organic light-emitting diodes by introducing buckminsterfullerene on the indium tin oxide anode. *Applied Physics Letters*, 87(6):063502, 2005.

[89] A. Crispin, X. Crispin, M. Fahlman, M. Berggren, and W. R. Salaneck. Transition between energy level alignment regimes at a low band gap polymer-electrode interfaces. *Applied Physics Letters*, 89(21):213503, 2006.

[90] S. Duhm, A. Gerlach, I. Salzmann, B. Bröker, R.L. Johnson, F. Schreiber, and N. Koch. PTCDA on Au(111), Ag(111) and Cu(111): Correlation of interface charge transfer to bonding distance. *Organic Electronics*, 9(1):111–118, 2008.

[91] C. J. Sandroff, D. A. Weitz, J. C. Chung, and D. R. Herschbach. Charge transfer from tetrathiafulvalene to silver and gold surfaces studied by surface-enhanced raman scattering. *The Journal of Physical Chemistry*, 87(12):2127–2133, 1983.

[92] J. Lu and K. P. Loh. High resolution electron energy loss spectroscopy study of zinc phthalocyanine and tetrafluoro tetracyanoquinodimethane on Au(111). *Chemical Physics Letters*, 468(1-3):28–31, 2009.

[93] T. Katayama, K. Mukai, S. Yoshimoto, and J. Yoshinobu. Thermally activated transformation from a charge-transfer state to a rehybridized state of tetrafluoro-tetracyanoquinodimethane on Cu(100). *The Journal of Physical Chemistry Letters*, 1(19):2917–2921, 2010.

[94] I. Fernández-Torrente, S. Monturet, K. J. Franke, J. Fraxedas, N. Lorente, and J. I. Pascual. Long-range repulsive interaction between molecules on a metal surface induced by charge transfer. *Physical Review Letters*, 99:176103, 2007.

[95] N. Gonzalez-Lakunza, I. Fernández-Torrente, K. J. Franke, N. Lorente, A. Arnau, and J. I. Pascual. Formation of dispersive hybrid bands at an organic-metal interface. *Physical Review Letters*, 100:156805, 2008.

[96] F. Jäckel, U. G. E. Perera, V. Iancu, K.-F. Braun, N. Koch, J. P. Rabe, and S.-W. Hla. Investigating molecular charge transfer complexes with a low temperature scanning tunneling microscope. *Physical Review Letters*, 100:126102, 2008.

[97] M. N. Faraggi, N. Jiang, N. Gonzalez-Lakunza, A. Langner, S. Stepanow, K. Kern, and A. Arnau. Bonding and charge transfer in metal-organic coordination networks on Au(111) with strong acceptor molecules. *The Journal of Physical Chemistry C*, 116(46):24558–24565, 2012.

[98] N. Abdurakhmanova, A. Floris, T.-C. Tseng, A. Comisso, S. Stepanow, A. De Vita, and K. Kern. Stereoselectivity and electrostatics in charge-transfer Mn- and Cs-TCNQ4 networks on Ag(100). *Nature Communications*, 3:940–, 2012.

[99] I. G. Hill, J. Schwartz, and A. Kahn. Metal-dependent charge transfer and chemical interaction at interfaces between 3,4,9,10-perylenetetracarboxylic bisimidazole and gold, silver and magnesium. *Organic Electronics*, 1(1):5–13, 2000.

[100] Y. Zou, L. Kilian, A. Schöll, T. Schmidt, R. Fink, and E. Umbach. Chemical bonding of PTCDA on ag surfaces and the formation of interface states. *Surface Science*, 600(6):1240–1251, 2006.

[101] S. Braun and W. R. Salaneck. Fermi level pinning at interfaces with tetrafluorotetracyanoquinodimethane (F4-TCNQ): The role of integer charge transfer states. *Chemical Physics Letters*, 438(4-6):259–262, 2007.

[102] T.-C. Tseng, C. Urban, Y. Wang, R. Otero, S. L. Tait, Manuel Alcamí, D. Écija, M. Trelka, J. M. Gallego, N. Lin, M. Konuma, U. Starke, A. Nefedov, A. Langner, C. Wöll, M. Á. Herranz, Fernando Martín, Nazario Martín, K. Kern, and R. Miranda. Charge-transfer-induced structural rearrangements at both sides of organic/metal interfaces. *Nature Chemistry*, 2(5):374–379, 2010.

[103] S. Lindner, M. Knupfer, R. Friedrich, T. Hahn, and J. Kortus. Hybrid states and charge transfer at a phthalocyanine heterojunction. *Physical Review Letters*, 109:027601, 2012.

[104] J. Ziroff, F. Forster, A. Schöll, P. Puschnig, and F. Reinert. Hybridization of organic molecular orbitals with substrate states at interfaces: PTCDA on silver. *Physical Review Letters*, 104:233004, 2010.

[105] X.-Y. Zhu. Electron transfer at molecule-metal interfaces: A two-photon photoemission study. *Annual Review of Physical Chemistry*, 53(1):221–247, 2002.

[106] C. H. Schwalb, S. Sachs, M. Marks, A. Schöll, F. Reinert, E. Umbach, and U. Höfer. Electron lifetime in a shockley-type metal-organic interface state. *Physical Review Letters*, 101:146801, 2008.

[107] E. Varene, I. Martin, and P. Tegeder. Optically induced inter- and intrafacial electron transfer probed by two-photon photoemission: Electronic states of sexithiophene on Au(111). *The Journal of Physical Chemistry Letters*, 2(3):252–256, 2011.

[108] B. W. Caplins, A. J. Shearer, D. E. Suich, E. A. Muller, and C. B. Harris. Measuring the electronic corrugation at the metal/organic interface. *Physical Review B*, 89:155422, 2014.

[109] N. V. Smith, M. M. Traum, and F. J. Di Salvo. Mapping energy bands in layer compounds from the angular dependence of ultraviolet photoemission. *Solid State Communications*, 15(2):211–214, 1974.

[110] F. J. Himpsel. Angle-resolved measurements of the photoemission of electrons in the study of solids. *Advances in Physics*, 32(1):1–51, 1983.

[111] A. Damascelli, Z. Hussain, and Z.-X. Shen. Angle-resolved photoemission studies of the cuprate superconductors. *Reviews of Modern Physics.*, 75:473–541, 2003.

[112] T. Ohta, A. Bostwick, T. Seyller, K. Horn, and E. Rotenberg. Controlling the electronic structure of bilayer graphene. *Science*, 313(5789):951–954, 2006.

[113] D. F. Padowitz, W. R. Merry, R. E. Jordan, and C. B. Harris. Two-photon photoemission as a probe of electron interactions with atomically thin dielectric films on metal surfaces. *Physical Review Letters*, 69:3583–3586, 1992.

[114] P. Szymanski, S. Garrett-Roe, and C. B. Harris. Time- and angle-resolved two-photon photoemission studies of electron localization and solvation at interfaces. *Progress in Surface Science*, 78(1):1–39, 2005.

[115] R. Haight. Electron dynamics at surfaces. *Surface Science Reports*, 21(8):275–325, 1995.

[116] H. Petek and S. Ogawa. Femtosecond time-resolved two-photon photoemission studies of electron dynamics in metals. *Progress in Surface Science*, 56(4):239–310, 1997.

[117] M. Weinelt. Time-resolved two-photon photoemission from metal surfaces. *Journal of Physics: Condensed Matter*, 14(43):R1099, 2002.

[118] X.-Y. Zhu. Electronic structure and electron dynamics at molecule–metal interfaces: implications for molecule-based electronics. *Surface Science Reports*, 56(1–2):1–83, 2004.

[119] J. Güdde, W. Berthold, and U. Höfer. Dynamics of electronic transfer processes at metal/insulator interfaces. *Chemical Reviews*, 106(10):4261–4280, 2006. PMID: 17031986.

[120] C. D. Lindstrom and X.-Y. Zhu. Photoinduced electron transfer at molecule-metal interfaces. *Chemical reviews*, 106(10):4281–4300, 2006.

[121] S. Hagen, P. Kate, M. V. Peters, S. Hecht, M. Wolf, and P. Tegeder. Kinetic analysis of the photochemically and thermally induced isomerization of an azobenzene derivative on Au(111) probed by two-photon photoemission. *Applied Physics A*, 93(2):253–260, 2008.

[122] W.-L. Chan, M. Ligges, A. Jailaubekov, L. Kaake, L. Miaja-Avila, and X.-Y. Zhu. Observing the multiexciton state in singlet fission and ensuing ultrafast multielectron transfer. *Science*, 334(6062):1541–1545, 2011.

[123] P. Tegeder. Optically and thermally induced molecular switching processes at metal surfaces. *Journal of Physics: Condensed Matter*, 24(39):394001, 2012.

[124] C. Bronner and P. Tegeder. Photo-induced and thermal reactions in thin films of an azobenzene derivative on Bi(111). *New Journal of Physics*, 16(5):053004, 2014.

[125] C. Kittel. *Introduction to solid state physics*. Wiley, 2005.

[126] S. Hunklinger. *Festkörperphysik*. Oldenbourg Verlag, 2009.

[127] H. Ibach and H. Lüth. *Festkörperphysik: Einführung in die Grundlagen*. Springer-Verlag, 2009.

[128] R. Gross and A. Marx. *Festkörperphysik*. De Gruyter Studium. De Gruyter, 2014.

[129] J. B. Pendry and S. J. Gurman. Theory of surface states: General criteria for their existence. *Surface Science*, 49(1):87 – 105, 1975.

[130] P. M. Echenique and J. B. Pendry. The existence and detection of rydberg states at surfaces. *Journal of Physics C: Solid State Physics*, 11(10):2065, 1978.

[131] N. V. Smith. Phase analysis of image states and surface states associated with nearly-free-electron band gaps. *Physical Review B*, 32:3549–3555, 1985.

[132] I. Tamm. Über eine mögliche Art der Elektronenbindung an Kristalloberflächen. *Zeitschrift für Physik*, 76(11):849–850, 1932.

[133] W. Shockley. On the surface states associated with a periodic potential. *Physical Review*, 56:317–323, 1939.

[134] P. O. Gartland and B. J. Slagsvold. Transitions conserving parallel momentum in photoemission from the (111) face of copper. *Physical Review B*, 12:4047–4058, 1975.

[135] P. Heimann, H. Neddermeyer, and H. F. Roloff. Ultraviolet photoemission for intrinsic surface states of the noble metals. *Journal of Physics C: Solid State Physics*, 10(1):L17, 1977.

[136] P. Sandl, U. Bischler, and E. Bertel. The interaction of atomic hydrogen with Cu(110). *Surface Science*, 291(1):29–38, 1993.

[137] P. Roos, E. Bertel, and K. D. Rendulic. Observation of an sp-derived surface resonance on Pt(111) indicating the crucial role of surface states in physisorption. *Chemical Physics Letters*, 232(5):537–541, 1995.

[138] T. Andreev, I. Barke, and H. Hoevel. Adsorbed rare-gas layers on Au(111): Shift of the shockley surface state studied with ultraviolet photoelectron spectroscopy and scanning tunneling spectroscopy. *Physical Review B*, 70:205426, 2004.

[139] F. Forster, A. Bendounan, F. Reinert, V. G. Grigoryan, and M. Springborg. The shockley-type surface state on Ar covered Au(111): High resolution photoemission results and the description by slab-layer DFT calculations. *Surface Science*, 601(23):5595–5604, 2007.

[140] A. Scheybal, K. Müller, R. Bertschinger, M. Wahl, A. Bendounan, P. Aebi, and T. A. Jung. Modification of the Cu(110) shockley surface state by an adsorbed pentacene monolayer. *Physical Review B*, 79:115406, 2009.

[141] J. Ziroff, P. Gold, A. Bendounan, F. Forster, and F. Reinert. Adsorption energy and geometry of physisorbed organic molecules on Au(111) probed by surface-state photoemission. *Surface Science*, 603(2):354–358, 2009.

[142] A. Bendounan and S. Aït-Ouazzou. Role of the shockley state in doping of organic molecule monolayer. *The Journal of Physical Chemistry C*, 120(21):11456–11464, 2016.

[143] H. Yamane and N. Kosugi. Site-specific organic/metal interaction revealed from shockley-type interface state. *The Journal of Physical Chemistry C*, 120(42):24307–24313, 2016.

[144] N. Nicoara, E. Román, J. M. Gómez-Rodríguez, J. A. Martín-Gago, and J. Méndez. Scanning tunneling and photoemission spectroscopies at the PTCDA/Au(111) interface. *Organic Electronics*, 7(5):287–294, 2006.

[145] F. S. Tautz. Structure and bonding of large aromatic molecules on noble metal surfaces: The example of PTCDA. *Progress in Surface Science*, 82(9–12):479–520, 2007.

[146] N. L. Zaitsev, I. A. Nechaev, P. M. Echenique, and E. V. Chulkov. Transformation of the Ag(111) surface state due to molecule-surface interaction with ordered organic molecular monolayers. *Physical Review B*, 85:115301, 2012.

[147] M. C. E. Galbraith, M. Marks, R. Tonner, and U. Höfer. Formation of an organic/metal interface state from a shockley resonance. *The Journal of Physical Chemistry Letters*, 5(1):50–55, 2014.

[148] H.-H. Yang, H.-H. Tsai, C.-F. Ying, T.-H. Yang, C.-C. Kaun, C.-H. Chen, and M.-T. Lin. Tuning molecule-substrate coupling via deposition of metal adatoms. *The Journal of Chemical Physics*, 143(18), 2015.

[149] M. W. Cole and M. H. Cohen. Image-potential-induced surface bands in insulators. *Physical Review Letters*, 23:1238–1241, 1969.

[150] D. Straub and F. J. Himpsel. Identification of image-potential surface states on metals. *Physical Review Letters*, 52:1922–1924, 1984.

[151] V. Dose, W. Altmann, A. Goldmann, U. Kolac, and J. Rogozik. Image-potential states observed by inverse photoemission. *Physical Review Letters*, 52:1919–1921, 1984.

[152] K. Giesen, F. Hage, F. J. Himpsel, H. J. Riess, and W. Steinmann. Two-photon photoemission via image-potential states. *Physical Review Letters*, 55:300–303, 1985.

[153] T. Fauster and W. Steinmann. Two-photon photoemission spectroscopy of image states. *Electromagnetic Waves: Recent Developments in Research*, 2:347–411, 1995.

[154] J. Güdde and U. Höfer. Femtosecond time-resolved studies of image-potential states at surfaces and interfaces of rare-gas adlayers. *Progress in Surface Science*, 80(3–4):49–91, 2005.

[155] U. Bovensiepen, H. Petek, and M. Wolf. *Dynamics at Solid State Surfaces and Interfaces: Volume 2: Fundamentals*. Dynamics at Solid State Surfaces and Interfaces. Wiley, 2012.

[156] P. M. Echenique, J. M. Pitarke, E. V. Chulkov, and A. Rubio. Theory of inelastic lifetimes of low-energy electrons in metals. *Chemical Physics*, 251(1–3):1–35, 2000.

[157] R. W. Schoenlein, J. G. Fujimoto, G. L. Eesley, and T. W. Capehart. Femtosecond studies of image-potential dynamics in metals. *Physical Review Letters*, 61:2596–2599, 1988.

[158] U. Höfer, I. L. Shumay, C. Reuß, U. Thomann, W. Wallauer, and T. Fauster. Time-resolved coherent photoelectron spectroscopy of quantized electronic states on metal surfaces. *Science*, 277(5331):1480–1482, 1997.

[159] R. W. Schoenlein, J. G. Fujimoto, G. L. Eesley, and T. W. Capehart. Femtosecond dynamics of the $n = 2$ image-potential state on Ag(100). *Physical Review B*, 41:5436–5439, 1990.

[160] S. Garrett-Roe, S. T. Shipman, P. Szymanski, M. L. Strader, A. Yang, and C. B. Harris. Ultrafast electron dynamics at metal interfaces: Intraband relaxation of image state electrons as friction. *The Journal of Physical Chemistry B*, 109(43):20370–20378, 2005. PMID: 16853636.

[161] W. R. Merry, R. E. Jordan, D. F. Padowitz, and C. B. Harris. Electrons at metal-insulator interfaces. *Surface Science*, 295(3):393–401, 1993.

[162] M. Wolf, E. Knoesel, and T. Hertel. Ultrafast dynamics of electrons in image-potential states on clean and Xe-covered Cu(111). *Physical Review B*, 54:R5295–R5298, 1996.

[163] J. D. McNeill, R. L. Lingle, R. E. Jordan, D. F. Padowitz, and C. B. Harris. Interfacial quantum well states of Xe and Kr adsorbed on Ag(111). *The Journal of Chemical Physics*, 105(9):3883–3891, 1996.

[164] W. Berthold, U. Höfer, P. Feulner, and D. Menzel. Influence of Xe adlayer morphology and electronic structure on image-potential state lifetimes of Ru(0001). *Chemical Physics*, 251(1–3):123–132, 2000.

[165] W. T. Berthold. *Zeitaufgelöste Zweiphotonen-Photoemission an den Bildpotentialzuständen der sauberen und edelgasbedeckten Cu(100)- und Ru(0001)-Oberfläche*. PhD thesis, Technische Universität München, 2001.

[166] W. Berthold, F. Rebentrost, P. Feulner, and U. Höfer. Influence of Ar, Kr, and Xe layers on the energies and lifetimes of image-potential states on Cu(100). *Applied Physics A*, 78(2):131–140, 2004.

[167] M. Pope and C. E. Swenberg. Electronic processes in organic solids. *Annual Review of Physical Chemistry*, 35(1):613–655, 1984.

[168] K. Takimiya, S. Shinamura, I. Osaka, and E. Miyazaki. Thienoacene-based organic semiconductors. *Advanced Materials*, 23(38):4347–4370, 2011.

[169] A. Pochettino. Photo-electric properties of anthracene. *Lincei Rendic*, 15:171–179, 1906.

[170] J. Königsberger and K. Schilling. Über Elektrizitätsleitung in festen Elementen und Verbindungen. I. Minima des Widerstandes, Prüfung auf Elektronenleitung, Anwendung der Dissoziationsformeln. *Annalen der Physik*, 337(6):179–230, 1910.

[171] R. G. Kepler. Charge carrier production and mobility in anthracene crystals. *Physical Review*, 119:1226–1229, 1960.

[172] M. Pfeiffer, A. Beyer, T. Fritz, and K. Leo. Controlled doping of phthalocyanine layers by cosublimation with acceptor molecules: A systematic seebeck and conductivity study. *Applied Physics Letters*, 73(22):3202–3204, 1998.

[173] G. Yu, J. Gao, J. C. Hummelen, F. Wudl, and A. J. Heeger. Polymer photovoltaic cells: Enhanced efficiencies via a network of internal donor-acceptor heterojunctions. *Science*, 270(5243):1789–1791, 1995.

[174] D. M. Adams, L. Brus, C. E. Chidsey, S. Creager, C. Creutz, C. R. Kagan, P. V. Kamat, M. Lieberman, S. Lindsay, R. A. Marcus, R. M. Metzger, M. E. Michel-Beyerle, J. R. Miller, M. D. Newton, D. R. Rolison, O. Sankey, K. S. Schanze, J. Yardley, and X.-Y. Zhu. Charge transfer on the nanoscale: current status. *The Journal of Physical Chemistry B*, 107(28):6668–6697, 2003.

[175] H. Alves, A. S. Molinari, H. Xie, and A. F. Morpurgo. Metallic conduction at organic charge-transfer interfaces. *Nature Materials*, 7(7):574–580, 2008.

[176] Z. Hu, Z. Zhong, Y. Chen, C. Sun, F. Huang, J. Peng, J. Wang, and Y. Cao. Energy-level alignment at the organic/electrode interface in organic optoelectronic devices. *Advanced Functional Materials*, 26(1):129–136, 2016.

[177] Z.-M. Bao, R.-P. Xu, C. Li, Z.-Z. Xie, X.-D. Zhao, Y.-B. Zhang, Y.-Q. Li, and J.-X. Tang. Switching hole and electron transports of molecules on metal oxides by energy level alignment tuning. *ACS Applied Materials & Interfaces*, 8(34):22410–22417, 2016. PMID: 27523576.

[178] C. Adachi, M. A. Baldo, S. R. Forrest, and M. E. Thompson. High-efficiency organic electrophosphorescent devices with tris(2-phenylpyridine)iridium doped into electron-transporting materials. *Applied Physics Letters*, 77(6):904–906, 2000.

[179] H. Yersin. *Triplet Emitters for OLED Applications. Mechanisms of Exciton Trapping and Control of Emission Properties*, pages 1–26. Springer Berlin Heidelberg, Berlin, Heidelberg, 2004.

[180] N. S. Sariciftci, L. Smilowitz, A. J. Heeger, and F. Wudl. Photoinduced electron transfer from a conducting polymer to buckminsterfullerene. *Science*, 258(5087):1474–1476, 1992.

[181] M. Hoffmann, K. Schmidt, T. Fritz, T. Hasche, V. M. Agranovich, and K. Leo. The lowest energy frenkel and charge-transfer excitons in quasi-one-dimensional structures: application to MePTCDI and PTCDA crystals. *Chemical Physics*, 258(1):73 – 96, 2000.

[182] X.-Y. Zhu, Q. Yang, and M. Muntwiler. Charge-transfer excitons at organic semiconductor surfaces and interfaces. *Accounts of Chemical Research*, 42(11):1779–1787, 2009. PMID: 19378979.

[183] C. Deibel, T. Strobel, and V. Dyakonov. Role of the charge transfer state in organic donor-acceptor solar cells. *Advanced Materials*, 22(37):4097–4111, 2010.

[184] A. E. Jailaubekov, A. P. Willard, J. R. Tritsch, W.-L. Chan, N. Sai, R. Gearba, L. G. Kaake, K. J. Williams, K. Leung, P. J. Rossky, and X.-Y. Zhu. Hot charge-transfer excitons set the time limit for charge separation at donor/acceptor interfaces in organic photovoltaics. *Nature Materials*, 12(1):66–73, 2013.

[185] J. C. Blakesley and N. C. Greenham. Charge transfer at polymer-electrode interfaces: The effect of energetic disorder and thermal injection on band bending and open-circuit voltage. *Journal of Applied Physics*, 106(3), 2009.

[186] M. Bokdam, D. Çakir, and G. Brocks. Fermi level pinning by integer charge transfer at electrode-organic semiconductor interfaces. *Applied Physics Letters*, 98(11), 2011.

[187] I. Lange, J. C. Blakesley, J. Frisch, A. Vollmer, N. Koch, and D. Neher. Band bending in conjugated polymer layers. *Physical Review Letters*, 106:216402, 2011.

[188] D. Çakir, M. Bokdam, M. P. de Jong, M. Fahlman, and G. Brocks. Modeling charge transfer at organic donor-acceptor semiconductor interfaces. *Applied Physics Letters*, 100(20), 2012.

[189] M. Fahlman, A. Crispin, X. Crispin, S. K. M. Henze, M. P. de Jong, W. Osikowicz, C. Tengstedt, and W. R. Salaneck. Electronic structure of hybrid interfaces for polymer-based electronics. *Journal of Physics: Condensed Matter*, 19(18):183202, 2007.

[190] W. Osikowicz, M.-P. de Jong, and W. R. Salaneck. Formation of the interfacial dipole at organic-organic interfaces: C60/polymer interfaces. *Advanced Materials*, 19(23):4213–4217, 2007.

[191] S. Braun, X. Liu, W. R. Salaneck, and M. Fahlman. Fermi level equilibrium at donor-acceptor interfaces in multi-layered thin film stack of TTF and TCNQ. *Organic Electronics*, 11(2):212–217, 2010.

[192] E. F. Aziz, A. Vollmer, S. Eisebitt, W. Eberhardt, P. Pingel, D. Neher, and N. Koch. Localized charge transfer in a molecularly doped conducting polymer. *Advanced Materials*, 19(20):3257–3260, 2007.

[193] I. Salzmann, G. Heimel, S. Duhm, M. Oehzelt, P. Pingel, B. M. George, A. Schnegg, K. Lips, R.-P. Blum, A. Vollmer, and N. Koch. Intermolecular hybridization governs molecular electrical doping. *Physical Review Letters*, 108(3):035502, 2012.

[194] H. Méndez, G. Heimel, A. Opitz, K. Sauer, P. Barkowski, M. Oehzelt, J. Soeda, T. Okamoto, J. Takeya, J.-B. Arlin, J.-Y. Balandier, Y. Geerts, N. Koch, and I. Salzmann. Doping of organic semiconductors: Impact of dopant strength and electronic coupling. *Angewandte Chemie International Edition*, 52(30):7751–7755, 2013.

[195] H. Méndez, G. Heimel, S. Winkler, J. Frisch, A. Opitz, K. Sauer, B. Wegner, M. Oehzelt, C. Rothel, S. Duhm, D. Többens, N. Koch, and I. Salzmann. Charge-transfer crystallites as molecular electrical dopants. *Nature Communications*, 6:–, 2015.

[196] O. T. Hofmann, P. Rinke, M. Scheffler, and G. Heimel. Integer versus fractional charge transfer at metal(/insulator)/organic interfaces: Cu(/NaCl)/TCNE. *ACS Nano*, 9(5):5391–5404, 2015. PMID: 25905769.

[197] I. Salzmann, G. Heimel, M. Oehzelt, S. Winkler, and N. Koch. Molecular electrical doping of organic semiconductors: Fundamental mechanisms and emerging dopant design rules. *Accounts of Chemical Research*, 49(3):370–378, 2016. PMID: 26854611.

[198] M. Gruenewald, L. K. Schirra, P.Winget, M. Kozlik, P. F. Ndione, A. K. Sigdel, J. J. Berry, R. Forker, J.-L. Brédas, T. Fritz, and O. L. A. Monti. Integer charge transfer and hybridization at an organic semiconductor/conductive oxide interface. *The Journal of Physical Chemistry C*, 119(9):4865–4873, 2015.

[199] A. Grueneis and D. V. Vyalikh. Tunable hybridization between electronic states of graphene and a metal surface. *Physical Review B*, 77:193401, 2008.

[200] H. Vázquez, F. Flores, R. Oszwaldowski, J. Ortega, R. Pérez, and A. Kahn. Barrier formation at metal-organic interfaces: dipole formation and the charge neutrality level. *Applied Surface Science*, 234(1–4):107 – 112, 2004. The Ninth International Conference on the Formation of Semiconductor Interfaces.

[201] H. Vázquez, W. Gao, F. Flores, and A. Kahn. Energy level alignment at organic heterojunctions: Role of the charge neutrality level. *Physical Review B*, 71:041306, 2005.

[202] H. Vázquez, F. Flores, and A. Kahn. Induced density of states model for weakly-interacting organic semiconductor interfaces. *Organic Electronics*, 8(2–3):241–248, 2007.

[203] I. G. Hill, A. Rajagopal, A. Kahn, and Y. Hu. Molecular level alignment at organic semiconductor-metal interfaces. *Applied Physics Letters*, 73(5):662–664, 1998.

[204] W. Brütting. *Physics of organic semiconductors*. John Wiley & Sons, 2012.

[205] M. T. Greiner, M. G. Helander, W.-M. Tang, Z.-B. Wang, J. Qiu, and Z.-H. Lu. Universal energy-level alignment of molecules on metal oxides. *Nature Materials*, 11(1):76–81, 2012.

[206] P. Amsalem, G. Heimel, M. Oehzelt, and N. Koch. The interface electronic properties of organic photovoltaic cells. *Journal of Electron Spectroscopy and Related Phenomena*, 204, Part A:177–185, 2015. Organic Electronics.

[207] R. Smoluchowski. Anisotropy of the electronic work function of metals. *Physical Review*, 60:661–674, 1941.

[208] G. Witte, S. Lukas, P. S. Bagus, and C. Wöll. Vacuum level alignment at organic/metal junctions: "cushion" effect and the interface dipole. *Applied Physics Letters*, 87(26), 2005.

[209] O. T. Hofmann, G. M. Rangger, and E. Zojer. Reducing the metal work function beyond pauli pushback: A computational investigation of tetrathiafulvalene and viologen on coinage metal surfaces. *The Journal of Physical Chemistry C*, 112(51):20357–20365, 2008.

[210] P. C. Rusu, G. Giovannetti, C. Weijtens, R. Coehoorn, and G. Brocks. Work function pinning at metal-organic interfaces. *The Journal of Physical Chemistry C*, 113(23):9974–9977, 2009.

[211] O. T. Hofmann, D. A. Egger, and E. Zojer. Work-function modification beyond pinning: When do molecular dipoles count? *Nano Letters*, 10(11):4369–4374, 2010.

[212] L. Lindell, D. Çakir, G. Brocks, M. Fahlman, and S. Braun. Role of intrinsic molecular dipole in energy level alignment at organic interfaces. *Applied Physics Letters*, 102(22), 2013.

[213] S. Winkler, J. Frisch, P. Amsalem, S. Krause, M. Timpel, M. Stolte, F. Würthner, and N. Koch. Impact of molecular dipole moments on fermi level pinning in thin films. *The Journal of Physical Chemistry C*, 118(22):11731–11737, 2014.

[214] E. Wruss, O. T. Hofmann, D. A. Egger, E. Verwüster, A. Gerlach, F. Schreiber, and E. Zojer. Adsorption behavior of nonplanar phthalocyanines: Competition of different adsorption conformations. *The Journal of Physical Chemistry C*, 120(12):6869–6875, 2016.

[215] R. Schlaf, C. D. Merritt, L. A. Crisafulli, and Z. H. Kafafi. Organic semiconductor interfaces: Discrimination between charging and band bending related shifts in frontier orbital line-up measurements with photoemission spectroscopy. *Journal of Applied Physics*, 86(10):5678–5686, 1999.

[216] H. Ishii, N. Hayashi, E. Ito, Y. Washizu, K. Sugi, Y. Kimura, M. Niwano, Y. Ouchi, and K. Seki. Kelvin probe study of band bending at organic semiconductor/metal interfaces: examination of fermi level alignment. *physica status solidi (a)*, 201(6):1075–1094, 2004.

[217] R. Schlesinger, Y. Xu, O. T. Hofmann, S. Winkler, J. Frisch, J. Niederhausen, A. Vollmer, S. Blumstengel, F. Henneberger, P. Rinke, M. Scheffler, and N. Koch. Controlling the work function of zno and the energy-level alignment at the interface to organic semiconductors with a molecular electron acceptor. *Physical Review B*, 87:155311, 2013.

[218] E. Mankel, C. Hein, M. Kühn, and T. Mayer. Electric potential distributions in space charge regions of molecular organic adsorbates using a simplified distributed states model. *physica status solidi (a)*, 211(9):2040–2048, 2014.

[219] E. Ito, Y. Washizu, N. Hayashi, H. Ishii, N. Matsuie, K. Tsuboi, Y. Ouchi, Y. Harima, K. Yamashita, and K. Seki. Spontaneous buildup of giant surface potential by vacuum deposition of Alq3 and its removal by visible light irradiation. *Journal of Applied Physics*, 92(12):7306–7310, 2002.

[220] K. Sugi, H. Ishii, Y. Kimura, M. Niwano, E. Ito, Y. Washizu, N. Hayashi, Y. Ouchi, and K. Seki. Characterization of light-erasable giant surface potential built up in evaporated Alq3 thin films. *Thin Solid Films*, 464-465(0):412 – 415, 2004. Proceedings of the 7th International Symposium on Atomically Controlled Surfaces, Interfaces and Nanostructures.

[221] Y. Okabayashi, E. Ito, T. Isoshima, H. Ito, and M. Hara. Negative giant surface potential of peeled Alq3 thin film. *Thin Solid Films*, 518(2):839–841, 2009. 8th International Conference on Nano-Molecular Electronics.

[222] O. Plekan, A. Cassidy, R. Balog, N. C. Jones, and D. Field. A new form of spontaneously polarized material. *Physical Chemistry Chemical Physics*, 13:21035–21044, 2011.

[223] W. Schottky. Halbleitertheorie der Sperrschicht. *Naturwissenschaften*, 26(52):843–843, 1938.

[224] N. F. Mott. Note on the contact between a metal and an insulator or semiconductor. In *Mathematical Proceedings of the Cambridge Philosophical Society*, volume 34, pages 568–572. Cambridge University Press, 1938.

[225] N. F. Mott. The theory of crystal rectifiers. *Proceedings of the Royal Society of London. Series A, Mathematical and Physical Sciences*, pages 27–38, 1939.

[226] W. Schottky. Zur Halbleitertheorie der Sperrschicht- und Spitzengleichrichter. *Zeitschrift für Physik*, 113(5):367–414, 1939.

[227] G. A. Rojas, Y. Wu, G. Haugstad, and C. D. Frisbie. Measuring the thickness and potential profiles of the space-charge layer at organic/organic interfaces under illumination and in the dark by scanning kelvin probe microscopy. *ACS Applied Materials & Interfaces*, 8(9):5772–5776, 2016. PMID: 26890658.

[228] N. Hayashi, H. Ishii, Y. Ouchi, and K. Seki. Examination of band bending at buckminsterfullerene C60/metal interfaces by the kelvin probe method. *Journal of Applied Physics*, 92(7):3784–3793, 2002.

[229] O. M. Ottinger, C. Melzer, and H. von Seggern. Pitfalls in kelvin probe measurements. *Journal of Applied Physics*, 106(2), 2009.

[230] S. Beck, D. Gerbert, T. Glaser, and A. Pucci. Charge transfer at organic/inorganic interfaces and the formation of space charge regions studied with infrared light. *The Journal of Physical Chemistry C*, 119(22):12545–12550, 2015.

[231] H. Hertz. Über einen Einfluss des ultravioletten Lichtes auf die electrische Entladung. *Annalen der Physik*, 267(8):983–1000, 1887.

[232] W. Hallwachs. Über den Einfluss des Lichtes auf electrostatisch geladene Körper. *Annalen der Physik*, 269(2):301–312, 1888.

[233] A. Einstein. Über einen die Erzeugung und Verwandlung des Lichtes betreffenden heuristischen Gesichtspunkt. *Annalen der Physik*, 322(6):132–148, 1905.

[234] S. Hüfner. *Photoelectron spectroscopy: principles and applications*. Springer Science & Business Media, 2013.

[235] C. R. Brundle. Elucidation of surface structure and bonding by photoelectron spectroscopy? *Surface Science*, 48(1):99–136, 1975.

[236] M. P. Seah and W. A. Dench. Quantitative electron spectroscopy of surfaces: A standard data base for electron inelastic mean free paths in solids. *Surface and Interface Analysis*, 1(1):2–11, 1979.

[237] W. S. M. Werner. Electron transport in solids for quantitative surface analysis. *Surface and Interface Analysis*, 31(3):141–176, 2001.

[238] N. Koch, N. Ueno, and A. T. S. Wee. *The molecule-metal interface.* John Wiley & Sons, 2013.

[239] S. Poulston, P. M. Parlett, P. Stone, and M. Bowker. Surface oxidation and reduction of CuO and Cu2O studied using XPS and XAES. *Surface and Interface Analysis*, 24(12):811–820, 1996.

[240] M. Valden, X. Lai, and D. W. Goodman. Onset of catalytic activity of gold clusters on titania with the appearance of nonmetallic properties. *Science*, 281(5383):1647–1650, 1998.

[241] A. Krüger, M. Bernien, C. F. Hermanns, and W. Kuch. X-ray-induced reversible switching of an azobenzene derivative adsorbed on Bi(111). *The Journal of Physical Chemistry C*, 118(24):12916–12922, 2014.

[242] K. K. Okudaira, S. Hasegawa, P. T. Sprunger, E. Morikawa, V. Saile, K. Seki, Y. Harada, and N. Ueno. Photoemission study of pristine and photodegraded poly(methyl methacrylate). *Journal of Applied Physics*, 83(8):4292–4298, 1998.

[243] P. Bröms, N. Johansson, R. W. Gymer, S. C. Graham, R. H. Friend, and W. R. Salaneck. Low energy electron degradation of poly(p-phenylenevinylene). *Advanced Materials*, 11(10):826–832, 1999.

[244] N. Koch, D. Pop, R. L. Weber, N. Böwering, B. Winter, M. Wick, G. Leising, I. V. Hertel, and W. Braun. Radiation induced degradation and surface charging of organic thin films in ultraviolet photoemission spectroscopy. *Thin Solid Films*, 391(1):81–87, 2001.

[245] D. Wisbey, N. Wu, Y. Losovyj, I. Ketsman, A. N. Caruso, D. Feng, J. Belot, E. Vescovo, and P. A. Dowben. Radiation-induced decomposition of the metal-organic molecule bis(4-cyano-2,2,6,6-tetramethyl-3,5-heptanedionato)copper(ii). *Applied Surface Science*, 255(6):3576–3580, 2009.

[246] D. Wegkamp, M. Meyer, C. Richter, M. Wolf, and J. Stähler. Photoinduced work function modifications and their effect on photoelectron spectroscopy. *Applied Physics Letters*, 103(15), 2013.

[247] T. Fauster. Two-photon photoemission. *Progress in Surface Science*, 46(2):177–186, 1994.

[248] T. Hertel, E. Knoesel, M. Wolf, and G. Ertl. Ultrafast electron dynamics at Cu(111): Response of an electron gas to optical excitation. *Physical Review Letters*, 76:535–538, 1996.

[249] N.-H. Ge, C. M. Wong, R. L. Lingle, J. D. McNeill, K. J. Gaffney, and C. B. Harris. Femtosecond dynamics of electron localization at interfaces. *Science*, 279(5348):202–205, 1998.

[250] Q. Yang, M. Muntwiler, and X.-Y. Zhu. Charge transfer excitons and image potential states on organic semiconductor surfaces. *Physical Review B*, 80:115214, 2009.

[251] E. Varene, L. Bogner, C. Bronner, and P. Tegeder. Ultrafast exciton population, relaxation, and decay dynamics in thin oligothiophene films. *Physical Review Letters*, 109:207601, 2012.

[252] C. Bronner and P. Tegeder. Relaxation dynamics of photoexcited charge carriers at the Bi(111) surface. *Physical Review B*, 89:115105, 2014.

[253] L. Bogner, Z. Yang, M. Corso, R. Fitzner, P. Bäuerle, K. J. Franke, J. I. Pascual, and P. Tegeder. Electronic structure and excited state dynamics in a dicyanovinyl-substituted oligothiophene on Au(111). *Physical Chemistry Chemical Physics*, 17:27118–27126, 2015.

[254] C. Bronner. Electronic structure and ultrafast charge carrier dynamics at the interfaces between molecular switches and the Au(111) surface investigated with time-resolved photoemission. Masterthesis, Freie Universität Berlin - Fachbereich Physik, 2010.

[255] S. Hagen. *Isomerization behavior of photochromic molecules in direct contact with noble metal surfaces*. PhD thesis, Freie Universität Berlin - Fachbereich Physik, 2009.

[256] W. Heisenberg. Über den anschaulichen Inhalt der quantentheoretischen Kinematik und Mechanik. *Zeitschrift für Physik*, 43(3):172–198, 1927.

[257] R. L. Fork, O. E. Martinez, and J. P. Gordon. Negative dispersion using pairs of prisms. *Optics Letters*, 9(5):150–152, 1984.

[258] C. Bronner. *Photoinduced and Thermal Reactions of Functional Molecules at Surfaces*. PhD thesis, Freie Universität Berlin - Fachbereich Physik, 2014.

[259] S. Hagen, F. Leyssner, D. Nandi, M. Wolf, and P. Tegeder. Reversible switching of tetra-tert-butyl-azobenzene on a Au(111) surface induced by light and thermal activation. *Chemical Physics Letters*, 444(1–3):85–90, 2007.

[260] M. Wolf and P. Tegeder. Reversible molecular switching at a metal surface: A case study of tetra-tert-butyl-azobenzene on Au(111). *Surface Science*, 603(10–12):1506–1517, 2009. Special Issue of Surface Science dedicated to Prof. Dr. Dr. h.c. mult. Gerhard Ertl, Nobel-Laureate in Chemistry 2007.

[261] C. Bronner, B. Priewisch, K. Rück-Braun, and P. Tegeder. Photoisomerization of an azobenzene on the Bi(111) surface. *The Journal of Physical Chemistry C*, 117(51):27031–27038, 2013.

[262] K. Giesen, F. Hage, H. J. Riess, W. Steinmann, R. Haight, R. Beigang, R. Dreyfus, P. Avouris, and F. J. Himpsel. Image potential states seen via two-photon photoemission and second harmonic generation. *Physica Scripta*, 35(4):578, 1987.

[263] D. Rieger, T. Wegehaupt, and W. Steinmann. Two-photon photoemission from adsorbate-induced states: Atomic oxygen on Cu(111). *Physical Review Letters*, 58:1135–1138, 1987.

[264] N. Fischer, S. Schuppler, T. Fauster, and W. Steinmann. Coverage-dependent electronic structure of Na on Cu(111). *Surface Science*, 314(1):89 – 96, 1994.

[265] R. Fischer and T. Fauster. Coupling of image states to quantum-well states for Au on Pd(111). *Physical Review B*, 51:7112–7115, 1995.

[266] C. B. Harris, N.-H. Ge, R. L. Lingle Jr., J. D. McNeill, and C. M. Wong. Femtosecond dynamics of electrons on surfaces and at interfaces. *Annual Review of Physical Chemistry*, 48(1):711–744, 1997. PMID: 15012454.

[267] A. Hotzel, K. Ishioka, E. Knoesel, M. Wolf, and G. Ertl. Can we control lifetimes of electronic states at surfaces by adsorbate resonances? *Chemical Physics Letters*, 285(3–4):271 – 277, 1998.

[268] M. Rohleder, K. Duncker, W. Berthold, J. Güdde, and U. Höfer. Momentum-resolved dynamics of Ar - Cu(100) interface states probed by time-resolved two-photon photoemission. *New Journal of Physics*, 7(1):103, 2005.

[269] A. Hotzel. Electron dynamics of image potential states in weakly bound adsorbate layers: A short review. *Progress in Surface Science*, 82(4–6):336 – 354, 2007. Dynamics of Electron Transfer Processes at Surfaces.

[270] U. Bovensiepen, H. Petek, and M. Wolf. *Dynamics at Solid State Surfaces and Interfaces: Volume 1 - Current Developments*. Wiley, 2010.

[271] D. Nobis, M. Potenz, D. Niesner, and T. Fauster. Image-potential states of graphene on noble-metal surfaces. *Physical Review B*, 88:195435, 2013.

[272] N. Armbrust, J. Güdde, U. Höfer, S. Kossler, and P. Feulner. Spectroscopy and dynamics of a two-dimensional electron gas on ultrathin helium films on Cu(111). *Physical Review Letters*, 116:256801, 2016.

[273] N.-H. Ge, C. M. Wong, and C. B. Harris. Femtosecond studies of electron dynamics at interfaces. *Accounts of Chemical Research*, 33(2):111–118, 2000. PMID: 10673319.

[274] X.-Y. Zhu and A. Kahn. Electronic structure and dynamics at organic donor/acceptor interfaces. *MRS Bulletin*, 35(6):443–448, 2011.

[275] J. Stähler, C. Gahl, and M. Wolf. Dynamics and reactivity of trapped electrons on supported ice crystallites. *Accounts of Chemical Research*, 45(1):131–138, 2011.

[276] O. L. A. Monti. Understanding interfacial electronic structure and charge transfer: An electrostatic perspective. *The Journal of Physical Chemistry Letters*, 3(17):2342–2351, 2012.

[277] C. Bronner, S. Stremlau, M. Gille, F. Brauße, A. Haase, S. Hecht, and P. Tegeder. Aligning the band gap of graphene nanoribbons by monomer doping. *Angewandte Chemie International Edition*, 52(16):4422–4425, 2013.

[278] C. Bronner, D. Gerbert, A. Broska, and P. Tegeder. Excitonic states in narrow armchair graphene nanoribbons on gold surfaces. *The Journal of Physical Chemistry C*, 120(45):26168–26172, 2016.

[279] M. S. Dyer and M. Persson. The nature of the observed free-electron-like state in a PTCDA monolayer on Ag(111). *New Journal of Physics*, 12(6):063014, 2010.

[280] M. Marks, N. L. Zaitsev, B. Schmidt, C. H. Schwalb, A. Schöll, I. A. Nechaev, P. M. Echenique, E. V. Chulkov, and U. Höfer. Energy shift and wave function overlap of metal-organic interface states. *Physical Review B*, 84:081301, 2011.

[281] M. Wießner, J. Kübert, V. Feyer, P. Puschnig, A. Schöll, and F. Reinert. Lateral band formation and hybridization in molecular monolayers: NTCDA on Ag(110) and Cu(100). *Physical Review B*, 88:075437, 2013.

[282] A. Yang, S. T. Shipman, S. Garrett-Roe, J. Johns, M. Strader, P. Szymanski, E. Muller, and C. Harris. Two-photon photoemission of ultrathin film PTCDA morphologies on Ag(111). *The Journal of Physical Chemistry C*, 112(7):2506–2513, 2008.

[283] L. Kilian, A. Hauschild, R. Temirov, S. Soubatch, A. Schöll, A. Bendounan, F. Reinert, T.-L. Lee, F. S. Tautz, M. Sokolowski, and E. Umbach. Role of intermolecular interactions on the electronic and geometric structure of a large π-conjugated molecule adsorbed on a metal surface. *Physical Review Letters*, 100:136103, 2008.

[284] J. V. Barth, H. Brune, G. Ertl, and R. J. Behm. Scanning tunneling microscopy observations on the reconstructed Au(111) surface: Atomic structure, long-range superstructure, rotational domains, and surface defects. *Physical Review B*, 42:9307–9318, 1990.

[285] S. Narasimhan and D. Vanderbilt. Elastic stress domains and the herringbone reconstruction on Au(111). *Physical Review Letters*, 69:1564–1567, 1992.

[286] K. Lauwaet, K. Schouteden, E. Janssens, C. Van Haesendonck, P. Lievens, M. I. Trioni, L. Giordano, and G. Pacchioni. Resolving all atoms of an alkali halide via nanomodulation of the thin NaCl film surface using the Au(111) reconstruction. *Physical Review B*, 85:245440, 2012.

[287] N. Takeuchi, C. T. Chan, and K. M. Ho. Au(111): A theoretical study of the surface reconstruction and the surface electronic structure. *Physical Review B*, 43:13899–13906, 1991.

[288] F. Reinert. Spin–orbit interaction in the photoemission spectra of noble metal surface states. *Journal of Physics: Condensed Matter*, 15(5):S693, 2003.

[289] R. H. Fowler. The analysis of photoelectric sensitivity curves for clean metals at various temperatures. *Physical Review*, 38:45–56, 1931.

[290] E. E. Huber. The effect of mercury contamination on the work function of gold. *Applied Physics Letters*, 8(7):169–171, 1966.

[291] W. M. H. Sachtler, G. J. H. Dorgelo, and A. A. Holscher. The work function of gold. *Surface Science*, 5(2):221 – 229, 1966.

[292] G. V. Hansson and S. A. Flodström. Photoemission study of the bulk and surface electronic structure of single crystals of gold. *Physical Review B*, 18:1572–1585, 1978.

[293] D. Straub and F. J. Himpsel. Spectroscopy of image-potential states with inverse photoemission. *Physical Review B*, 33:2256–2262, 1986.

[294] D. P. Woodruff, W. A. Royer, and N. V. Smith. Empty surface states, image states, and band edge on Au(111). *Physical Review B*, 34:764–767, 1986.

[295] S. D. Kevan and R. H. Gaylord. High-resolution photoemission study of the electronic structure of the noble-metal (111) surfaces. *Physical Review B*, 36:5809–5818, 1987.

[296] R. Paniago, R. Matzdorf, G. Meister, and A. Goldmann. Temperature dependence of shockley-type surface energy bands on Cu(111), Ag(111) and Au(111). *Surface Science*, 336(1):113 – 122, 1995.

[297] C. Reuß, W. Wallauer, and T. Fauster. Image states of Ag on Au(111). *Surface Review and Letters*, 03(04):1547–1554, 1996.

[298] S. LaShell, B. A. McDougall, and E. Jensen. Spin splitting of an Au(111) surface state band observed with angle resolved photoelectron spectroscopy. *Physical Review Letters*, 77(0):3419–3422, 1996.

[299] K. Schouteden, P. Lievens, and C. Van Haesendonck. Fourier-transform scanning tunneling microscopy investigation of the energy versus wave vector dispersion of electrons at the Au(111) surface. *Physical Review B*, 79:195409, 2009.

[300] N. E. Christensen and B. O. Seraphin. Relativistic band calculation and the optical properties of gold. *Physical Review B*, 4:3321–3344, 1971.

[301] R. Courths, H. G. Zimmer, A. Goldmann, and H. Saalfeld. Electronic structure of gold: An angle-resolved photoemission study along the Λ line. *Physical Review B*, 34:3577–3585, 1986.

[302] T. Rangel, D. Kecik, P. E. Trevisanutto, G.-M. Rignanese, H. Van Swygenhoven, and V. Olevano. Band structure of gold from many-body perturbation theory. *Physical Review B*, 86:125125, 2012.

[303] B. Yan, B. Stadtmuller, N. Haag, S. Jakobs, J. Seidel, D. Jungkenn, S. Mathias, M. Cinchetti, M. Aeschlimann, and C. Felser. Topological states on the gold surface. *Nature Communications*, 6:–, 2015.

[304] D. A. King, T. E. Madey, and J. T. Yates. Interaction of oxygen with polycrystalline tungsten. I. sticking probabilities and desorption spectra. *The Journal of Chemical Physics*, 55(7):3236–3246, 1971.

[305] D. A. King. Thermal desorption from metal surfaces: A review. *Surface Science*, 47(1):384–402, 1975.

[306] D. L. S. Nieskens, A. P. van Bavel, and J. W. Niemantsverdriet. The analysis of temperature programmed desorption experiments of systems with lateral interactions; implications of the compensation effect. *Surface Science*, 546(2–3):159–169, 2003.

[307] T. J. Rockey, M. Yang, and H.-L. Dai. Adsorption energies, inter-adsorbate interactions, and the two binding sites within monolayer benzene on Ag(111). *The Journal of Physical Chemistry B*, 110(40):19973–19978, 2006.

[308] W. Liu, F. Maaß, M. Willenbockel, C. Bronner, M. Schulze, S. Soubatch, F. S. Tautz, P. Tegeder, and A. Tkatchenko. Quantitative prediction of molecular adsorption: Structure and binding of benzene on coinage metals. *Physical Review Letters*, 115:036104, 2015.

[309] J. L. Falconer and J. A. Schwarz. Temperature-programmed desorption and reaction: Applications to supported catalysts. *Catalysis Reviews*, 25(2):141–227, 1983.

[310] H. Ibach. *Physics of surfaces and interfaces*, volume 10. Springer, 2006.

[311] R. S. Mulliken. Molecular compounds and their spectra. III. the interaction of electron donors and acceptors. *The Journal of Physical Chemistry*, 56(7):801–822, 1952.

[312] R. G. Kepler, P. E. Bierstedt, and R. E. Merrifield. Electronic conduction and exchange interaction in a new class of conductive organic solids. *Physical Review Letters*, 5:503–504, 1960.

[313] D. S. Acker, R. J. Harder, W. R. Hertler, W. Mahler, L. R. Melby, R. E. Benson, and W. E. Mochel. 7, 7, 8, 8-tetracyanoquinodimethane and its electrically conducting anion-radical derivatives. *Journal of the American Chemical Society*, 82(24):6408–6409, 1960.

[314] L. R. Melby. Substituted quinodimethans: VIII. salts derived from the 7,7,8,8-tetracyanoquinodimethan anion–radical and benzologues of quaternary pyrazinium cations. *Canadian Journal of Chemistry*, 43(5):1448–1453, 1965.

[315] C. N. R. Rao, S. N. Bhat, and P. C. Dwedi. Spectroscopy of electron donor-acceptor systems. *Applied Spectroscopy Reviews*, 5(1):1–170, 1972.

[316] R. C. Wheland and E. L. Martin. Synthesis of substituted 7, 7, 8, 8-tetracyanoquinodimethanes. *The Journal of Organic Chemistry*, 40(21):3101–3109, 1975.

[317] F. Wudl, D. Wobschall, and E. J. Hufnagel. Electrical conductivity by the bis (1, 3-dithiole)-bis (1, 3-dithiolium) system. *Journal of the American Chemical Society*, 94(2):670–672, 1972.

[318] J. Tanaka, M. Tanaka, T. Kawai, T. Takabe, and O. Maki. Electronic spectra and electronic structure of TCNQ complexes. *Bulletin of the Chemical Society of Japan*, 49(9):2358–2373, 1976.

[319] G. A. Thomas, D. E. Schafer, F. Wudl, P. M. Horn, D. Rimai, J. W. Cook, D. A. Glocker, M. J. Skove, C. W. Chu, R. P. Groff, J. L. Gillson, R. C. Wheland, L. R. Melby, M. B. Salamon, R. A. Craven, G. De Pasquali, A. N. Bloch, D. O. Cowan, V. V. Walatka, R. E. Pyle, R. Gemmer, T. O. Poehler, G. R. Johnson, M. G. Miles, J. D. Wilson, J. P. Ferraris, T. F. Finnegan, R. J. Warmack, V. F. Raaen, and D. Jerome. Electrical conductivity of tetrathiafulvalenium-tetracyanoquinodimethanide (TTF-TCNQ). *Physical Review B*, 13:5105–5110, 1976.

[320] A. J. Heeger. Semiconducting and metallic polymers: the fourth generation of polymeric materials (nobel lecture). *Angewandte Chemie International Edition*, 40(14):2591–2611, 2001.

[321] S. K. Wells, J. Giergiel, T. A. Land, J. M. Lindquist, and J. C. Hemminger. Beam-induced modifications of tcnq multilayers. *Surface Science*, 257(1):129–145, 1991.

[322] J. Giergiel, S. Wells, T.A. Land, and John C. Hemminger. Growth and chemistry of tcnq films on nickel (111). *Surface Science*, 255(1):31–40, 1991.

[323] S. R. Burema and M.-L. Bocquet. A sum rule for inelastic electron tunneling spectroscopy: an ab initio study of a donor (TTF) and acceptors (TCNE, TCNQ and DCNQI) parallelly oriented on Cu(100). *Physical Chemistry Chemical Physics*, 15:16111–16119, 2013.

[324] V. Feyer, M. Graus, P. Nigge, G. Zamborlini, R. G. Acres, A. Schöll, F. Reinert, and C. M. Schneider. The geometric and electronic structure of TCNQ and TCNQ+Mn on Ag(001) and Cu(001) surfaces. *Journal of Electron Spectroscopy and Related Phenomena*, 204, Part A:125–131, 2015. Organic Electronics.

[325] M. M. Kamna, T. M. Graham, J. C. Love, and P. S. Weiss. Strong electronic perturbation of the Cu(111) surface by 7,7,8,8-tetracyanoquinonedimethane. *Surface Science*, 419(1):12–23, 1998.

[326] D. Stradi, B. Borca, S. Barja, M. Garnica, C. Diaz, J. M. Rodriguez-Garcia, M. Alcami, A. L. Vazquez de Parga, R. Miranda, and F. Martin. Understanding the self-assembly of TCNQ on Cu(111): a combined study based on scanning tunnelling microscopy experiments and density functional theory simulations. *RSC Advances*, 6:15071–15079, 2016.

[327] C. Park, G. A. Rojas, S. Jeon, S. J. Kelly, S. C. Smith, B. G. Sumpter, M. Yoon, and P. Maksymovych. Weak competing interactions control assembly of strongly bonded TCNQ ionic acceptor molecules on silver surfaces. *Physical Review B*, 90:125432, 2014.

[328] C. Wäckerlin, C. Iacovita, D. Chylarecka, P. Fesser, T. A. Jung, and N. Ballav. Assembly of 2D ionic layers by reaction of alkali halides with the organic electrophile 7,7,8,8-tetracyano-p-quinodimethane (TCNQ). *Chemical Communications*, 47:9146–9148, 2011.

[329] R. J. Murdey and W. R. Salaneck. Charge injection barrier heights across multilayer organic thin films. *Japanese Journal of Applied Physics*, 44(6R):3751, 2005.

[330] J. I. Martínez, F. Flores, J. Ortega, S. Rangan, C. Ruggieri, and R. Bartynski. Chemical interaction, space-charge layer, and molecule charging energy for a TiO2/TCNQ interface. *The Journal of Physical Chemistry C*, 119(38):22086–22091, 2015.

[331] J. T. Sun, Y. H. Lu, W. Chen, Y. P. Feng, and A. T. S. Wee. Linear tuning of charge carriers in graphene by organic molecules and charge-transfer complexes. *Physical Review B*, 81:155403, 2010.

[332] R. Ishikawa, M. Bando, Y. Morimoto, and A. Sandhu. Doping graphene films via chemically mediated charge transfer. *Nanoscale Research Letters*, 6(1):111, 2011.

[333] M. Garnica, D. Stradi, S. Barja, F. Calleja, C. Diaz, M. Alcami, N. Martin, A. L. Vazquez de Parga, F. Martin, and R. Miranda. Long-range magnetic order in a purely organic 2D layer adsorbed on epitaxial graphene. *Nature Physics*, 9(6):368–374, 2013.

[334] I. Fernández-Torrente, K. J. Franke, and J. I. Pascual. Structure and electronic configuration of tetracyanoquinodimethane layers on a Au(111) surface. *International Journal of Mass Spectrometry*, 277(1–3):269–273, 2008. Electron-induced atomic and molecular processes: A special issue honoring Eugen Illenberger on his 65th birthday.

[335] H. Yan, S. Li, Q. Yan, C.and Chen, and L. Wan. Adsorption of TTF, TCNQ and TTF-TCNQ on Au(111): An in situ ECSTM study. *Science in China Series B: Chemistry*, 52(5):559–565, 2009.

[336] J. I. Martínez, E. Abad, F. Flores, and J. Ortega. Simulating the organic-molecule/metal interface TCNQ/Au(111). *physica status solidi (b)*, 248(9):2044–2049, 2011.

[337] T. Sumimoto, K. Kudo, T. Nagashima, S. Kuniyoshi, and K. Tanaka. Formation of TTF-TCNQ charge-transfer complex in co-evaporated films. *Synthetic Metals*, 70(1):1251–1252, 1995.

[338] J. Caro, S. Garelik, and A. Figueras. Anisotropic materials prepared by OCVD: Organic molecular conductors. *Chemical Vapor Deposition*, 2(9), 1996.

[339] P. Jakob and D. Menzel. Benzene multilayers: A model for their anisotropic growth from vibrational spectroscopy and thermal desorption. *Surface Science*, 220(1):70–95, 1989.

[340] P. Tegeder, M. Danckwerts, S. Hagen, A. Hotzel, and M. Wolf. Structural transition in cyclooctatetraene adsorbed on Ru(001) probed by thermal desorption and two-photon photoemission spectroscopy. *Surface Science*, 585(3):177–190, 2005.

[341] W. Gao and A. Kahn. Electrical doping: the impact on interfaces of pi-conjugated molecular films. *Journal of Physics: Condensed Matter*, 15(38):S2757, 2003.

[342] T. Katayama, K. Mukai, S. Yoshimoto, and J. Yoshinobu. Reactive rearrangements of step atoms by adsorption and asymmetric electronic states of tetrafluoro-tetracyanoquinodimethane on Cu(100). *Physical Review B*, 83:153403, 2011.

[343] L. Romaner, G. Heimel, J.-L. Brédas, A. Gerlach, F. Schreiber, R. L. Johnson, J. Zegenhagen, S. Duhm, N. Koch, and E. Zojer. Impact of bidirectional charge transfer and molecular distortions on the electronic structure of a metal-organic interface. *Physical Review Letters*, 99:256801, 2007.

[344] G. M. Rangger, O. T. Hofmann, L. Romaner, G. Heimel, B. Bröker, R.-P. Blum, R. L. Johnson, N. Koch, and E. Zojer. F4TCNQ on Cu, Ag, and Au as prototypical example for a strong organic acceptor on coinage metals. *Physical Review B*, 79:165306, 2009.

[345] Y. Xu, O. T. Hofmann, R. Schlesinger, S. Winkler, J. Frisch, J. Niederhausen, A. Vollmer, S. Blumstengel, F. Henneberger, N. Koch, P. Rinke, and M. Scheffler. Space-charge transfer in hybrid inorganic-organic systems. *Physical Review Letters*, 111:226802, 2013.

[346] D. Qi, W. Chen, X. Gao, L. Wang, S. Chen, K. P. Loh, and A. T. S. Wee. Surface transfer doping of diamond (100) by tetrafluoro-tetracyanoquinodimethane. *Journal of the American Chemical Society*, 129(26):8084–8085, 2007.

[347] W. Chen, S. Chen, D. C. Qi, X. Y. Gao, and A Wee. Surface transfer p-type doping of epitaxial graphene. *Journal of the American Chemical Society*, 129(34):10418–10422, 2007.

[348] X. Tian, J. Xu, and X. Wang. Band gap opening of bilayer graphene by F4-TCNQ molecular doping and externally applied electric field. *The Journal of Physical Chemistry B*, 114(35):11377–11381, 2010.

[349] Y. Qi, U. Mazur, and K. W. Hipps. Charge transfer induced chemical reaction of tetracyano-p-quinodimethane adsorbed on graphene. *RSC Advances*, 2:10579–10584, 2012.

[350] W. Humphrey, A. Dalke, and K. Schulten. Vmd: Visual molecular dynamics. *Journal of Molecular Graphics*, 14(1):33–38, 1996.

[351] B. K. Min, A. R. Alemozafar, M. M. Biener, J. Biener, and C. M. Friend. Reaction of Au(111) with sulfur and oxygen: Scanning tunneling microscopic study. *Topics in Catalysis*, 36(1):77–90, 2005.

[352] W. Gao, T. A. Baker, L. Zhou, D. S. Pinnaduwage, E. Kaxiras, and C. M. Friend. Chlorine adsorption on Au(111): chlorine overlayer or surface chloride? *Journal of the American Chemical Society*, 130(11):3560–3565, 2008.

[353] K. E. Hermann and M. A. Van Hove. LEEDpat, Version 4.2, 2014.

[354] M. Narita and C. U. Pittman Jr. Preparation of tetrathiafulvalenes (TTF) and their selenium analogs-tetraselenafulvalenes (TSeF). *Synthesis*, 1976(08):489–514, 1976.

[355] G. Schukat, A. M. Richter, and E. Fanghänel. Synthesis, reactions, and selected physico-chemical properties of 1,3-and 1,2-tetrachalcogenafulvalenes. *Sulfur reports*, 7(3):155–231, 1987.

[356] M. R. Bryce. Recent progress on conducting organic charge-transfer salts. *Chemical Society Reviews*, 20:355–390, 1991.

[357] M. Adam and K. Müllen. Oligomeric tetrathiafulvalenes: Extended donors for increasing the dimensionality of electrical conduction. *Advanced Materials*, 6(6):439–459, 1994.

[358] M. R. Bryce. Tetrathiafulvalenes as π-electron donors for intramolecular charge-transfer materials. *Advanced Materials*, 11(1):11–23, 1999.

[359] M. Fourmigué and P. Batail. Activation of hydrogen-and halogen-bonding interactions in tetrathiafulvalene-based crystalline molecular conductors. *Chemical reviews*, 104(11):5379–5418, 2004.

[360] M. Iyoda, M. Hasegawa, and Y. Miyake. Bi-TTF, bis-TTF, and related TTF oligomers. *Chemical reviews*, 104(11):5085–5114, 2004.

[361] P. Frère and P. J. Skabara. Salts of extended tetrathiafulvalene analogues: relationships between molecular structure, electrochemical properties and solid state organisation. *Chemical Society Reviews*, 34(1):69–98, 2005.

[362] T. Enoki and A. Miyazaki. Magnetic TTF-based charge-transfer complexes. *Chemical reviews*, 104(11):5449–5478, 2004.

[363] J. M. Spruell, A. Coskun, D. C. Friedman, R. S. Forgan, A. A. Sarjeant, A. Trabolsi, A. C. Fahrenbach, G. Barin, W. F. Paxton, S. K. Dey, M. A. Olson, D. Benítez, E. Tkatchouk, M. T. Colvin, R. Carmielli, S. T. Caldwell, G. M. Rosair, S. G. Hewage, F. Duclairoir, J. L. Seymour, A. M. Z. Slawin, W. A. Goddard, M. R. Wasielewski, G. Cooke, and J. F. Stoddart. Highly stable tetrathiafulvalene radical dimers in [3]catenanes. *Nature Chemistry*, 2(10):870–879, 2010.

[364] R. Pfattner, S. T. Bromley, C. Rovira, and M. Mas-Torrent. Tuning crystal ordering, electronic structure, and morphology in organic semiconductors: Tetrathiafulvalenes as a model case. *Advanced Functional Materials*, 26(14):2256–2275, 2015.

[365] A. Jana, M. Ishida, J. S. Park, S. Bähring, J. O. Jeppesen, and J. L. Sessler. Tetrathiafulvalene-(TTF-) derived oligopyrrolic macrocycles. *Chemical Reviews*, 2016.

[366] J. Fraxedas, S. Garcia-Gil, S. Monturet, N. Lorente, I. Fernandez-Torrente, K. J. Franke, J. I. Pascual, A. Vollmer, R.-P. Blum, N. Koch, and P. Ordejon. Modulation of surface charge transfer through competing long-range repulsive versus short-range attractive interactions. *The Journal of Physical Chemistry C*, 115(38):18640–18648, 2011.

[367] J. I. Martínez, E. Abad, C. González, J. Ortega, and F. Flores. Theoretical characterization of the TTF/Au (1 1 1) interface: STM imaging, band alignment and charging energy. *Organic Electronics*, 13(3):399–408, 2012.

[368] C. E. Klots, R. N. Compton, and V. F. Raaen. Electronic and ionic properties of molecular TTF and TCNQ. *The Journal of Chemical Physics*, 60(3):1177–1178, 1974.

[369] R. N. Compton and C. D. Cooper. Negative ion properties of tetracyanoquinodimethan: Electron affinity and compound states. *The Journal of Chemical Physics*, 66(10):4325–4329, 1977.

[370] C. Jin, R. E. Haufler, R. L. Hettich, C. M. Barshick, R. N. Compton, A. A. Puretzky, A. V. Dem'yanenko, and A. A. Tuinman. Synthesis and characterization of molybdenum carbide clusters monc4n, (n = 1 to 4). *Science*, 263(5143):68–71, 1994.

[371] R. M. Metzger, B. Chen, U. Höpfner, M. V. Lakshmikantham, D. Vuillaume, T. Kawai, X. Wu, H. Tachibana, T. V. Hughes, J. W. Sakurai, H. Baldwin, C. Hosch, M. P. Cava, L. Brehmer, and G. J. Ashwell. Unimolecular electrical rectification in hexadecylquinolinium tricyanoquinodimethanide. *Journal of the American Chemical Society*, 119(43):10455–10466, 1997.

[372] B. Milián, R. Pou-Amérigo, R. Viruela, and E. Ortí. On the electron affinity of TCNQ. *Chemical Physics Letters*, 391(1–3):148–151, 2004.

[373] K. Kanai, K. Akaike, K. Koyasu, K. Sakai, T. Nishi, Y. Kamizuru, T. Nishi, Y. Ouchi, and K. Seki. Determination of electron affinity of electron accepting molecules. *Applied Physics A*, 95(1):309–313, 2009.

[374] S. S. Naghavi, T. Gruhn, V. Alijani, G. H. Fecher, C. Felser, K. Medjanik, D. Kutnyakhov, S. A. Nepijko, G. Schönhense, R. Rieger, M. Baumgarten, and K. Müllen. Theoretical study of new acceptor and donor molecules based on polycyclic aromatic hydrocarbons. *Journal of Molecular Spectroscopy*, 265(2):95–101, 2011.

[375] S. A. Pshenichnyuk, A. Modelli, E. F. Lazneva, and A. S. Komolov. Resonance electron attachment to tetracyanoquinodimethane. *The Journal of Physical Chemistry A*, 118(34):6810–6818, 2014.

[376] G. M. Rangger, L. Romaner, O. T. Hofmann, G. Heimel, M. G. Ramsey, and E. Zojer. Analysis of bonding between conjugated organic molecules and noble metal surfaces using orbital overlap populations. *Journal of chemical theory and computation*, 6(11):3481–3489, 2010.

[377] O. Rana, R. Srivastava, G. Chauhan, M. Zulfequar, M. Husain, P. C. Srivastava, and M. N. Kamalasanan. Modification of metal-organic interface using F4-TCNQ for enhanced hole injection properties in optoelectronic devices. *physica status solidi (a)*, 209(12):2539–2545, 2012.

[378] I. Robel, B. A. Bunker, and P. V. Kamat. Single-walled carbon nanotube-cds nanocomposites as light-harvesting assemblies: Photoinduced charge-transfer interactions. *Advanced Materials*, 17(20):2458–2463, 2005.

[379] V. Lemaur, M. Steel, D. Beljonne, J.-L. Brédas, and J. Cornil. Photoinduced charge generation and recombination dynamics in model donor/acceptor pairs for organic solar cell applications: a full quantum-chemical treatment. *Journal of the American Chemical Society*, 127(16):6077–6086, 2005.

[380] L. E. Kreno, K. Leong, O. K. Farha, M. Allendorf, R. P. Van Duyne, and J. T. Hupp. Metal–organic framework materials as chemical sensors. *Chemical reviews*, 112(2):1105–1125, 2011.

[381] A. C. Fahrenbach, S. C. Warren, J. T. Incorvati, A.-J. Avestro, J. C. Barnes, J. F. Stoddart, and B. A. Grzybowski. Organic switches for surfaces and devices. *Advanced Materials*, 25(3):331–348, 2013.

[382] X. L. Zhou, X.-Y. Zhu, and J. M. White. Photodissociation of intraadsorbate bonds at adsorbate-metal interfaces. *Accounts of Chemical Research*, 23(10):327–332, 1990.

[383] S. K. Jo and J. M. White. Correlation of photoelectron yields and photodissociation rates of chloromethane on platinum (111) and carbon-covered platinum (111). *Journal of physical chemistry*, 94(17):6852–6854, 1990.

[384] S.-J. Dixon-Warren, E. T. Jensen, and J. C. Polanyi. Direct evidence for charge-transfer photodissociation at a metal surface: CCl4/Ag(111). *Physical Review Letters*, 67(17):2395, 1991.

[385] K. Ozasa, S. Nemoto, T.i Isoshima, E. Ito, M. Maeda, and M. Hara. Photoinduced reduction and pattern preservation of giant surface potential on tris (8-hydroxyquinolinato) aluminum (III) thin films. *Applied Physics Letters*, 93(26), 2008.

[386] S. Ryu, J. Chang, and S. K. Kim. Interfacial electron dynamics and hot-electron-driven surface photochemistry of carbon tetrachloride on Ag(111). *The Journal of chemical physics*, 123(11):114710, 2005.

[387] N. Crivillers, A. Liscio, F. Di Stasio, C. Van Dyck, S. Osella, D. Cornil, S. Mian, G. M. Lazzerini, O. Fenwick, E. Orgiu, F. Reinders, S. Braun, M. Fahman, M. Mayor, J. Cornil, V. Palermo, F. Cacialli, and P. Samori. Photoinduced work function changes by isomerization of a densely packed azobenzene-based sam on au: a joint experimental and theoretical study. *Physical Chemistry Chemical Physics*, 13(32):14302–14310, 2011.

[388] G. J. Dutton, W. Jin, J. E. Reutt-Robey, and S. W. Robey. Ultrafast charge-transfer processes at an oriented phthalocyanine/C60 interface. *Physical Review B*, 82:073407, 2010.

[389] L. A. Vermeulen and M. E. Thompson. Stable photoinduced charge separation in layered viologen compounds. *Nature*, 358(6388):656–658, 1992.

[390] R. M. Williams, M. Koeberg, J. M. Lawson, Y.-Z. An, Y. Rubin, M. N. Paddon-Row, and J. W. Verhoeven. Photoinduced electron transfer to C60 across extended 3-and 11-bond hydrocarbon bridges: creation of a long-lived charge-separated state. *The Journal of Organic Chemistry*, 61(15):5055–5062, 1996.

[391] M. A. Loi, P. Denk, H. Hoppe, H. Neugebauer, C. Winder, D. Meissner, C. Brabec, N. S. Sariciftci, A. Gouloumis, P. Vázquez, and T. Torres. Long-lived photoinduced charge separation for solar cell applications in phthalocyanine–fulleropyrrolidine dyad thin films. *Journal of Materials Chemistry*, 13(4):700–704, 2003.

[392] S. Å. Lindgren and L. Walldén. Cu surface state and Cs valence electrons in photoelectron spectra from the Cu(111)/Cs adsorption system. *Solid State Communications*, 28(3):283–286, 1978.

[393] C. M. Whelan, C. J. Barnes, C. G. H. Walker, and N. M. D. Brown. Benzenethiol adsorption on Au(111) studied by synchrotron ARUPS, HREELS and XPS. *Surface Science*, 425(2–3):195–211, 1999.

[394] G. Dutton, D. P. Quinn, C. D. Lindstrom, and X.-Y. Zhu. Exciton dynamics at molecule-metal interfaces: C60/Au(111). *Physical Review B*, 72:045441, 2005.

[395] P. Pervan, P. Lazić, M. Petrović, I. Šrut Rakić, I. Pletikosić, M. Kralj, M. Milun, and T. Valla. Li adsorption versus graphene intercalation on Ir(111): From quenching to restoration of the Ir surface state. *Physical Review B*, 92:245415, 2015.

[396] L. Dong, Z. Gao, and N. Lin. Self-assembly of metal–organic coordination structures on surfaces. *Progress in Surface Science*, 91(3):101–135, 2016.

[397] B. Fraboni, A. Fraleoni-Morgera, Y. Geerts, A. Morpurgo, and V. Podzorov. Organic single crystals: An essential step to new physics and higher performances of optoelectronic devices. *Advanced Functional Materials*, 26(14):2229–2232, 2016.

[398] C. D. Dimitrakopoulos and P. R. L. Malenfant. Organic thin film transistors for large area electronics. *Advanced Materials*, 14(2):99–117, 2002.

[399] A. Troisi and G. Orlandi. Charge-transport regime of crystalline organic semiconductors: Diffusion limited by thermal off-diagonal electronic disorder. *Physical Review Letters*, 96:086601, 2006.

[400] B. Bluelle, A. Troisi, R. Haeusermann, and B. Batlogg. Charge transport perpendicular to the high mobility plane in organic crystals: Bandlike temperature dependence maintained despite hundredfold anisotropy. *Physical Review B*, 93:035205, 2016.

[401] H. Yamane, S. Kera, K. K. Okudaira, D. Yoshimura, K. Seki, and N. Ueno. Intermolecular energy-band dispersion in PTCDA multilayers. *Physical Review B*, 68:033102, 2003.

[402] Q. Xin, S. Duhm, F. Bussolotti, K. Akaike, Y. Kubozono, H. Aoki, T. Kosugi, S. Kera, and N. Ueno. Accessing surface brillouin zone and band structure of picene single crystals. *Physical Review Letters*, 108:226401, 2012.

[403] T. J. Emge, M. Maxfield, D. O. Cowan, and T. J. Kistenmacher. Solution and solid state studies of tetrafluoro-7,7,8,8-tetracyano-p-quinodimethane, TCNQF4. evidence for long-range amphoteric intermolecular interactions and low-dimensionality in the solid state structure. *Molecular Crystals and Liquid Crystals*, 65(3-4):161–178, 1981.

[404] V. Capek and E. Silinsh. Organic molecular crystals: Interaction, localization, and transport phenomena, 1994.

[405] T. Schultz, R. Schlesinger, J. Niederhausen, F. Henneberger, S. Sadofev, S. Blumstengel, A. Vollmer, F. Bussolotti, J.-P. Yang, S. Kera, K. Parvez, N. Ueno, K. Müllen, and N. Koch. Tuning the work function of gan with organic molecular acceptors. *Physical Review B*, 93:125309, 2016.

[406] J. M. Fernandes, M. R. Kiran, H. Ulla, M. N. Satyanarayan, and G. Umesh. Investigation of hole-injection in a-NPD using capacitance and impedance spectroscopy techniques with F4TCNQ as hole-injection layer: Initial studies. *Superlattices and Microstructures*, 76:385–393, 2014.

[407] F. Guillain, J. Endres, L. Bourgeois, A. Kahn, L. Vignau, and G. Wantz. Solution-processed p-dopant as interlayer in polymer solar cells. *ACS applied materials & interfaces*, 8(14):9262–9267, 2016.

[408] H. Bässler. Charge transport in disordered organic photoconductors a monte carlo simulation study. *physica status solidi (b)*, 175(1):15–56, 1993.

[409] O. T. Hofmann. Institute of Solid State Physics, TU Graz, 2016. Personal Communication.

[410] S. A. Buntin, L. J. Richter, R. R. Cavanagh, and D. S. King. Optically driven surface reactions: Evidence for the role of hot electrons. *Physical Review Letters*, 61:1321–1324, 1988.

[411] M. Bauer and M. Aeschlimann. Dynamics of excited electrons in metals, thin films and nanostructures. *Journal of electron spectroscopy and related phenomena*, 124(2):225–243, 2002.

[412] Hermann Nienhaus. Electronic excitations by chemical reactions on metal surfaces. *Surface Science Reports*, 45(1):1–78, 2002.

[413] M. Bauer, A. Marienfeld, and M. Aeschlimann. Hot electron lifetimes in metals probed by time-resolved two-photon photoemission. *Progress in Surface Science*, 90(3):319–376, 2015.

[414] M. Aeschlimann, M. Bauer, and S. Pawlik. Competing nonradiative channels for hot electron induced surface photochemistry. *Chemical physics*, 205(1):127–141, 1996.

[415] M. Bauer, S. Pawlik, and M. Aeschlimann. Electron dynamics of aluminum investigated by means of time-resolved photoemission. In *Optoelectronics and High-Power Lasers & Applications*, pages 201–210. International Society for Optics and Photonics, 1998.

[416] E. Knoesel, A. Hotzel, and M. Wolf. Ultrafast dynamics of hot electrons and holes in copper: Excitation, energy relaxation, and transport effects. *Physical Review B*, 57(20):12812, 1998.

[417] M. Aeschlimann, M. Bauer, S. Pawlik, R. Knorren, G. Bouzerar, and K. H. Bennemann. Transport and dynamics of optically excited electrons in metals. *Applied Physics A*, 71(5):485–491, 2000.

[418] R. Porath, T. Ohms, M. Scharte, J. Beesley, M. Wessendorf, O. Andreyev, C. Wiemann, and M. Aeschlimann. Relaxation of hot electrons in solids of reduced dimensions. In *Low-Dimensional Systems: Theory, Preparation, and Some Applications*, pages 227–239. Springer, 2003.

[419] F. Ladstädter, P. F. de Pablos, U. Hohenester, P. Puschnig, C. Ambrosch-Draxl, P. L. de Andrés, F. J. García-Vidal, and F. Flores. Hot-electron lifetimes in metals: A combined ab initio calculation and ballistic electron emission spectroscopy analysis. *Physical Review B*, 68(8):085107, 2003.

[420] M. Lisowski, P. A. Loukakos, U. Bovensiepen, and M. Wolf. Femtosecond dynamics and transport of optically excited electrons in epitaxial Cu films on Si(111)-7x7. *Applied Physics A*, 79(4-6):739–741, 2004.

[421] A. Goldmann, R. Matzdorf, and F. Theilmann. Experimental hot-electron and photohole lifetimes at metal surfaces - what do we know? *Surface science*, 414(1):L932–L937, 1998.

[422] J. J. Quinn and R. A. Ferrell. Electron self-energy approach to correlation in a degenerate electron gas. *Physical Review*, 112(3):812, 1958.

[423] J. Cao, Y. Gao, H. E. Elsayed-Ali, R. J. D. Miller, and D. A. Mantell. Femtosecond photoemission study of ultrafast electron dynamics in single-crystal Au(111) films. *Physical Review B*, 58:10948–10952, 1998.

[424] C. A. Schmuttenmaer, M. Aeschlimann, H. E. Elsayed-Ali, R. J. D. Miller, D. A. Mantell, J. Cao, and Y. Gao. Time-resolved two-photon photoemission from Cu(100): Energy dependence of electron relaxation. *Physical Review B*, 50:8957–8960, 1994.

[425] W. S. Fann, R. Storz, H. W. K. Tom, and J. Bokor. Direct measurement of nonequilibrium electron-energy distributions in subpicosecond laser-heated gold films. *Physical Review Letters*, 68(18):2834, 1992.

[426] W. S. Fann, R. Storz, H. W. K. Tom, and J. Bokor. Electron thermalization in gold. *Physical Review B*, 46(20):13592, 1992.

[427] C.-K. Sun, F. Vallée, L. H. Acioli, E. P. Ippen, and J. G. Fujimoto. Femtosecond-tunable measurement of electron thermalization in gold. *Physical Review B*, 50(20):15337, 1994.

[428] S. Ogawa, H. Nagano, and H. Petek. Hot-electron dynamics at Cu (100), Cu (110), and Cu (111) surfaces: mcomparison of experiment with fermi-liquid theory. *Physical Review B*, 55(16):10869, 1997.

[429] J. J Quinn. The range of hot electrons and holes in metals. *Applied Physics Letters*, 2(9):167–169, 1963.

[430] I. G. Gurtubay, J. M. Pitarke, and P. M. Echenique. Exchange and correlation effects in the relaxation of hot electrons in noble metals. *Physical Review B*, 69(24):245106, 2004.

List of Publications

Publications Related to this Thesis

Extended Space Charge Region and Unoccupied Molecular Band Formation in Epitaxial F_4TCNQ Films
David Gerbert, Friedrich Maaß and Petra Tegeder
Submitted (2017)

Connecting Band Formation and Charge Transfer at Metal/Organic Interfaces
David Gerbert, Oliver Hofmann and Petra Tegeder
In Preparation (2017)

Studying a Thermally Reversible Photo-Induced Charge Transfer at the TCNQ/Au(111) Interface
David Gerbert and Petra Tegeder
In Preparation (2017)

Publications Not Related to this Thesis

Excitonic States in Narrow Armchair Graphene Nanoribbons on Gold Surfaces
Christopher Bronner, David Gerbert, Alexander Broska and Petra Tegeder
J. Phys. Chem. C **120** (45), 26168-26172 (2016)

Charge Transfer at Organic/Inorganic Interfaces and the Formation of Space Charge Regions Studied with Infrared Light
Sebastian Beck, David Gerbert, Tobias Glaser and Annemarie Pucci
J. Phys. Chem. C **119** (22), 12545-12550 (2015)

Impact of the plasmonic near- and far-field resonance-energy shift on the enhancement of infrared vibrational signals
Jochen Vogt, Christian Huck, Frank Neubrech, Andrea Toma, David Gerbert and Annemarie Pucci
Phys. Chem. Chem. Phys. **17**, 21169-21175 (2015)

IR spectroscopic studies of charge transfer in organic semiconductors
Sebastian Beck, David Gerbert, Christian Krekeler, Tobias Glaser and Annemarie Pucci
Proc. SPIE 9137 **9137**, 91370T (2014)

Surface-Enhanced Infrared Spectroscopy Using Nanometer-Sized Gaps
Christian Huck, Frank Neubrech, Jochen Vogt, Andrea Toma, David Gerbert, Julia Katzmann, Thomas Härting and Annemarie Pucci
ACS Nano **8** (5), 4908-4914 (2014)

List of Conference Contribiutions

Band Formation at the F_4TCNQ-Au(111) interface
David Gerbert and Petra Tegeder
Poster
International Conference on Internal Interfaces, Marburg, Germany, 2016

Characterizing Charge-Transfer Effects at Metal/Organic Interfaces by means of Two-Photon Photoemission
David Gerbert and Petra Tegeder
Presentation
DPG Spring Meeting, Regensburg, Germany, 2016

Studying the F_4TCNQ/Au(111) Interface with Two-Photon Photoemission
David Gerbert, Sascha Feldmann and Petra Tegeder
Poster
DPG Spring Meeting, Regensburg, Germany, 2016

Characterizing Charge-Transfer Effects at Metal-Organic Interfaces by Two-Photon Photoemission
David Gerbert, Sascha Feldmann and Petra Tegeder
Poster
9. HGSFP Winterschool, Obergurgl, Austria, 2016

Characterizing Charge-Transfer Effects at Metal-Organic Interfaces by Two-Photon Photoemission
David Gerbert, Sascha Feldmann and Petra Tegeder
Poster
13. European Conference on Molecular Electronics, Strasbourg, France, 2015

Controlled photo-induced work function manipulation of the TCNQ/Au(111) interface
David Gerbert and Petra Tegeder
Presentation
DPG Spring Meeting, Berlin, Germany, 2015

Photo-induced effects in TCNQ adsorbed on Au(111)
David Gerbert and Petra Tegeder
Poster
578. Wilhelm and Else Heraeus Seminar on 'Charge-Transfer Effects in Organic Heterostructures', Bad Honnef, Germany, 2014

IR spectroscopic study of molecular orientation and interaction in emittersystems for blue organic light emitting diodes
David Gerbert, Tobias Glaser, Sebastian Beck, Christian Lennartz and Annemarie Pucci
Poster
DPG Spring Meeting, Dresden, Germany, 2014

All contributions listed here were as presenting author.

List of Supervised Theses

Untersuchung des molekularen Mischsystems TTF/TCNQ mittels Zwei-Photonen-Photoemission
Jakob Steidel, Ruprecht-Karls-Universität Heidelberg, Juni 2016
Bachelor Thesis

Untersuchung der F_4TCNQ/Gold(111) Grenzfläche mittels winkelaufgelöster Zwei-Photonen-Photoemissionsspektroskopie
Helge-Boj Hansen, Ruprecht-Karls-Universität Heidelberg, Januar 2016
Scientific Internship

Elektronische Eigenschaften von Tetrathiafulvalen auf Gold(111)
Manuel Brand, Ruprecht-Karls-Universität Heidelberg, Juni 2015
Bachelor Theses

Investigating the Electronic Structure of the F_4TCNQ/Au(111) Interface by means of Two-Photon Photoemission Spectroscopy
Sascha Feldmann, Ruprecht-Karls-Universität Heidelberg, Mai 2015
Bachelor Theses

Adsorption und elektronische Eigenschaften von F_4TCNQ auf Gold(111)
Hendrik Hoffmann, Ruprecht-Karls-Universität Heidelberg, Mai 2015
Bachelor Theses

Elektronische Eigenschaften von Tetraazaperopyrenen auf Gold(111)
Alexander Broska, Ruprecht-Karls-Universität Heidelberg, Juli 2014
Master Theses

Untersuchung der elektronischen Struktur eines auf Au(111) adsorbierten TAPP-Derivates mithilfe von Zwei-Photonen-Photoemissionsspektroskopie
André Hermannsdorfer, Ruprecht-Karls-Universität Heidelberg, April 2014
Scientific Internship

Zwei-Photonen-Photoemissionsspektroskopie and Gold(111)-Oberflächen
Rebecca Schäfer, Ruprecht-Karls-Universität Heidelberg, Januar 2014
Scientific Internship

Acknowledgements

An dieser Stelle möchte ich mich bei allen bedanken, die mich im Laufe meiner Promotion unterstützt und begleitet haben. Insbesondere danke ich:

Frau Prof. Dr. Petra Tegeder für die Möglichkeit, in ihrer Arbeitsgruppe am Physikalisch-Chemischen Institut zu promovieren, die hervorragende Betreuung und für die Freiheit, eigene Schwerpunkte setzen zu dürfen. Außerdem möchte ich mich besonders für die Unterstützung der Teilnahme an zahlreichen Konferenzen und zwei Forschungsaufenthalten in Oxfordshire und New York City bedanken.

Frau Prof. Dr. Annemarie Pucci für die freundliche Übernahme der offiziellen Erstbetreuung und des Erstgutachtens.

Herrn Prof. Dr. Wolfgang Kowalsky für die bereitwillige Übernahme des Zweitgutachtens.

Herrn Dr. Oliver T. Hofmann für die fruchtbaren Diskussionen und den Input durch DFT Rechnungen.

meinen Kollegen Christopher Bronner, Marc Hänsel, Friedrich Maaß, Michael Schulze, Arnulf Stein und Stephan Stremlau für die tolle Arbeitsumgebung, die immerwährende Hilfsbereitschaft und die vielen hilfreichen Diskussionen. Besonders danke ich Chris für seine umfassende Einführung in den experimentellen Aufbau und Marc für die tolle, gemeinsame Zeit im Labor und in NYC.

allen Mitarbeitern der AG Pucci für die regen Diskussionen. Besonders Sabina Hillebrandt, Michael Sendner, Dr. Sebastian Beck und Dr. Tobias Glaser durch die ich immer Einblicke in die Welt der IR-Spektroskopie am InnovationLab erhalten habe.

allen Forschungspraktikanten, Bachelorstudenten und Masterstudenten, die ich in den letzten Jahren betreuen durfte und die mit mir so manche Stunde im Labor verbracht haben. Insbesondere bedanke ich mich bei Sascha Feldmann für eine tolle Zeit in Strasbourg.

meinen Freunden und ehemaligen Kommilitonen Stefan Arnold, Randolf Beerwerth, Karin Firnkes, Markus Gölz, Alexander Gorel, Fabian Klein und Mark Schafbuch, die mir über das Studium hinaus erhalten geblieben sind und mit denen ich viele schöne, gemeinsame Stunden verbringen durfte.

Ein ganz besonderer Dank gilt meinen Eltern, Großeltern und Geschwistern, die immer an mich geglaubt und mich jederzeit bestmöglich unterstützt haben.

Und zu guter Letzt gilt mein größter Dank Tessa, die mein Leben auf den Kopf stellt und bereichert, für Entspannung und Ausgleich sorgt, und deren große Unterstützung, Verständnis und aufbauenden Worte maßgeblich zum Gelingen dieser Arbeit beigetragen haben.

DANKE!